Sloshing and Thermal Mixing

Connor Rohmann-Shaw

Submitted in accordance with the requirements for the degree of

Doctor of Philosophy

The University of Leeds

EPSRC Centre for Doctoral Training in Fluid Dynamics

February 2022

Declaration

The candidate confirms that the work submitted is his own, except where work which has formed part of jointly authored publications has been included. The contribution of the candidate and the other authors to this work has been explicitly indicated below. The candidate confirms that appropriate credit has been given within the thesis where reference has been made to the work of others.

Acknowledgements

First and foremost, I say thank you to my academic supervisors Duncan Borman and Mark Wilson. Their support and kindness throughout my time in Leeds, and the weird COVID days that followed has been immense. They have both challenged and encouraged me in equal measures at times when I needed it most. For that, I will always be grateful.

To my office pals, you know who you are... My memories of our time in Leeds will always bring a smile to my face because of you. I was beyond fortunate to be surrounded by a group so talented and generous. All of you have contributed to this thesis in one way or another.

Thank you to my friends and family. The love and laughs you've given me these last few years have kept me going. I couldn't have done it without you.

I would like to thank members of the fuel team at BAE Systems. Conversations with them at both Leeds and Warton Aerodrome offered invaluable insight and inspiration for the work contained in this thesis.

I would also like to thank all those involved in running the CDT in Fluid Dynamic at Leeds. My involvement there was a privilege one of the greatest learning experiences of my life. I also extend my thanks to the EPSRC, whose funding made this research possible.

For Lisa.

Abstract

Modern aircraft increasingly use fuel as a heat sink to help manage the ever-growing thermal loads generated during flight operations. As warm fuel is recirculated into cooler tanks, fuel streams of varying temperature are mixed together. This, coupled with dynamic sloshing of the free surface in response to aircraft accelerations gives rise to a highly complex system that is not well understood. In this thesis, a computational methodology is established for studying such flows.

The ability of the Volume of Fluid (VOF) OpenFOAM solver `interFoam` to accurately predict sloshing under resonant conditions is tested over a range of excitation frequencies, including the first 3 natural modes. Its performance in doing so is validated against experiments.

Issues regarding two-equation RANS models and their overproduction of turbulence beneath the free surface are reviewed extensively. A variety of turbulence modelling strategies to help overcome this are identified and tested against benchmark experimental data. These model formulations are then applied to the simulation of sloshing at resonance across a range of forcing amplitudes.

A profound sensitivity to turbulence model is demonstrated — subsurface eddy viscosity is found to vary by up to 4 orders of magnitude when modelling sloshing at the first natural frequency. This is found to have only a subtle damping effect on free surface response. However, erroneous levels of turbulent diffusivity in the subsurface have much more serious implications when attempting to model the transport of heat by unresolved eddies. A stabilised $k-\omega$ SST model, featuring an additional buoyancy source term in the k-equation is identified as the most robust in accurately predicting subsurface turbulence.

Having established a numerical model that can properly account for free surface mo-

tions and subsurface turbulence, a parametric study of sloshing and thermal mixing is undertaken. In order to establish a base-line case, buoyancy-driven mixing in partially filled static tanks is analysed. The ability of 2D models to model convective mixing is validated against high fidelity 3D LES simulations. Despite some differences in the developed flow patterns, good agreement is found when comparing macroscopic mixing rates over a range of initial temperature conditions.

Sloshing is then introduced with tank motions across a range of forcing amplitudes, modal frequencies and fill heights. A metric is established for measuring the mixing enhancement from slosh-induced motions relative to the static tank cases.

At low amplitude excitations, sloshing does not significantly enhance mixing, which remains buoyancy-dominated. At medium to high forcing amplitude excitations, the effects of sloshing are highly variable depending on the characteristic behaviour of each mode shape. Shallow and intermediate flow regimes are found to produce superior environments for mixing. A transition from standing to travelling waves results in a subsurface flow field more broadly influenced by the dynamic free surface. An interesting case is identified in which high amplitude sloshing is observed to suppress mixing. The interaction of convective currents with the dynamic surface region is found to restrict the circulation of warmer liquid into low-energy regions away from the surface.

The role of sloshing in thermal mixing is demonstrated to be highly complex, with a particularly high degree of sensitivity to the parameters. However, this thesis makes a first step in identifying some of the key physics. Furthermore, by taking a rigorous approach in assessing the relevant physical models, a numerical framework is established for simulating such flows. This tool can be used in the design and analysis of aircraft fuel systems, and easily extends to other applications.

Contents

List of Figures

List of Tables

Nomenclature

List of Abbreviations

CDT	Centre for Doctoral Training
DNS	Direct Numerical Simulation
FTMS	Fuel Thermal Management System
FVM	Finite-Volume Method
LES	Large Eddy Simulation
RANS	Reynolds Averaged Navier-Stokes
RMS	Root Mean Square
SPH	Smooth Particle Hydrodynamics
VOF	Volume of Fluid

Dimensionless Groups

Gr	Grashof number
Pr	Parndtl number
Pr_t	Turbulent prandtl number
Ra	Rayleigh number
Re	Reynolds number

Ri Richardson number

Greek Letters

α Volume fraction, $[-]$

β Thermal expansion coefficient $[\mathrm{kg} \cdot \mathrm{K}^{-1}]$

$\boldsymbol{\omega}$ Vorticity vector $[\mathrm{s}^{-1}]$

$\boldsymbol{\tau}$ Shear stress tensor $[\mathrm{N} \cdot \mathrm{m}^{-2}]$

η Wave amplitude [m]

Γ Scalar diffusivity $[\mathrm{m}^2 \cdot \mathrm{s}^{-1}]$

κ Thermal diffusivity $[\mathrm{m}^2 \cdot \mathrm{s}^{-1}]$

κ^* Von Karman constant $-$

κ_{eff} Effective thermal diffusivity, $\kappa + \kappa_{\mathrm{turb}}$ $[\mathrm{m}^2 \cdot \mathrm{s}^{-1}]$

κ_{turb} Turbulent thermal diffusivity $[\mathrm{m}^2 \cdot \mathrm{s}^{-1}]$

μ Dynamic viscosity $[\mathrm{kg} \cdot \mathrm{m}^{-1} \cdot \mathrm{s}^{-1}]$

μ_T Dynamic turbulent viscosity $[\mathrm{kg} \cdot \mathrm{m}^{-1} \cdot \mathrm{s}^{-1}]$

ν Kinematic viscosity $[\mathrm{m}^2 \cdot \mathrm{s}^{-1}]$

ν_T Kinematic turbulent viscosity $[\mathrm{m}^2 \cdot \mathrm{s}^{-1}]$

ν_T^* Kinematic turbulent viscosity ratio $[-]$

ν_{eff} Effective kinematic viscosity, $\nu + \nu_T$ $[\mathrm{m}^2 \cdot \mathrm{s}^{-1}]$

ω Forcing frequency $[\mathrm{rad} \cdot \mathrm{s}^{-1}]$

ω^* Non-dimensional forcing frequency $[-]$

ω_n Modal frequency $[\mathrm{rad} \cdot \mathrm{s}^{-1}]$

ϕ Generic scalar

ρ Density [$\mathrm{kg} \cdot \mathrm{m}^{-3}$]

ρ_0 Reference density [$\mathrm{kg} \cdot \mathrm{m}^{-3}$]

ρ_v Temperature-dependent density [$\mathrm{kg} \cdot \mathrm{m}^{-3}$]

σ Surface tension coefficient [$-$]

Latin Letters

$\bar{T}$ Mean temperature [K]

$\bar{u}_i$ Reynolds-averaged/spatially filtered velocity [$\mathrm{m} \cdot \mathrm{s}^{-1}$]

ΔT Temperature difference [K]

$\dot{Q}$ Rate of change of internal heat [W]

A Forcing amplitude [m]

A^* Non-dimensional forcing amplitude [$-$]

A_θ Roll amplitude [rad]

c_p Specific heat capacity under constant pressure [$\mathrm{J} \cdot \mathrm{kg}^{-1}$]

D Van Driest function [$-$]

E_{mix} Enchancement factor for mixing [$-$]

g Gravity [$\mathrm{m} \cdot \mathrm{s}^{-2}$]

h Free surface height [m]

h_{fs} Tank fill height [m]

I Turbulence intensity [$-$]

k Thermal conductivity [$\mathrm{W} \cdot \mathrm{m}^{-1} \cdot \mathrm{K}^{-1}$]

k_n	Wave number [m^{-1}]
L_i	Length in each spatial dimension [m]
N	Total number of data points [−]
n_i	Number of grid cells in each dimension [−]
p	Pressure [$\mathrm{N} \cdot \mathrm{m}^{-2}$]
p^*	Modified pressure [$\mathrm{N} \cdot \mathrm{m}^{-2}$]
S_{ij}	Mean strain rate tensor [s^{-1}]
T	Temperature [K]
t	Time [s]
t_b^*	Non-dimensional buoyancy time-scale [−]
T_0	Reference temperature [K]
t_b	Buoyancy time-scale [s]
U_i	Time-averaged velocty [$\mathrm{m} \cdot \mathrm{s}^{-1}$]
u_i	Velocity [$\mathrm{m} \cdot \mathrm{s}^{-1}$]
u_i'	Turbulent velocity fluctuation [$\mathrm{m} \cdot \mathrm{s}^{-1}$]
$U_{i,\mathrm{RMS}}$	Root-mean-squared velocity [$\mathrm{m} \cdot \mathrm{s}^{-1}$]
V^*	Normalised coefficient of variation [−]
x	Horizontal spatial dimension [−]
x^*/X^*	Horizontal dimension scaled by tank length [−]
y	Vertical spatial dimension [−]
y^*/Y^*	Vertical dimension scaled by tank length [−]
y^+	Non-dimensional wall distance [−]

Chapter 1

Introduction

1.1 Research motivation: Aircraft fuel thermal management systems

Modern aircraft capabilities are constantly exceeding the limits seen by those of previous incarnations. The growing need for speed and manoeuvrability demands greater performance from the gas turbine engines and actuator systems. In civil aircraft, the expectations on range and economy of flight are increasing, as is the complexity of avionics. Electrical systems are used more and more to control and provide as much information about the aircraft as possible. Despite the variety of mission profiles that can define the performance requirements of aircraft and the resulting myriad, what they share in common is the ever increasing thermal loads generated by such advances.

Advanced military aircraft in particular have some design requirements that not only increase the generation of heat, but also complicate the issue of dealing with thermal loads. In addition to high flight speeds (required heat sink increases at some rate above linearly with respect to Mach number) and the ability to perform dynamic manoeuvres, a desire to reduce their detectable footprint means airframes

are constructed from composites that happen to be poor dissipators of heat. Air cooling comes at the cost of an unacceptable drag penalty for high performance aircraft, and so ram air intrusions are kept to a minimum. Even if this were not the case, ram air is less effective as a coolant at hypersonic speeds as the air temperature increases. For future aircraft, this issue will only become more common.

In search of creative solutions to thermal management problems, aerospace engineers increasingly turn to fuel as a heat sink. Aviation fuels generally fall into the group of hydrocarbons known as kerosene. These fuels can be optimised for use as a heat sink by adding catalysts to modify their properties, allowing endothermic reactions to take place which can then facilitate further heat absorption, and thus increasing the overall capacity of the fuel to absorb thermal loads.

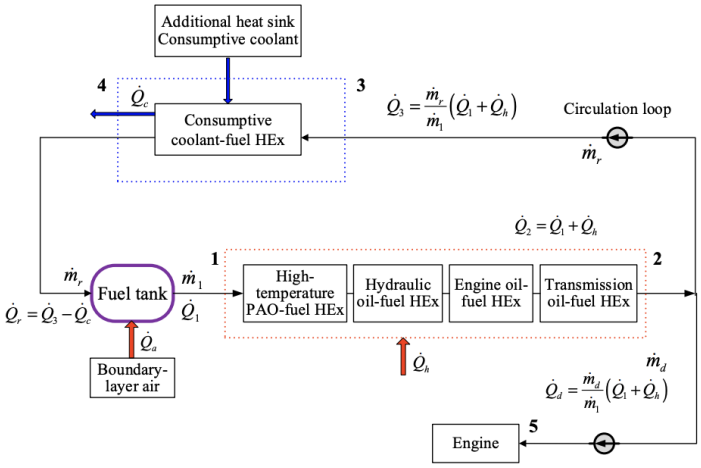

Figure 1.1: Example fuel thermal management system architecture, illustrating heat sources/sinks with recirculating fuel lines (Pang et al., 2018)

Fuel thermal management systems (FTMS) may take on many forms, with the optimisation of their configuration being an active area of research and development. Many system architectures have been proposed in the literature, the most fundamental feature being the recirculation of fuel and regulation of flow rates as a function of thrust requirements and thermal load. One such concept can be seen in **Fig.** 1.1. Fuel is pumped from the feeder tanks to the engine, potentially passing through numerous heat exchangers along the way — each coupled with various

subsystems, e.g. engine oil, transmission oil, hydraulic oil etc.

Depending on the thrust requirements at any given time, unburnt fuel is diverted, recirculated ($\dot{m}_r$) and returned to the feeder fuel tanks. If thermal loads from subsystems increase, the flow rate through fuel lines, $\dot{m}_1$ can be increased so as to permit the fuel to absorb heat at a greater rate without exceeding critical temperatures. This can be done independently of thrust requirements as the excess unburnt fuel can simply be returned to the feeder tank. Warm fuel may be passed through a heat exchanger and cooled by ram air (In some cases this might not be possible e.g. during take-off/landing taxiing when a flow of cool air is not available) before returning to the feeder tank, where the heated fuel is allowed to mix with the cooler liquid residing within. Running fuel at an elevated temperature also has secondary benefits in improving the engine thermodynamic cycle, which in turn reduces the specific fuel consumption, making the propulsion system more economical (Huang et al., 2004).

Heating fuel also serves to alleviate some challenges of 'cold fuel management'. Aircraft fuels are comprised of a mixture of hydrocarbons, which typically do not share the same freezing point. As the mixture cools, the constituent parts with the highest freezing point begin to solidify, forming wax crystals. In aviation vernacular this is a process known as 'waxing', which can be problematic if these crystals are allowed to enter fuel lines and cause blockages (Moir and Seabridge, 2011). Freezing points of jet fuels vary, but typically fall within the range of $T = -60°C \rightarrow -40°C$. For aircraft flying at very high altitudes and/or operating along Arctic routes, the threat of waxing in fuel tanks must be taken seriously. Water droplets entering the fuel system can also be problematic. After cruising at altitude, even without latent water impurities present in the fuel, humid air can enter fuel tanks via venting systems and quickly condense upon contacting cold structures (Langton et al., 2009). **Fig.** 1.2 charts the relevant fuel states at lower temperatures.

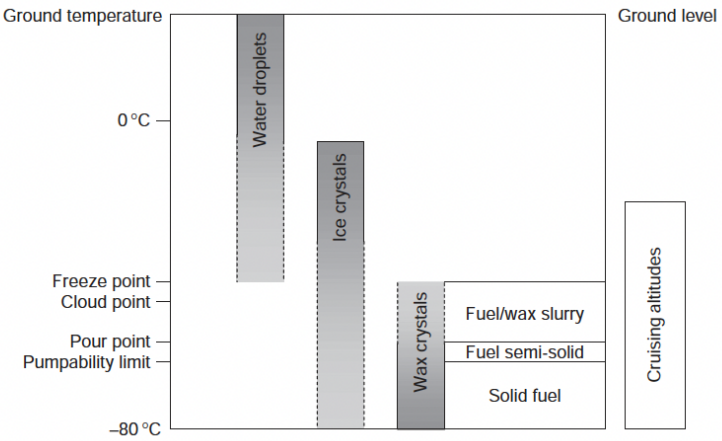

Figure 1.2: Effects of cold temperatures on operating fuel states Langton et al. (2009)

Models have been developed to describe the demands on the FTMS throughout flight operation, with the aim of using these to find optimal performance given the physical and design constraints. Alyanak and Allison (2016) propose one example of a very simple formulation for predicting fuel temperature as a function of lumped heat sinks/sources throughout the aircraft:

$$mc_v \frac{dT_{fuel}}{dt} = \dot{Q}_{env} + \left(1 - \frac{\dot{m}_{burned}}{\dot{m}_{flow}}\right)\dot{Q}_{sink} - \dot{Q}_{out}, \tag{1.1}$$

where T_{fuel} is the temperature of the fuel in the feeder tank, m is the fuel mass internal to the tank at any given time, c_v is the fuel specific heat capacity in the case of a constant volume system, $\dot{Q}_{env}$ is the heat lost/added to the tank from the environment (e.g radiation, conduction through tank walls), $\dot{m}_{burned}$ is the rate at which fuel mass is burned through combustion, $\dot{m}_{flow}$ is the flow rate extracted from the tank and $\dot{Q}_{out}$ is heat rejected from the fuel. Pang et al. (2018) present a more developed model, which they couple to a fuel-system control algorithm with the aims of controlling and optimising the FTSM performance while adhering to upper fuel temperature limits.

The issue with models such as this is that they typically used 1D thermal

network models, in which subsystems are treated as 'lumped' parameters in terms of their thermodynamic impact. The temperature of fuel inside feeder tanks is assumed uniform, i.e. the heated fuel re-entering the feed tank spontaneously mixes with the cooler body of fuel. The operating conditions inside feeder tanks are actually quite complex. Not only is fuel being pumped out and fed to the engine, and recirculated warm fuel being pumped back in, but also cold fuel from other tanks is fed in to ensure that the feeder tank is never completely depleted (essential to ensure feed pumps to the engine are not starved). This leads to an interesting system in which we have a confluence of mixing fuel streams of different temperatures, and perhaps the assumption of there being a homogeneous fuel temperature inside the tanks is a gross simplification.

Commercial flight is actually quite a calm affair. Other than take-off/landing, flight tends to take place under steady 1g conditions. For the comfort and safety of passengers, extreme accelerations are avoided, but the nature of military aviation demands them. For advanced/military aircraft, flight can be characterised by sudden accelerations, high-g manoeuvres and even negative-g flight during inversions. This leads to dynamic conditions within fuel systems, with sloshing inevitable.

Liquid sloshing of a fuel body in which multiple fuel streams of different temperatures are pumped in/out of makes for an extremely interesting system, not only from an application-specific engineering perspective, but also to the fluid dynamicist. In the next chapter we'll see that sloshing is a complex problem that has been covered widely in the literature. However, the interaction between sloshing and thermal considerations has gained extremely limited coverage. Of the scant research in existence to date regarding thermodynamic sloshing, no attention has been paid to thermal mixing internal to liquid bodies, and the role sloshing plays in that process.

1.1.1 Research scope

This research was initialised by a proposal of interest by BAE Systems, in which they had outlined some of the key challenges and unanswered questions they had regarding sloshing. These included a number of issues internal to the fuel system e.g. the impact of sloshing on thermal mixing in the fuel, vapour concentrations, fuel waxing, heat transfer coefficients and how a better understanding of sloshing might inform internal tank design and pump orientations.

Sloshing and thermal mixing inside unique, aircraft-specific tanks with complex geometries when coupled to in-flight accelerations is a complicated problem. Rather that attempt to tackle such a complex problem all in one go, this research is intended to serve as a jumping off point in which we start at the very beginning. Therefore, this work focuses on sloshing and thermal mixing in 'simpler' scenarios, so that we can begin to gain a fundamental understanding of how the two phenomena interact.

1.2 Thesis aim and contributions

1.2.1 Aim

In this thesis, the primary aim is to develop an understanding of the role dynamic liquid sloshing plays in thermal mixing. This will be achieved through a series of research contributions. On a chapter-by-chapter basis, these are as follows:

1.2.2 Research contributions

1. In **Chapter** 2, the research is contextualised with an overview of sloshing fundamentals and a more broad view of the challenges posed by sloshing in industry.

2. A numerical framework for modelling isothermal sloshing flows is described in **Chapter** 3, based on the `OpenFOAM` solver `interFoam`. The model is validated against experimental measurements of subsurface pressure and free surface response data, covering a range of sloshing regimes and scenarios. The model's performance is tested under challenging resonant conditions, over a range of natural frequencies.

3. In **Chapter** 4, some issues regarding the well-documented overproduction of turbulence in free surface flows are addressed — in particular, when solving the Reynolds Averaged Navier-Stokes (RANS) equations. Various turbulence modelling approaches are tested against benchmark experiments.

4. In **Chapter** 5, the profound way in which the prediction of subsurface eddy viscosity is affected by the turbulence modelling strategy for resonant sloshing flows is demonstrated. Eddy diffusivity is an important component in modelling thermal mixing in turbulent flows. Therefore, this is a critical step.

5. The `interFoam` solver is extended to include heat transfer in **Chapter** 6. The Boussinesq approximation is used to account for the effects of buoyancy in thermal mixing.

6. The numerical model is used in **Chapter** 7 to investigate the behavioural characteristics of sloshing, and the subsequent impact of thermal mixing, over a wide range of resonant conditions. This covers an extensive sweep through the parameter space, with a view to understanding how subsurface mixing is influenced by sloshing frequency mode, forcing amplitude, fill height ratio and buoyancy. A metric is established, for evaluating the enhancement of thermal mixing from sloshing relative to tanks that are stationary.

Chapter 2

An overview of sloshing

2.1 Liquid sloshing in the wider industry

Sloshing is the dynamic response by which a free surface responds to external excitations. Although sloshing can often be quite benign, fluid bodies excited at resonance can suddenly exhibit violent responses even to very small amplitude disturbances. Large fluid motions in vehicles can result in structural damage from substantial forces and moments associated with sloshing impacts. Vehicular stability can become compromised, leading to unsafe conditions if not properly accounted for.

Most people will experience sloshing in some form on a daily basis by simply going about their daily business. Walking with a glass of water, or even a pint of beer (Cappello et al., 2015) is a perfect case in point; the surface of the water moves and oscillates in response to the rhythmic footsteps of the person carrying the glass. Walking too quickly (increase in frequency) or unsteadily (increased amplitude of oscillation) will likely cause the water to spill. Cappello et al. (2015) demonstrated that conveniently, a pint of beer comes well equipped with its own native method of slosh mitigation — the foam head serving as a damping mechanism, making spillages less likely.

Typically, the engineer is concerned with sloshing within the context of more serious industrial applications. Its extensive study in the aviation, space flight and marine industries is reflected in the considerable volume of historical literature available.

Sloshing in the space and rocket industry

Much of the earliest formal research into sloshing dynamics was undertaken in the post-WWII era, during the early stages of rocket development (Fox and Kuttler, 1983). The dominant author from this early work is undoubtedly H. Norman Abramson (Abramson and Ransleben Jr, 1960; Abramson et al., 1961a,b, 1963; Abramson, 1966). Launch vehicles containing liquid propellants often operate with fuel sloshing frequencies that are close to the control system frequencies. Small lateral excitations can cause large amplitude response near resonance. This in turn can cause large stresses on the tank structure, particularly if sloshing frequencies are close to the modal bending frequencies (Abramson, 1966). More serious is the potential for instability; liquid fuel accounts for a large proportion of the total mass of the rocket and so sloshing if left unchecked can seriously alter a vehicle's trajectory (Chu, 1964).

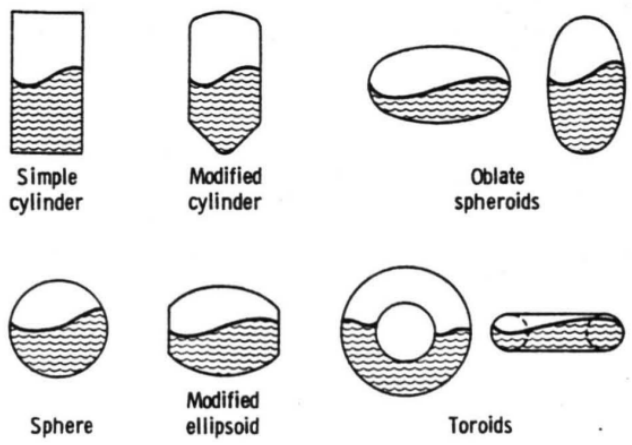

Figure 2.1: Rocket tank geometries that inspired early sloshing studies (Abramson, 1966)

Many of the earliest analytical models developed for modelling sloshing were motivated by finding solutions for cylindrical and spherical (other examples shown in **Fig.** 2.1) tank geometries pertinent to the launch vehicles of the time. Early analytical methods were restricted to small-amplitude linear sloshing, with the assumptions of incompressible, irrotational and inviscid fluids in rigid tanks. Abramson (1966) reported the emergence of non-linearities that arise from sloshing at resonance; wave-breaking of steep waves can produce new modes of sloshing. In spherical and cylindrical tanks, the free surface activity becomes highly 3-dimensional swirling behaviour. More complex tank geometries (and modelling challenges) often arise from the inclusion of slosh-mitigating modifications to the internal fuel tank design. These range from simple solutions such as ring-baffles (Abramson and Garza, 1964), compartmentalisation and more exotic devices such as floating lids (Abramson and Ransleben Jr, 1961). Analytical models at the time were poorly equipped to deal with non-linearities and extending the theory to deal with complex geometries was difficult (and still is). Experiments were therefore extremely valuable, with extensive study into similitude and the use of scaled models in prototyping at the design stage (Abramson et al., 1958).

Sloshing in aviation

Sloshing in aircraft must be carefully controlled in order to maintain flight stability during any manoeuvre that typically falls within the scope of a particular aircraft's mission. Aircraft fuel systems are often comprised of numerous tanks distributed throughout the aircraft, connected by an elaborate network of fuel lines. An example of the fuel tank layout for a civilian aircraft is shown in **Fig.** 2.2. We can see commercial and cargo planes tend to have a relatively simple tank configuration. A high proportion of the fuel is stored within the wings, with some tanks situated at the centre and aft of the fuselage. Storing much of the fuel in wing tanks puts the fuel's weight close to the centre of lift during airborne flight, which allows bending

moments and stresses in the wing structure to be minimised.

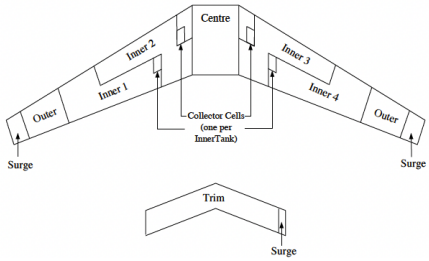

(a) Fuel tank distribution in civillian aircraft

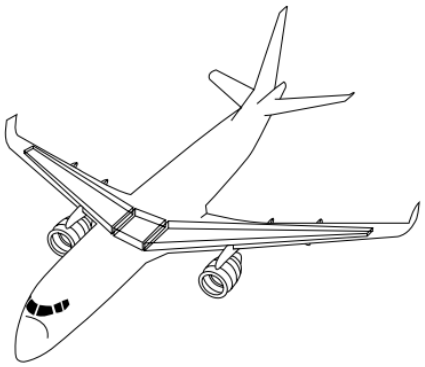

(b) Cargo plane

Figure 2.2: Civil aircraft fuel tank configurations (Langton et al., 2009)

In fighter/military aircraft there is a great impetus on economical usage of space. Wings tend to be shorter and much thinner, with less available internal space, so fuel tanks must be crammed into tight spaces within the fuselage, assembled and worked around other systems occupying space within the body. **Fig.** 2.3 gives a more detailed look at typical fighter fuel systems. We can see the added complexity compared to **Fig.** 2.2, and the design drivers associated with advanced aircraft can give rise to a broad range of unusual tank geometries.

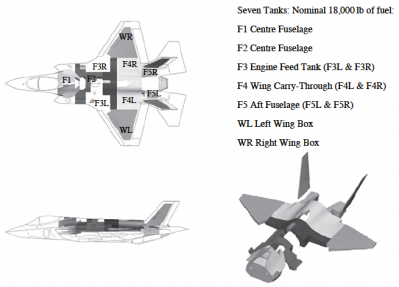

(a) Fuel tank distribution of a Joint Strike Fighter Moir and Seabridge (2011)

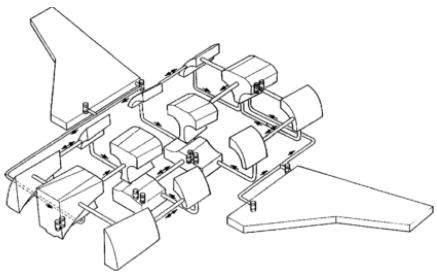

(b) Fuel system of a British Aerospace EAP (Moir and Seabridge, 2011)

Figure 2.3: Fighter aircraft fuel tank configurations

Fuel slosh within the wing tanks is known to interact with the aero-elasticity phonemonon (Farhat et al., 2013; Sabri and Lakis, 2011, 2010). Firouz-Abadi et al. (2014) modelled the effects of sloshing on wing flutter using a spring-

damper system as a mechanical model of the fluid, and Euler-Bernoulli beam theory to model wing displacements. It was found that coupling between the natural frequencies of sloshing modes and torsional/bending modes can result in both stabilising and de-stabilising effects depending on the parameters. The stabilising effect was later confirmed by Hall et al. (2015) who deployed a multi-physics solver, modelling the fuel explicitly using Smooth Particle Hydrodynamics (SPH).

Sloshing can also cause unwanted fuel migration, which can in turn have a de-stabilising effect on the aircraft due to a shift in centre of gravity (CG). Furthermore, having an uneven/broken free surface can make fuel level gauging difficult and unreliable. Wing tanks are enveloped by the structural members of the wing interior; ribs and stiffeners making up the wing frame serve the secondary function of compartmentalising the fuel tank and mitigating excessive fuel shift. The ribs come equipped with bleed holes that allow fuel to move from one compartment to another in a controlled manner. Internal design of the wing tank is typically driven by the competing factors of stability and weight-saving goals. Zheng et al. (2021) & Li et al. (2018) used an SPH code coupled with a topology-optimisation algorithm to propose improved wing tank designs, demonstrating reduced slosh, improved structural stiffness and more reliable fuel gauge monitoring.

As touched upon already, the ever-increasing thermal loads generated by aircraft means fuel is being increasingly relied upon as a way of dissipating heat from the aircraft. Typically, the FTMS is modelled as a 1D thermal network, with various heat loads and resistances representing subsystem components. Only recently has there been an interest in deploying full fidelity models to help in the understanding of thermal mixing in aircraft fuel tanks subject to in-flight accelerations. As of yet, this is a surprisingly nascent field of research.

Sloshing in the marine industry

The marine industry has produced a considerable contribution to sloshing research. Surveying the literature reveals much more material available in the public domain for marine applications than was found for the aviation industry. Ocean-going vessels are often subject to unpredictable wave loads. The ability to maintain stability in the face of such loads is vital for a ship to maintain good sea-keeping. Partially filled containers and free surfaces come in the form of ballast tanks, grain cargo and liquid cargoes such as oil and Liquefied Natural Gas (LNG).

LNG transport is challenging due to the high technology involved in the storage requirements. The volume of natural gas can be reduced by a factor of 600 through condensation, but in order to do so its temperature must be reduced to its boiling point at atmospheric pressure, $T = -163°C$. The containment tank must also be sufficiently insulated so as to reduce boil-off during transit. Typically, ship cargo tanks are compartmentalised by longitudinal and transverse bulkheads in order to increase stability and reduce impact loads on tank walls. However, LNG tank design drivers (examples shown in **Fig.** 2.4) are heavily influenced by the need to keep a low surface-volume ratio in order to minimise heat flux across the tank's limits (Gavory and De Seze, 2009). As a consequence, tanks are often designed in a way counter-intuitive to classic slosh-mitigating reasoning. For this reason, much of the marine-based sloshing research has been focussed on the application specific to LNG carriers.

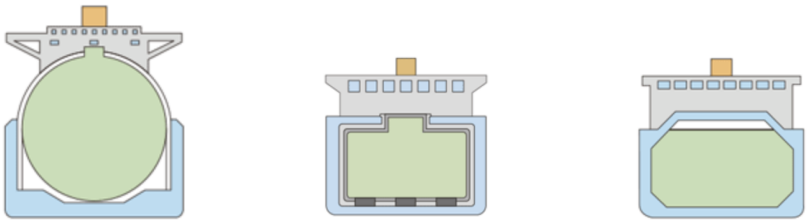

(a) Spherical-type LNG tank (b) IMO-type LNG tank (c) Membrane-type LNG tank

Figure 2.4: 3 categories of LNG tank design (MOL)

Sloshing motions can become strongly coupled with the global motion of the ships. A combination of wave excitation, tank motion and sloshing response of internal fluids can cause very complex behaviour. Bai et al. (2015) developed a finite-difference model coupled with the level-set method for surface tracking and simulated sloshing induced by realistic ship motions. As the model was 2D this was limited to 3 degrees of freedom: surge, heave and pitching motions, and the coupling between ship and sloshing motion was coupled only one way. They demonstrated the high sensitivity of internal tank pressure and wave amplitude responses to the forcing frequency, tank fill height and sea-wave amplitude. Non-linearities were found to be more prevalent at low filling levels. Other authors have extended this type of analysis to two-way coupling (Hu et al., 2017; Lee et al., 2007), although the sloshing fluid is most often modelled using potential flow equations which has its limitations for high amplitude sloshing.

Peric et al. (2009) used a finite-volume/volume-of-fluid model to investigate sloshing in tanks undergoing pitching motion in rectangular and LNG-type tanks. As 3D models are often impractical for long run-time simulations, they made some efforts to assess the effect of reducing the model to 2 dimensions and how this influenced the prediction of pressure loads at the tank walls. It was found that for the simple rectangular geometry, 2D and 3D behaviour was very similar, whereas in more irregular shaped tanks the 2D model had a tendency to predict high pressure spikes after wave impacts. Yu et al. (2017) used `Fluent` and experiments to investigate the effectiveness of floating plates in membrane-type LNG carriers in reducing sloshing. They found wave run-up was reduced, with significantly decreased impact pressures on the tank walls.

Sloshing in thermodynamic systems

Marine engineering research has recently spawned some of the very few publications investigating the effects of sloshing on thermodynamic systems. Wu and Ju (2021)

used the VOF method in `Fluent` to study the effects of sloshing on boil-off-gas (BOG) generation in LNG tanks. Their model predicted a greatly increased rate of BOG production during sloshing compared to static conditions. The increase in heat transfer at the liquid-gas interface resulted in elevated rates of LNG evaporation. Grotle and Æsøy (2017) and Grotle (2018) used the VOF method in `OpenFOAM` to analyse the effects of sloshing on the thermodynamic response in LNG fuel tanks, which utilise a 'pressure build-up unit' to generate natural gas vapour in order to pressurise the tank and supply fuel lines. They demonstrated via experiments and modelling that sloshing greatly enhanced heat transfer across the surface, which resulted in an increased rate of vapour condensation. This is generally undesirable as mass transfer across the interface results in an corresponding pressure drop in the cavity, which in turn diminishes the fuel system's effectiveness in terms of delivering fuel at pressure. Elsewhere there has been a flurry of interest in the effects of sloshing on the thermodynamic properties of cryogenically stored fluids (Liu et al., 2021, 2020, 2019b,a; Liu and Li, 2018) in the last few years.

Despite the abundance of sloshing research undertaken over the last 60+ years, there have been few publications addressing the role of sloshing in thermal mixing processes. This is despite there being many scenarios for which it is applicable and probably of some importance. The few examples that do exist are very recent (most publications in the last 5 years), with Grotle and Æsøy (2017) publishing the only significant experimental data that clearly relates sloshing to the speed-up of thermal mixing inside a container. Even then, the data is limited to a very select few cases. What's more, the work so far has only focussed on liquids with an initially homogeneous temperature profile, concerned more with heat transfer across the interface and container walls. No research as of yet has been able to shed any light on the way in which sloshing can influence subsurface mixing in liquids for which the temperature profile is more complex.

2.2 Modelling sloshing

The previous section gave a few examples of sloshing studies and their industrial context. The work discussed was meant to give a taster for some relevant applications, but given the vast swathes of past research into the field of sloshing it is ifar from being exhaustive. For a more extensive review of sloshing, the reader is referred to the extensive works of Ibrahim (2005) and Ibrahim (2020).

Sloshing research has often been driven by the pertinent technological needs of the time. Similarly, the research methods deployed in the investigation of sloshing phenomena have evolved as new modelling capabilities have become available. We will summarise and discuss some of the analysis tools for modelling sloshing flows as follows.

2.2.1 Natural frequencies of a partially filled rectangular container

An approximation for the natural frequencies of fluid sloshing in a rectangular container can be made using linear potential flow theory. The following solution is taken from the extensive review of sloshing by Abramson (1966), which references Lamb (1924) as the original source of this derivation. The assumption of incompressible, inviscid and irrotational flow allows a description of the flow field in a 3D rectangular tank as a potential function, Φ satisfying the Laplace equation:

$$\frac{\partial^2 \Phi}{\partial x^2} + \frac{\partial^2 \Phi}{\partial y^2} + \frac{\partial^2 \Phi}{\partial z^2} = 0. \tag{2.1}$$

Applying kinematic and dynamic boundary conditions at the surface, in addition to vanishing velocity at the wall yields the velocity potential:

$$\Phi(x,y,z,t) = \sum_{n=1}^{\infty}\sum_{m=0}^{\infty}\Big[\alpha_{mn}(t)\cos(k_n x)\cos(k_m y)\Big]\cosh\Big[k_{mn}(y+h_{\text{fs}})\Big], \tag{2.2}$$

where h_{fs} is the liquid fill height, α_{mn} is a time-dependent coefficient. k_m and k_n are the wave numbers in the y and x-coordinates respectively:

$$k_m = \frac{m\pi}{L_y}, \quad k_n = \frac{n\pi}{L_x}, \tag{2.3}$$

where n and m are integers corresponding to each modal wave number. A combined wave number for sloshing with two degrees of freedom, k_{mn} can be expressed as:

$$k_{nm} = \pi\Big(\frac{m^2}{L_y^2} + \frac{n^2}{L_x^2}\Big)^{\frac{1}{2}}, \tag{2.4}$$

where L_x is the tank length, L_y is the tank breadth. The free surface elevation, η can be written as the following expansion:

$$\eta(x,y,z,t) = \sum_{n=1}^{\infty}\sum_{m=0}^{\infty} A_{mn}(t)\cos(k_m x)\cos(k_n y), \tag{2.5}$$

where g is gravitational acceleration and ω_n is n^{th} modal frequency. The modal frequency for sloshing waves is given by the general dispersion relation for water waves in 3D:

$$\omega_n^2 = g k_{mn}\tanh(k_{mn}h_{\text{fs}}), \tag{2.6}$$

which in 2 dimensions reduces to:

$$\begin{aligned}\omega_n^2 &= gk_n \tanh(k_n h_{\text{fs}}) \\ &= \left(\frac{ng\pi}{L_x}\right)\tanh\left(\frac{nh_{\text{fs}}\pi}{L_x}\right).\end{aligned} \tag{2.7}$$

Tank motions with only one degree of freedom are considered within this thesis and so any estimations of natural frequencies will be calculated using **Eq.** 2.7. Notice in **Eq.** 2.7 that the hyperbolic function $\tanh(nh_{\text{fs}}\pi/L_x)$ tends towards unity as the argument $(nh_{fs}\pi/L_x) > 1$. This means that for deep water sloshing, as $h_{\text{fs}}/L_x > 1$ the resonant frequencies become independent of fill height and can be approximated as:

$$\omega_n \approx \left(\frac{n\pi g}{L_x}\right)^{\frac{1}{2}}. \tag{2.8}$$

Sloshing at resonance

If a partially filled container is subject to motions at frequencies close to the natural frequency of the system i.e. as $\omega/\omega_n \to 1$ the free surface response can suddenly become violent with only a small amount of additional energy being supplied to the system. This is known as resonance. Viscous damping is the mechanism by which energy is dissipated in sloshing flows. With this in mind, one serious limitation of linear potential flow solutions is the prediction of infinite wave response amplitude when excited at resonant frequencies. Simple intuition tells us this is unphysical. Faltinsen et al. (2000); Faltinsen and Timokha (2009) used a non-linear multi-modal approach to demonstrate that in reality, an upper limit to response amplitude occurs not only due to viscous dissipation, but as a consequence of energy being redistributed to higher sloshing modes. Linear potential flow models are further hampered by an inability to provide good accounts of sloshing near resonance due to the occurrence of strong non-linearities in the system e.g. wave breaking, wall impacts etc.

Ordinarily, the first natural frequency ω_1 is of primary concern, and receives the most attention. Sloshing at the primary natural frequency generally incurs the greatest free surface response. Wave impacts on the walls generate large forces and moments which can lead to structural damage. In terms of stability and impact loads, higher modes of interest are usually restricted to the anti-symmetric i.e. the 'odd' modes $n = 1, 3....$ Their mode shape surface profiles, being anti-symmetric result in greater lateral excitations in comparison to the symmetric modes corresponding to the even mode numbers $n = 2, 4....$ Mode shapes for the first natural frequencies are shown in **Fig.** 2.5. We can see that for the symmetric modes, peaks and troughs are interchangeable through vertical motion alone, and so these mode shapes are unlikely to cause a significant shift in centre of gravity.

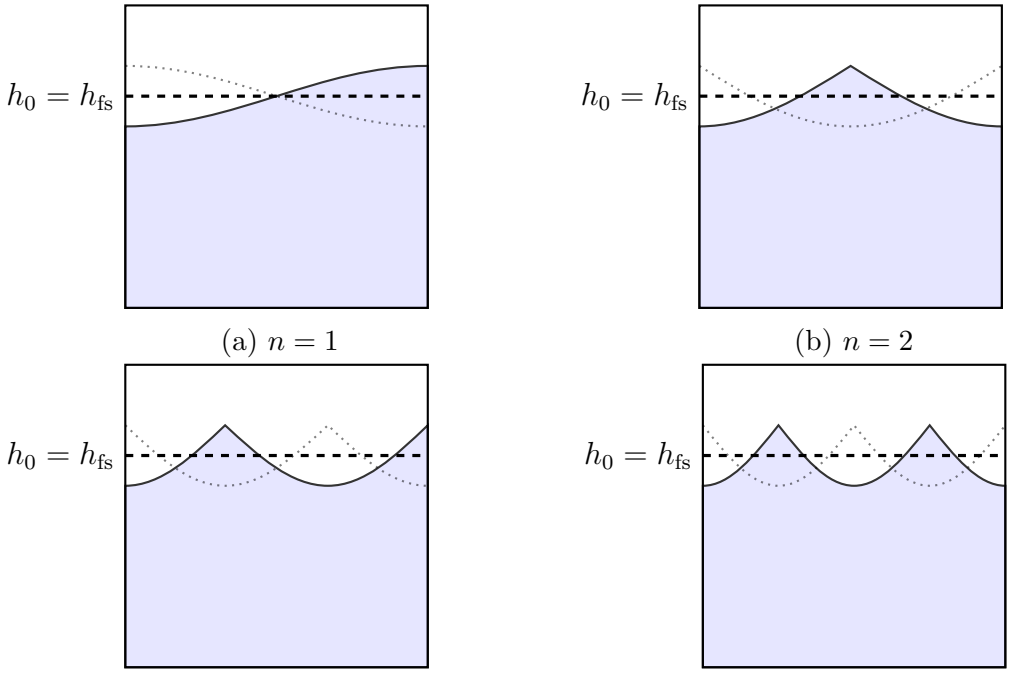

(a) $n = 1$ (b) $n = 2$

(c) $n = 3$ (d) $n = 4$

Figure 2.5: Sloshing modes at first four natural frequencies. Anti-symmetric mode shapes on the left, with symmetric mode shapes on the right.

Free surface behaviour at resonance is not universal. Regimes of flow patterns exist which are highly influenced by the ratio of liquid fill depth to tank length. Tanks with a fill height ratio $h_{fs}/L_x >\sim 0.4$ form standing waves (Faltinsen and

Timokha, 2009) as in **Fig.** 2.6a. Wave breaking occurs less easily in deep sloshing and can take a long time to reach a 'steady-state'. Sloshing at shallower fill height ratios $h_{\text{fs}}/L_x < 0.4$ is characterised by travelling waves, with hydraulic jumps forming (see example in **Fig.** 2.6b). Wave breaking is more prevalent at shallow depths, with non-linearities developing more easily and wall impacts being more forceful. The increased complexity of shallow flows and the dissipative nature of wave breaking means a steady-state is often more readily achieved (Faltinsen and Timokha, 2009).

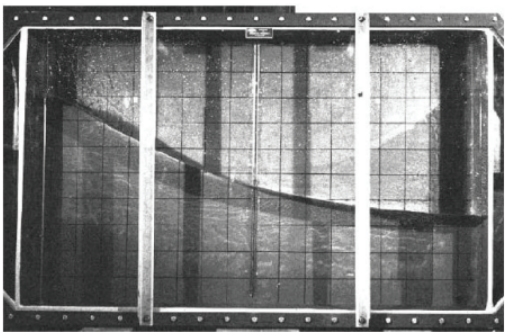

(a) Deep sloshing, standing wave (Faltinsen, 2017)

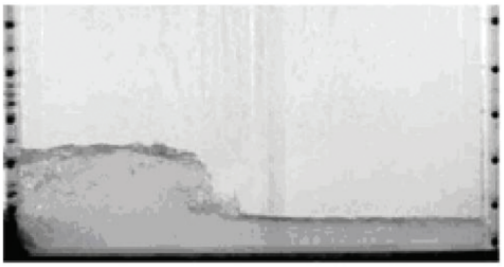

(b) Intermediate fill height (Faltinsen, 2017)

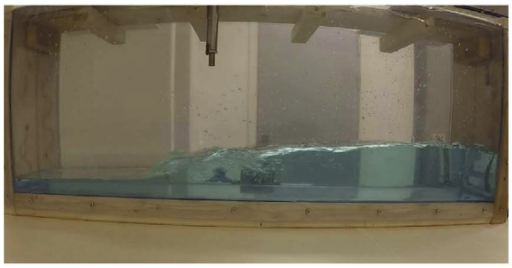

(c) Shallow travelling wave (Grotle et al., 2017)

Figure 2.6: Sloshing wave regimes

2.3 Sloshing simulation

Rapid growth in readily available computer power and the development of numerical methods have allowed the possibility of studying sloshing flows with ever-more complex simulations. A wide variety of numerical recipes have been implemented throughout the research but they can be broadly categorised into non-viscous and

viscous techniques.

2.3.1 Potential flow models

Non-viscous analysis has typically involved mathematical models underpinned by potential flow theory. Faltinsen, who along with Abramson should be considered one of the godfathers of sloshing analysis due to his influential contributions to the field, was one of the first to use numerical methods for studying sloshing (Faltinsen, 1978). A boundary element method (BEM) was used to simulate non-linear sloshing in a rectangular tank under pure sway motion. The underlying theory was developed further such that free surface wave motions are decomposed into an infinite set of modes, capturing non-linearities provided that wave amplitudes are kept small (Faltinsen et al., 2000; Faltinsen and Timokha, 2001). Truncating the numerical model to include only the first twenty modal frequencies allows excellent results to be generated very quickly and efficiently. Despite the ingenuity in their development, these models are limited in that they are unable to handle important sloshing features such as high amplitude waves and wave-breaking. Furthermore, the accuracy of their results break down in shallow water conditions, where viscosity and wall shear-stress become more influential.

2.3.2 Viscous flow models

In more recent times, solving the full Navier-Stokes equations with computational fluid dynamics (CFD) has become a viable option, and is now a popular choice for simulating sloshing. Fully viscous numerical models are not affected by the same limitations as potential-flow solvers in terms of capturing complex flow behaviour. Not only that, their integration into a variety of open-source and proprietary software packages means they are much more readily usable for analysis and so their popularity will likely continue. However, that does not mean their implementation

is simple or easy. Indeed the development of free surface tracking techniques has been a hotbed of research for the last few decades.

Marker and Cell (MAC)

One of the earliest such techniques is the Marker and Cell (MAC) method, developed by researchers at Los Alamos in the 1960's (Harlow and Welch, 1965). MAC is a finite-difference Eulerian-grid based solver which uses Lagrangian particle tracking to trace the interface (McKee et al., 2008). Armenio and La Rocca (1996) coupled MAC with the RANS equations to study sloshing tanks undergoing roll motions. At the time, MAC was found to be prohibitively expensive, and was not sufficiently good at predicting large amplitude sloshing and wave impacts on the tank walls. Arai et al. (1992) used MAC to study 3-dimensional liquid cargo sloshing, finding superior agreement with experiments compared to wave response predictions from linear theory, demonstrating some the earliest advantages of viscous flow models. Further examples of MAC applied to sloshing are Popov et al. (1992, 1993b,a) who conducted a series of studies into the design of liquid containers on road vehicles.

Volume of Fluid (VOF)

Despite some early popularity, the MAC method was supplanted by the volume of fluid (VOF) method developed by Hirt and Nichols (1981). VOF is a Eulerian grid-based technique in which an indicator function is used to track the interface as it moves across the grid. The indicator function, or 'Volume Fraction', α, where $\alpha \in [0, 1]$. Presence of the interface is indicated in cells where $0 < \alpha < 1$.

VOF is advantageous in that solving the advection of volume fraction via the integral form of a transport equation can guarantee mass conservation throughout the domain. Its known limitations are that it may struggle to accurately capture curvature of the interface. For flows in which surface tension is influential, this can

be a real issue.

Maintaining good resolution of the interface is crucial to a well-implemented VOF model. Interface capturing schemes have been typically divided into two categories — geometric and compression-based. Piece-wise linear interface construction (PLIC) is a popular geometric method. PLIC improves the estimation of advective fluxes through cell faces by using linear-interpolation to reconstruct the interface at cell level (Youngs, 1982). A popular compression-based method is the Compressive Interface Capturing Scheme for Arbitrary Meshes (CICSAM) presented by Ubbink (1997). Rather than attempting to obtain a geometrical representation of the interface, boundedness and accuracy is achieved through using a blend of high-order numerical schemes for discretising the advection term. Both of the aforementioned methods have been widely implemented, and are available for use in popular commercial codes such as `Fluent`. Historically, the `OpenFOAM` VOF solvers have been formulated to maintain a sharp interface through the inclusion of an additional compression term in the α-transport equation (Jasak and Weller, 1995). This will be expanded upon in the next chapter. `OpenFOAM 8.1` (and subsequent versions) was updated to also include a family of PLIC schemes.

Celebi and Akyildiz (2002) were some of the earliest to study sloshing using the VOF method. Using their finite-difference based solver, they investigated the effects of including baffles in rectangular tanks. Their attempts to model highly non-linear, violent sloshing were thwarted however due to the lack of including a turbulence model. Akyildız and Ünal (2006) extended this work to include comparison of subsurface pressure measurements with experiments in tanks undergoing roll motions. Reasonable results were found, with particularly good agreement at certain roll frequencies. Liu and Lin (2008) used VOF coupled again with a finite-difference method and Large Eddy Simulation turbulence model to model sloshing under both 1 and 6 degrees of freedom (DOF). Their analysis compared linear analytical theory, experiments and numerical results, finding that at high amplitudes the VOF

simulations were much better at matching the experiments than theory. Their work highlights that VOF can be seen as a powerful tool to simulate challenging, violent sloshing flows under conditions that go beyond the limits of analytical models. Rhee (2005) deployed VOF within the finite volume framework using `Fluent` to model sloshing in sway and roll cases. The results were validated against pressure probe readings from real tank tests and showed good qualitative and quantitative performance over the full range of cases.

More recently, `OpenFOAM`, which is a finite-volume based solver, has proved very popular for solving sloshing flows. Examples of publications using `OpenFOAM` will be presented in the following chapter as part of a focussed discussion around the use of `interFoam`.

Level-Set (LS)

An alternative grid-based surface tracking technique to VOF is the level-set method. An advection equation is solved for a scalar quantity known at the 'level-set', which indicates the distance between the cell and free surface (Sussman et al., 1994). The level-set value is set to zero at the interface. This method is an attractive alternative to VOF in that it is able to capture interface curvature well. Chen et al. (2007); Battaglia et al. (2018) each give strong examples of level-set finite volume solvers being able to accurately replicate experimental data of sloshing in rectangular tanks. One of the drawbacks of the level-set approach is that it is not so robust in conserving mass as the VOF method.

Very recently, a coupled volume of fluid/level-set (CLSVOF) approach has gained some popularity, taking the combined advantages of mass conservation (VOF) and interface curvature capture (LS). Liu et al. (2016) deployed the CLSVOF method to study the effects of turbulence modelling strategy on shallow water sloshing simulation. Comparison with a selection of cases to the experimental

data demonstrated very good resolution of challenging behaviour such as travelling wave fronts and spilling breakers.

Smooth Particle Hydrodynamics (SPH)

A popular alternative to grid-based methods of solving free surface flow problems is Smooth Particle Hydrodynamics (SPH). Originally derived in the 1970's (Gingold and Monaghan, 1977; Lucy, 1977), SPH is a Lagrangian mesh-free method which represents the fluid and flow variables by a set of discrete particles. Applying a weighting function allows flow variables to be interpolated and found anywhere throughout the domain (Vignjevic and Campbell, 2009).

SPH's Lagrangian formulation naturally lends itself well to handling complex free surface behaviour, and has been utilised extensively in sloshing research through the last decade (Green and Peiró, 2018; Shao et al., 2012; Gotoh et al., 2014), in particular to that of predicting pressure loads in LNG tankers (Pilloton et al., 2022; Ma et al., 2018, 2020; Rudman and Cleary, 2009; Marrone et al., 2017). Its versatility has seen it further applied to a range of applications such as geotechnics (Peng et al., 2019) and granular flows (Nguyen et al., 2017).

2.4 Summary

In this chapter, we have given a general overview of some challenges faced in industry with regards to sloshing. Although this research is motivated with aerospace applications in mind, we've seen that sloshing research is voluminous and driven by the needs of a wide range of industries.

One of the key takeaways from this chapter is that upon surveying the literature, it became clear that despite such an abundance of attention paid to sloshing over the last few decades, the phenomenon of thermal mixing in sloshing flows has

been seldom studied. Of the few studies involving sloshing within a thermodynamic system, almost all of them have come within the last 5 years, which does hint at a growing interest.

Another noticeable absence is the lack of recorded data or study into turbulence in the subsurface of sloshing flows. Authors have investigated the impact of including turbulence models on the accuracy of predicting free surface behaviour. However, the role of sloshing in generating turbulence in the subsurface remains relatively unexplored. In order to understand thermal mixing in the subsurface of sloshing flows, this is essential.

In this thesis, numerical modelling will be used to study sloshing, turbulence and thermal mixing inside fuel tanks. Experimental data will be used to validate methods where possible.

Chapter 3

A numerical framework for modelling sloshing flows

The simulation work in this thesis is primarily conducted in `OpenFOAM` version `4.1`, which was the most recent release at the commencement of this research. A very small number of complimentary simulations are also performed in `Ansys Fluent`. In this chapter we will briefly discuss `OpenFOAM` before presenting the model equations for `interFoam`, a VOF-based solver for modelling free surfaces. We will then present an overview of turbulence modelling, before focussing on the performance of `interFoam` in being applied specifically to sloshing flows. This will include a review of the available validating literature, with the addition of 3 further original validation studies.

3.1 Introduction to OpenFOAM

. `OpenFOAM` is an open-source multi-physics tool-kit written in `C++`, with an object-orientated library of utilities designed for the numerical simulations of continuum mechanics (Weller et al., 1998). Object-orientation is particularly attractive in build-

ing user-friendly code for problems in fluid mechanics, which are governed by the need for solving partial differential equations. The code visually resembles the familiar mathematical symbolic representation of the model equations. This makes accessing, understanding and manipulating the solver a less esoteric task for users with only rudimentary knowledge of the programming language such as this author.

Unlike most proprietary CFD software releases, `OpenFOAM` is not designed to operate as one unified top-level solver, but instead divided into a set of individual pre-compiled solvers, each with a unique combination of physical modelling capabilities. Solvers are categorised by their key physics, for example:

- Combustion: `reactingFoam`.
- Heat transfer: `buoyantFoam`
- Cavitation: `cavitatingFoam`

For consistency of convention, each solver is named as a portmanteau of `OpenFOAM` and some other word, usually suggesting something about the fundamental physical features of that particular solver, e.g. '`interFoam`' in which the primary feature is to track the interface between two fluid phases. Dividing the software into such specialised solvers might seem restrictive compared to commercial programmes such as `Fluent` or `CFX` which contain seemingly endless modelling options which can be selected at run-time within a singular GUI. However, `OpenFOAM` allows ease of access to the code, and the class-based system of libraries allows users to compile bespoke solvers for their own needs without too much trouble.

3.2 InterFoam

The `interFoam` solver is used for the initial isothermal sloshing simulations in this thesis. `interFoam` is a finite-volume solver, deploying the volume-of-fluid (VOF)

method of interface-tracking which is able to model two incompressible, immiscible homogeneous fluids. VOF uses a transport equation for advecting the scalar volume fraction, α of each phase, where volume fraction is an indicator function representing the relative occupancy of each fluid in a cell. The volume-fraction convention throughout this thesis will be as follows:

$$\textbf{if} \begin{cases} \alpha = 1, & \text{Liquid} \\ \alpha = 0, & \text{Air,} \\ 0 < \alpha < 1, & \text{Interface} \end{cases} \tag{3.1}$$

The transport equation for the phase volume fraction is as follows:

$$\frac{\partial \alpha}{\partial t} + \nabla \cdot (\boldsymbol{u}\alpha) + \nabla \cdot \{\boldsymbol{u_c}\alpha(1-\alpha)\} = 0, \tag{3.2}$$

where $\boldsymbol{u}$ is the velocity vector. The third term in **Eq.** 3.2 is an additional advection term (Jasak and Weller, 1995), including an artificial compression velocity, $\boldsymbol{u_c}$:

$$\boldsymbol{u_c} = C_\alpha |\boldsymbol{u}| \frac{\nabla \alpha}{|\nabla \alpha|} \tag{3.3}$$

This term is activated in regions of $0 < \alpha < 1$, creating artificial velocities normal to the surface in order to counteract numerical diffusion and maintain a sharp interface. The compression coefficient C_α can be set in the `fvSolution` dictionary within the `system` directory of the `OpenFOAM` case structure. In this thesis we shall take $C_\alpha = 1$ throughout. Mass and continuity transport are given in vector format by the following:

$$\nabla \cdot \boldsymbol{u} = 0, \tag{3.4}$$

$$\frac{\partial(\rho \boldsymbol{u})}{\partial t} + \nabla \cdot (\rho \boldsymbol{u}\boldsymbol{u}) = -\nabla p^* - (\boldsymbol{g} \cdot \boldsymbol{h})\nabla(\rho) + \nabla \cdot \boldsymbol{\tau} + \rho \boldsymbol{f_b}, \tag{3.5}$$

where $p^* = p - \rho \boldsymbol{g} \cdot \boldsymbol{h}$ is the modified pressure, $\boldsymbol{h}$ is the distance vector, $\boldsymbol{\tau}$ is the viscous stress tensor $\boldsymbol{\tau} = 2\mu_{\text{eff}}\boldsymbol{S}$ and $\boldsymbol{S}$ is the mean rate of strain tensor, $\boldsymbol{S} = \frac{1}{2}\Big(\nabla \boldsymbol{u} + (\nabla \boldsymbol{u})^T\Big)$ The 'pressure shift', p^* subtracts the hydrostatic pressure contribution from the pressure $p^* = p - \rho \boldsymbol{g} \cdot \boldsymbol{h}$ for easier implementation of boundary conditions. Surface tension, $\boldsymbol{f_b}$ is included via the Brackbill surface force continuum model (Brackbill et al., 1992) as a body force:

$$\boldsymbol{f_b} = \sigma \kappa_{surf} \nabla \alpha, \tag{3.6}$$

where σ is the surface tension coefficient and κ_{surf} is the mean curvature of the free surface:

$$\kappa_{surf} = -\nabla \cdot \left(\frac{\nabla \alpha}{|\nabla \alpha|} \right). \tag{3.7}$$

Transport properties in each cell are calculated as a linear interpolation of the two phase properties based on the local volume fraction:

$$\rho(\boldsymbol{x}, t) = \alpha \rho_1 + (1 - \alpha)\rho_2, \tag{3.8}$$

$$\mu(\boldsymbol{x}, t) = \alpha \mu_1 + (1 - \alpha)\mu_2, \tag{3.9}$$

where μ_i and ρ_i are the dynamic viscosity and density of each respective phase.

interDyMFoam

The `interDyMFoam` solver is an offspring of `interFoam` with added mesh motion capabilities — the '`DyM`' component referring to 'dynamic mesh'. Tank motion parameters can be controlled using the `dynamicMeshDict` dictionary stored within the `constant` directory in the `OpenFOAM` case structure.

Using these features, tank motion has been simulated by using a dynamic mesh throughout this thesis. Essentially, this is exactly equivalent to modifying the gravity term in the momentum equation to include additional time-dependent body forces on the fluid. This equivalence was confirmed by running some test cases for comparing the two methods. For ease of use, the dynamic mesh method was used. In hindsight, the modified gravity vector would be the recommended method due to the additional computational overheads involved in updating the mesh at each time-step. It is also recommended that a future study be carried out to evaluate the relative speed-up that can be achieved using the modified gravity approach. This is a potentially important point considering the extensive run-times involved in modelling sloshing flows - for 3D simulations in particular.

3.3 Turbulence modelling

Turbulence is a phenomenon in which instabilities develop within fluids, dominated by rotational flow structures commonly known as 'eddies'. Turbulence consists of a wide range of spectral content and can be described by the 'energy cascade'. Most of the turbulent kinetic energy is contained with large eddies, which extract energy from the mean flow at length scales similar to that of the geometry enveloping the fluid.

These eddies are not able to persist; through a process of vortex stretching, eddies are lengthened along the axis of rotation. This in turn reduces their cross-sectional length scale, and conservation of momentum dictates that the rate of rotation — and hence vorticity — must increase accordingly. An equation for vorticity can be obtained by taking the curl of the momentum equation:

$$\frac{D\boldsymbol{\omega}}{Dt} = \nu\nabla^2\boldsymbol{\omega} + \boldsymbol{\omega}\cdot\nabla\boldsymbol{u}. \tag{3.10}$$

where $\boldsymbol{\omega} = \nabla \times \boldsymbol{u}$. The second term on the right-hand side of **Eq.** 3.10 is known as the vortex-stretching term, which represents the interaction of eddies with mean-flow velocity gradients. As eddies stretch and become smaller they themselves are then stretched further via interaction with larger eddies, this process continuing on until they are small enough such that viscous forces become dominant and their energy is dissipated into heat.

Turbulence presents a difficult challenge in modelling fluid flows primarily due to the fact that resolving the smallest eddies requires prohibitively small length and time-scales (for a more comprehensive overview, readers are directed to the work of Pope and Pope (2000) amongst others). For relatively low Reynolds number flows, the Navier-Stokes equations can be solved directly using Direct Numerical Simulation (DNS). DNS resolves all flow scales and can be an extremely powerful tool, but the intense computational requirements needed to run even basic simulations render it a tool primarily for academic endeavours at present. Its use in most industrial applications is impractical. In order to make simulating turbulent flows achievable, we are left with no option but finding ways of modelling some or all of the spectral content. Two popular and well-establishes means of doing so, both of which are used in this thesis are described as follows.

3.3.1 Reynolds-Averaged Navier-Stokes

The Reynolds-Averaged Navier Stokes (RANS) equations use 'Reynolds decompositioning', a statistical method of separating out the mean and time-varying components of the flow variables. For example, velocity and pressure are decomposed as follows:

$$u = \bar{u_i} + u_i', \quad p = \bar{p} + p', \tag{3.11}$$

where $\bar{u_i}$ and $\bar{p}$ are time-averaged velocity and pressure, u' and p' are the instantaneous velocity and pressure fluctuations. The same process can be repeated for any scalar quantity:

$$\phi = \bar{\phi} + \phi'. \tag{3.12}$$

For unsteady RANS models (U-RANS), rather than being time-averaged the equations are ensemble-averaged. Conceptually, ensemble-averaging is the process of running a number of simultaneous and theoretically identical experiments in parallel. Local flow properties at certain points in time are averaged across the experimental data set. Turbulent fluctuations are then defined as being the difference between data measured in a single experiment and across the entire ensemble. The U-RANS equations are a mathematical realisation of such a concept, without having to run numerous experiments/models. As a result, the flow variables in U-RANS equations are a function of both time and space. The ensemble average of a generic scalar quantity is commonly expressed using the following notation:

$$\phi = \langle \phi \rangle + \phi'. \tag{3.13}$$

The applicability of using U-RANS equations to model transient flows is based on the assumption of a sufficient separation of scales. For globally unsteady flows — such as sloshing —- this requires that the frequency of turbulent fluctuations occurs on much smaller time-scales and at higher frequencies than unsteadiness of the bulk fluid motions. Due to the relatively long time-scales at which tank motion is applied in this thesis, it is assumed that this requirement is met. This does not mean however that this assumption is universally applicable to all sloshing flows. For example, RANS models may not be appropriate for the simulation of fluid excitations driven by high frequency vibrations at the flow boundaries.

The Navier-Stokes equations of mass and momentum in tensor format are as follows:

$$\frac{\partial u_i}{\partial x_i} = 0, \tag{3.14}$$

$$\frac{\partial(\rho u_i)}{\partial t} + \frac{\partial(\rho u_i u_j)}{\partial x_j} = -\frac{\partial p}{\partial x_i} + \frac{\partial \tau_{ij}}{\partial x_j} + f_i, \tag{3.15}$$

where u_i is velocity, p is pressure, f_i is a vector containing body forces and τ_{ij} is the mean viscous shear stress tensor $\tau_{ij} = \mu\left(\frac{\partial u_i}{\partial x_j} + \frac{\partial u_j}{\partial x_i}\right)$. Substituting **Eq.** 3.11 into **Eq.** 3.14 and **Eq.** 3.15 yields the Reynolds-averaged mass and momentum equations:

$$\frac{\partial \bar{u}_i}{\partial x_i} = 0, \tag{3.16}$$

$$\frac{\partial(\rho \bar{u}_i)}{\partial t} + \frac{\partial(\rho \overline{u_i u_j})}{\partial x_j} = -\frac{\partial \bar{p}}{\partial x_i} + \bar{f}_i + \frac{\partial \bar{\tau}_{ij}}{\partial x_j} - \frac{\partial(\rho \overline{u_i' u_j'})}{\partial x_j}. \tag{3.17}$$

Eq. 3.17 resembles **Eq.** 3.15 closely, with the exception of the additional

fourth term on the RHS marked in red. The term $-\rho\overline{u_i'u_j'}$ represents the effects of unsteady velocity fluctuations on the mean flow and is commonly known as the Reynolds stress tensor. The upshot of this is that we now have an additional six unknowns ($\overline{u'u'}$, $\overline{v'v'}$, $\overline{w'w'}$, $\overline{u'v'}$, $\overline{u'w'}$ and ,$\overline{v'w'}$) which need to be solved. This is known as the closure problem, as we now have more unknowns than equations with which to solve them.

A key principle that helps condense this problem is the Boussinesq eddy viscosity hypothesis. This states that analogously to the way in which the shear stress tensor relates viscous stresses to the local rate of deformation via Newton's law of viscosity, the Reynolds stresses can be thought of as being related to the rate of deformation via a constant of proportionality known as eddy viscosity:

$$\tau_{\mathrm{T},ij} = \rho\overline{u_i'u_j'} = \mu_T\left(\frac{\partial \bar{u}_i}{\partial x_j} + \frac{\partial \bar{u}_j}{\partial x_i}\right) - \frac{2}{3}\rho k\delta_{ij}. \tag{3.18}$$

where k is the turbulent kinetic energy $k = \frac{1}{2}(\bar{u'}^2+\bar{v'}^2+\bar{w'}^2)$ per unit mass of fluid and δ_{ij} is the Kronecker delta function. Note, the bar notation will be dropped from the descriptions of Reynolds averaged flow properties for the remainder of this thesis.

Eddy viscosity turbulence models are founded upon this key hypothesis, with the effects of turbulence effectively being modelled and represented in the RANS equation as an enhanced viscosity. Numerous recipes for calculating eddy viscosity have been developed over the years, ranging from zero-equation algebraic formulations (mixing length model), the one-equation Spalart-Allmaras model (Spalart and Allmaras, 1992), two-equation models $k-\epsilon$ (Jones and Launder, 1972), RNG $k-\epsilon$ (Yakhot and Orszag, 1986), $k-\omega$ (Wilcox et al., 1998) and $k-\omega$ SST (Menter, 1994) to the seven-equation Reynolds stress model (Hanjalić and Launder, 1972).

Two-equation models tackle the closure problem by solving transport equa-

tions for the turbulent variables, typically k and either the turbulent dissipation rate, ϵ or specific turbulence dissipation rate (or turbulent frequency), ω where $\omega \sim \epsilon/k$. The physical interpretation of ω is the rate at which turbulent kinetic energy dissipates into heat per unit mass.

$k-\omega$ SST model

In this thesis we will base most of the RANS modelling work on variations of the $k-\omega$ SST model, due to its known versatility and the fact that other authors have achieved good results when predicting free surface behaviour during sloshing (Ha et al., 2012; Tahmasebi et al., 2020). Tahmasebi et al. (2020) conducted a rigorous comparison of RANS models in modelling shallow water sloshing, finding both the $k-\omega$ SST and non-linear $v2-f-k-\epsilon$ (Lien and Kalitzin, 2001) models to be superior and virtually inseparable in replicating a select few experiments with quite demanding surface profiles. We will find later that two-equation models in general have been demonstrated to have some shortcomings when modelling subsurface turbulence, and will require modifications to improve their performance. For now we will discuss the standard SST model and give a description of the equations and modelling constants.

The SST model was originally formulated by Menter (1994) as a means of addressing the relative weakness of both the $k-\epsilon$ and $k-\omega$ models by applying a blending function to switch between the two. The $k-\epsilon$ model is unable to accurately resolve near-wall behaviour and therefore requires the application of wall functions, and is thus known to perform poorly in flows with adverse pressure gradients and separation. The $k-\omega$ model can be integrated through the boundary layer, but is known to be highly sensitive to inlet boundary conditions. The incompressible $k-\omega$ SST model equations as implemented in `OpenFOAM 4.1` are as follows:

$$\frac{\partial k}{\partial t} + u_j \frac{\partial k}{\partial x_j} = P_k - P_b - \beta^* k\omega + \frac{\partial}{\partial x_j}\left[\left(\nu + \sigma^* \frac{k}{\omega}\right)\frac{\partial k}{\partial x_j}\right], \tag{3.19}$$

$$\frac{\partial \omega}{\partial t} + u_j \frac{\partial \omega}{\partial x_j} = P_\omega - \beta \omega^2 + \frac{\sigma_d}{\omega} \frac{\partial k}{\partial x_j} \frac{\partial \omega}{\partial x_j} + \frac{\partial}{\partial x_j} \Big[\Big(\nu + \sigma \frac{k}{\omega} \Big) \frac{\partial \omega}{\partial x_j} \Big]. \tag{3.20}$$

Turbulent eddy viscosity is then calculated as:

$$\nu_T = \frac{a_1 k}{\max(a_1 \omega, F_2 S)}, \tag{3.21}$$

where $S = \sqrt{2 S_{ij} S_{ij}}$ and $a_1 = 0.31$. The model coefficients are a blend of inner and outer constants, corresponding to the respective constants taken from the $k - \epsilon$ and $k - \omega$ models. For each coefficient, we will derive a blended of version of the generic coefficient ϕ:

$$\phi = F_1 \phi_1 + (1 - F_1) \phi_2, \tag{3.22}$$

Table 3.1 shows the full list of constants needed for closure of the $k - \omega$ SST model.

$\boldsymbol{k - \epsilon}$		$\boldsymbol{k - \omega}$		**SST**	
α_1	0.5532	α_2	0.4403	a_1	0.31
β_1	0.075	β_2	0.0828	β^*	0.09
σ_{k1}	0.85	σ_{k2}	1.0	κ^*	0.41
$\sigma_{\omega 1}$	0.5	$\sigma_{\omega 2}$	0.856		

Table 3.1: List of closure coefficients used for $k - \omega$ SST turbulence model

The blending functions F_1 and F_2 are calculated as follows:

$$F_1 = \tanh(\Lambda_1^4), \quad \Lambda_1 = \min\Big\{ \max\Big(\frac{\sqrt{k}}{\beta^* \omega y_{wall}}, \frac{500\nu}{y_{wall}^2 \omega} \Big), 10 \Big\} \tag{3.23}$$

$$F_2 = \tanh(\Lambda_1^4), \quad \Lambda_1 = \min\Big\{\max\Big(\frac{2\sqrt{k}}{\beta^*\omega y_{wall}}, \frac{500\nu}{y_{wall}^2\omega}\Big), 100\Big\} \tag{3.24}$$

where y_{wall} is the normal distance to the wall.

3.3.2 Large Eddy Simulation

Large Eddy simulations (LES) attempt to reduce the computational requirements of turbulence by resolving only large energy-containing eddies. Small eddies are less affected by the geometry of the flow environment, and so their behaviour is more isotropic and universal. Spatial filtering, which uses the grid size Δ as a cut-off length, is used to separate the resolved and modelled scales.

LES simulations are desirable in that they give a more accurate representation of the flow field than RANS models; much of the transfer of momentum and mixing of scalars is undertaken by larger eddies which can be resolved explicitly (Zhiyin, 2015). The models needed to account for sub-grid-scale (SGS) turbulence are also typically much more simple than the additional transport equations needed to achieve closure in RANS modelling. The major drawback is the computational cost. Not only is the mesh resolution requirement more demanding than for RANS, LES simulations are required by definition to be transient and 3D as otherwise their interpretation of resolved eddies would be physically meaningless. Another difficulty with LES is that there really is no such thing as a truly 'mesh-independent' solution per se. Due to the way in which spatial filtering is applied, unlike in RANS simulations, changing the mesh resolution inherently changes the model. As cell size $\Delta \to 0$, the model tends towards DNS with an increasing proportion of the spectral content being resolved.

The spatial filtering procedure on the velocity is as follows:

$$\bar{\boldsymbol{u}}(\boldsymbol{x},t) = \iiint G(\boldsymbol{x},\boldsymbol{x'},\Delta)\boldsymbol{u}(\boldsymbol{x'},t)dx'_1dx'_2dx'_3, \tag{3.25}$$

where $\bar{\boldsymbol{u}}$ is the spatially filtered velocity and $G(\boldsymbol{x},\boldsymbol{x'},\Delta)$ is the filter function. The same process can be repeated for each of the flow variables. Finite volume methods typically use the 'top-hat' filter:

$$G(\boldsymbol{x},\boldsymbol{x'},\Delta) = \begin{cases} \frac{1}{\Delta^3} & \textbf{if} \quad |\boldsymbol{x}-\boldsymbol{x'}| \leq \Delta/2 \\ 0 & \textbf{if} \quad |\boldsymbol{x}-\boldsymbol{x'}| > \Delta/2 \end{cases} \tag{3.26}$$

where Δ is the cut-off width or 'delta function', which is often taken to be the cube root of the computational grid cell volume $\Delta = \sqrt[3]{\Delta x \Delta y \Delta z}$. For a uniform, structured orthogonal grid this would simply reduce to the length of each cell. Filtering the Navier-Stokes equations yields the following for mass and momentum:

$$\frac{\partial \bar{u}_i}{\partial x_i} = 0, \tag{3.27}$$

$$\frac{\partial(\rho\bar{u}_i)}{\partial t} + \frac{\partial(\rho\bar{u}_i\bar{u}_j)}{\partial x_j} = -\frac{\partial \bar{p}}{\partial x_i} + \bar{f}_i + \mu\Big(\frac{\partial \bar{u}_i}{\partial x_j} + \frac{\partial \bar{u}_j}{\partial x_i}\Big) - \frac{\partial \tau_{ij}^{\mathrm{SGS}}}{\partial x_j}. \tag{3.28}$$

where $\tau_{ij}^{\mathrm{SGS}} = \rho(\overline{u_i u_j} - \bar{u}_i\bar{u}_j)$ is the sub-grid scale (SGS) stress tensor. As with the RANS closure problem, a method of calculating this extra term is required, to account for the effects of small-scale fluctuations on the resolved flow. Based on the assumption of isotropy on small scales, Smagorinsky (1963) postulated that the sub-grid stresses can be modelled via the eddy viscosity concept, relating them to the strain rate of the locally resolved flow field. The Smagorinky closure model, which we will use for the few LES simulations within this thesis calculates the sub-grid

stresses as follows:

$$\tau_{ij} = 2\mu_{\text{SGS}}\bar{S}_{ij}; \tag{3.29}$$

where $\bar{S}_{ij}$ is the spatially filtered strain rate tensor $\bar{S}_{ij} = \frac{1}{2}\left(\frac{\partial \bar{u}_i}{\partial x_j} + \frac{\partial \bar{u_j}}{\partial x_i}\right)$ and sub-grid scale eddy viscosity μ_{SGS} is given by:

$$\mu_{\text{SGS}} = \rho(C_{\text{SGS}}\Delta)^2\sqrt{2\bar{S}_{ij}\bar{S}_{ij}}, \tag{3.30}$$

where C_{SGS} is a tunable constant.

Is LES feasible for sloshing flows?

Although expensive, sloshing in 3D with very fine grid resolutions and for long run-times is certainly possible provided the geometry is simple enough. Liu et al. (2016) investigated the relative performance of using laminar, RANS and LES models and their newly formulated Very Large Eddy Simulation (VLES) turbulence model to simulate shallow water sloshing, comparing their results to images and data from the experiments of Delorme et al. (2009). For this flow regime, a laminar assumption was totally inappropriate with poor prediction of free surface behaviour and subsurface pressure power spectra. LES results were ever so slightly superior to RANS in some cases, and inferior in others. Generally, both gave very good results but the LES simulations were reported as requiring 2-5 times more CPU time, which makes them difficult to justify.

Within the context of this thesis, what we'll come to later is a study of how sloshing affects thermal mixing within a wide parameter space. LES, and even 3D RANS simulations make such an endeavour difficult to achieve in reasonable time. For this reason, LES will be used sparingly in this thesis. It will be used at

times for 'validation', and as a sanity check in assessing the performance of models with lower fidelity in the absence of experimental data. This will be particularly important for convective thermal mixing in the subsurface, for which validation through experiments is difficult.

3.4 Finite volume method

The finite volume method is a technique for solving partial differential equations in discrete time and space. The finite volume method is a two-step process. First the flow domain is sub-divided into a finite number of small control volumes or 'cells', which together make up the computational grid or 'mesh'. Time-discretisation is also needed for unsteady flows. The second step is to transform the constitutive equations into a set of algebraic equations which can be solved.

The advection-diffusion equation for a generic scalar property ϕ reads in its integral form as follows:

$$\int_V \frac{\partial(\rho\phi)}{\partial t} dV + \int_V \nabla \cdot (\rho \boldsymbol{u}\phi) dV = \int_V \nabla \cdot (\Gamma \nabla\phi) dV \tag{3.31}$$

where Γ is the scalar diffusivity. Each term is integrated over a control volume or cell. Applying Gauss' theorem gives:

$$\int_V \frac{\partial(\rho\phi)}{\partial t} dV + \oint_S (\rho \boldsymbol{u}\phi) \cdot \boldsymbol{n} dS = \oint_S (\Gamma \nabla\phi) \cdot \boldsymbol{n} dS \tag{3.32}$$

where n is the unit normal vector to the cell surface. **Eq.** 3.32 states that the local rate of change in quantity of some scalar ϕ is equal to the advective/diffusive flux in/out of each control volume. Thus any local losses are compensated by gains elsewhere and global conservation is maintained. This feature is paramount to

the attractiveness of applying the FVM to modelling fluids, whose governing equations are fundamentally concerned with the transport and conservation of mass, momentum and energy.

Diffusion

The diffusion term is relatively simple to discretise. Due to its lack of prevailing flow directionality, the diffusion across cell face f_{PE} can be approximated with good accuracy using a second-order central-differencing scheme:

$$\int_{S_{\mathrm{PE}}} (\Gamma \nabla \phi) \cdot \boldsymbol{n} dS = \Gamma \Big(\frac{\phi_E - \phi_P}{x_E - x_P} \Big) \cdot \boldsymbol{S}_{\mathrm{PE}} \tag{3.33}$$

where S_{PE} is the surface area of the cell face between cells P and E, $x_E - x_P$ is distance between cell centroids and Γ is the coefficient of diffusivity.

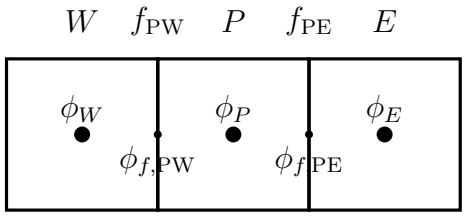

Figure 3.1: Scalar values stored at cell centres and evaluated at cell faces on the finite volume computational grid.

The total diffusive flux between cell P (shown in **Fig.** 3.1) and its neighbours E & W can be assessed by a summation of flux on each face

$$\begin{aligned} \oint_{S_{\mathrm{P}}} (\Gamma \nabla \phi) \cdot \boldsymbol{n} dS &= \sum_f \boldsymbol{S} \cdot (\Gamma \nabla \phi)_f \\ &= \Gamma \left[\Big(\frac{\phi_E - \phi_P}{x_E - x_P} \Big) \cdot \boldsymbol{S}_{\mathrm{PE}} + \Big(\frac{\phi_P - \phi_W}{x_P - x_W} \Big) \cdot \boldsymbol{S}_{\mathrm{PW}} \right] \end{aligned} \tag{3.34}$$

Advection

The advection term of **Eq.** 3.32 is discretised as follows:

$$\begin{aligned}\oint_S (\rho \boldsymbol{u}\phi)\cdot \boldsymbol{n} dS &= \sum_f \boldsymbol{S}_f \cdot (\rho \boldsymbol{u}\phi)_f, \\ &= \sum_f \boldsymbol{S}_f \cdot (\rho \boldsymbol{u})_f \phi_f, \\ &= \sum_f F\phi_f,\end{aligned} \tag{3.35}$$

where F is the mass flux through the cell face, $F = \boldsymbol{S}_f \cdot (\rho \boldsymbol{u})_f$. Advective scalar transport is challenging as local flow-directionality needs to be accounted for. A primary requisite of a good numerical scheme is that ϕ remains bounded. Not only that, but the scheme must be stable and accurate, with the ability to resist generating spurious oscillations in the regions of sharp discontinuities. In order to achieve this, an appropriate discretisation scheme must be used to interpolate ϕ to cell faces, ϕ_f. We will describe some of the numerical schemes relevant to the work in this thesis, referred to by their names as specified in `OpenFOAM`.

The simplest approach is the `upwind` scheme, where ϕ_f is taken as being equal to the upstream cell-centred value:

$$\phi_{f,\mathrm{PE}} = \begin{cases} \phi_P & \textbf{if} \quad F \geq 0 \\ \phi_E & \textbf{if} \quad F < 0. \end{cases} \tag{3.36}$$

The simplicity of this scheme allows the preservation of boundedness at the expense of introducing numerical diffusion and subsequently lowering accuracy.

For higher-order accuracy, the `linear` scheme uses central-differencing to interpolate cell values to faces from both upstream and downstream cells. Referring back to **Fig.** 3.1, the scalar value $\phi_{f,\mathrm{PE}}$ would be calculated as follows:

$$\phi_{f,\mathrm{PE}} = \phi_P \lambda_{\mathrm{int}} + \phi_E (1 - \lambda_{\mathrm{int}}) \tag{3.37}$$

where λint is the interpolation function based on the gradient and distance from cell centre to cell face:

$$\lambda_{\mathrm{int}} = \frac{x_{EP} - x_P}{x_E - x_P}. \tag{3.38}$$

Despite offering higher accuracy (second-order), the linear scheme is known to produce unphysical oscillations in regions of steep gradients and cannot guarantee boundedness. `OpenFOAM` includes a collection of total variation diminishing (TVD) and normalised variable diagram (NVD) schemes. These typically blend the stability and boundedness of the upwind scheme with the accuracy of high-order schemes. An example of blending with the linear scheme reads as follows:

$$\phi_{f,PE} = \gamma \phi_{\mathrm{PE,linear}} + (1 - \gamma) \phi_{\mathrm{PE,upwind}}, \tag{3.39}$$

where γ is a blending factor. In this thesis we will commonly use two TVD schemes; the `limitedLinear` scheme for momentum advection and `vanLeer` for the advective transport of volume fraction. The blending factors for both `limitedLinear` and `vanLeer` are as follows. First for `limitedLinear`:

$$\gamma = \max(\min(2r/k, 1), 0) \tag{3.40}$$

where k is a user-defined input taken to be 1 and r is the ratio of successive gradients:

$$r = 2\frac{\boldsymbol{d} \cdot (\nabla\phi)_P}{\phi_E - \phi_P}. \tag{3.41}$$

The `vanLeer` Van Leer (1974) blending function reads:

$$\gamma = \frac{(r + |r|)}{(1 + |r|)}. \tag{3.42}$$

3.5 Model validation

3.5.1 From the literature

`interFoam` has proven to be a robust tool for modelling a wide variety of free surface flows — sloshing included. We will conduct our own validation studies, but first we will strengthen the argument with a quick survey of some examples from the literature.

Merchant et al. (2016) used `interFoam` to model shallow water sloshing, demonstrating excellent agreement with the experimentally measured subsurface pressure impulses of both Hinatsu (2001) and Rafiee et al. (2011). Jäger (2019) found further good performance (see **Fig.** 3.2) in the prediction of sloshing impacts due to tank rolling from the experiments of Botia-Vera et al. (2010), which were conducted as part of their ongoing project for generating benchmark cases for testing SPH codes. As an aside, the collected works of Souto-Iglesias et al. (2011, 2012) & Delorme et al. (2009) deserve particular praise in general due to their efforts in generating repeatable experiments and sharing their data in an accessible way. Jin et al. (2020) found good results matching the experimental free surface wave heights in a tank undergoing pure sway motion reported by Jin et al. (2014), and the experimental free surface behaviour of tanks with a vertical slot baffle (Faltinsen

et al., 2011).

Xue et al. (2019) conducted a series of benchmark tests for a variety of tank shapes, validating `interFoam` against experimental results measured in prismatic (Didier et al., 2014; Arai, 1984), rectangular (Liu and Lin, 2008), cylindrical (Chen et al., 2007; Akyıldız et al., 2013) and spherical (Chiba et al., 2016) tanks. Li et al. (2012) deployed `interFoam` in the coupling of internal fuel tank sloshing and ship motions, with good validation against experimental measurements of ship heave and roll motions in the frequency domain. Chen and Xue (2018) further tested the performance of `interFoam` over a range of fill heights for sloshing under pure sway in rectangular tanks. Once again, they found excellent agreement with their own experiments and when matching the data from Liu et al. (2016). Sanapala et al. (2016) showed `interFoam` to be robust over a range of conditions, matching the experimental measurements by Ozdemir et al. (2010) of wave response under both resonant and non-resonant excitation conditions.

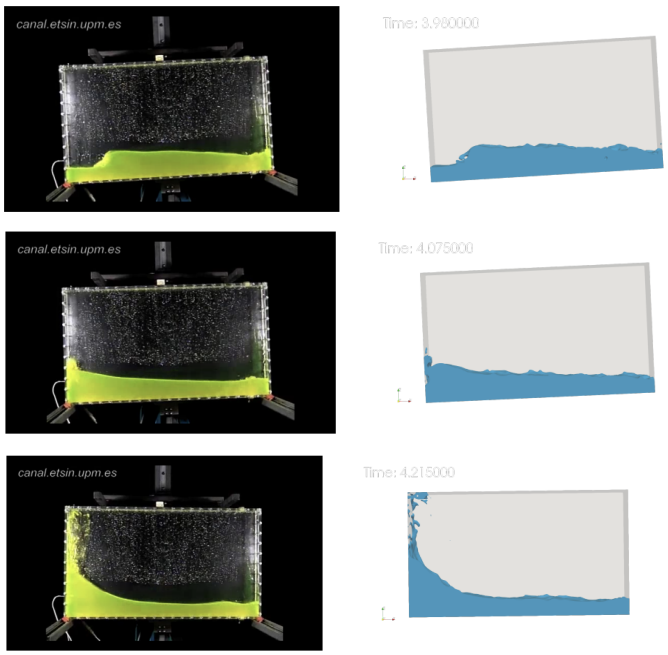

Figure 3.2: Comparison of `interFoam` (right) to experiments (left) in modelling in sloshing wave impact (Jäger, 2019)

We can see from the dates on these citations that `interFoam` has become

a popular choice for researchers investigating sloshing flows over the last decade or so. Surveying the literature has revealed numerous cases of excellent performance over a range of operating conditions and tank geometries. We will make a further contribution by performing some validation studies of our own.

3.5.2 Numerical model set-up

The initial conditions at $t = 0$ are for the flow to be completely at rest. The initial volume fraction field representing the fluid phases is defined using the `setFields` utility. Water is introduced into the domain in cell regions specified as $\alpha = 1$ using the `setFieldsDict` dictionary. All remaining cells are left at their default initial values of $\alpha = 0$. The $k - \omega$ SST turbulence model with equations as described in **Section** 3.3.1 is used throughout this validation study. Boundary conditions for each of the flow variables are listed in **Table** 3.2. A viscous sub-layer solution and wall-function blending is imposed for specific dissipation rate, ω at the wall:

$$\omega_{wall} = (\omega_{vis} + \omega_{log})^{\frac{1}{2}}, \tag{3.43}$$

where:

$$\omega_{vis} = \frac{6\nu}{0.075 y_{wall}^2}, \tag{3.44}$$

and

$$\omega_{log} = \frac{\sqrt{k}}{0.09^{1/4}\kappa^* y_{wall}}. \tag{3.45}$$

No-slip conditions are imposed on the velocity field at the wall. A zero-gradient condition is applied for all other flow variables.

Variable	Wall condition	Description
k	$\partial k/\partial \hat{n} = 0$	Zero-gradient
ω	`omegaWallFunction`	ω-wall function
$\boldsymbol{u}$	$u_x = u_y = u_z = 0$	No-slip
p^*	$\partial p^*/\partial \hat{n} = 0$	Zero-gradient
α	$\partial \alpha/\partial \hat{n} = 0$	Zero-gradient

Table 3.2: Model boundary conditions for RANS simulations

Numerical schemes used for the discretisation of each term are listed in **Table** 3.3. The `vanLeer` scheme is chosen for the advection term in the volume-fraction equation to account for steep gradients at the interface, while the `interfaceCompression` scheme is used for the compression term in the α-equation (Jasak and Weller, 1995). Second-order schemes are used for the remaining advection terms.

Term	Scheme
Velocity advection	`Gauss limitedLinearV 1`
Volume fraction advection	`Gauss limitedVanLeer 01`
Interface compression	`Gauss interfaceCompression`
Turbulent kinetic energy	`Bounded Gauss linearUpwind`
Specific dissipation rate	`Bounded Gauss linearUpwind`
Gradients	`Gauss linear`
Laplacian	`Gauss linear`
Transient	`Euler`

Table 3.3: Discretisation schemes

A summary of the solver controls is listed in **Table** 3.4. The compression coefficient introduced in **Eq.** 6.8 is set to $C_\alpha = 1$ so as to apply a nominal amount of counter-diffusion at the interface. Sub-cycling gives the user the option of solving the α-equation n times per outer iteration loop of the PISO solver. In theory, this allows the time-step to be relaxed. However, throughout this thesis the stability will be controlled by maximum global Courant number. Solving the α-equation via the explicit MULES solver requires a restrictive Courant number, $Co \leq 0.1$ which is maintained throughout this thesis.

Control Paramater	Value	Description
C_α	1	Compression coefficient
# sub-cycles	1	α-equation sub-cycles
Co	0.1	Courant number
Tolerance	10^{-8}	Convergence tolerance

Table 3.4: Solution controls

3.5.3 Intermediate sloshing under roll motion; validation against experiments of Chen et al. (2013b)

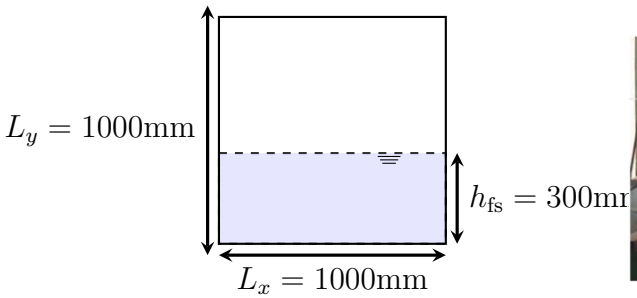

(a) Tank schematic

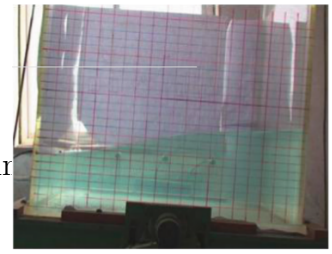

(b) Experimental rig

Figure 3.3: Tank dimensions and image from experimental setup

Sloshing in a partially filled tank at 'intermediate' filling ratio undergoing roll motions is modelled, with comparison of results to the experimental pressure probe data provided by the work of Chen et al. (2013a). The authors themselves used this data to validate their own SPH code. 4 cases are considered, corresponding to 4 excitation frequencies as listed in **Table** 3.5. The tank (**Fig.** 3.3) has dimensions of length $L_x = 1000$mm, height $L_y = 1000$mm, with a filling level $h_{\text{fs}} = 300$mm, giving a fill ratio of $h_{\text{fs}}/L_x = 0.3$. Pressure is measured by a probe placed 100mm beneath the initial free surface height. For details of the set-up of the numerical model, see **Section** 5.2.1

Case	**Forcing Frequency**, ω [rad.s^{-1}]	ω/ω_1	**Period**, T [s]
1	0.95	0.20	6.61
2	3.09	0.65	2.03
3	3.81	0.80	1.64
4	5.47	1.15	1.15

Table 3.5: Excitation frequencies and time periods for different case set-ups

Fig. 3.4 shows strong agreement between the pressure probe time-series data. Amplitude and frequency of pressure variation is predicted particularly well for cases 1 and 2. Case 4, which is the closest frequency to resonance is a little more challenging due to the erratic behaviour seen in the data. At times the gauge pressure drops to $p = 0$ as the free surface dips beneath the probe's location, exposing it to air (and atmospheric pressure). Despite this, the model is able to capture the irregular behaviour very well.

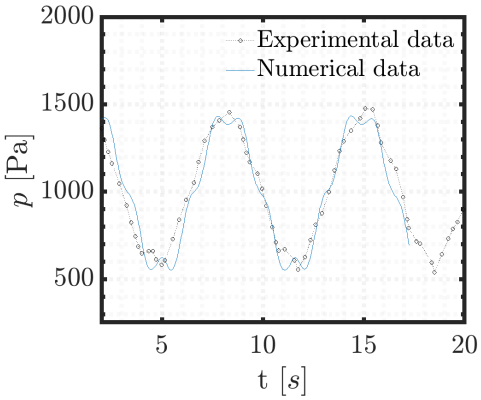

(a) Case 1

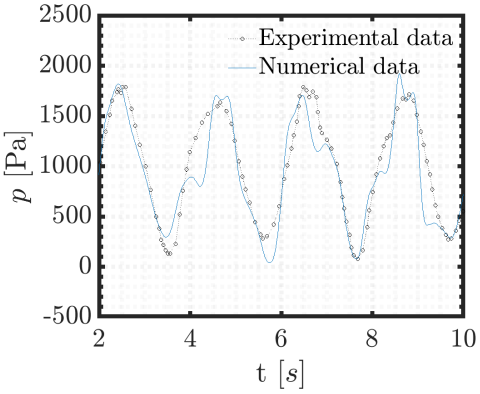

(b) Case 2

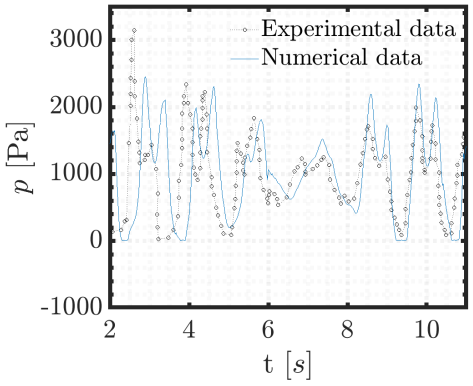

(c) Case 4

Figure 3.4: Comparison of simulated and experimental pressure probe predictions

Good prediction of wall pressure in the subsurface tells us implicitly that the motion of the free surface is being accurately represented by the model. To further confirm this, in **Fig.** 3.5 we superimpose the numerically predicted free surface on to snapshots of the experiments for case 3 provided by Chen et al. (2013a). The various stages of flow development, from a travelling bore-front to an elongation of the free surface as it climbs steeply up the side-walls in response to the inclination of the tank are all captured successfully by the model.

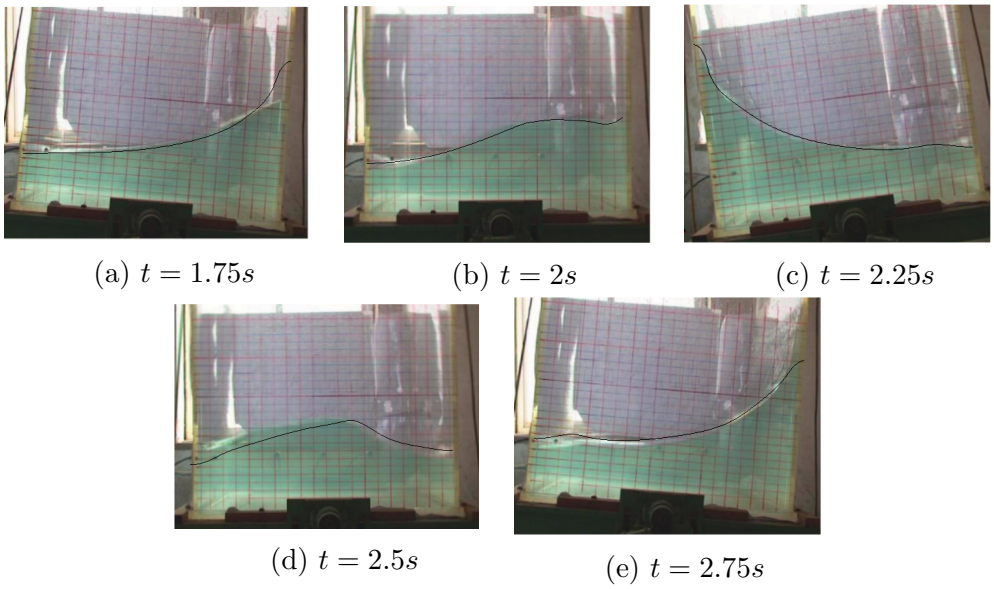

(a) $t = 1.75s$ (b) $t = 2s$ (c) $t = 2.25s$

(d) $t = 2.5s$ (e) $t = 2.75s$

Figure 3.5: Numerically predicted free surface profile superimposed over pictures taken of the experimental rig. **Case 3** from Chen et al. (2013a).

3.5.4 Shallow water sloshing under roll excitation; validation against the experiments of Armenio and La Rocca (1996)

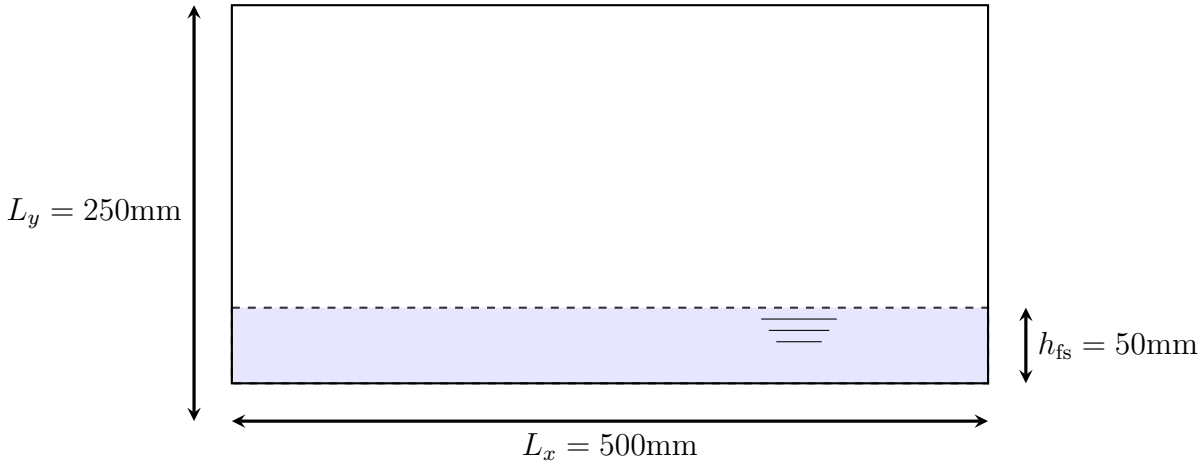

Figure 3.6: Tank schematic

Description

The shallow water regime is challenging due to the increasing occurence of non-linearities such as wave-breaking; travelling waves/hydraulic jumps form, which have a much greater propensity for collapsing than the standing waves formed at deeper fill ratios. For this reason it is essential we test the capabilities of `interFoam` in modelling sloshing within this regime. Armenio and La Rocca (1996) conducted experiments of a tank undergoing rolling action, using an ultrasonic sensor to detect the interface location. This is measured at 150mm from the tank side wall. Tank dimensions (see **Fig.** 3.6 for schematic) are height $L_y = 250\text{mm}$, length $L_x = 500\text{mm}$ with a liquid filling depth of h_{fs} =50mm, giving a fill ratio of $h_{\text{fs}}/L_x = 0.1$. The roll amplitude is $A_\theta = 0.91$. **Fig.** 3.7 shows a comparison of the measured and predicted free surface height, $h_{\text{fs}}(t)$ plotted as a function of time, with tank rolling frequency $\omega = 5.05\text{rad/s}$.

Response frequency, and amplitude of wave peaks and troughs are aligned

very closely, although there are some small differences. The simulated surface motions are more regular, with a consistent double-peak pattern. The response signal from the experiments shows much more variation period-to-period — sometimes the double-peak pattern is clear and present, and sometimes it is completely absent. This would suggest that shallow water sloshing is inherently more unstable and irregular than intermediate and deep water sloshing, which makes these cases more difficult to capture numerically. With this in mind, the results of any numerical investigations involving shallow fill height cases throughout the rest of this thesis might be considered with a little more caution than for the deep fill tank simulations.

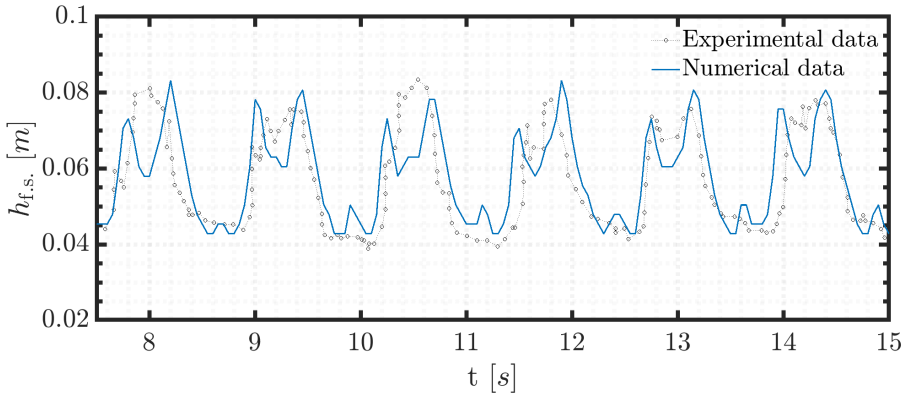

Figure 3.7: Free surface height vs time, `interFoam` results compared with experiments of Armenio and La Rocca (1996). Fill ratio $h_{\text{fs}}/L_x = 0.1$, forcing amplitude $A_\theta = 0.91$ and frequency $\omega = 5.05$

3.5.5 Finite depth sloshing under pure sway motions; validation against the experiments of Jin et al. (2014)

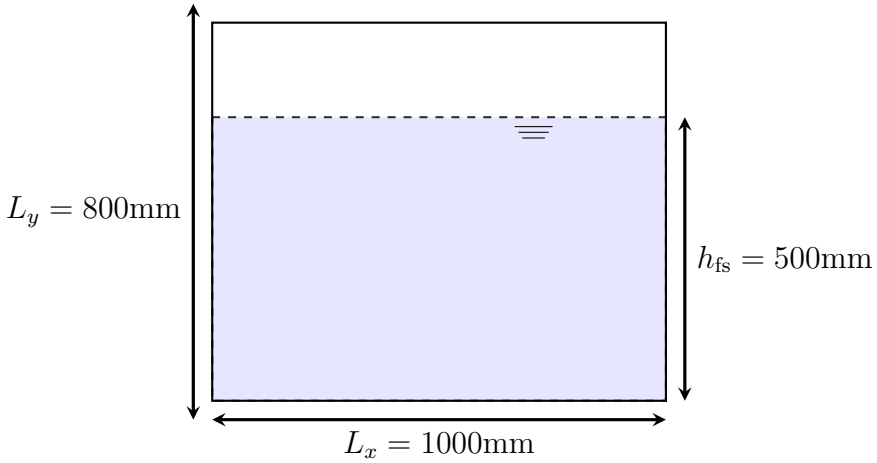

Figure 3.8: Tank schematic

To test the performance of `interFoam` in modelling sloshing flows at 'finite depth', which is characterised by the formation of standing waves, the experiments of Jin et al. (2014) were replicated. Their research investigated the sensitivity of sloshing response as a function of excitation frequency. The tank dimensions (as in **Fig.** 3.8) are length $L_x = 1000\text{mm}$, height $L_y = 800\text{mm}$ with a fill depth of $h_{\text{fs}} = 500\text{mm}$, giving a fill ratio of $h_{\text{fs}}/L_x = 0.5$. The tank motion is of pure sway, with a constant sway amplitude of $A = 2.5\text{mm}$. Each experiment was allowed to run for 40s, and so the duration of simulations are matched accordingly.

One of the difficulties in sourcing quality experimental data for validation of numerical sloshing models is that the lab conditions i.e. forcing parameters (amplitude, frequency) aren't always reported correctly. Due to the high sensitivity of sloshing behaviour to the parameters, this can render them totally useless for the purposes of validation. Jin et al. (2014) measured both sway amplitude and frequency of tank motions in their lab set-up using a laser displacement sensor (including the results in their publication), demonstrating that their rig is able to maintain a constant value for both parameters throughout. This gives us a high

degree of confidence in using these results as a benchmark.

Experimental and numerical wave heights are plotted in **Fig.** 3.9 as a function of excitation frequency, which is normalised to the primary mode predicted from linear theory $\omega_1 = 5.32\text{rad.s}^{-1}$ The figure gives a clear demonstration of resonance in action; sharp peaks are visible at the first and third natural frequencies $\omega = \omega_1$ and $\omega = \omega_3$ where $\omega_3/\omega_1 = 1.81$. Snapshots taken from the experiments showing corresponding free surface mode shapes for these frequencies are shown in **Fig.** 3.10. Tank motions at $n = 2$ ($\omega/\omega_1 = 1.48$) reveal no visible increase in wave response.

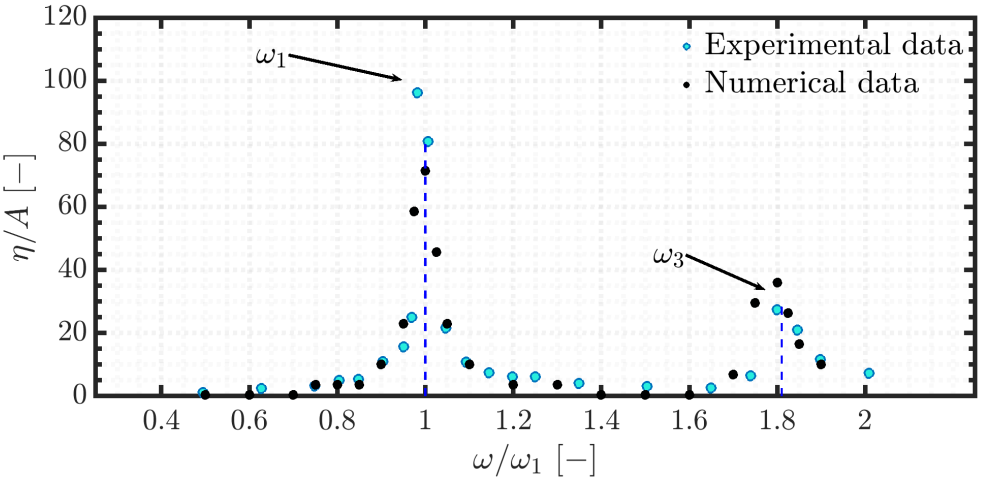

Figure 3.9: Comparison of predicted maximum wave heights, simulations and experimental data of Jin et al. (2014)

The model captures this resonance well, the location and shape of the peaks being in almost total agreement. There is a small discrepancy in the predicted maximum wave amplitude found at the two peaks, but this is to be expected. A very minor tweak in the imposed forcing frequency can cause a big difference due to the local steepness of the response curve. With some fine tuning it is possible the data could become more aligned.

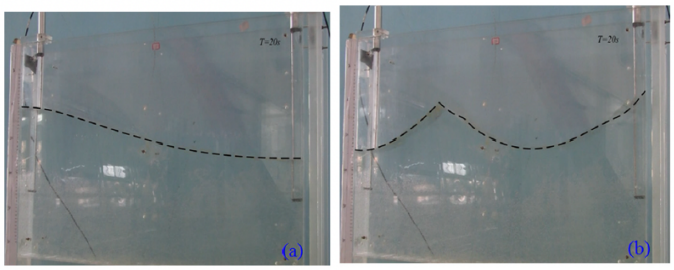

(a) $\omega = \omega_1$ (b) $\omega = \omega_3$

Figure 3.10: Mode shapes at resonant frequencies $n = 1, 3$ from experiments of Jin et al. (2014)

3.5.6 Summary

`interFoam` has been shown to be a reliable model for modelling sloshing over a wide range of conditions. It has proven to be robust in accurately capturing free surface behaviour and subsurface pressure variations. This has been tested at resonance, with predicted natural frequencies matching up closely with both experiments and theory. Furthermore, we have tested the model through a variety of regimes: 'shallow', 'intermediate' and 'finite depth' sloshing. The results presented both in this chapter and throughout the recently published literature give us a high degree of confidence that `interFoam` is an appropriate tool for studying sloshing flows.

As a general note on the use of experimental data for validating numerical sloshing models, it was found that most data is presented as a singular time-series, or simply as a maximum value over time through one test run. Little attention is paid to the repeatability of these experiments, and experimental uncertainty is often unreported in any quantitative manner. The usefulness of experimental data for validating numerical models would be strengthened considerably by the inclusion of quantitative measures such as error bars. It is strongly encouraged that this is to be done in the future. Souto-Iglesias et al. (2012) similarly highlighted this requirement in their investigation into the repeatability of sloshing experiments. They found that repeatability is indeed sensitive to parameters such as fluid viscosity and tank

aspect ratio. They suggested that sensitivity studies should be performed to identify combinations of parameters which allow for a high degree of repeatability within the experiments. Furthermore, they recommend the need for uncertainty analysis and error bounds to be included in data reports to help in the process of validating CFD codes. It would seem that for the most part, these demands have seldom been met.

Chapter 4

Turbulence modelling and stratified multiphase flows

4.1 Interactions between turbulence and the free surface

The simulation of multiphase stratified flows poses a significant challenge, requiring a model that encapsulates the location and behaviour of the free surface, whilst also capturing the kinematics of each phase, whether they be liquid or gas. The previous chapter has demonstrated the success of deploying a VOF model coupled with the unsteady RANS equations in predicting the dynamic behaviour of the free surface in simple linear harmonic sloshing flows. This satisfies the *first* requirement. To satisfy the second aspect, we need to analyse and evaluate the kinematic behaviour in the sub-surface (water) and super-surface (air) regions of the flow. The interaction between the sub-surface dynamics and the motion of the free surface are particularly important to mixing, and although the literature on sloshing flows is beyond extensive, there is rarely any attention given to the behaviour and flow structures (be they turbulent or otherwise) that develop beneath the free surface.

The stark lack of data and measurements of hydrodynamic properties in comparison, i.e. velocity field, turbulence properties (turbulent kinetic energy, eddy viscosity) for sloshing flows in particular is most likely due to the difficulty in measuring spatially variant and time-dependent quantities in an unsteady flow constrained by moving boundaries in which the morphology of the bulk fluid is continually evolving. Measured properties are often confined to point data at a fixed location. To understand the nature of the evolving sub-surface flow structures we need a full picture of the flow field.

It is also true that the effects of the free surface motion on scalar mixing has seldom been the point of interest when considering sloshing. The emphasis is almost exclusively on the wave response (and the prediction thereof), pressure spikes at specific probe locations and the forces and moments acting on the tank wall. This is understandable as the engineer is often mainly concerned with the structural integrity of the fuel/storage tanks under high impact loads, and the effects of free surface motion on the overall stability of the vehicle at large. A detailed description of the sub-surface has perhaps not been necessary to make an engineering assessment. If we are interested in the mixing of scalar quantities within sloshing flows however, knowledge of the free surface behaviour alone is not enough.

Perhaps what is least well understood in sloshing flows is the role of turbulence. When the forcing parameters are weak, e.g low amplitude or a forcing frequency well removed from any natural mode, the role of turbulence is likely also similarly weak. This notion is reinforced by the success that both linear and non-linear potential flow theory models have had in predicting wave response at small excitation amplitudes. The assumptions underlying these models that the flow be inviscid and irrotational break down as non-linear effects such as wave over-turning and breaking become more significant. Turbulence and vorticity generation is profuse in the post-wave-breaking surf zone. Furthermore, in the regions in which the free surface interacts with the walls, viscous effects will be felt more strongly.

Within the literature, despite the scarcity of analysis of the sub-surface kinematics of sloshing flows, efforts have been made to understand the nature of turbulence in simple free surface flow configurations e.g. air-water channel, pipe flow. The most insightful of which have consisted of experimental measurements as well as high-fidelity numerical simulations (of which the physical models used have increased in complexity as the research has advanced).

Rashidi and Banerjee (1988) performed experimental velocity measurements using high speed photography to trace a turbulent open channel flow field seeded with oxygen bubbles. They found that for stably stratified flows (water flowing beneath air in this case), the vertical turbulent velocity fluctuations in the water are reduced at the free surface, with a subsequent enhancement of velocity fluctuations in the stream-wise and span-wise directions. Gravity and surface tension plays a vital role in this damping mechanism normal to the free surface. This is in agreement with the observations made by Satoru et al. (1982), who made similar attempts to characterise the velocity fluctuations in an open channel flow, this time using laser Doppler velocimetry. Nagaosa and Saito (1997) present the results of their DNS model, again observing the characteristic suppression of vertical motions at the interface. The turbulent flow and pressure fluctuations at the surface are ultimately unable to overcome the combined forces of surface tension and negative buoyancy (gravity) to transport itself through the free surface, and so the energy is redistributed into the surface-parallel plane. Nagaosa and Saito (1997) also observe and describe the mechanism by which the near-surface region is replenished by flow structures originating in the near-wall turbulent boundary layer. Vortical structures are released into the main flow periodically, and are the primary source of turbulence away from the wall, playing a key role in the transport of heat and mass up to and across the interface. This is reinforced by the findings of Rashidi and Banerjee (1988), who posited that these vortical structures are released due to the formation of high and low-speed streaks in the turbulent boundary layer becoming unstable. Rashidi and Banerjee (1990) found the same phenomenon occurring at

the free surface when a local shear is imposed by the action of the gas layer above. This streak formation leads to the intermittent release of rolling turbulent structures into the mean flow, enhancing momentum and scalar mixing throughout the depth of the flow.

Much of this earlier work was focussed on the turbulent profile beneath the free surface, with little attention paid to the effect of the free surface on the air flow above. Lombardi et al. (1996) performed DNS simulations to resolve the flow in both the liquid and gas phases. A separate momentum equation was solved for each fluid, which were then coupled at the interface by imposing continuity of shear stress and velocity. In the liquid phase they found that both the intensity of destruction and production of turbulence is greatest closest to the free surface, while in the gas phase, the flow field sees the liquid very much like it would a solid wall. This is apparent by the asymptotically increasing turbulence dissipation as the surface is approached. The modelling approach deployed by Lombardi et al. (1996) has the limitation of the free surface being constrained to be smooth and flat, meaning the nuances of interaction between turbulence and surface tension are lost. Fulgosi et al. (2003) expanded the physical model even further, adding more complexity with their DNS simulations in modelling counter-current (air flowing upstream as water flows downstream) two phase air-water flow with a deformable interface. Fulgosi et al. (2003) demonstrate wall-like behaviour at the interface in the lighter fluid — the air sees the free surface much like a flexible solid wall. Unlike at the wall however, rather than the turbulence intensity tending towards zero, it reduces to some low but non-zero value at the surface, with a degree of anisotropy less than at the solid wall.

Again, it must be reiterated that these observations are taken from the studies of open-channel flow. The main purpose of discussing these findings is to get a feel for the mechanisms of turbulence development in wall-bounded shear-flows, and the way in which turbulent flow structures interact with the free surface.

Although sloshing flows have now been studied intensively for decades, the role and production of turbulence has barely been formally examined in a quantitative manner. Despite open-channel and sloshing flows having plenty of similarities — they are both stably stratified multiphase flows, with freely deformable interfaces featuring two distinct homogeneous unmixed fluids — most of these studies have featured for the most part steady-state flows. Sloshing is fundamentally a transient, globally unsteady phenomenon, making statistical analysis more difficult. We can assume that the general interaction between turbulence and the free surface will be the same; the impact of the interface on the local turbulence being markedly different depending on which fluids 'sees' the surface. The similarities to sloshing in terms of the mechanisms of turbulence production will really depend on the case parameters. In shallow-water cases we would expect this to hold. In deep water sloshing (when $h/l \geqslant 1$), the tank base has barely any influence on the free surface at all Faltinsen (2017).

To summarise, from the findings of various authors' experiments and simulations there is a consensus on the following points:

1. The effect of the free surface on the turbulence in the heavier fluid is an increase in anisotropy. There is a decrease in the magnitude of the vertical velocity fluctuations, but not necessarily a decrease in the magnitude of turbulent kinetic energy, as the decrease in vertical velocity fluctuation w' can be proportionally compensated by an increase in the surface-plane fluctuations u', v'

2. The lighter fluid (provided that the density ratio between the two fluids is large) interacts with the heavier fluid as if it were a solid wall. An effective boundary layer is formed, as turbulence is dissipated and diminishes to some small but finite value as the interface is approached

3. In the absence of significant generation *at* the free surface on the liquid-side,

the primary source of turbulence in a stratified flow with solid boundaries is the detachment of vortical structures from the turbulent boundary layer at the wall.

4.2 VOF, Two-equation RANS models and the over-prediction of turbulence in multiphase flows

In the previous section, we gained a very brief overview of some experimental/numerical insights that have been made into turbulent, stratified multiphase flows. In this section we will discuss some of the challenges involved in using the numerical tools available to us when attempting to capture these physics accurately.

4.2.1 Turbulence and the Volume of Fluid method

In the previous chapters, we introduced the numerical formulation of VOF and some examples of its usage in modelling sloshing. The volume of fluid model is an attractive option for multiphase flow simulations, proven to perform well for a variety of fluid flows, despite its simplicity. The single-fluid formulation is easy to implement, and is a reasonable approach provided the two-way dynamic coupling of the momentum of the two fluids is not strong. Essentially, the VOF model treats the whole domain as a single fluid, except at the interface where the surface tension term in the momentum equation becomes active. One of the drawbacks of the VOF model is the free surface is often diffuse — spread over a number of cells rather than being represented by a sharp discontinuity. As discussed in **Chapter** 3, techniques can be implemented to compress the interface, or compute local fluxes based on linear piece-wise reconstruction at the interface. Despite these efforts we are often

still left with a region of approximately 3 cells thick (regardless of mesh resolution) over which the transition from one fluid to another is represented by a sharp volume fraction gradient $\partial\alpha/\partial\hat{n}$. For multiphase flows with large density ratios, this thin layer represents a region in which the flow is represented by un-physical transport properties (density, viscosity etc.). Spurious velocity currents and large velocity gradients can develop in this region, the impact of which can be problematic (Pan et al., 2015; Meier et al., 2002; Samkhaniani and Ansari, 2016).

4.2.2 Over-production of turbulence beneath the free surface

It is widely reported in the literature that RANS models often over-predict turbulence beneath the free surface. This has been apparent in simulations of simple wave propagation (Devolder et al. (2017), Devolder et al. (2018), Elhanafi et al. (2017), and more complex interfacial regions involving wave breaking (Mayer and Madsen, 2001; Larsen and Fuhrman, 2018).

Devolder et al. (2017) observed excessive wave damping when they deployed the $k-\omega$ SST turbulence model in conjunction with the VOF method in a numerical wave flume. By running both turbulent and laminar simulations, they were able to determine that the contribution from turbulence was the source of discrepancy. High levels of eddy viscosity beneath the interface region caused energy to dissipate from the free surface, resulting in the wave amplitude decaying over the flume's length.

These observations pertaining to the issues of two-equations RANS models were not the first. Their work echoed the findings of Bradford (2000), who found the $k-\epsilon$ model to over-predict turbulent kinetic energy in waves prior to breaking, with pre-breaking wave amplitudes less than those measured experimentally. Mayer and Madsen (2001) demonstrate via asymptotic stability analysis that the $k-\omega$ equation is conditionally unstable in regions of potential flow, explaining the excessive

damping repeatedly found in simulations of simple wave propagation. They offer an ad-hoc fix for the problem, modifying the usual k-equation source term for shear production:

$$P_k = \tau_{ij}\frac{\partial u_i}{\partial x_j} = p_0 \nu_T, \quad p_0 = 2S_{ij}S_{ij}, \tag{4.1}$$

by replacing the dependency on strain-rate (and hence local mean velocity gradients) with a dependency on flow vorticity:

$$P_k = p_\Omega \nu_T, \quad p_\Omega = 2\Omega_{ij}\Omega_{ij}. \tag{4.2}$$

The trajectory of particles beneath travelling waves are largely orbital in nature, and so a near-potential flow exhibiting low vorticity should exist, in which case $\Omega_{ij} \approx 0$. Including the local rate of rotation directly in the P_k term therefore should have a stabilising effect by limiting the amount of k production in low-vorticity regions. For uniform, parallel shear flows such as open-channel flow or stratified flow in closed conduits, the model reverts back to its original form as $S_{ij} \approx \Omega_{ij}$. This adjustment allows a wave-train to perpetuate without the same decay that is observed over long periods. However, Mayer and Madsen (2001) do emphasise that this modification does not represent a fundamental solution to the instability problem.

4.2.3 Buoyancy modified k-ω SST (`BM`)

Devolder et al. (2018) suggests altering the $k-\omega$ SST model by modifying the k-equation to include a buoyancy source term and making sure to use the fully compressible formulation of the equation. The incompressible RANS equations were not formulated with multiphase flows in mind, and yet are often employed in their sim-

ulation. Even though we do have two incompressible and immiscible fluids (which individually could be treated using the incompressible formulations of the turbulent transport equations), when using a VOF scheme, the density $\rho = \rho(x, y, z)$ is spatially variant in the interface region. Therefore, removing density from within each of the derivative terms is mathematically inconsistent.

Brown et al. (2014) pointed out that all incompressible multiphase solvers included in `OpenFOAM` use the incompressible formulation (see **Eq.** 3.19, with the density only implicitly included via kinematic viscosity $\nu = \mu/\rho$). This allows for excessive diffusion of turbulence across the interface, and hence non-physical wave damping Jacobsen (2011). The widespread use of the incompressible multiphase solvers in `OpenFOAM`, particularly `interFoam` (as highlighted in **Chapter** 3), suggests that the results of many researchers have likely been affected by this same problem, perhaps unbeknownst to them. Fan and Anglart (2020) have attempted to resolve these issues by publishing a set of generalised VOF solvers `varRhoTurbVOF`, which utilise a library of fully compressible turbulence models.

The transport equation for k in the buoyancy modified model, as suggested by Devolder et al. (2017) is as follows:

$$\frac{\partial \rho k}{\partial t} + u_j \frac{\partial \rho k}{\partial x_j} = \rho P_k - \boxed{\rho P_b} - \rho \beta^* k\omega + \frac{\partial}{\partial x_j}\left[\left(\mu + \rho\sigma_k \frac{k}{\omega}\right)\frac{\partial k}{\partial x_j}\right], \tag{4.3}$$

where the bouyancy production source term P_b (highlighted in red **Eq.** 4.3) is based on the simple gradient diffusion hypothesis :

$$\boxed{P_b = -\frac{g_i}{\rho}\overline{\rho' u_i'} = p_b \nu_T, \quad p_b = \alpha_b^* N^2, \quad N^2 = \frac{g_i}{\rho}\frac{\partial \rho}{\partial x_i}.} \tag{4.4}$$

where α_b^* is the turbulent Schmidt number, $\alpha_b^* = 1/0.85$ and N is the Brunt–Väisälä frequency. This term was similarly introduced by Van Maele and

Merci (2006) to improve the modelling capabilities of buoyant plumes to good effect. The basic principle is that turbulence is enhanced in an unstably stratified environment (e.g. hot plume emitted beneath a cooler atmosphere), and suppressed when the stratification is stable (e.g. hot smoke layer residing beneath a ceiling above a cooler layer of air, in which turbulent kinetic energy will be spent trying to overcome adverse buoyancy forces). The inference of including this term in a multiphase model is that turbulence will be similarly suppressed at the air-liquid interface. In this region we have stable stratification with an extremely large density ratio $\rho_{\text{water}}/\rho_{\text{air}} \approx 1000$ spread across a thin layer. The term $\partial\rho/\partial x_i$ becomes very large at the interface, making P_b an overwhelming destruction term, and as $\nu_t \propto k/\omega$, the eddy viscosity then vanishes at the free surface. Devolder et al. (2018) demonstrate that this laminarisation of flow in the immediate surface region mitigates the decay of wave heights for simple travelling waves. Furthermore, by using their model to simulate the spilling breaker experiments of Ting and Kirby (1994), it was found to produce improved results for predicting the flow dynamics in the post-wave breaking surf zone. Good agreement was achieved when comparing measurements of the undertow velocity, turbulent kinetic energy and the free surface wave profile. The model is shown to be robust across a range of localised flow conditions. The ability of the buoyancy production term P_b to become inactive in the chaotic surf zone allows the highly turbulent subsurface zone to be captured. Note: throughout the remainder of this thesis, the buoyancy-modified $k-\omega$ SST model will be referred to using the style `BM`, while the standard unmodified model will be referred to as `KWSST`.

Comments on the buoyancy-modified formulation of the $k-\omega$ SST model

The work of Devolder et al. (2018) represents a step forward in turbulence modelling for multiphase flows. Not only have they highlighted the importance of using fully compressible turbulence models for variable-density incompressible multiphase flows,

they also brought to attention how widely this requirement had been neglected (not always addressed in popular CFD codes). Furthermore, they offer up a solution to over-production of turbulence beneath the interface.

However, there are some fundamental issues with the buoyancy-modified model that are worth discussing:

1. The density gradient term, $\frac{\partial \rho}{\partial x_i}$ in **Eq.** 4.4 requires a numerical approximation of the local density gradient at the interface. As we know, within the VOF paradigm of surface tracking techniques, density is calculated via linear interpolation based on local volume fraction: $\rho = \alpha\rho_1 + (1-\alpha)\rho_2$. Therefore, the additional k source term (**Eq.** 4.4) is dependent on this volume fraction gradient, which is itself a non-physical numerical approximation of a real, physical surface. Furthermore, the tendency of the interface to be smeared over a number of cells (3 from experience), makes this term sensitive to grid resolution.

2. Using the simple gradient hypothesis in the source term formulation is based on good physical and mathematical arguments when applied to turbulence enhancement/suppression due to thermally induced density gradients (Van Maele and Merci, 2006). However, simply destroying turbulent kinetic energy at the free surface does not reflect the mechanism of redistribution demonstrated in experiments.

3. The modifications made to the model fail to address the fundamental instability of RANS models in regions of near-potential flow highlighted by Mayer and Madsen (2001). Although the growth of turbulent kinetic energy may occur most problematically in the near-surface region, the free surface itself is not necessarily the singular source of excessive turbulence.

4.2.4 Stabilised k-ω SST model (STB)

Larsen and Fuhrman (2018) further developed the $k-\omega$ SST model for free surface flows, using a modification that can be applied to all two-equation RANS models. This new modification attempts to stabilise the production of turbulence in regions of near-potential flow. Despite acknowledging the work of Devolder et al. (2017), and being in agreement that the features of compressibility and a buoyancy source term are vital, it is suggested that their model still fails to address the underlying problems of instability. Recalling the work of Mayer and Madsen (2001), they present an extended stability analysis to conclude that all two-equation models are in fact unconditionally unstable in regions of potential flow beneath surface waves, resulting in an exponential growth in eddy viscosity and turbulent kinetic energy. To mitigate this, they introduce a stress-limiting feature to the model equations, which we will present in full. The k-equation is unchanged from the buoyancy modified model:

$$\frac{\partial \rho k}{\partial t} + u_j \frac{\partial \rho k}{\partial x_j} = \rho P_k - \rho P_b - \rho \beta^* k\omega + \frac{\partial}{\partial x_j}\Big[\Big(\mu + \rho\sigma^* \frac{k}{\omega}\Big)\frac{\partial k}{\partial x_j}\Big], \tag{4.5}$$

as is the scale equation for specific dissipation rate:

$$\frac{\partial \rho \omega}{\partial t} + u_j \frac{\partial \rho \omega}{\partial x_j} = \rho P_\omega - \rho \beta \omega^2 + \rho \frac{\sigma_d}{\omega}\frac{\partial k}{\partial x_j}\frac{\partial \omega}{\partial x_j} + \frac{\partial}{\partial x_j}\Big[\Big(\mu + \rho\sigma \frac{k}{\omega}\Big)\frac{\partial \omega}{\partial x_j}\Big]. \tag{4.6}$$

The new stress-limiting feature is introduced into the calculation of eddy viscosity:

$$\nu_T = \frac{a_1 k}{\max\left(a_1\omega, F_2\sqrt{p_0}, \boxed{a_1\lambda_2\frac{\beta}{\beta^*\alpha^*}\frac{p_0}{p_\Omega}}\omega\right)}. \tag{4.7}$$

where α^* is a closure constant (Menter, 1994) and the production terms due to strain and rotation are given by:

$$p_0 = 2S_{ij}S_{ij}, \qquad p_\Omega = 2\Omega_{ij}\Omega_{ij}, \tag{4.8}$$

The modification to the calculation of eddy viscosity is in the third argument of the denominator $a_1\lambda_2\frac{\beta}{\beta^*\alpha}\frac{p_0}{p_\Omega}$, which is active only when $p_0 \gg p_\Omega$. This will occur when the strain rate is much greater than the vorticity. This is intended to curtail the erroneous, unstable growth of turbulent quantities in regions beneath surface waves, in which the flow is often weakly rotational, but with some finite strain rate. In regions where $p_0 \approx p_\Omega$, such as in channel flows, or in the post wave-breaking surf zone where we might have $p_\Omega > p_0$, by definition of the way in which this term is activated, the original behaviour of the model is restored.

During the writing of this thesis, very recent publications have deployed this turbulence model to good effect. Qu et al. (2021) compared its performance to the standard and buoyancy-modified $k-\omega$ SST in simulating breaking waves past a vertical cylinder, finding a great reduction in subsurface turbulence, reflecting a more physically realistic representation of the flow. The stabilised model has been demonstrated to out-perform the buoyancy modified $k-\omega$ SST in modelling wave-breaking processes. Larsen and Fuhrman (2018) found much improved agreement of predicting turbulence and undertow profiles in spilling waves, validated against the experiments of Ting and Kirby (1994). This was further extended to plunging waves over breaker bars (Larsen et al., 2020), again exhibiting superior results in controlling pre-breaking turbulence levels, agreeing well with experiments. The model has since been added to the `OpenFOAM` release version `v1912`. Note: throughout the remainder

of this thesis, the stabilised $k-\omega$ SST model will be referred to using the style `STB`.

4.2.5 Egorov's method of turbulence damping at the interface

Another widely used technique for interface turbulence damping is Egorov's method of treating the interface similarly to how we would deal with solid walls (Egorov et al., 2004). This approach is included in commercial codes such as `STAR-CCM` and `Ansys Fluent`.

For example, applied to the $k-\omega$ model, the destruction term $-\rho\beta\omega^2$ in the ω-equation is balanced (Lo et al., 2010) by a source term:

$$\frac{D\omega}{Dt} = \rho P_\omega - \rho\beta\omega^2 + \boxed{S_{\omega,i}} + 2(1-F_1)\rho\frac{\sigma_d}{\omega}\frac{\partial k}{\partial x_j}\frac{\partial \omega}{\partial x_j} + \frac{\partial}{\partial x_j}\Big[\Big(\mu + \rho\sigma_\omega\frac{k}{\omega}\Big)\frac{\partial\omega}{\partial x_j}\Big], \quad (4.9)$$

where:

$$S_{w,i} = A_i\Delta y\beta\rho_i\Big(\frac{6B\mu_i}{\beta\rho_i\Delta n^2}\Big)^2, \quad (4.10)$$

and where A_i is the interface density:

$$A_i = 2\alpha_i|\nabla\alpha_i|. \quad (4.11)$$

β is a model closure constant, Δy is the local grid size, B is a damping coefficient, ρ_i and μ_i are the respective density and dynamic viscosity of each fluid and Δn is the distance between the cell centre and the interface. For a well defined interface it would be reasonable to assume $\Delta y = \Delta n$. It is imperative that **Eq.** 4.11 includes the gradient of volume fraction; a sloped interface represented by a step function could contain values $\alpha = 0, 1$ in the cells directly adjacent to the free

surface, and therefore would not be recognised as an interface region.

In single phase regions this term equals zero and so the term is inactive. At the free surface ($0 < \alpha < 1$) this source term results in an asymptotic increase in turbulence dissipation as the interface is approached.

Numerous authors have applied this method with improved results for air velocity and turbulent quantities in stratified turbulent channel flow (Gada et al. (2017), Fan and Anglart (2019) and Frederix et al. (2018)), condensation heat transfer in a circular tube Qiu et al. (2018), pressure losses in stratified and wavy-stratified pipe flow (Lo et al., 2010), oil and gas slug flows in pipes (Fiebach et al., 2016) and prolonged wave propagation (Elhanafi et al., 2017). Given that it is a feature embedded into such widely used commercial codes, it has no doubt been used in many other studies, perhaps without being explicitly reported.

Comments on Egorov's method of damping

Despite the success of the Egorov model as reported by numerous authors, it certainly has some issues. Firstly, the damping coefficient B is a tunable parameter and mesh-dependent; selecting an appropriate value is not immediately obvious. Some tuning procedure is needed in order to optimise the level of damping required for any combination of a given flow-type and grid resolution. A further limitation is the fact that it acts symmetrically about the interface — wall-like damping is applied to both phases. The magnitude of damping depends on the dynamic viscosity and density of each fluid as $S_{\omega,i} \propto \mu_i^2/\rho_i$. For stratified flows with fluids of large density ratios, the action of the lighter fluid on its heavier counterpart is not dynamically significant. The free surface as far as the heavier fluid is concerned, is best represented as a stress-free boundary. Once again, this attempted fix fails to reflect that turbulence is not so much destroyed at the interface as it is energetically redistributed into the dimensions co-planar to the free surface.

4.3 Benchmark experimental turbulent free surface channel flow, and the calibration of two-equation RANS models

Good arguments have been made in the literature professing some inadequacies of RANS models at predicting turbulence and undertow velocity profiles in the subsurface of multiphase flows. Various remedies have been presented and discussed. In order to test these modifications we need to demonstrate their capabilities by comparing with some experimental data.

The ultimate aim in this avenue of investigation is to gain some confidence in modelling sloshing flows with appropriate turbulence models. Over-production of turbulence can not only damp wave motions, but also erroneously enhance subsurface scalar mixing due to excessive turbulent diffusion. This is critical if we are to model sloshing-driven thermal mixing.

However, we should proceed cautiously and first run the models on a much simpler flow problem. This has two benefits. Firstly, sloshing flows are dynamic, unstable and their features are highly dependent on both the forcing parameters and geometry. Secondly, detailed data for turbulence in the undertow of sloshing flows is as of yet scarce/non-existent, and so we seek a case with data of sufficient quality against which we can calibrate our evaluations of the various modelling approaches.

4.3.1 Experiments

Introduction

The experimental study of local flow structures in stratified flows by Fabre et al. (1987) gives us such data. They investigated co-current stratified air-water flows

in slightly inclined closed channels. A detailed schematic of the experimental rig is shown in **Fig.** 4.1. The channel was inclined with a slope of .1%, dropping in altitude towards the exit downstream. Three different flow configurations were considered, each with variable air flow-rate. Water flow-rate was kept constant. **Table** 4.1 lists the respective air and water flow rates for each, with the case names assigned to them as in the original paper (**Run 250,400,600**).

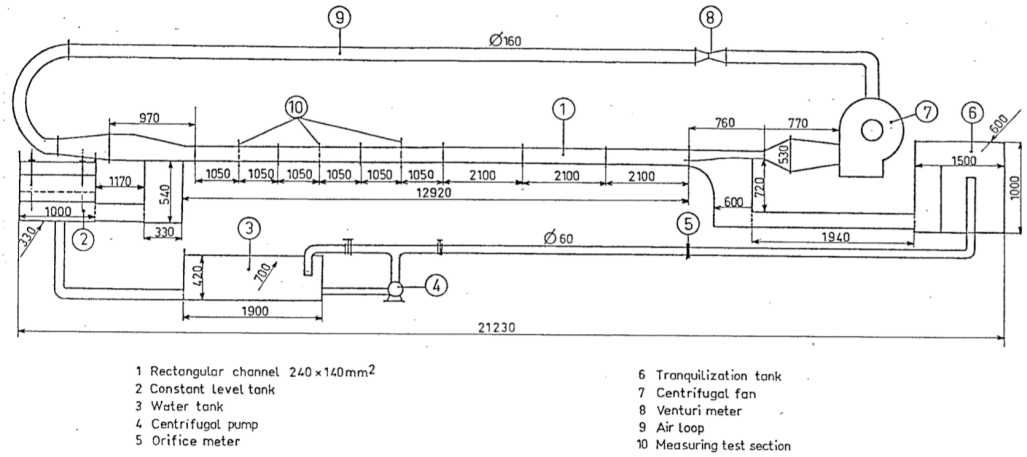

Figure 4.1: Experimental rig, showing inclined closed conduit and recirculating flow channels (Fabre et al., 1987)

Experiment Run	**Inlet flow rate** $[L/s]$	
-	Water	Air
250	3.0	45.4
400	3.0	75.4
600	3.0	118.7

Table 4.1: Water and air flow rates for each experimental run

Data of the following flow properties are recorded and tabulated in the publication:

- Time-averaged horizontal velocity, U_x.
- Time-averaged vertical velocity, U_y.
- Turbulent kinetic energy, k.

- Reynolds stress, $-\overline{u'v'}$.

Measurements were made using a combination of laser Doppler anemometry and hot-wire anemometry. They also provide details of pressure gradient and the free surface height (measured using capacitance probes) for each flow regime. A simplified representation of the set-up, with data-sampling line, is depicted in **Fig.** 4.2.

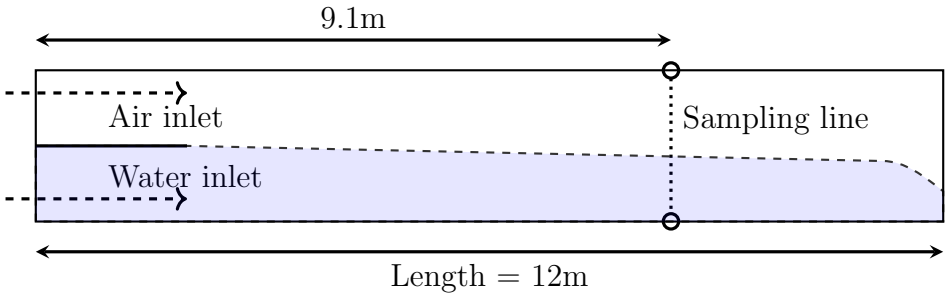

Figure 4.2: Wave response amplitude measurement

Elsewhere in the literature, the velocity, turbulent kinetic energy and pressure gradient data generated by these experiments has been often used for validation; by Fan and Anglart (2019, 2020) to demonstrate the merits of their modifications to turbulence models coupled with VOF methods, by Frederix et al. (2018) in assessing the performance of their two-phase Euler-Euler model featuring Egorov surface turbulence damping, by Terzuoli et al. (2008) to compare the performance of their `Neptune CFD` code (built specifically for modelling internal flows in nuclear plants) to that of `Fluent` and `CFX`, and by Gada et al. (2017) to test the integration of the Egorov model into the two-phase Euler-Euler solver in the commercial software `STAR-CCM+`. Clearly these experiments have proved invaluable so far as to provide a set of quality tabulated data for a simple, yet surprisingly challenging flow problem. This data has served as a solid benchmark for muti-phase turbulence modelling of free surfaces on large scales.

We will follow the procedure of some of the authors mentioned — comparing turbulent kinetic energy and velocity profile predictions to the data. We will

also go further and analyse the effects of modelling approach on the prediction of final water depth. Most importantly, we will also use the measured Reynolds stress data to calculate the experimental eddy viscosity, which is a quantity of utmost importance in validating the performance of any two-equation RANS model.

Eddy viscosity data collection

The Boussinesq hypothesis (the fundamental theory on which Eddy Viscosity RANS models are founded upon) relates the Reynolds stresses to the mean flow field by approximating them to be proportional to the strain rate of the flow, with the eddy viscosity serving as the constant of proportionality:

$$-\overline{u_i' u_j'} = \nu_T\left(\frac{\partial u_i}{\partial x_j} + \frac{\partial u_j}{\partial x_i}\right) - \frac{2}{3}\overline{u_i' u_i'}\delta_{ij}. \tag{4.12}$$

For parallel shear flows such as the one described in the experiments be Fabre et al. (1987), where we have straight flow conditions:

$$U_x = U_x(y), \tag{4.13}$$

where U_x is the time-averaged horizontal/axial velocity, with no mean flow normal to the horizontal,

$$U_y = U_z = 0 \tag{4.14}$$

and a positive finite strain-rate:

$$\frac{\partial U_x}{\partial y} > 0, \tag{4.15}$$

then **Eq.** 4.12 reduces to (Shen et al., 2000):

$$-\overline{u'v'} = \nu_T\left(\frac{\partial U_x}{\partial y}\right). \tag{4.16}$$

Parallel shear flows are expected (Kuo and Acharya, 2012) to have negative values of $\overline{u'v'}$. Particles transported vertically upwards by a positive velocity fluctuation $u' > 0$ will maintain their momentum in the x-direction (**Fig.** 4.3 shows an example of velocity fluctuations caused by eddies imposed on mean velocity gradients). Assuming a positive vertical velocity gradient $\frac{\partial U_x}{\partial y} > 0$, then at this new level the particle's x-momentum will represent a negative fluctuation in the local velocity field, $u' < 0$ and hence $\overline{u'v'} < 0$. The sign of $\overline{u'v'}$ would not change if $v' < 0$ as this would result in a negative fluctuation $u' > 0$ as this particle instead assumes position in a less energetic layer of fluid closer to the wall. **Eq.** 4.16 suggests that negative $\overline{u'v'}$ requires $\frac{\partial U_x}{\partial y} > 0$ in order for the eddy viscosity to be positive. Negative eddy viscosity $\nu_T < 0$ would imply that the energy of turbulent fluctuations is being transferred back to the mean flow rather than down the energy cascade via eddy dissipation.

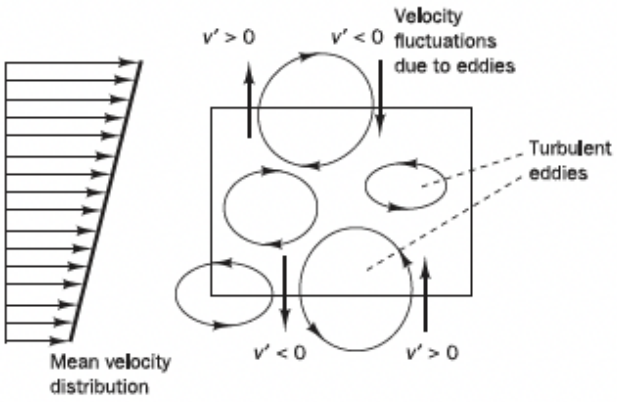

Figure 4.3: Velocity fluctuations due to eddies

Fabre et al. (1987) did not explicitly report eddy viscosity in their publication, but they did provide tabulated data for $-\overline{u'v'}$ and U_x as a function of channel

height. Unfortunately, U_x and $\overline{u'v'}$ were measured at different heights throughout the channel (although at the same point in the flow-wise direction), and so the locations of their respective measurements do not coincide exactly. According to **Eq.** 4.16, in order to calculate eddy-viscosity, the Reynolds stress component $\overline{u'v'}$ and velocity gradient $\partial U_x/\partial y$ are required. In order to obtain these values at corresponding points, velocity gradients were calculated at the measurement locations of $\overline{u'v'}$ using a combination of interpolation and central-differencing. Naturally, this process does contain a degree of approximation and uncertainty, which is acknowledged. **Fig.** 4.4 illustrates graphically the process of differencing and interpolation needed to calculate and align the local velocity gradients to the Reynolds stress. The red dots in each sub-figure represent the values used for the final calculation of $\nu_T(y)$. The calculation procedure was undertaken as follows:

1. Use central differencing scheme to calculate the strain rate, $\frac{\partial U_x}{\partial y}$:

$$\frac{\partial U_x}{\partial y}|_{i+\frac{1}{2}} = \frac{U_{x,i+1} - U_{x,i}}{y_{i+1} - y_i} \tag{4.17}$$

2. Reset the index system so that the i^{th} node represents a location in y at which we have measured data for $\overline{u'v'}$.

3. Let $\frac{\partial U_x}{\partial y}|_{i+\frac{1}{2}}$ and $\frac{\partial U_x}{\partial y}|_{i-\frac{1}{2}}$ be the calculated derivatives located directly adjacaent to the location at which $\overline{u'v'}|_i$ is measured

4. Interpolate to find $\frac{\partial U_x}{\partial y}|_i$:

$$\frac{\partial U_x}{\partial y}|_i = \frac{\partial U_x}{\partial y}|_{i-\frac{1}{2}} + \frac{\partial^2 U_x}{\partial y^2}|_i \Delta y \tag{4.18}$$

where:

$$\frac{\partial^2 U_x}{\partial y^2}|_i = \Big(\frac{\partial U_x}{\partial y}|_{i+\frac{1}{2}} - \frac{\partial U_x}{\partial y}|_{i-\frac{1}{2}}\Big)\Big(\frac{1}{y_{i+\frac{1}{2}} - y_{i-\frac{1}{2}}}\Big), \tag{4.19}$$

and

$$\Delta y = y_i - y_{i-\frac{1}{2}}. \tag{4.20}$$

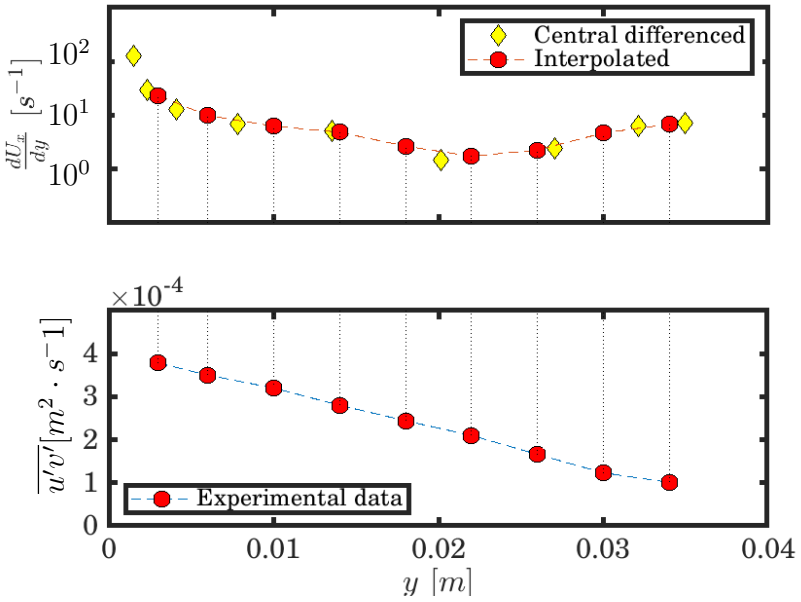

Figure 4.4: Graphical illustration of interpolating $\frac{\partial U_x}{\partial y}$ such that we can directly calculate ν_T at locations at which we have experimentally measured $\overline{u'v'}$

Fig. 4.5 shows the calculated eddy viscosity as a function of height for each experimental run. For both runs 400 & 600 ν_T is calculated to be negative close to the free surface and upper wall of the channel. This is likely due to the negative vertical velocity gradients in these regions, and the development of secondary flows (as reported in Fabre et al. (1987)). The contributions of secondary flow structures to the Reynolds stress tensor are neglected when assuming 2D parallel flow conditions.

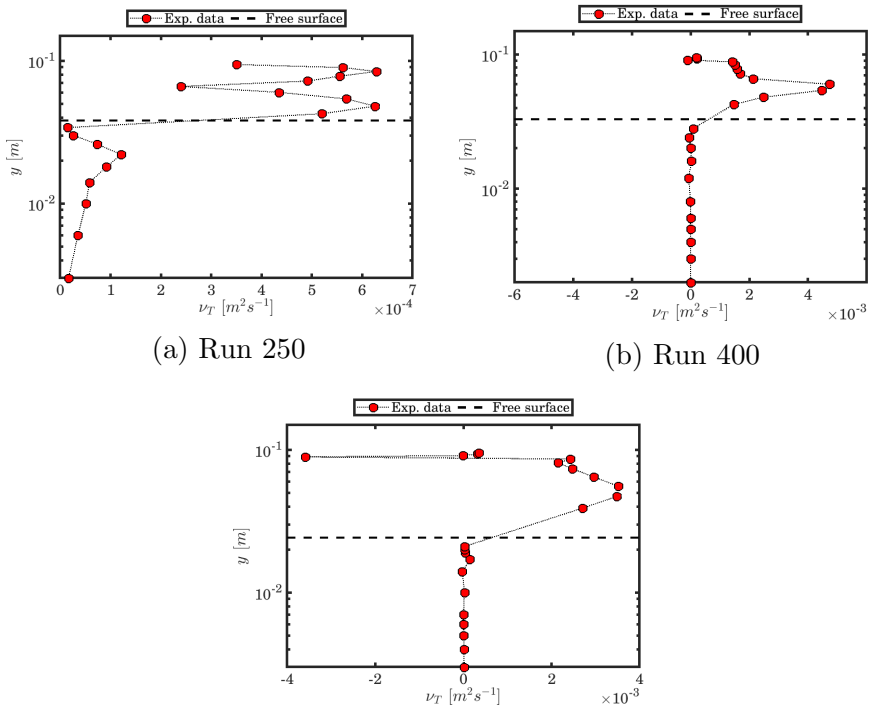

(a) Run 250

(b) Run 400

(c) Run 600

Figure 4.5: Experimental eddy viscosity, as calculated from the data provided by Fabre et al. (1987)

4.3.2 Numerical model

Solution domain

Once again, the `interFoam` solver is used. The solution domain (**Fig.** 4.6) is a 2D realisation of the experimental set up. The channel's entrance is split into two sections — air and water inlets — which are segregated by a baffle extending 0.5m downstream of the entrance, after which the two flow streams are allowed to meet within the same conduit.

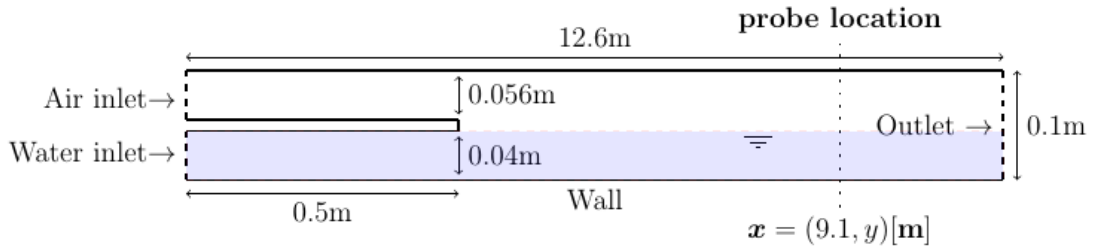

Figure 4.6: Schematic of the numerical domain, *not* to scale.

Initial and boundary conditions

-	$\boldsymbol{u}$	α	p^*	k	ω
Walls	No-slip	$\frac{\partial \alpha}{\partial \hat{n}} = 0$		$\frac{\partial k}{\partial \hat{n}} = 0$	`omegaWallFunction`
Air inlet	Fixed flow-rate	$\alpha = 0$	$\frac{\partial p^*}{\partial \hat{n}} = 0$	k intensity	Fixed value
Water inlet	Fixed flow-rate	$\alpha = 1$		k intensity	Fixed value
Outlet	$\frac{\partial \boldsymbol{u}}{\partial \hat{n}} = 0$	$\frac{\partial \alpha}{\partial \hat{n}} = 0$	$p_{total} = 0$	$\frac{\partial k}{\partial \hat{n}} = 0$	$\frac{\partial \omega}{\partial \hat{n}} = 0$

Table 4.2: Boundary conditions for numerical model

Throughout the entire domain, at time $t = 0$ the volume fraction is initially set as $\alpha = 0$, namely the flume is filled only with air. Provided we impose sensible boundary conditions, the water level should gradually rise to a certain depth before attaining a quasi-steady-state. A good prediction of the force balance and hence momentum transfer at fluid interface should allow the liquid depth to rise downstream of the inlet to a height that is in agreement with the experimental observations as $t \to \infty$. The water height, $h_{\text{f.s.}}(x)$ as it enters the domain is equal to the inlet height $h_{\text{f.s.}}(0) = h_{inlet} = 0.4\text{m}$. The dimensions of the water inlet was chosen to be some value in excess of the maximum reported free surface height from the experiments. To improve stability and speed of convergence, the velocity field is initialised as equal to that of the air flow inlet velocity $\boldsymbol{u_0} = \{u_{\text{x,inlet}}, 0, 0\}$. Boundary conditions are listed in **Table** 4.2.

Turbulence models

In **Section** 4.2, we described numerous modifications to the RANS model equations designed to improve performance in predicting stratified multiphase flows. Starting with the $k-\omega$ SST model as our baseline turbulence model, we will compare its performance to that of the buoyancy-modified, compressible formulation suggested by Devolder et al. (2018) and the stress-limiting, stabilised model of Larsen and Fuhrman (2018). Throughout the remainder of this thesis, these models will be referred to in shorthand as `kwSST`, `BM` and `STB` respectively. The respective features of each model are listed in **Table** 4.3.

Model	Compressible	Buoyancy source term	Eddy viscosity limiter
`kwSST`	-	-	-
`BM`	✓	✓	-
`STB`	✓	✓	✓

Table 4.3: Matrix of physical model features for each turbulence model formulation

Each of these turbulence models will be deployed both with and without Egorov's interface damping model. The damping coefficient will be adjusted through the range B=$\{0,50,100\}$, where $B = 0$ corresponds to no damping. This gives 3 turbulence models, 3 discrete levels of damping and 3 experimental set-ups, for a total of 27 permutations. A matrix of simulations is listed in **Table** 4.4).

-	`kwSST`			`BM`			`STB`		
$B =$	0	50	100	0	50	100	0	50	100
Run 250	✓	✓	✓	✓	✓	✓	✓	✓	✓
Run 400	✓	✓	✓	✓	✓	✓	✓	✓	✓
Run 600	✓	✓	✓	✓	✓	✓	✓	✓	✓

Table 4.4: Matrix of simulations

4.3.3 Results

Summary of the presentation of results

Sub-figure	Description
A	Turbulent kinetic energy k vs. channel height, y.
B	Mean axial velocity (co-directional to the flow) U_x vs. channel height, y.
C	Eddy viscosity ν_T vs. scaled channel height y^*, where $y^* = y/h_{\text{f.s.}}$. This normalisation to the free surface is done to more easily compare the eddy viscosity profiles close to the interface
D	Time-dependent water depth $h_{\text{f.s.}}(t)$ vs. time, t at $x = 9.1$m. Initial free surface depth at $h_{\text{f.s.}}(x,t) = h_{\text{f.s.}}(9.81, 0) = 0$, as it takes some time for initial inflow of water to reach that far downstream of the inlet. Measured water depth from experiments are also plotted for comparison. A value of $h_{\text{f.s.}}$ converging to $h_{\text{f.s.}} \to h_{\text{exp}}$ as $t \to t_\infty$ is a good result.

Table 4.5: Description of each sub-figure in the following results section. Sub-figure A: top-left, sub-figure B: top-right, sub-figure C: bottom-left, sub-figure D: bottom right

The results will mostly be presented in a consistent format; four sub-figures (starting top-left, the top-right, bottom-left, bottom-right) with contents as shown in **Table** 4.5: Initially, we will use them to determine the capability of each turbulence model, without Egorov damping, to accurately replicate the experimental results. We will then analyse the effect of deploying each turbulence model formulation *with* Egorov damping. This will be done for all 3 air flow rates.

Sensitivity to turbulence model, without damping, B=0: Run 250

Fig. 4.7 shows the performance of each turbulence model without the addition of damping at the interface. We can see that the `kwSST` model performs very poorly on all counts. Firstly, the prediction of k is vastly incorrect. Throughout the depth, k is over-predicted at some points by several orders of magnitude. The mathematical inconsistencies in using the incompressible formulation of the k-equation (Fan and

Anglart, 2020) results in the high levels of turbulence generated in the air being diffused across the free surface and all the way through the water down to the tank floor. `BM` and `STB` provide much more reasonable results for k in the water. Neither model captures the profile of k through the air well, with the minima being located in the near-wall region. The experiments show this should be somewhere close to the vertical mid-point of the surface and roof. Using the compressible formulation and buoyancy term featured in both models allows the solver to capture the jump in turbulence across the interface which was evident in the experiments.

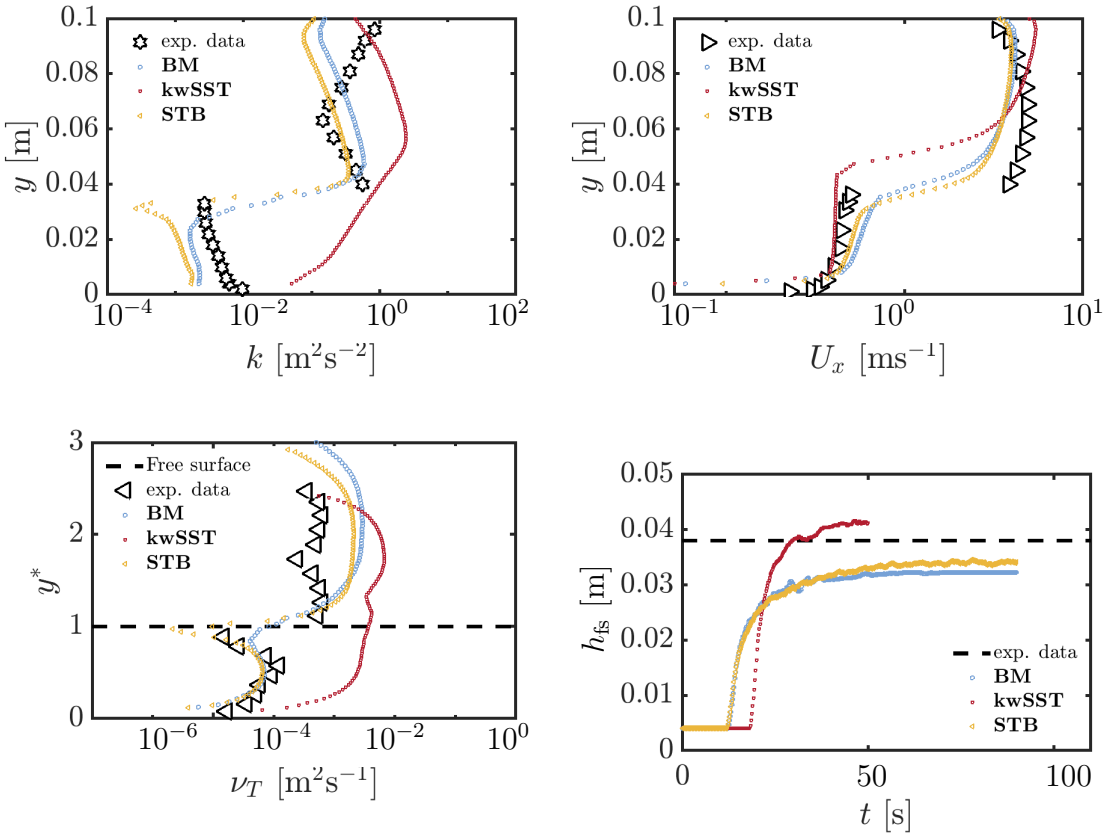

Figure 4.7: **Run 250**, without free surface damping, sensitivity of results to turbulence model used

As we might expect, such poor prediction of k by `kwSST` subsequently leads to similarly inaccurate results for eddy viscosity, ν_T, which is overestimated by several orders of magnitude throughout both the liquid and gas phases. `BM` and `STB` again perform much better, yielding mostly accurate results throughout the subsurface. `STB` matches the experimental data almost exactly. The parabolic profile

seen here agrees with measurements using two-colour laser dopplometry by Nezu and Rodi (1986). BM gives similar results to STB except for the region immediately beneath the free surface, where ν_T is over-predicted. The superior performance of STB in this region showcases the need for stabilisation in regions of low vorticity beneath the interface.

All models perform poorly at predicting mean stream-wise velocity U_x in the air. The experimental velocity measurements of flow in the air formed a parabolic velocity profile typical of closed pipe/channel flow, with the maximum occurring centrally to the free surface and channel ceiling. Each model formulation predicts the maximum to occur close the wall.

Finally, we can see that none of the models are able to allow the solution to tend towards a suitable wave height, $h_{\text{f.s.}}$ as $t \to \infty$ Ultimately, the liquid depth is under-predicted by both BM, STB and over-predicted by kwSST. The over-prediction of $h_{\text{f.s.}}$ by kwSST is a consequence of the gross over-estimation of eddy viscosity, with a ratio of predicted to experimental $\nu_T(y)/\nu_{T,\text{exp.}}(y) = \mathcal{O}(10^2)$, and an eddy viscosity ratio $\nu_T/\nu = \mathcal{O}(10^3)$ in the top layer of the water. The eddy viscosity levels are such that the effective viscosity, $\nu_{\text{eff}} = \nu + \nu_T$ is greatly enhanced, making the flow much more resistant to deformations by shear stresses at the interface and walls. Conversely, the under-prediction of $h_{\text{f.s.}}$ by STB and BM indicates momentum transfer across the interface not being captured accurately.

Sensitivity to Turbulence model, with damping, B=50: Run 250

Fig. 4.8 shows the results with interfacial damping included. The kwSST results are still very poor. Simply applying damping at the interface does not seem to be anywhere near sufficient to compensate for the issue of using an incompressible formulation of the equations.

Throughout the entire depth of the channel, BM and STB under-predict k

by a fairly consistent margin of error in the range $|k_{\text{numerical}} - k_{\text{exp.}}| \approx \mathcal{O}(10^0 - 10^1)$. Qualitatively speaking, the curves look good, if not for this shift to the left. As the interface is approached from both air and water sides, k decreases asymptotically, $k \to 0$ as $y \to h_{\texttt{f.s.}}$. This is a direct result of the damping function.

Both `STB` and `kwSST` show greatly improved prediction of ν_T in the air, which (with the exception of a central inflection point) is predicted with great accuracy. `STB`'s prediction of ν_T through the subsurface is actually made worse, no longer agreeing so closely with experiments. `BM`'s prediction of ν_T is now in exact agreement with `STB`.

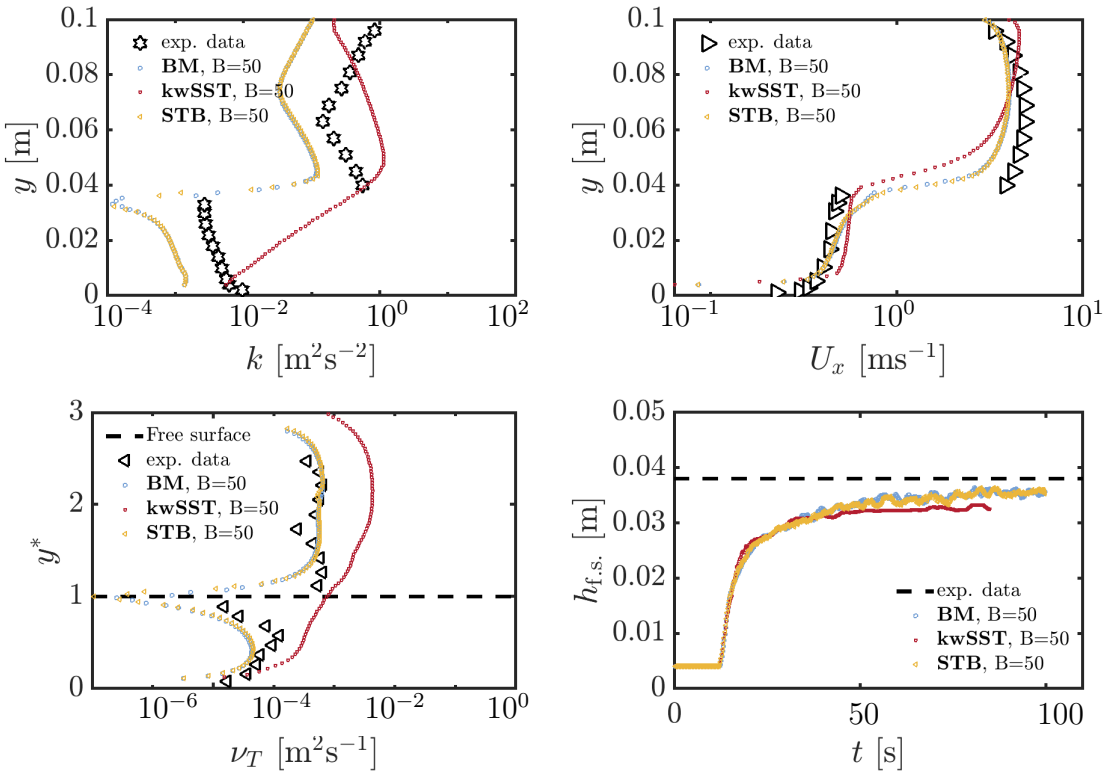

Figure 4.8: Run **250**, with free surface damping, sensitivity of results to turbulence model used

The prediction of stream-wise velocity is better predicted by `kwSST` in the water, with velocity, shear and curvature of velocity gradient $\partial^2 U_x / \partial y^2$ more closely in line with the experiment. However, the velocity in the air shows no improvement — the maximum again occuring close to the wall. `STB` and `BM` show improved

prediction of velocity in the air, slightly underpredicting $U_x(y)$, but with the location $U_{x,\max}$ shifting towards the centre of the channel, in line with the measured data. This is compensated by a slight over-prediction of velocity in the water, indicating excessive transfer of momentum from air→water across the interface.

This is reflected in the asymptotic water depth $h_{\text{f.s.}}$. In order to satisfy mass continuity, an increase in water velocity requires a reduction in water depth. This illustrates the strong interdependency of turbulence, the enhancement of momentum transfer cross the interface and ultimately, its effects on the hydrodynamic properties of the flow.

Sensitivity of model BM to damping coefficient, B: Run 250

So far, it has been demonstrated that `BM` does a reasonable job of predicting turbulence in the water, while `STB` performs even better. Including a damping function allows them both to obtain improved results for k and U_x in the air. For the remaining analysis concerning Run 250, we will set aside `kwSST`. The incompressible model formulation has been demonstrated as being not fit for purpose. Its incusion in the analyis for Runs 400 and 600 will purely be for illustrative purposes, rather than in the anticipation that it might yield better results under different flow conditions. In **Fig.** 4.9 we focus on the `BM` turbulence model, and demonstrate the sensitivity of the solution to the choice of damping coefficient, B.

Increasing B incrementally through $B = 0, 50, 100$ more accurately captures the flow behaviour in the air each time. At $B = 100$, the profile of k reflects those of the experiments almost exactly. However, the consistent shift to the left remains.

Improving the profile of k in the air comes at the price of worsening the turbulent behaviour in the water. Increasing the damping coefficient forces the region of asymptotic destruction of k to spread further down into the liquid sub-

surface, causing the simulation results to fall away from the measured data quite profoundly. Consequentially, the subsurface eddy viscosity is similarly diminished close the surface.

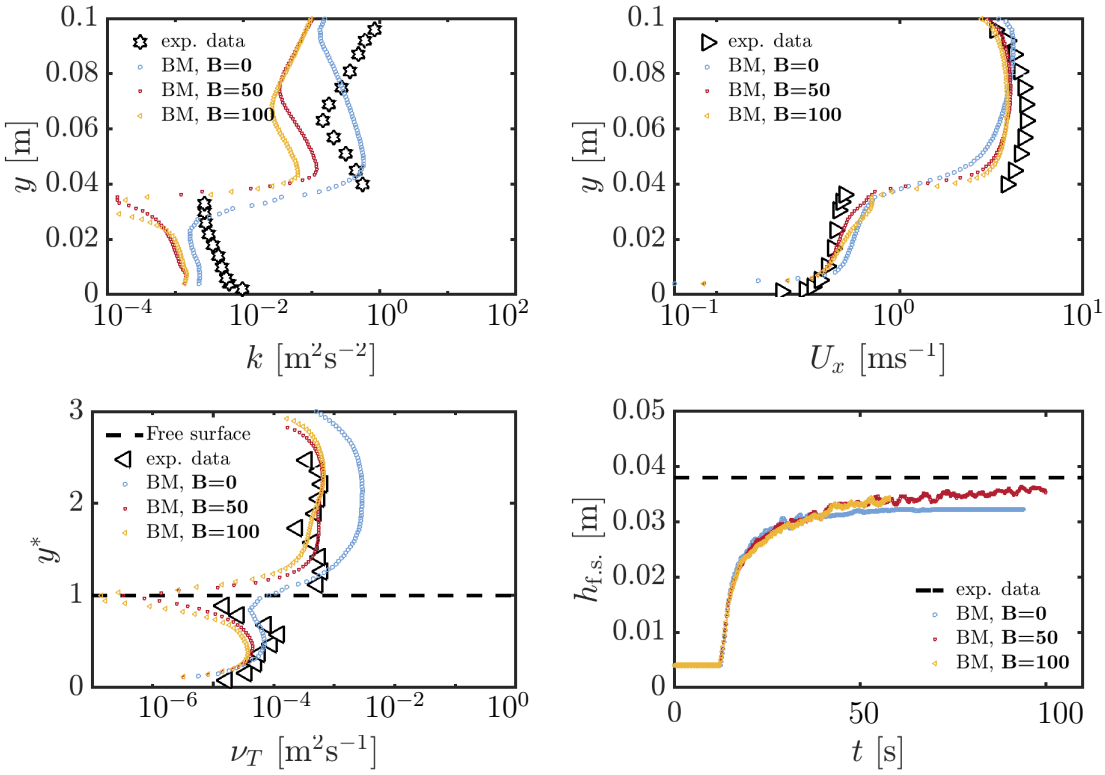

Figure 4.9: **Run 250**, T. Model - BM, sensitivity to damping coefficient B

Sensitivity of model STB to damping coefficient, B: Run 250

In **Fig.** 4.10 we again cycle through B, this time with model `STB`. The increase in B from $B = 50 \rightarrow 100$ yields very similar result. Little is changed except for the location of $k_{\text{air,min}}$, and the decreased turbulent quantities in the local interface region due to the activity of the damping function. Overall, the solution of ν_T and $h_{\text{f.s.}}$ is much less sensitive to B; $h_{\text{f.s.}}$ shows a very small improvement.

Damping reduces the accuracy of eddy viscosity prediction in the water, despite improving in the air. That `STB` seems more robust in predicting subsurface eddy viscosity lends credence to the abilities of its stress-limiting stabilisation feature. Its superior prediction of turbulence in this region points to the issues being

associated with instabilities in the subsurface, and not just excessive production at the interface.

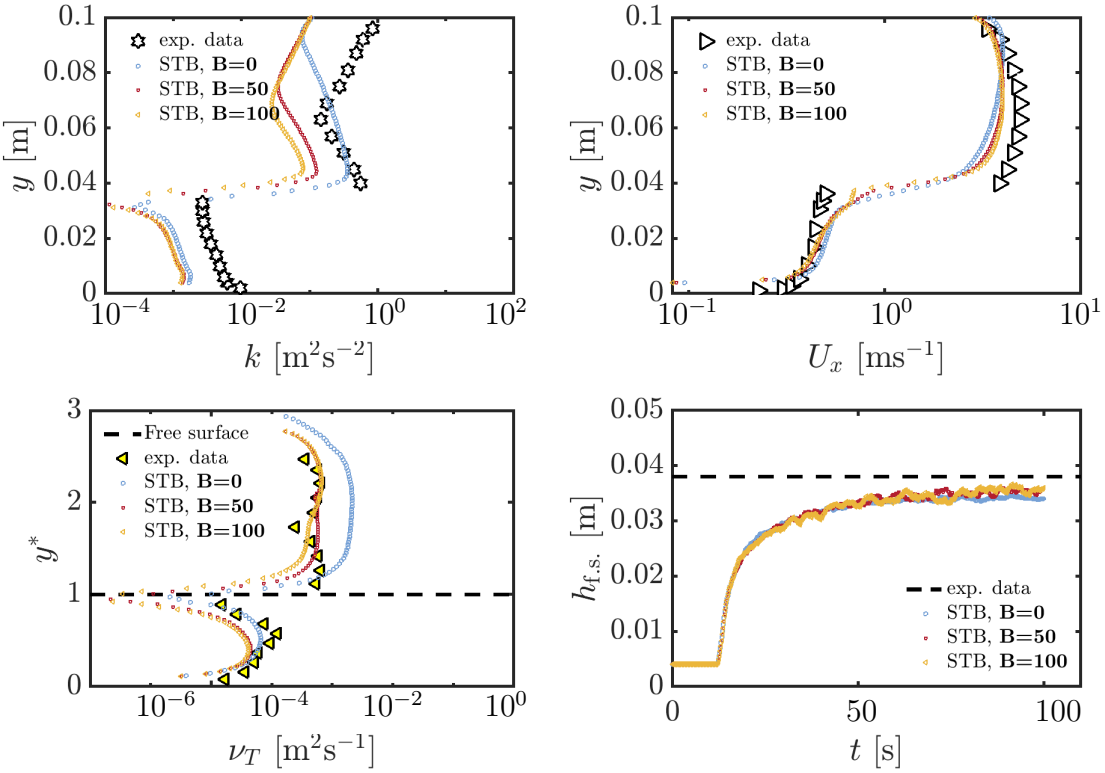

Figure 4.10: **Run 250**, T. Model - STB, sensitivity to damping coefficient B

Sensitivity to turbulent kinetic energy inlet conditions: Run 250

So far, we have found that combining a well-formulated turbulence model with an appropriate degree of damping at the surface can provide us with very good qualitative agreement with the experiments. However, across the board, there is a trend of under-predicting the turbulent kinetic energy. One candidate for explaining this discrepancy would be the condition for turbulent kinetic energy prescribed at the inlet. The boundary condition deployed (see **Table** 4.2) calculates k from the inlet velocity, $\boldsymbol{u}$ and a user-defined turbulence intensity, I_k:

$$k_{\text{inlet}} = \frac{3}{2}(I_k|\boldsymbol{u}|)^2. \tag{4.21}$$

The nominal setting for turbulence intensity taken for all simulations so far has been $I_k = 5\%$. The prediction of k throughout the depth of the channel has been roughly 5 times less than that of the experiments. Therefore, it would seem sensible to increase the turbulence intensity to $I_k = 10\%$ in an attempt to force the solution to converge towards the data. **Fig.** 4.11 shows that in fact, the inlet conditions have an undetectable effect on the solution. The turbulent boundary layer in the air grows downstream of the first contact with the free surface, and even further downstream has fully developed to a point that the turbulent flow features are independent of the inlet conditions.

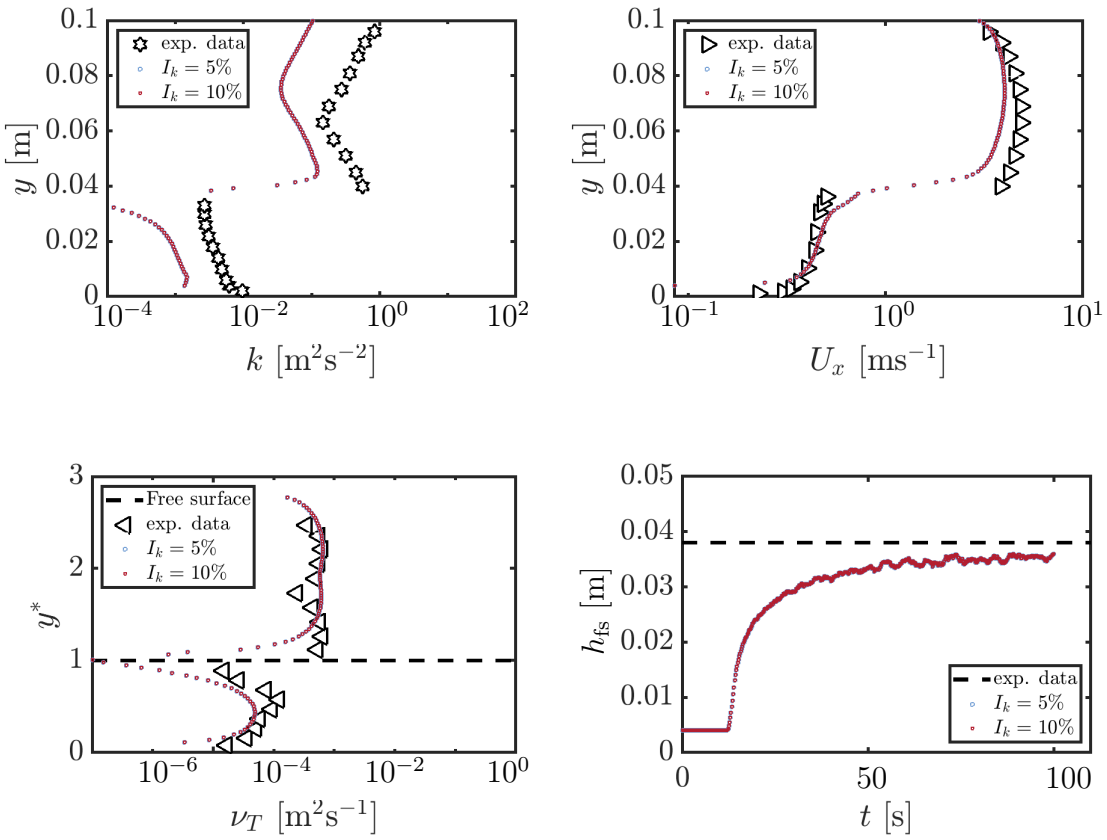

Figure 4.11: **Run 250**, T. Model - `STB`, sensitivity to turbulence intensity at the inlet

Sensitivity to turbulence model, without damping: Run 400

We now simulate Run 400, to determine whether our findings translate across different flow regimes. Run 400 differs from Run 250 only in the increased flow rate

in the air, jumping from 45.4 $\rightarrow$ 75.4$L.s^{-1}$, with a subsequently higher Reynolds number in the air. Fabre et al. (1987) report that for Runs 400 and 600, secondary flows develop in the cross section of the channel (**Fig.** 4.12), leading to an increase in turbulence close to the interface in the air and a decreased production close to the wall in the water.

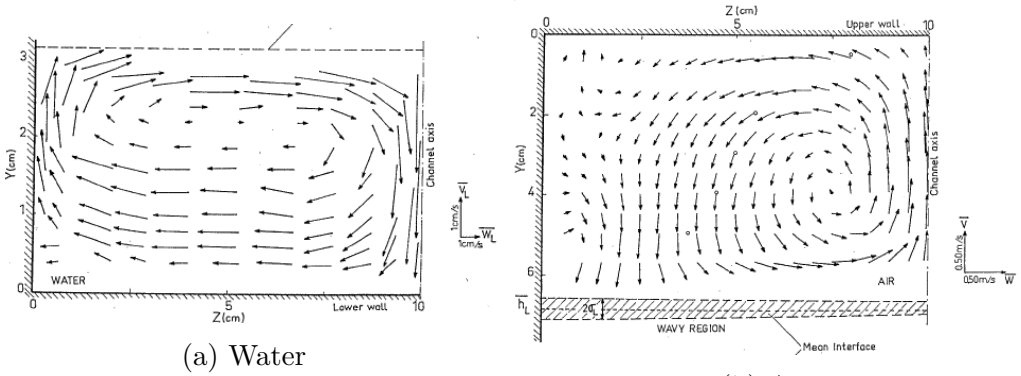

(a) Water

(b) Air

Figure 4.12: **Run 400**: secondary flow structures in the channel cross-section

Secondary flows in the cross-section means that the simplification of the eddy viscosity calculation made in **Eq.** 4.16 no longer holds. Contributions from additional off-diagonal components of the Reynolds stress tensor are now required. These are not provided in the report, and so the eddy viscosity data plotted here-on in cannot be seen as reliable and so will not be considered strongly in our analysis. This was reflected in the negative eddy viscosity calculations reported in the introduction.

Fig. 4.13 shows results for each turbulence model formulation without surface damping. `BM` and `STB` behave very similarly across all parameters, with them differing only in the prediction of water eddy viscosity close to the surface, where $\nu_{T,\mathrm{BM}}(y) > \nu_{T,\mathrm{STB}}(y)$. This causes `BM` to predict a slightly lower final $h_{\mathrm{f.s.}}$. Interestingly, the experimental profiles of k and U_x have a respective minimum and maximum close the roof. This profile resembles the numerical predictions of k for Run 250. This suggests that the flow rate jump from 45.4 $\rightarrow$ 75.4$L.s^{-1}$ represents some characteristic change in flow regimes, which perhaps explains the

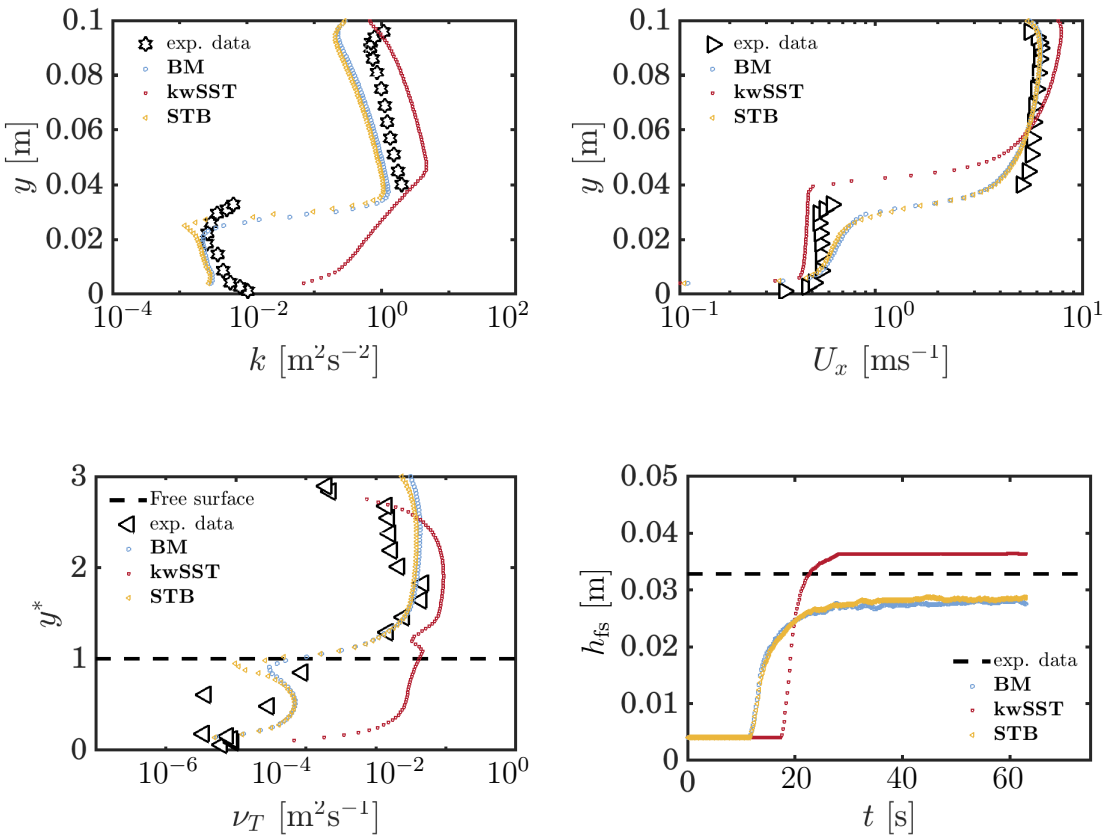

Figure 4.13: **Run 400**, performance of turbulence models without surface damping

extra sensitivity of Run 250.

Sensitivity to turbulence model, with damping, B=50: Run 400

Again, activating the surface damping function results in improved prediction of mean stream-wise velocity. The ultimate water depth, $h_{\mathrm{f.s.}}$ is predicted with good precision; the asymptotic solution converging nicely onto the experimentally measured surface depth, $h_{\mathrm{f.s.}} \rightarrow h_{\mathrm{exp}}$ as $t \rightarrow \infty$. `STB` and `BM` give very similar results across the board.

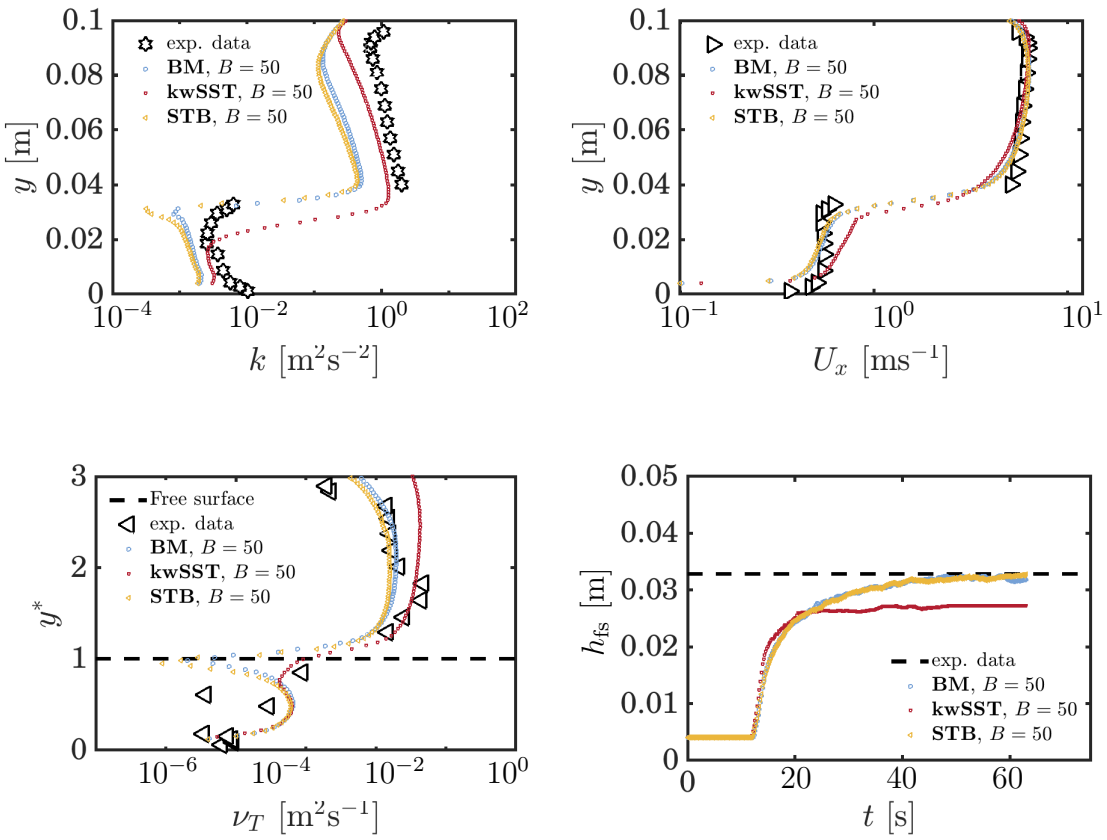

Figure 4.14: **Run 400**, performance of turbulence models with surface damping

Sensitivity of models `BM` and `STB` to damping coefficient, B: Run 400

As with Run 250, we look more closely at the effects of combining turbulence damping with the `STB` and `BM` model formulations.

Fig. 4.15 confirms that the migration of $k_{\mathrm{air,min}}$ is directly correlated to damping coefficient. In the case of `BM` with damping coefficient $B = 100$, it appears that some non-physical instability in the air has developed, so this result will be ignored. **Fig.** 4.16 shows the results of increasing damping coefficient for `STB`. Not only does $k_{\mathrm{air,min}}$ migrate away from the measured data, but the turbulent kinetic energy throughout the depth of the water is shifted further away from the experiments as B is increased.

The only improvement made by including the damping function is the superior prediction of the fully developed $h_{\mathrm{f.s.}}$. This tells us that for a free surface

flow over large scales such as this, the transfer of energy and momentum across the interface is highly sensitive to the turbulent flow field. In this case, the height at which the water ultimately settles is dependent on shearing effects at the surface. The damping function appears to be able to better capture the physics local to the interface in this regard, as is evident in the superior prediction of $h_{\text{f.s.}}$. However, it would appear that depending on the flow parameters, surface damping, if not applied with care can be detrimental to predicting the flow features in regions away from the surface.

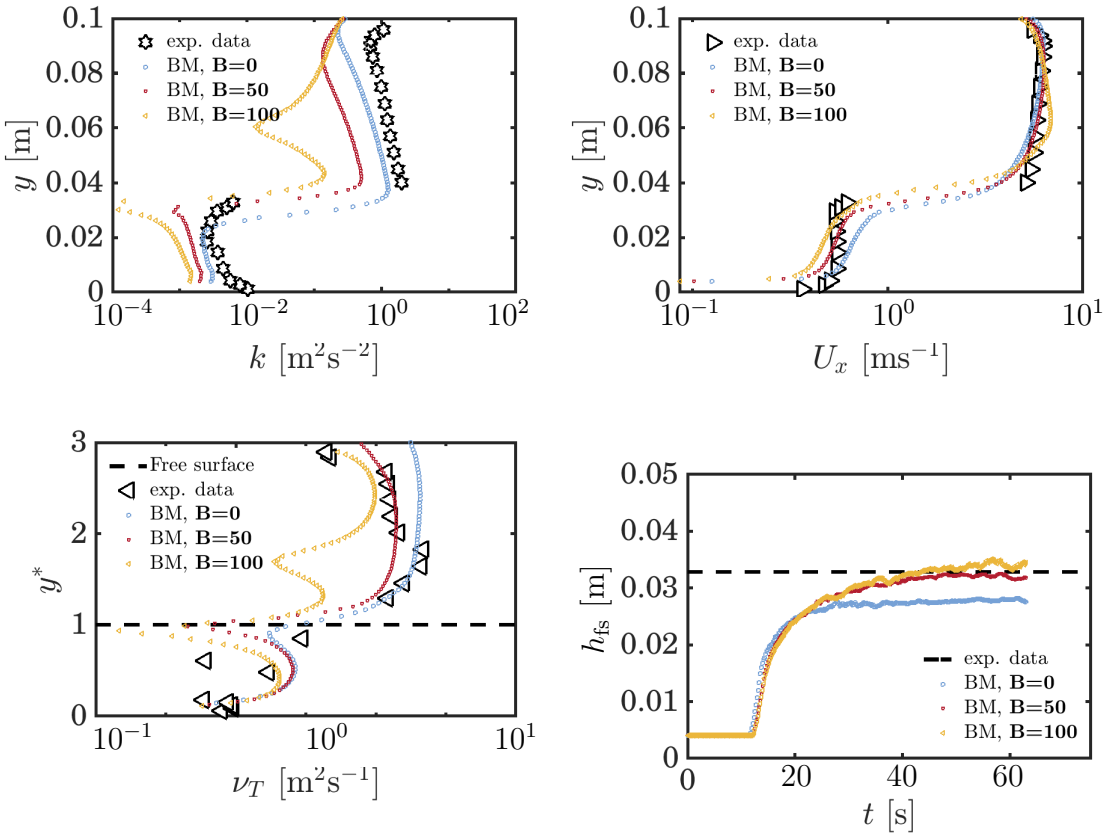

Figure 4.15: **Run 400**, sensitivity of turbulence model `BM` to damping coefficient, B

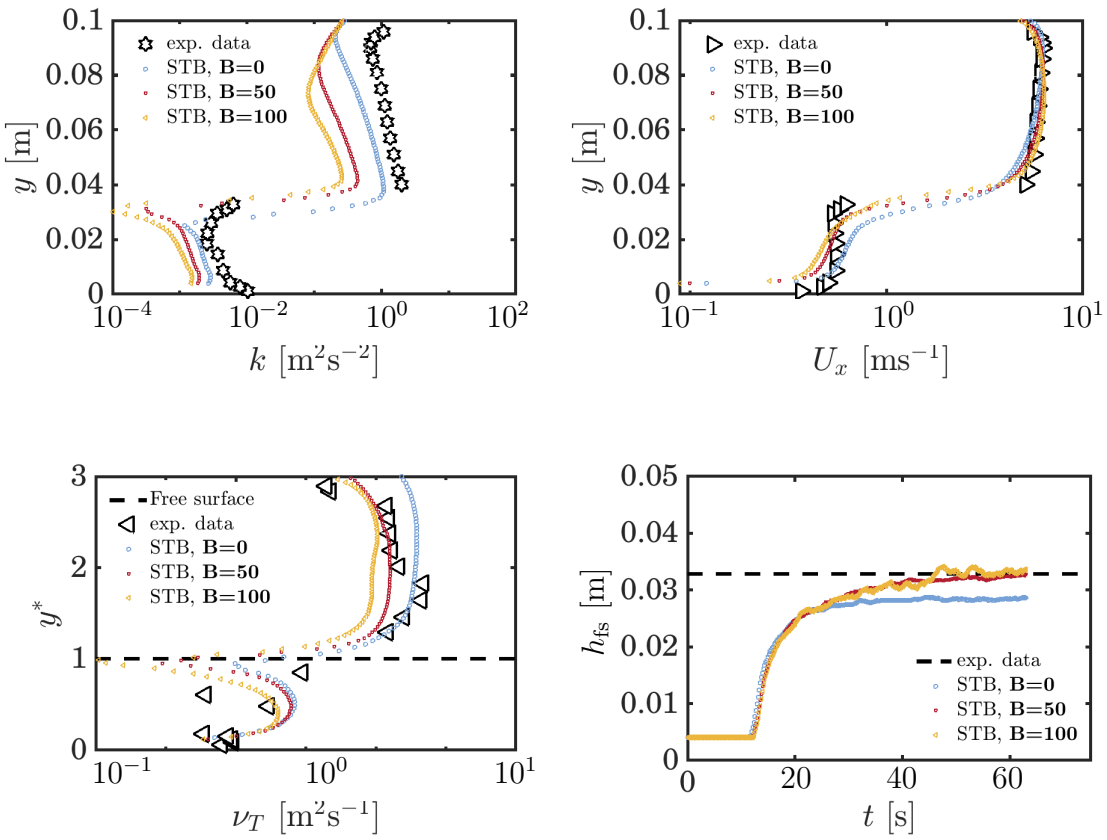

Figure 4.16: **Run 400**, sensitivity of turbulence model `STB` to damping coefficient, B

Sensitivity to turbulence model, with and without damping: Run 600

Finally, we run the same analysis for Run 600. Compared to Run 400, the experimental flow rate in the air jumps from 75.4 $\rightarrow$ 117.4$L.s^{-1}$. The ultimate mean water depth decreases from 31.5 $\rightarrow$ 21.5cm. The reduction in ultimate water depth reflects a large increase in momentum transfer to the water.

Fig. 4.17 shows that for these flow conditions, the `BM` and `STB` model formulations produce very good results with no interfacial damping. Both models predict extremely similar profiles across the board.

We see familiar profiles in which the models consistently under-predict k by some factor, although the profiles are in good agreement. There is further strong agreement for U_x and $h_{\text{h.s.}}$. Eddy viscosity is over-predicted in the air by a small

margin, but agrees closely with the experiments immediately about the interface.

Activating the damping function with $B = 50$ allows the final depth to be improved more accurately for `BM`, but slightly over-predicted by `STB` (accompanied by a corresponding increase in eddy viscosity beneath the surface). Very close agreement is achieved for ν_T in the air all the way from the surface up to the top wall. Interestingly, at this higher flow rate in the air, increasing the surface damping does little to change the position of $k_{\text{air,min}}$.

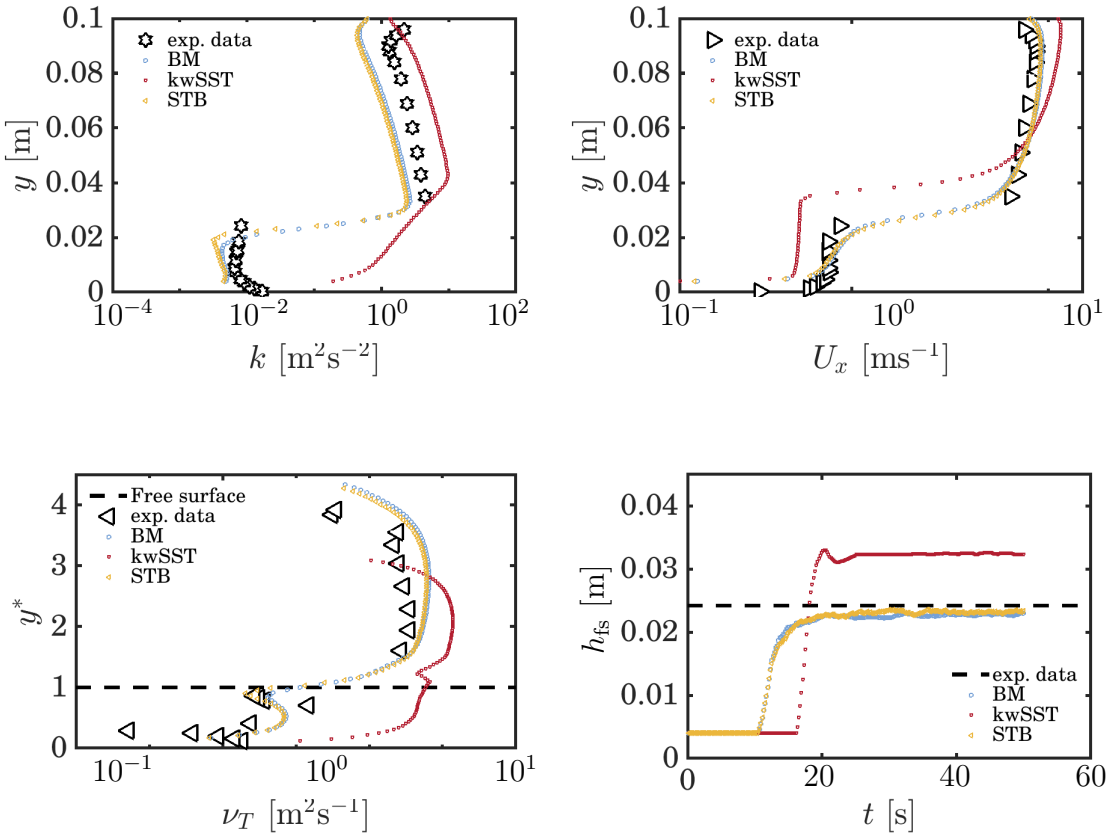

Figure 4.17: **Run 600**, sensitivity to turbulence model, without damping ($B = 0$)

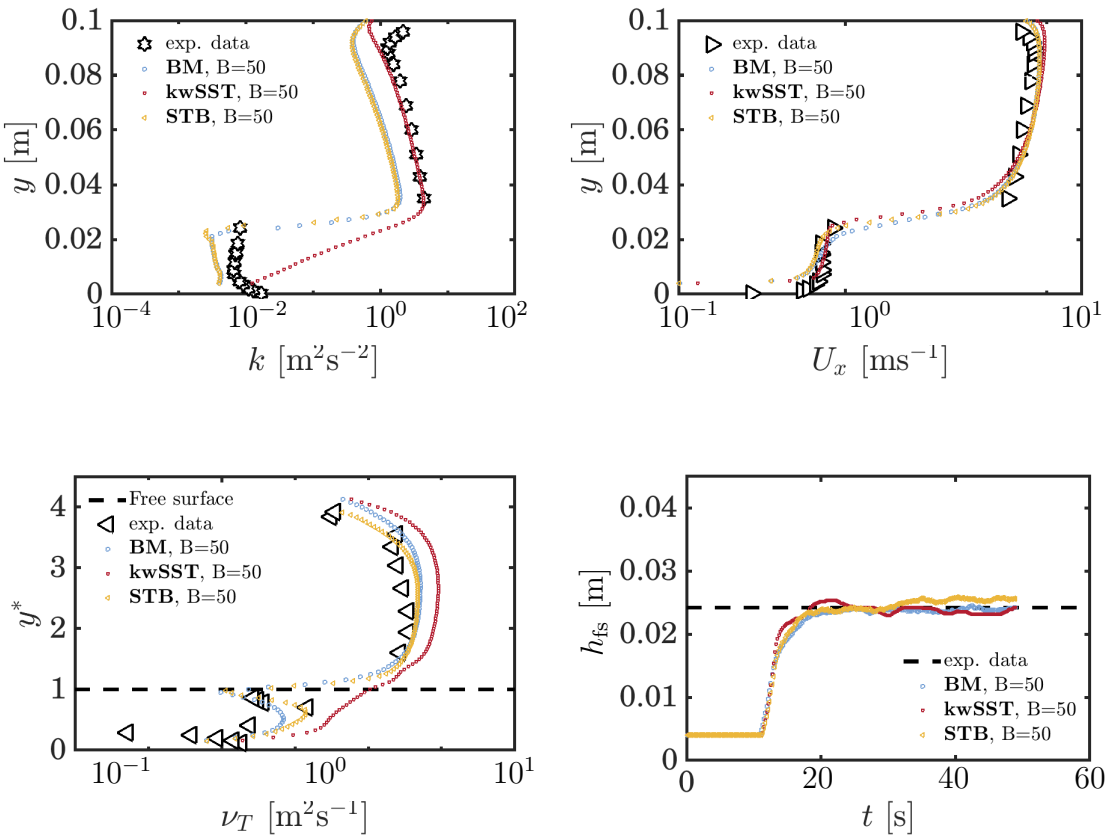

Figure 4.18: **Run 600**, sensitivity to turbulence model, with damping ($B = 50$)

4.4 Conclusions

In this chapter we have discussed some of the prevailing issues surrounding turbulence modelling in multiphase flows, namely the over-production of turbulence beneath the free surface when using two-equation RANS models. Modified $k-\omega$ SST turbulence models suggested by Devolder et al. (2017) (`BM`) and Larsen and Fuhrman (2018) (`STB`) have been presented and tested by replicating the various experimental flow scenarios and corresponding data published by Fabre et al. (1987). Egorov's method (Egorov et al., 2004) of wall-like turbulence damping at the interface has similarly been applied. These model formulations were compared to the native incompressible $k-\omega$ SST (`kwSST`) model which is included as a default option in `interFoam`.

It was found that `kwSST` is not able to respect or capture some of the fundamental flow physics at the free surface. Turbulence from the air is free to diffuse across the interface, which from the literature we know to be demonstrably un-physical. The result of this is a predicted eddy viscosity several orders of magnitude greater than the experiments through the subsurface. For simulating mixing processes, this is totally unacceptable, as turbulent transport of scalars must be modelled through eddy diffusivity relations in RANS modelling.

The `BM` and `STB` model formulations showed great improvement in matching the turbulent properties. `STB` was found to be particularly robust in capturing subsurface eddy viscosity without further modifications. `BM` had a tendency to predict slightly higher ν_T close to the surface, despite the inclusion of the buoyancy source term in the k-equation. This suggests that the stress-limiting feature of the stabilised model was activated near the free surface in a near potential-flow region.

Including artificial damping at the interface showed mixed results. Eddy viscosity in the air was brought closer to the experiments, which further allowed the steady-state liquid depth to agree well with the experimental measurements. This implies the shear stress at the surface was captured with a greater accuracy by introducing wall-like damping at the surface.

However, improving conditions had a negative impact on prediction of eddy viscosity in the subsurface. **Fig.** 4.10 shows that damping at the interface has an adverse effect, moving the eddy viscosity predictions away from the data, vanishing to zero after initially showing excellent agreement. This is an undesirable consequence, given that wall-like interface damping is physically applicable in the air, but not really representative in the water.

Overall, the stabilised model would appear to be the more robust approach for capturing subsurface turbulence. In the experiments of Fabre et al. (1987), the driving factor in how the flow develops in terms of steady-state water depth

was the action of wind shear at the surface over a very large scale interface. For sloshing flows, this will be much less important. Liquid motions in response to tank excitations dominate the internal dynamics of the tank, and so predicting air turbulence and shear stress at the surface is much less important. If we are to be concerned with subsurface mixing, an accurate representation of turbulence in the liquid is very much key.

Chapter 5

Sloshing and turbulence modelling

5.1 Introduction

The previous chapter demonstrated the relative performance of various turbulence models with/without a damping treatment at the free surface, when applied to a stratified, wall-bounded shear flow through a weakly inclined closed conduit.

In general, `KWSST` model failed on all counts without the inclusion of interface damping. Not only were the velocity profiles poorly captured in the air phase, the erroneous physical representation of turbulence at the free surface polluted the liquid-phase results especially. `BM` and `STB` models behaved quite similarly, with `BM` generally predicting a higher eddy viscosity beneath the free surface.

The merits of including turbulence damping in the physical model for that particular flow scenario were evident and demonstrable. Transfer of momentum at the free surface was implicitly validated via accurate prediction of the ultimate depth at which the flow reaches a steady-state, far downstream of the inlet. Values of turbulent quantities (k, ν_T) throughout the depth of both the liquid and gas phases were well described qualitatively, if not always in total quantitative agreement with the experiments. In addition, the prediction of the stream-wise velocity profile above

the free surface is clearly more accurate when enforcing turbulence damping at the interface using Egorov's method.

We must be careful when extrapolating meaning from these results when choosing which of the available numerical model formulations to proceed with when simulating sloshing flows. Sloshing and channel flows have plenty of similarities. They both feature two wall-bounded, stably stratified and homogeneous fluid phases, separated by an interface. The gas-liquid interface produces a wall-like shear layer in the air, but is effectively seen as a zero-stress boundary as far as the much heavier fluid phase is concerned. Furthermore, the two material phases feature very little mixing on the molecular level - with only sporadic macroscopic mixing taking place. For these reasons, we might think that applying the Egorov turbulence damping model at the interface would probably be an appropriate choice for sloshing flows also, given the clear benefits found in **Chapter** 4. However, the Egorov damping model is designed to act on large-scale free surface flows. The wall-like turbulent dissipation at the interface is therefore perhaps best equipped at dealing with flows where surface break-up effects are avoided, and the interface remains as one singular coherent structure throughout the duration of the simulation. This cannot be guaranteed for sloshing flows — particularly at high amplitudes in which violent fluid motions can occur. What's more, the role of surface break-up and the introduction of a local increase of turbulence dissipation to the bulk flow is likely to have an influence on the mixing properties within. It is expected that the simplicity of the Egorov damping model might be problematic in such scenarios. The Egorov model is so far untested in its application to flow phenomena such as wave breaking, wall impacts and splashing. Given the prominence of such features in sloshing flows under certain excitation conditions, it's vital we investigate the sensitivities of including the damping model.

5.1.1 Chapter outline

This chapter is structured as follows:

1. **Problem case description**:

   Set-up of a nominal scenario with which to proceed and demonstrate the sensitivities involved in modelling turbulence in sloshing flows. The numerical model set-up will also be described.

2. **Grid-independence**: Ensuring that the results presented henceforth are not mesh-dependent.

3. **Sensitivities to turbulence model**:

   We will first look at how each of the baseline model formulations (`KWSST`, `BM`, `STB`) performs in terms of predicting sloshing response to a range of forcing amplitudes. This will be supplemented by comparisons to some high resolution 3D Large Eddy Simulations. In addition to the reaction of the free surface, the sensitivity of the subsurface flow-field (turbulence and velocity profiles) to the chosen model formulation will then be explored.

4. **Sensitivities to damping model**:

   Finally, the application of damping functions will be tested for sloshing flows, to determine whether the benefits that were clear to see when attempting to match the experiments of Fabre et al. (1987) are still desirable.

5.2 Problem case description

In order to explore the performance of the various turbulence modelling approaches laid out so far, when applied to sloshing flows, a simple case is introduced upon which the rest of this chapter and some work in the following chapters will be based.

Tank geometry, fill height and excitation conditions

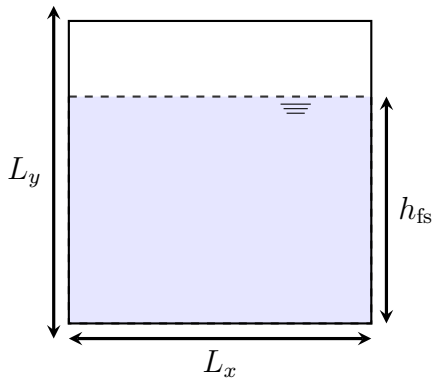

Figure 5.1: Schematic of tank geometry and filling level. Tank breadth, L_z is measured normal to the page.

A notional fuel tank is defined, which for simplicity will have an aspect ratio of 1, i.e. the height and length of the tank, $L_x = L_y$ (**Table** 5.1). Many of the simulations will consider only a 2D tank, but for the cases in which 3D is considered, the 'in-page' dimensional length of the tank will be $L_z = 0.05$m. This gives an aspect ratio in depth of $L_z/L_x = L_z/L_y = 0.1$.

The relatively thin tank is chosen for a number of reasons. Firstly, a 3D tank allows us to deploy an LES model — thus allowing us to investigate the performance of 2D simulations to higher fidelity models in which subsurface turbulence is being resolved. However, these 3D models come at a significant computational expense, and so a relatively thin 3^{rd} dimension allows us to include some 3-dimensionality without incurring unworkable run-times and having to compromise

too much on mesh resolution through-thickness.

Secondly, a thin tank suppresses the development of out-of plane surface motion, effectively resulting in pseudo-2D sloshing in terms of the free surface behaviour. The rationale that sloshing flows can be considered 2D-planar, provided that $L_z \ll L_x$ is similarly followed by Antuono et al. (2012); Bouscasse et al. (2013); Colagrossi et al. (2004) in their experimental investigations, often choosing $L_z/L_x = 0.1$. This perhaps goes against the usual idea that 2D simulations can effectively be thought of as a cross-section of an infinitely long domain, for flows in which 3D effects are negligible. The in-plane walls in the 3D model are treated with a zero-stress condition so that viscous effects are not introduced, therefore allowing the 3D simulations to replicate the 2D conditions as closely as possible and allow for more meaningful comparisons.

Sloshing flows are most sensitive to the forcing parameters close to resonance, and so it makes sense to also test the turbulence models under the condition of resonant excitation. The forcing and geometric parameters will be expressed in terms of non-dimensional quantities as in **Table** 5.2.

Dimension	**Length** [m]
L_x	0.5
L_y	0.5
L_z	0.1

Table 5.1: Tank dimensions

A forcing frequency $\omega^* = 1$ is used for all simulations. The fill ratio $h^*_{\text{fill}} = h_{fs}/L_x$ is chosen to be 0.7, which corresponds to the 'finite-depth' deep sloshing (Faltinsen, 2017) regime, typically characterised by the generation of standing waves. In terms of real values, these correspond to a forcing frequency of $\omega = 7.75$rad/s and a fill height of $h_{\text{fs}} = 0.35$m. The tank will be excited through 1 degree of freedom, with linear harmonic sway in the x-direction (as indicated in **Fig.** 5.2). A range of forcing amplitudes will be covered, and will therefore vary. Each of the simulations

is run for a duration of 40s. We'll see later that this was chosen on account of being sufficient time for the subsurface turbulence to fully develop.

Symbol	**Derivation**	**Description**
ω^*	ω/ω_1	Dimensionless excitation frequency
A^*	A/L_x	Dimensionless forcing amplitude
h^*_{fill}	h_{fs}/L_y	Fill height ratio

Table 5.2: Dimensionless sloshing parameters

5.2.1 Numerical model set-up

Once again, the `interFoam` solver is used throughout this chapter, unmodified from the native `OpenFOAM 4.1` version other than for the additional turbulence models/features that have been introduced. Linear harmonic sway motions are applied to the tank as depicted in **Fig.** 5.2.

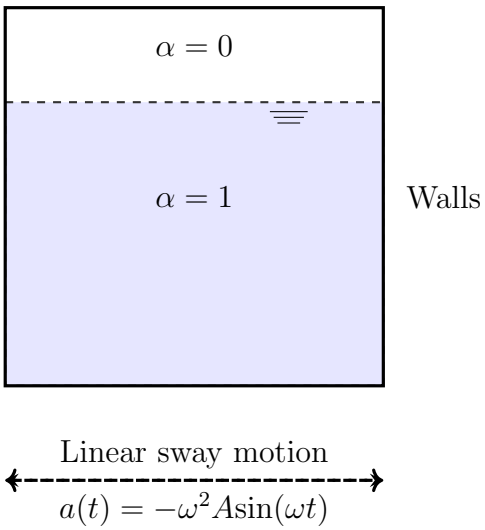

Figure 5.2: Initial and boundary conditions, with sway motion

The boundary conditions for each of the flow variables for the RANS simulations are as listed in **Section** 3.5.2. For the LES simulations, the boundary conditions for k and ω do not apply. Van driest wall treatment is included for near-wall damping of sub-grid-scale eddy viscosity. The LES delta function in **Eq.** 3.26 is modified to read as:

$$\Delta = \min\left(\frac{\kappa^* y_{wall}}{C_s} D, \sqrt[3]{\Delta x \Delta y \Delta z}\right), \tag{5.1}$$

where C_s is a model constants. D is the Van Driest function (Van Driest, 1956), which can be expressed as follows:

$$D = 1 - \exp(-y^+/A^+) \tag{5.2}$$

where y^+ is the dimensionless wall-normal distance and A^+ is a model constant.

5.3 Grid sensitivity

As an inital step, we must assess the sensitivity of grid resolution on the prediction of sloshing response for various turbulence models. This was done for a combination of 2D and 3D models. The matrix of simulations considered for the grid study are listed in **Table** 5.3.

Grid, $n_i =$	100	200	400
2D STB	✓	✓	✓
2D BM	✓	✓	✓
3D LES	✓	✓	✓
3D STB	✓	✓	✓

Table 5.3: Matrix of simulations: combinations of 3D/2D models and grid resolutions

For each respective turbulence model formulation, a sequence of 3 simulations was performed. These each pertain to a 'coarse, 'medium' and 'fine' mesh refinement level. Each grid is twice finer than that of the previous e.g. $\Delta x_{\text{fine}} = \Delta x_{\text{medium}}/2 = \Delta x_{\text{coarse}}/4$. Skewed and high aspect ratio cells can cause severe distortion of the interface. Therefore, the mesh strategy is kept very simple — a uniform structured grid (example in **Fig.** 5.3) is generated, allowing ultimate mesh quality to be preserved at the interface. This is true for both 2D and 3D simulation grids, and leads to a very simple Cartesian grid with equal grid spacing in all directions, $\Delta x = \Delta y = \Delta z$.

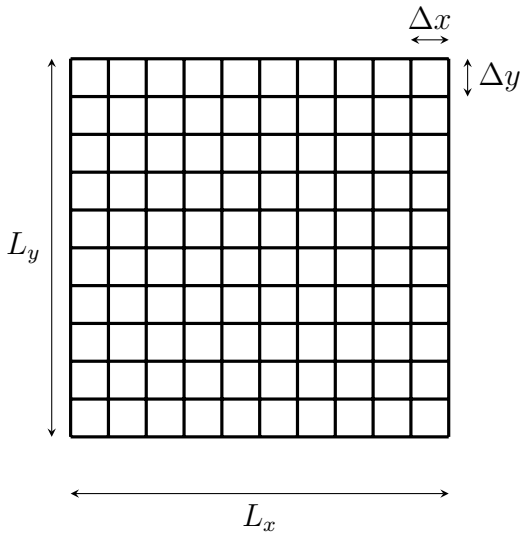

Figure 5.3: Uniform structured grid used throughout

The grid resolution (as in **Table** 5.3) for each mesh will be referenced based on the number of cells defined in each spatial dimension, n_i, rather than total number of cells in the grid overall. As the grid is isotropic and perfectly orthogonal throughout, $n_i = n_x = n_y = 5n_z = L_x/\Delta x$. A typical summary of what this means in terms of overall mesh size is listed in **Table** 5.4. I

Grid Refinement	$\boldsymbol{n_i}$	**Tot. cells (2D)**	**Tot. cells (3D)**
Coarse	100	10,000	200,000
Medium	200	40,000	800,000
Fine	400	160,000	3,200,000

Table 5.4: Grid refinement of the discretised solution domain

2D free surface response

For the 2D simulations, the non-dimensional amplitudes, $A^* = A/L_x = 0.02, 0.01$ are chosen. Forcing with an amplitude of $A^* = 0.02$ for this set-up generates a large free surface response with all the features of wave over-turning, splashing and roof impacts occurring with regularity. These are all features that are likely to be challenging for any numerical model to capture, and would be particularly sensitive to a computational mesh with inadequate resolution. Although forcing with an

amplitude of $A^* = 0.01$ is more than enough to initiate a large wave response, roof impacts do not occur. In turn, violent surface breakup and spray is less likely. Choosing these two amplitudes therefore allows us to investigate grid sensitivities for different behavioural phenomena.

Forcing amplitude, $A^* =$	0.01	0.02
`2D STB`	✓	✓
`2D BM`	✓	✓

Table 5.5: Matrix of simulations: 2D models and forcing amplitudes

The matrix of turbulence model-forcing amplitude combinations for each of the simulations in the 2D grid resolution study is listed in **Table** 5.5. The free surface response was measured by monitoring the free surface wave amplitude at the wall, η (see **Fig.** 5.4, where:

$$\eta = h(0,t) - h_0. \tag{5.3}$$

This was done by importing the raw field data into `Paraview`, defining an iso-surface of $\alpha = 0.5$ and exporting its co-ordinates into a text file. This data was then further processed in `MATLAB` in order to find the interface height $h(x,t) = h(0,t)$ (iso-surface y-co-ordinate) at $x = 0$.

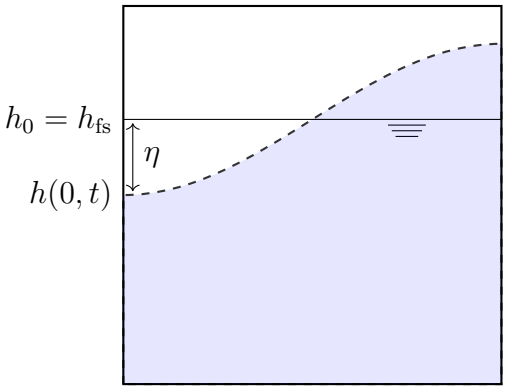

Figure 5.4: Wave response amplitude measurement

Fig. 5.5 shows the predicted wave response vs. time through the dura-

tion of the simulation, for 2D simulations using the buoyancy-modified (BM) and buoyancy-modified+stabilised (STB) models at each of the 3 grid refinement levels, with an amplitude of $A^* = 0.02$.

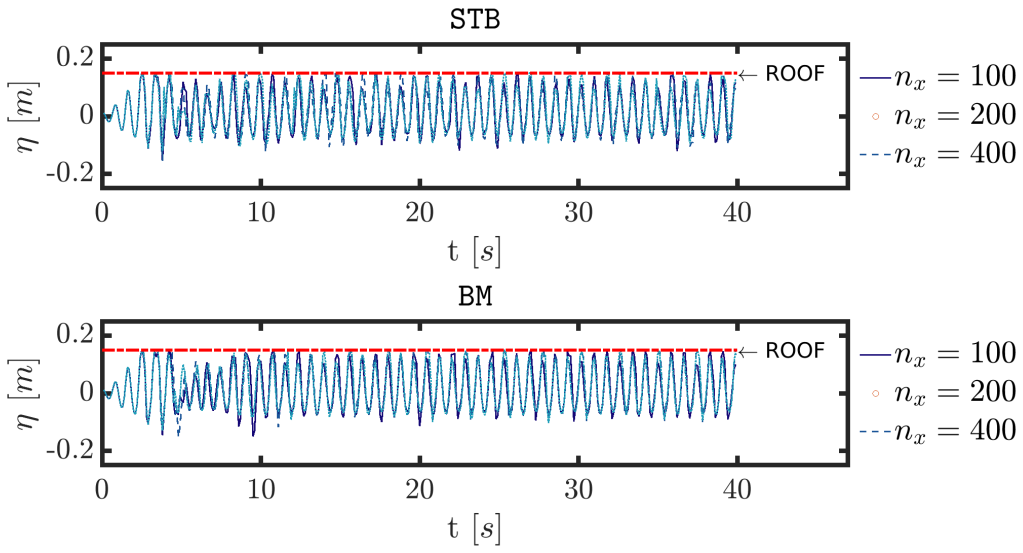

Figure 5.5: Wave amplitude, η, at the wall vs. time for BM and STB models, for 3 grid refinement levels at resolution $n_i = 100, 200, 400$, $\boldsymbol{A^* = 0.02}$

There are a few behavioural characteristics of the time-series wave response to take note of. Firstly, we can see that for each simulation, there is an initial lead-up time in which the system is gearing up to its peak energy state. Once this is reached — the point at which an equilibrium of energy input and dissipation is achieved — the flow exhibits steady, periodic behaviour. This occurs at approximately $t = 10s$. The red-dashed line in **Fig.** 5.5 indicates tank's roof location. We can see that for this scenario, roof impacts occur almost every period of oscillation. Roof impact events result in some complex phenomena, and are likely to introduce non-persistent transients into the flow due to their chaotic nature. Conversely, due to being highly dissipative events, the wave-breaking associated with such impacts are also known to damp out other persistent, low-frequency transients and speed up the time in which a quasi-steady-state system is achieved (Faltinsen, 2017).

The time-series wave response data indicates that the dynamic behaviour of the bulk flow is not highly sensitive to the grid resolution. Wave response predictions

for even the coarse and fine grid simulations are in very close agreement. This is true also when varying the turbulence model but maintaining the same grid resolution. **Fig.** 5.6 shows the last 15s worth of data taken from the simulations using each of the two modified $k-\omega$ SST models with grid resolution $n_i = 400$. Very close agreement is found between the two.

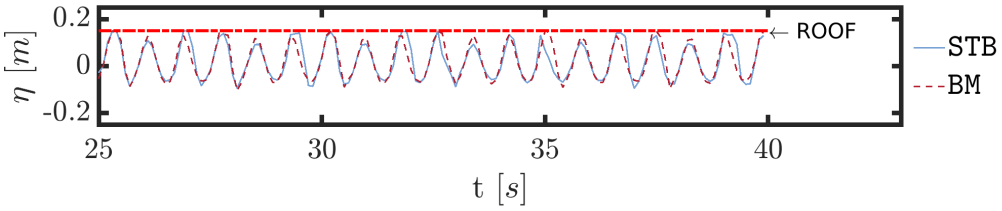

Figure 5.6: Direct comparison of predicted wave response at highest grid refinement $n_i = 400$ for the `STB` and `BM` models, with forcing amplitude $\boldsymbol{A^* = 0.02}$

Despite the primary response parameters (frequency, amplitude) being in very close agreement overall, viewing an instantaneous snapshot of the flow can tell a slightly different story. **Fig.** 5.7 shows the free surface captured at $t = 40$s. Y^* and X^* are the locally scaled tank co-ordinates $X^* = x/L_x$ and $Y^* = y/L_y$. This snapshot at $t = 40$s is chosen to capture how the flow might evolve differently during and in the immediate aftermath of a roof impact, and how mesh-sensitive this can be.

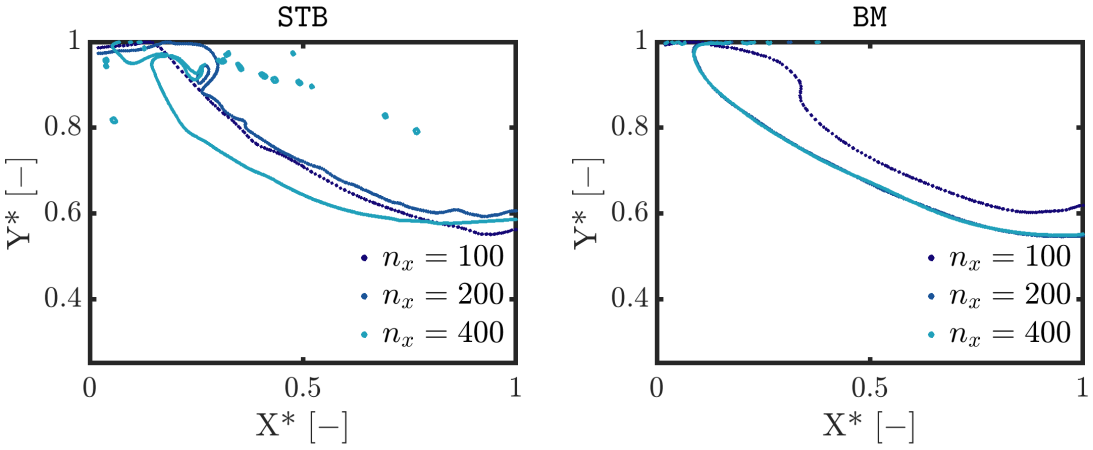

Figure 5.7: Snapshot of the free surface for 3 grid refinement levels at resolution $n_i = 100, 200, 400$, $\boldsymbol{A^* = 0.02}$, at time $t = 40$, showing grid dependency of the free surface profile during a roof impact event for the `STB` and `BM` formulations

The STB model predicts a free surface profile much less smooth. In the fine grid simulation, surface break-up is more noticeable. For the '$n_x = 400$' data, a collection of droplets has formed, airborne but on their way to crash back towards the free surface. This is likely due to the reduced effective viscosity local to the interface in comparison with the BM model simulation. This idea will be explored in more detail later on in this chapter, but for the time being we can say that in terms of grid resolution, the STB model is likely to be more sensitive. The prediction of splashing which features flow structures on much smaller scales than the bulk flow/interface requires a finer grid to fully resolve. Ultimately though, we are primarily interested in the bulk liquid phase response and the thermal mixing within the subsurface.

Deploying the BM predicts a much smoother surface with no splashing evident. At this moment, the free surface maintained its continuity through the roof impact. Referring back to **Fig.** 5.6, it is clear that these momentary deviations don't effect the overall behaviour of the system very much.

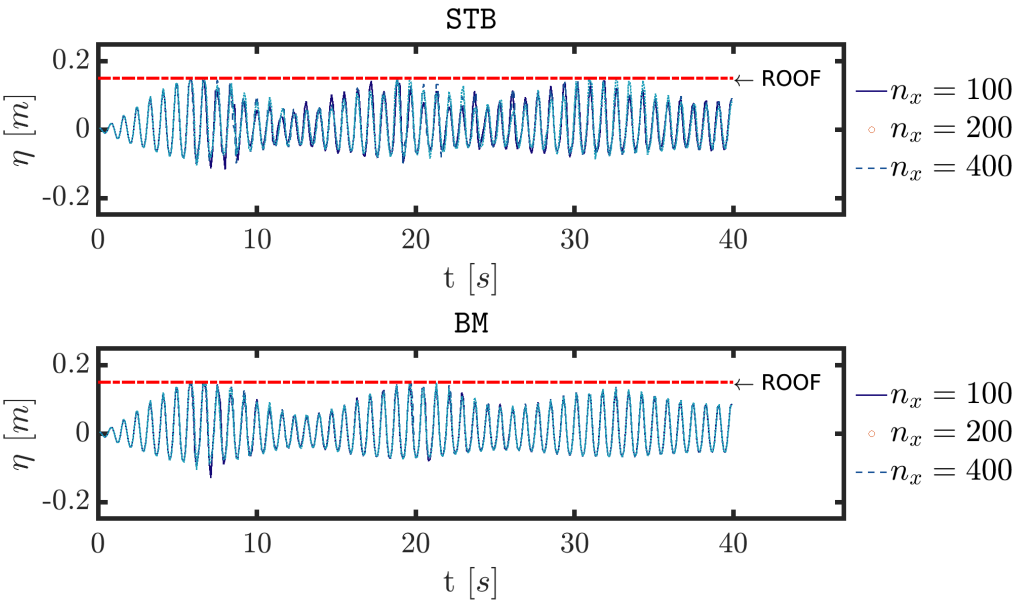

Figure 5.8: Wave amplitude, η, at the wall vs. time for BM and STB models, for 3 grid refinement levels at resolution $n_i = 100, 200, 400$, $\boldsymbol{A^* = 0.01}$

Fig. 5.8 shows the free surface response with a reduced forcing amplitude of $A^* = 0.01$. This time, the surface response fails to reach a steady-state. 'Beating'

occurs, a known feature of liquid sloshing, whereby the response amplitude becomes modulated as a consequence of low-frequency transients. This feature is widely reported throughout the literature (Zhang and Sun, 2014; Shao et al., 2012; Faltinsen et al., 2000), and is known to occur at near-resonance. These transients take longer to decay for deep sloshing, as viscous damping is less influential and non-linearities due to wave-breaking are generated less readily than at shallower depths. The way in which the system repeatedly builds up to a response amplitude such as to just about touch the roof of the tank, before decaying again, is captured with little sensitivity to the grid.

Fig. 5.9 shows the two finest grids for each turbulence model overlaid , again with strong agreement. Finally, a snapshot of the free surface at time, $t = 40$s is plotted in **Fig.** 5.10. We can see that once again, the `STB` model is more mesh-sensitive, but with a deviation less pronounced than in the higher forcing amplitude case considered previously.

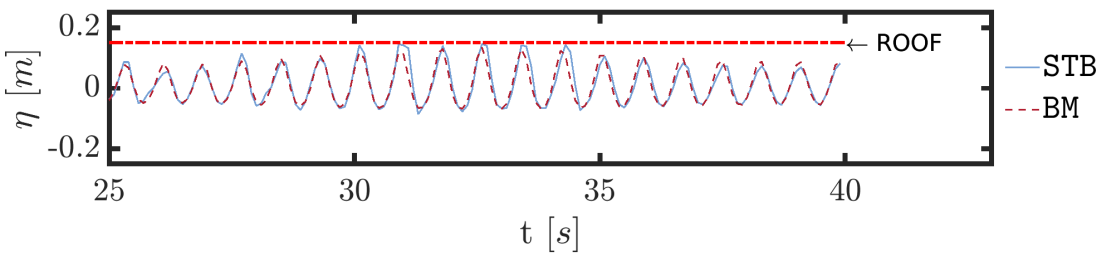

Figure 5.9: Direct comparison of predicted wave response at highest grid refinement $n_i = 400$ for the `STB` and `BM` models, with forcing amplitude $\boldsymbol{A^* = 0.01}$

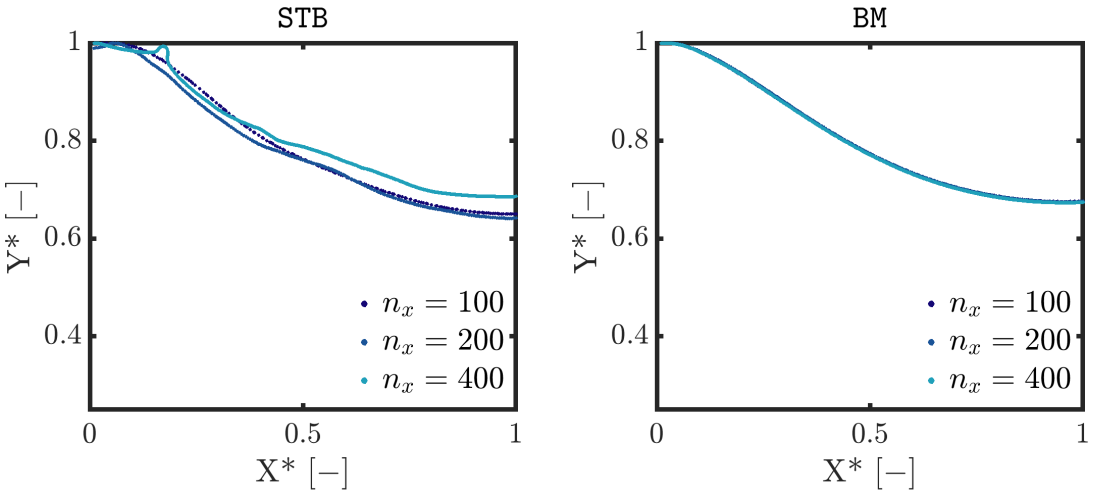

Figure 5.10: Snapshot of the free surface for 3 grid refinement levels at resolution $n_i = 100, 200, 400$. $\boldsymbol{A^* = 0.01}$

3D free surface response

The same analysis method as in the previous sub-section is repeated for 3D simulations. Due to the computational expense of running long transient 3D models, it was decided to omit using the `BM` model, instead running only one of the RANS models — the `STB` model. Additionally, the Smagorinsky LES model (as this is the only LES model considered in this thesis it will be referred to simply as `LES`) was deployed.

Forcing amplitude, $A^* =$	0.002	0.01
`3D LES`	✓	✓
`3D STB`	✓	✓

Table 5.6: Matrix of simulations: 3D models and forcing amplitudes

The maximum forcing amplitude for any 3D case is $A^* = 0.01$. Amplitudes higher than that, at resonance, result in the development of high velocity, small structures during wave breaking and roof impacts. These result in a significant penalty in CPU-time when considering the restrictions on Courant number that are required to maintain stability and boundedness within the solver. The 3D simulations considered in the grid study are listed in **Table** 5.6:

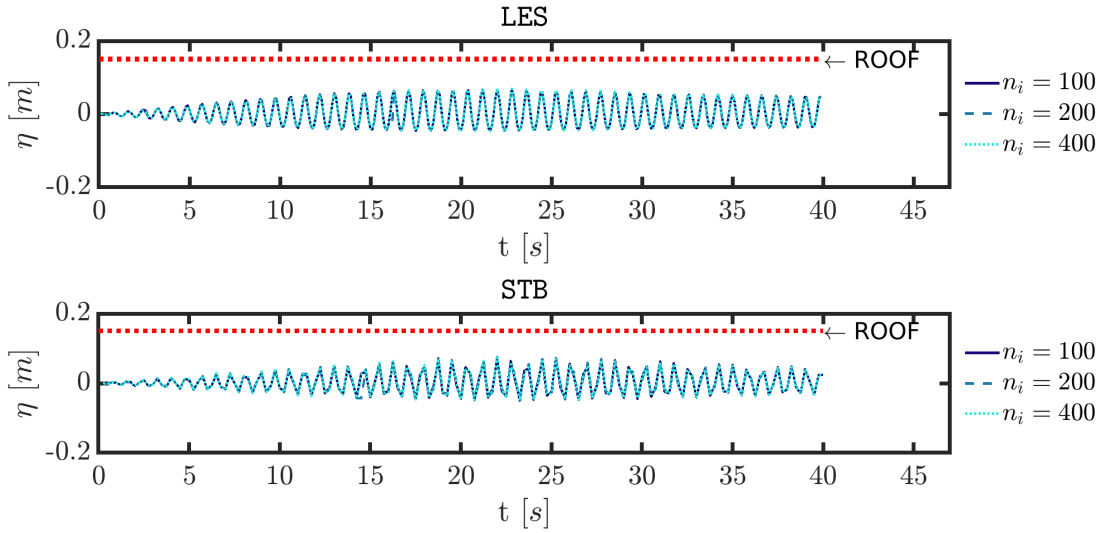

Figure 5.11: Wave amplitude η, at the wall vs. time for `LES` and `STB` simulations, for 3 grid refinement levels at resolution $n_i = 100, 200, 400$, with forcing amplitudes $\boldsymbol{A^* = 0.002}$ and constant forcing frequency $\omega^* = 1$

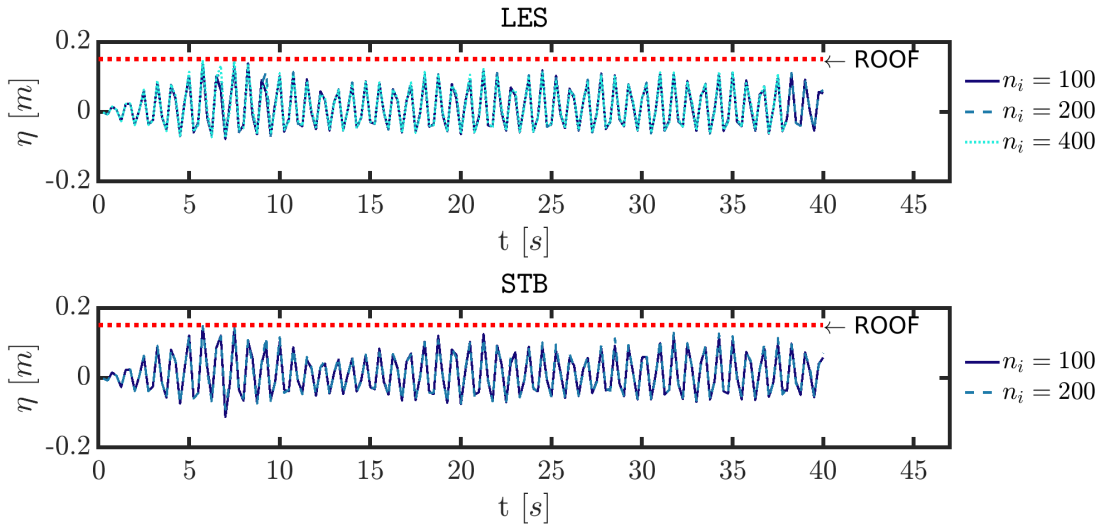

Figure 5.12: Wave amplitude η, at the wall vs. time for `LES` and `STB` simulations, for 3 grid refinement levels at resolution $n_i = 100, 200, 400$ with forcing amplitudes $\boldsymbol{A^* = 0.01}$ and constant forcing frequency $\omega^* = 1$

Figs. 5.11 & 5.12 show the wave response amplitude plotted vs. time for each simulation. As with the 2D simulations, wave response does not demonstrate high sensitivity to grid resolution when considering these forcing parameters. With each of the wave response-time curves overlaid on top of one another, it is difficult to notice any differences at all. The run-up times, peak response amplitude and frequency of modulation of the beating waves all agree closely. It should be noted

that some of these figures feature a more jagged-looking profile. This is due to the reduced frequency (and subsequently less smooth time-series curve) at which data was stored, in an effort to reduce computation time and to be economical with storage requirements.

Summary of results

Table 5.7 lists the root mean square (RMS) wave response amplitude, η_{RMS} for each of the simulations considered throughout this grid-resolution study. RMS wave amplitude is calculated as:

$$\eta_{\text{RMS}} = \sqrt{\frac{1}{N}\sum_{i=1}^{N}\eta_i(t)^2} \tag{5.4}$$

where $\eta_i(t) = h(0,t) - h_0$, is the wave amplitude, calculated as the difference between the time-dependent depth at the wall, $h(x,t) = h(0,t)$ and the initial height of the free surface at rest, $h_0 = h(0,0)$. The subscript i denotes the i^{th} time-step. The size of the data set, $N = t_{\text{final}}/\Delta t$ is 300 in this case, which is sampled through final $30s$ of the simulation, with at least 10 data points per period of oscillation.

To illustrate the narrow range in which η_{RMS} is predicted over the $30s$ sampling period for each model, the coefficient of variation for each set of grid results per model-amplitude combination has been calculated. The maximum variation for each data set was for for the 3D `STB` $A^* = 0.01$ data set, at only 1.66%. Interestingly, the lowest variation was found in the sequence of `LES` simulations. This is surprising, given the increased grid demands of LES models that are required to accurately capture unsteady flow structures in the velocity field. Despite the observation of increased surface break-up droplet formation at higher grid resolutions for the 2D `STB` model at $A^* = 0.02$, this formulation is found to be no more grid-sensitive to `BM` in terms of RMS wave response.

A^* [−]	$A^* = 0.01$				$A^* = 0.02$			
Grid, $n_i =$	100	200	400	-	100	200	400	-
Model	$\eta_{\mathrm{RMS}}[\times 10^{-2} m]$			**Variation** [%]	$\eta_{\mathrm{RMS}}[\times 10^{-2} m]$			**Variation** [%]
2D STB	6.16	6.26	6.27	1.09	7.85	7.97	7.89	0.68
2D BM	6.03	6.16	6.14	0.84	8.04	8.00	8.01	0.73
A^* [−]	$A^* = 0.002$				$A^* = 0.01$			
Model	$\eta_{\mathrm{RMS}}[\times 10^{-2} m]$			**Variation** [%]	$\eta_{\mathrm{RMS}}[\times 10^{-2} m]$			**Variation** [%]
3D STB	3.32	3.44	3.34	1.94	6.13	6.30	-	-
3D LES	3.26	3.26	3.25	0.17	6.18	6.38	6.31	1.66

Table 5.7: Root mean squared wave amplitude at the wall, η^*_{RMS} for BM and STB with increasing grid resolutiont, n_i. Coefficient of variation is calculated for each model/amplitude combination data set

Fig. 5.13 shows a comparison of the RMS wave height of a total of 12 simulations and 4 different turbulence modelling approaches. The 3D LES results yield the highest wave response. The 2D and 3D STB simulations are very similar, which somewhat validates the assumption that having a very thin 3-Dimensional tank will effectively eliminate 3D flow effects, or at least so much as to not be evident in the free surface response. For the $n_i = 400$ resolution fine grid level, predicted η_{RMS} for 2D STB, 3D STB and 3D LES are in extremely close agreement. The 2D BM simulations results in the lowest amplitude wave response of all. Again, the hypothesis here is that this is due to the falsely enhanced viscosity that results from using a model that his been shown to be unstable. In the next sub-section this point will be illustrated more clearly.

With all this in mind, we will proceed for the rest of the chapter using the 'fine' grid of $n_i = 400$, with 2D simulations. This grid resolution provides a converged solution across a range of parameters and is computationally feasible even for long run-time transient simulations. For 3D simulations, matching these resolutions is only achievable at the cost of significant run-time, with simulations typically taking weeks in terms of wall-clock time (and many thousands of CPU hours) to complete. Furthermore, the strong agreement between the 2D and 3D simulations at the fine

grid resolution suggests that a 3D model isn't merited considering the additional overheads involved.

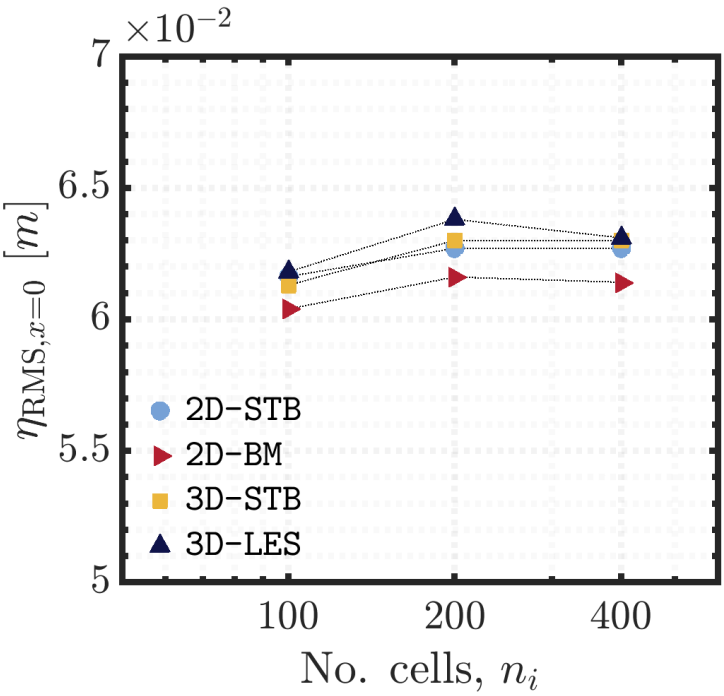

Figure 5.13: RMS of wave height at the wall vs. grid resolution n_i, as predicted by 2D `STB` and `BM` models and 3D `STB` and `LES` models, for simulations with constant forcing frequency $\omega^* = 1$ and amplitude $\boldsymbol{A^* = 0.01}$.

5.4 RANS model sensitivity

In this sub-section, the choice of turbulence model for sloshing flows will be examined more closely. Again, we will look at the influence on free surface response to external excitations — so far, all results indicate that this is an area of weak sensitivity. Building on that, the flow behaviour in the subsurface will be analysed — the aspect in which most of our interest will be focussed. To reiterate the findings from surveying the literature, the influence of modelling approach on the prediction of flow kinematics and turbulence in the subsurface has gained little research attention when analysing sloshing flows. For the consideration of mixing processes coupled to slosh-induced motions, this gap in the research must be filled.

Forcing amp, $A^* =$	**0.002**	**0.01**	**0.02**
`STB`	✓	✓	✓
`BM`	✓	✓	✓
`KWSST`	✓	✓	✓

Table 5.8: Matrix of simulations - turbulence model and forcing amplitude combinations

Table 5.8 shows the matrix of simulations used for the analyses in this section. Overall, a combination of 3 forcing amplitudes and 3 turbulence model gives a total of 9 simulations, which will allow us to illustrate the relative impact of using each model over a range of forcing amplitudes. Each of the simulations in this section are 2D, with the same forcing frequency and fill height applied as before. The incompressible $k-\omega$ SST model (`KWSST`), that is used as a default option in `interFoam` has been included despite being shown to perform poorly in the previous chapter. Results produced by using this model are included for illustrative purposes, and also to highlight the fact that a severe increase in subsurface turbulence in sloshing flows could easily be missed if monitoring free surface behaviour alone.

5.4.1 Free surface response

The time-series data of wall wave height, η vs. time is shown in **Fig.** 5.14. As observed in the grid-resolution study, the free surface motion does not show a high degree of sensitivity to the choice of turbulence model. As the forcing amplitude is increased, some localised deviations in terms of response amplitude peaks are observed, but the global behaviour remains very much the same. Interestingly, the frequency of modulation for $A^* = 0.002$ is much lower than $A^* = 0.01$, and this behaviour is captured identically by each model.

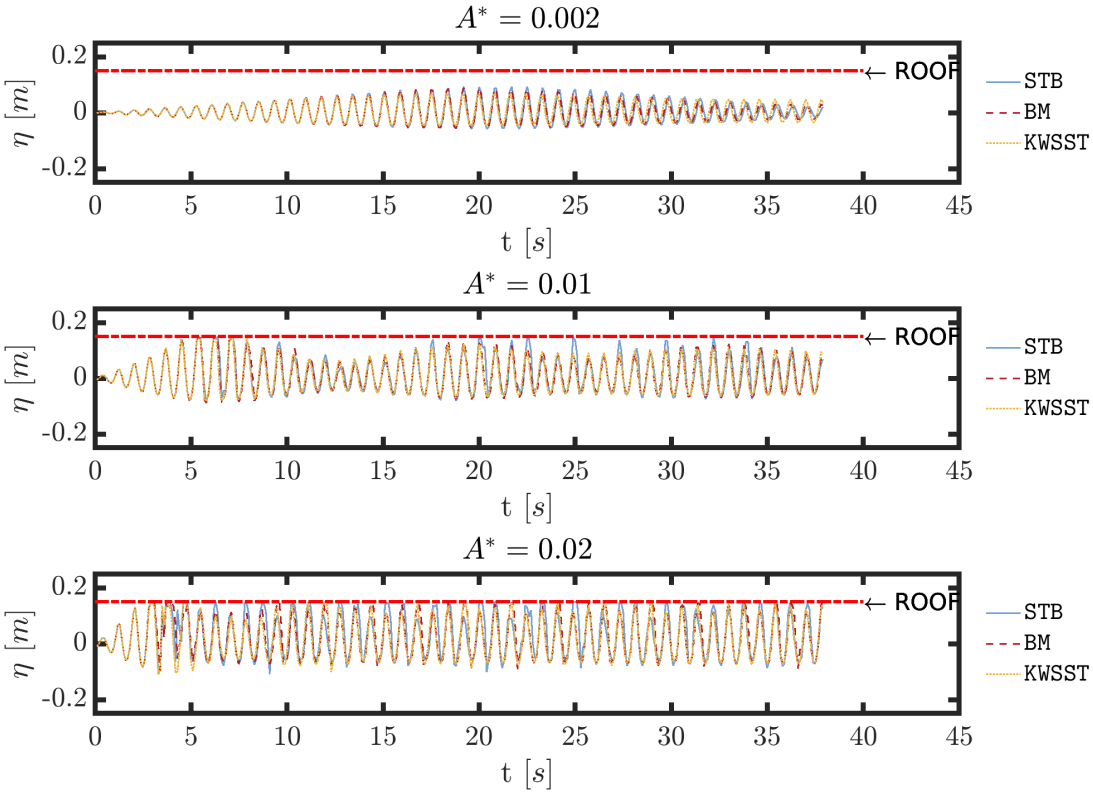

Figure 5.14: Wave amplitude, η, at the wall vs. time for simulations with turbulence models `STB`, `BM` and `KWSST`, with constant forcing frequency $\omega^* = 1$ at amplitudes $\boldsymbol{A^* = 0.002}$ (top) $\boldsymbol{A^* = 0.01}$ (middle) $\boldsymbol{A^* = 0.02}$ (bottom)

$A^* =$	0.002	0.01	0.02
Model	$\eta_{\mathrm{RMS}}[\times 10^{-2} m]$		
STB	3.75	6.56	8.42
BM	3.5	6.28	8.01
KWSST	3.26	6.18	7.76

Table 5.9: RMS wall wave amplitude, η_{RMS} for STB, BM and KWSST with increasing amplitudes, A.

Table 5.9 lists the RMS wave response amplitude predicted by each of the 9 simulations. A clear trend, illustrated by **Fig.** 5.15 is evident in that the STB model predicts the greatest wave response across the range of amplitudes. This is followed by BM and lastly KWSST which produces the most modest response to excitation.

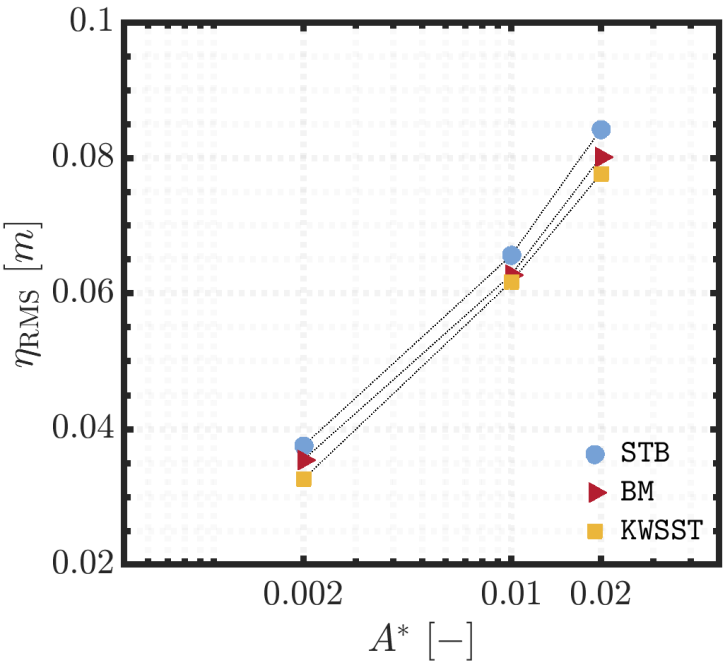

Figure 5.15: RMS wall wave height, η_{RMS} vs. dimensionless forcing amplitude for each turbulence model formulation

5.4.2 Subsurface kinematics

Beyond the motion of the free surface, subsurface kinematics are particularly important to scalar mixing processes within sloshing fluids. It would seem safe to assume that the subsurface flow — intrinsically coupled to the dynamic motion of the free surface — develops in such a way as to enhance scalar (and hence thermal) mixing. Heat transfer in fluids is driven by a combination of forced/natural convection and molecular conduction (diffusion). Two-equation RANS models are formulated such that the advective mixing of scalars by turbulent eddies are modelled and mathematically subsumed into an enhanced diffusion term of the RANS equations. Accurately predicting subsurface eddy viscosity is vitally important to ensure that mixing on un-resolved spatial and temporal scales is captured correctly. In **Chapter** 4, it was demonstrated that accomplishing this is far from trivial.

Data collection in the subsurface

Data is collected at each time-step ($\Delta t = 0.05s$) for each of the velocity components u_x, u_y and for the turbulent properties k, ν_T at 100 discrete points along a centre-line of the tank as shown in **Fig.** 5.16, using the `singleGraph` utility in `OpenFOAM`. This vertical sampling line spans the entire depth of the tank. A simple algorithm in `Matlab` is then used to filter out the above-surface data:

1. Loop through the line-data to determine the free surface location by volume fraction, $h(t) = y_{\alpha=0.5}(t)$, where the free surface is defined is the first vertical location at which $\alpha < 0.5$.

2. Determine the minimum free surface height, $h_{min} = \min(h(t))$ measured along the centre-line across all sampling times.

3. Filter out the 'above surface' data at each time-step by ignoring all data where $y > h_{min}$.

Taking the cut-off point to be $y = h_{\min}$ for all time-steps means that at certain points in time, a small amount of the data measured just below the free surface will be lost, as in most instances $h(t) > h_{\min}$. By only calculating the RMS/mean values at fixed points in space at which we are guaranteed to be only considering 'subsurface' data at every time-step, this makes the comparisons through statistical analysis more meaningful.

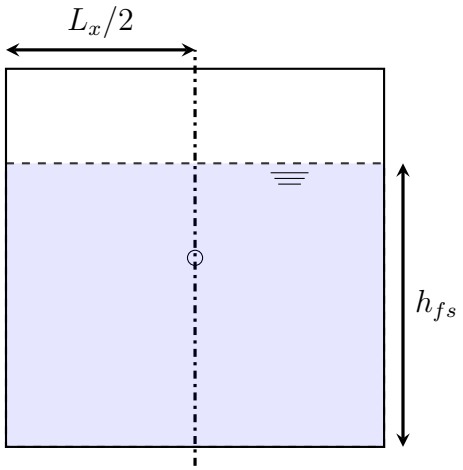

Figure 5.16: Tank with vertical centre-line along which we take measurements

In order to perform Fourier analysis of the velocity field at a singular discrete location, time-series data is also measure at a point (marked by a circle in **Fig.** 5.16) beneath the free surface. This is taken to be 1cm below $h_{\min}$ so as to be within the energetic flow region directly beneath the interface. This time-series data is then transformed into the frequency domain using a Fast Fourier Transform (FFT) algorithm.

As before, the length of each simulation is 40s, and data collection takes place during the period $t = 10 \rightarrow 40$s.

Velocity in the subsurface

Fig. 5.17 shows the depth-dependent RMS velocity components in the subsurface scaled by $\sqrt{gh_{fs}}$ for simulations of dimensionless amplitude $A^* = 0.002$. Each component is calculated as follows:

$$U_{\mathrm{i,RMS}}(z) = \sqrt{\frac{1}{N}\sum_{j=1}^{N} u_{\mathrm{i,j}}^2(z,t)}. \tag{5.5}$$

where the subscript i refers to the spatial dimension, and the subscript j refers to the j^{th} time-step. Liquid depth is scaled to the initial free surface height:

$$y^* = y/h_{fs} \tag{5.6}$$

The RMS x-velocity component is typically at least an order of magnitude greater than that of the y-component. This is to be expected — long the tank centre-line, the dominant flow component is in the primary direction of excitation, which in this case is the x-direction. The prediction of $U_{x,\mathrm{RMS}}$ through the depth of the tank is in very close agreement for each model. More variability is found when it comes to predicting the vertical velocity component.

Models `KWSST` and `BM` predict a smooth, monotonic profile for $U_{y,\mathrm{RMS}}$ through liquid depth, with a steady increase towards the free surface. `STB` follows a similar profile up to around $y^* \approx 0.4$. Above this point there is then a noticeable jump of roughly one order of magnitude between $y^* \approx 0.4 \rightarrow 0.6$. After which, there is a slight decrease in velocity before again increasing as the free surface is approached. This suggests that the `STB` model is predicting there to be a distinct region of higher energy flow in the upper portion of the liquid, which is not picked up by the other model formulations.

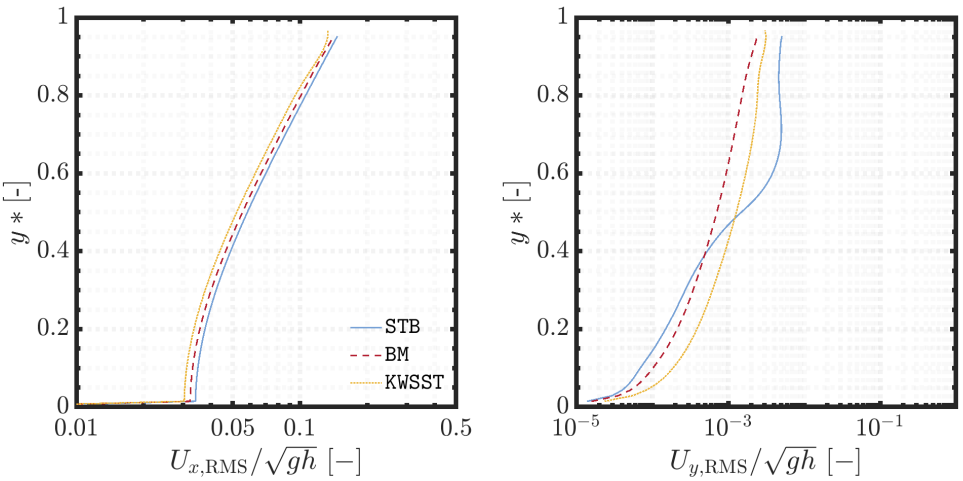

Figure 5.17: $U_{x,RMS}$ (co-axial to the direction of tank motion) and $U_{y,RMS}$ vs. non-dimensional distance from the tank bottom (scaled to height of free surface), $y^* = y/h_{f.s.}$, $\boldsymbol{A^* = A/L_x = 2 \times 10^{-3}}$.

Fig. 5.18 shows the FFT plot of the velocity data sampled at a point. Fluctuations in the x-direction are overwhelmingly dominated by oscillations at the primary natural frequency, f_1. This reflects sloshing response of the bulk fluid being driven by the tank forcing frequency, $\omega = \omega_1 = 2\pi f_1$. The rest of the FFT plot is flat away from the primary mode, except for a small peak at a frequency just higher than $f = f_8$. This is picked up by all 3 of the models, suggesting an additional high frequency but weak flow structure that has developed near the free surface.

The FFT plot of the vertical velocity reveals two distinct peaks. One peak occurs at a frequency just below $f = f_4$, while another occurs at a frequency well below that of the first natural frequency. This is perhaps evidence of the low frequency transients associated with the wave modulation seen in the time-series wave response curves in the previous section. Again, the FFT plot shows good agreement between each of the turbulence models in terms of the location and magnitude of peaks.

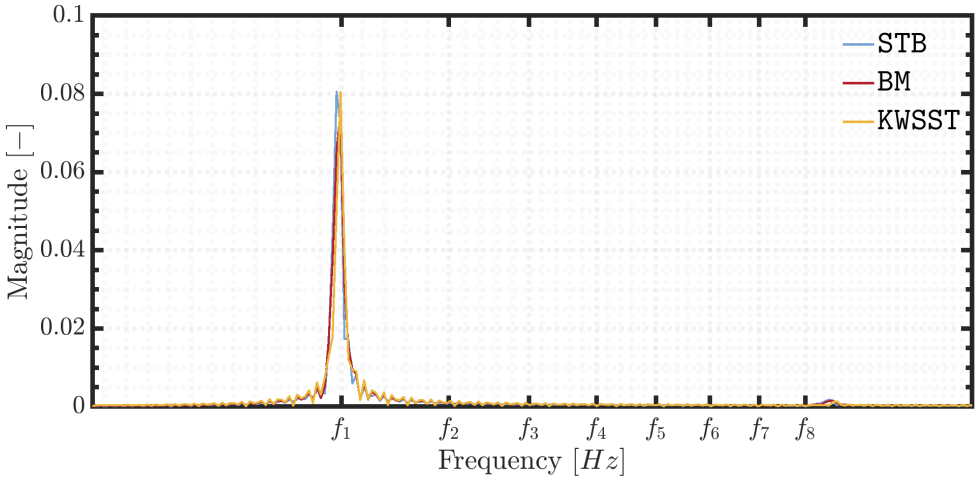

(a) FFT plot - horizontal velocity component, u_x.

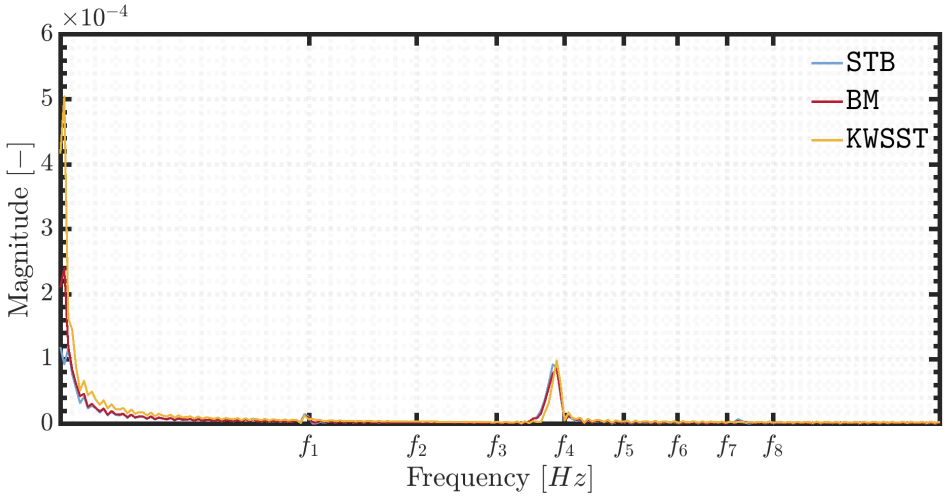

(b) FFT plot - vertical velocity component, u_y.

Figure 5.18: Fourier analysis, $\boldsymbol{A^* = A/L_x = 2 \times 10^{-3}}$.

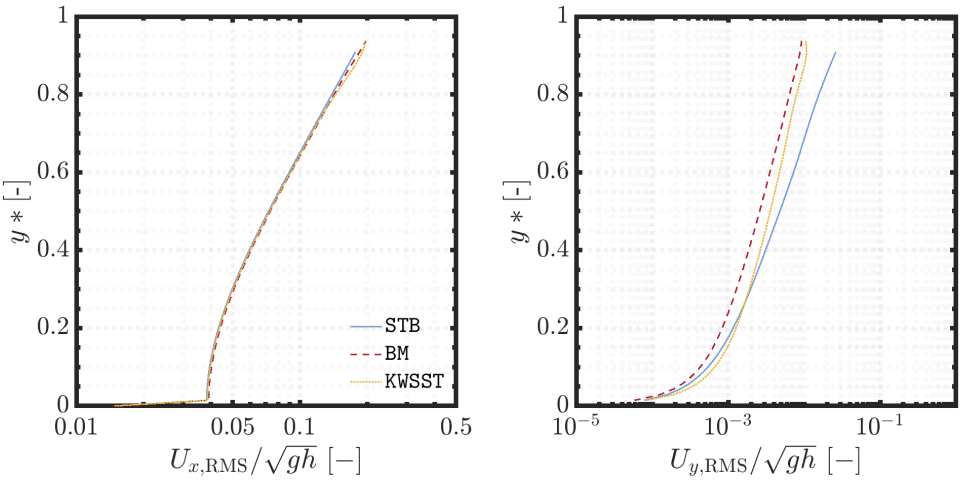

Figure 5.19: $U_{x,RMS}$ (co-axial to the direction of tank motion) and $U_{y,RMS}$ vs. non-dimensional distance from the tank bottom (scaled to height of free surface), $y^* = y/h_{f.s.}$, $\boldsymbol{A^* = A/L_x = 1 \times 10^{-2}}$.

Fig. 5.19 shows the RMS velocity components through the depth of the subsurface at a forcing amplitude, $A^* = 0.01$. Once again, there is little difference in x-velocity prediction through liquid depth — the curves are almost identical. Vertical motion with higher velocity is predicted by the `STB` in the top half of the subsurface, again indicating a more energetic flow-field beneath the interface.

The FFT plot in **Fig.** 5.20 shows similar behaviour to the previous case in terms of the horizontal motions. However, the Fourier analysis of vertical velocity now shows significant differences between the model predictions. Modal peaks at $f = f_4$ and at some very low frequency again dominate for the `KWSST` and `BM` models.

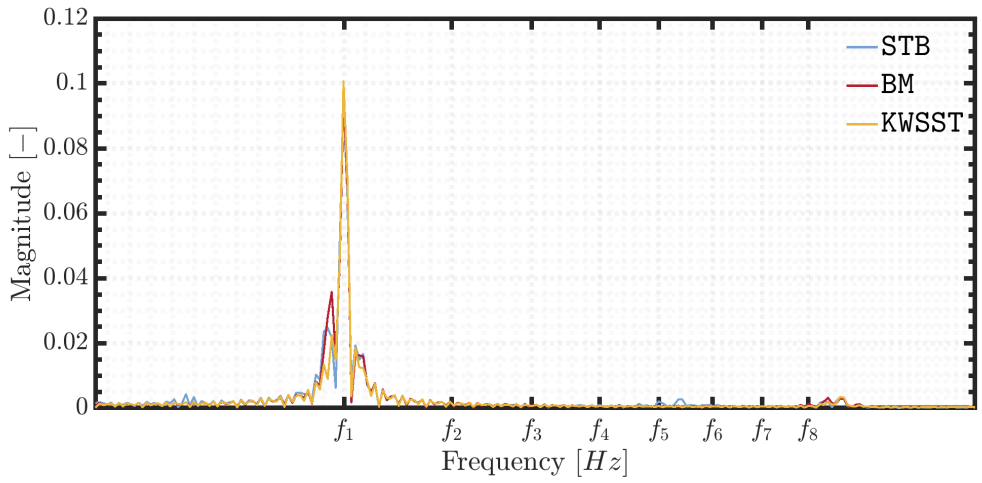

(a) FFT plot - horizontal velocity component, u_x.

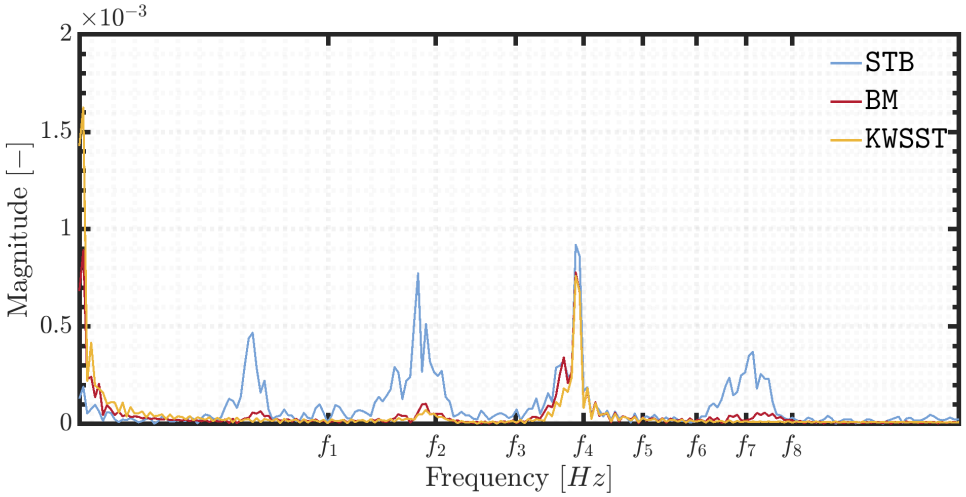

(b) FFT plot - horizontal velocity component, u_x.

Figure 5.20: Fourier analysis, $\boldsymbol{A^* = A/L_x = 1 \times 10^{-2}}$.

The STB results show the same peak but with further significant peaks at $f = f_2$, $f = f_7$ and at an additional low frequency. This follows the behaviour described by Faltinsen and Timokha (2009), whereby non-linearities develop at high response amplitudes, with energy dispersion from steep waves transferred into other modes. It would again seem that the stabilised model formulation has a greater tendency for transient flow structures to develop in the subsurface.

Finally, in **Fig.** 5.21 the RMS velocity components for the highest forcing amplitude simulations, $A^* = 0.02$ are presented. Once again, there is near-exact agreement in the horizontal velocity component, but with a slightly higher prediction of vertical velocity through the entire subsurface by the STB model formulation.

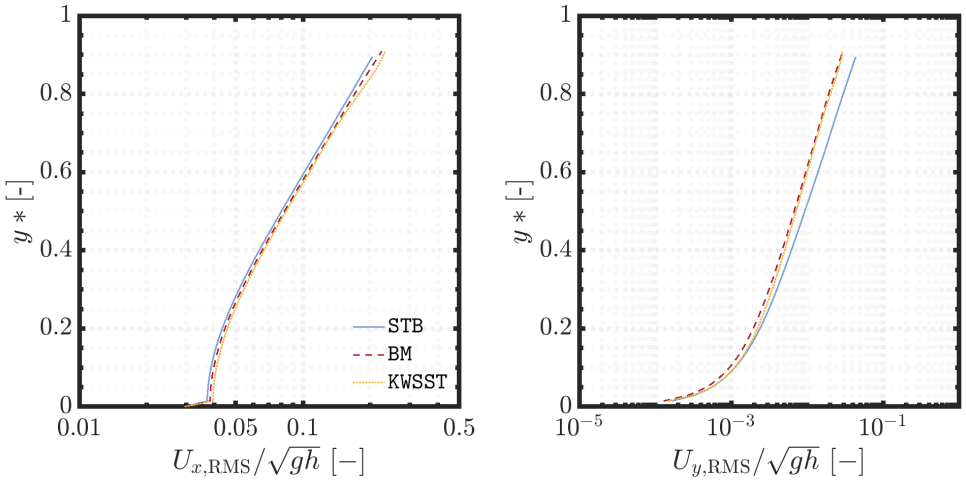

Figure 5.21: $U_{x,RMS}$ (co-axial to the direction of tank motion) and $U_{y,RMS}$ vs. non-dimensional distance from the tank bottom (scaled to height of free surface), $y^* = y/h_{f.s.}$, $\boldsymbol{A^* = A/L_x = 2 \times 10^{-2}}$.

Fourier analysis of the vertical velocity under excitations of $A^* = 0.02$ reveals that strong peaks are now emerging at $f = f_2, f_4, f_7$ and at some frequency $f < f_1$ for each one of the models, matching what STB was already predicting in the previous example at half the forcing amplitude. For the STB model, each of the modal peaks are now of an even greater magnitude than before. The peak at $f = f_2$ has grown to be of similar magnitude to the peak at $f = f_4$. Remembering that this forcing amplitude is the case at which violent roof impacts occur, it would seem

that these events, and the disruption caused to the free surface is initiating more complex and non-linear behaviour in the velocity field beneath the surface.

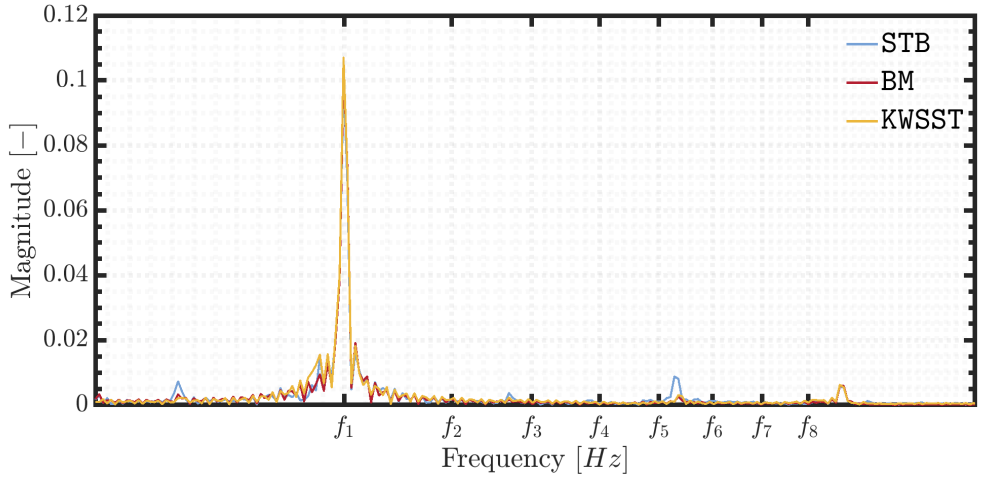

(a) FFT plot - horizontal velocity component, u_x

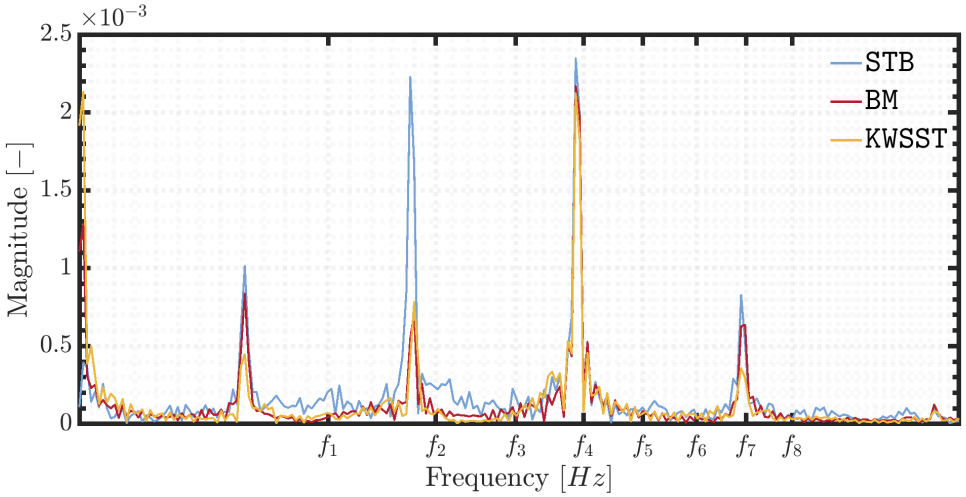

(b) FFT plot - vertical velocity component, u_y

Figure 5.22: Fourier analysis, $\boldsymbol{A^* = A/L_x = 2 \times 10^{-2}}$.

5.4.3 Turbulence in the subsurface (and in the air)

In this section, the influence of model formulation on the prediction of turbulence in the subsurface is examined, with the same set of model-amplitude combinations. Boussinesq-type turbulence models treat the turbulent quantities of eddy viscosity and turbulent kinetic energy as non-directional scalar quantities. Therefore, rather than calculating the RMS of the time-series data, a simple time-averaged depth-dependent calculation will suffice. The turbulent properties are each calculated as follows:

$$\nu_T(z) = \frac{1}{N}\sum_{j=1}^{N} \nu_{T,j}(z,t_j), \quad k(z) = \frac{1}{N}\sum_{j=1}^{N} k_j(z,t_j) \tag{5.7}$$

Turbulent kinetic energy in the water

In **Fig.** 5.23, we see is a similar story to what was found in **Chapter** 4, when comparing the predictive capabilities of each model to the experimental data of Fabre et al. (1987). The incompressible, unmodified `KWSST` model produces much higher levels of turbulent kinetic energy through the liquid depth than the stabilised model. However, unlike then, the levels of turbulence produced by `BM` is very similar `KWSST` except in a small region directly beneath the free surface. This is evidence of the buoyancy source (**Eq.** 4.4) working to suppress turbulence at the interface — as it is designed to do.

The stabilised `STB` model consistently predicts turbulent kinetic energy at much lower levels that the two other model formulations — several orders of magnitude in fact, particularly towards the tank's base. Not only that, but qualitatively, the profile is markedly different.

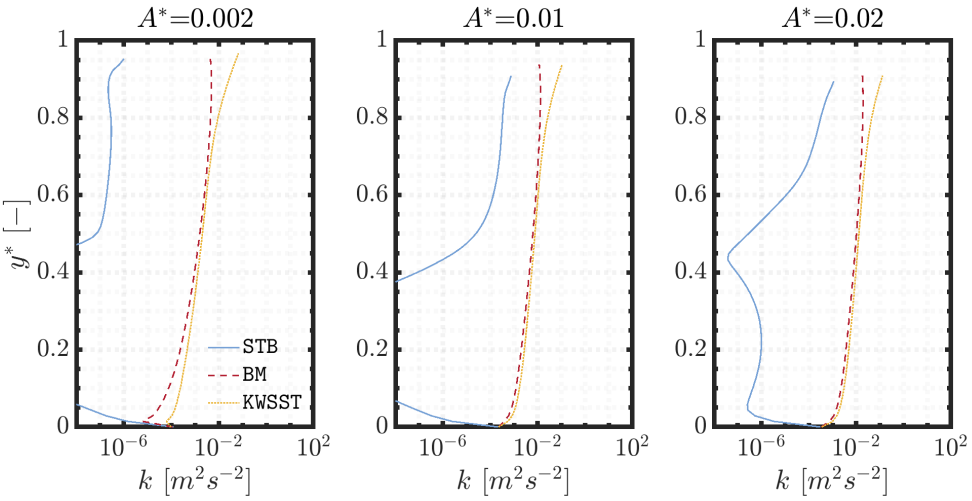

Figure 5.23: Spatially averaged turbulent kinetic energy in the water, $\bar{\nu}_T^*$ vs time, t, for turbulence models `STB`, `BM` & `KWSST`, with varying forcing amplitude, A^*.

Figs. 5.24,5.25 & 5.26 show contours of k as the flow-field develops through time, with snapshots taken at $t = 10, 20, 30, 40$s. Using the `KWSST` and `BM` models, the growth of k initiates in the interface region, before spreading and forming a continuous diffuse region throughout the entire subsurface. Only at the walls is this behaviour encumbered by the action of the wall functions. More specifically, at a closer look, it would seem that the initial region of turbulence starts at the interface itself in the case of the `KWSST` model, whereas we can see the epicentre of this high-k region actually lies initially just below the free surface for the `BM` model.

These contour maps are in complete contrast with what is predicted by the `STB` model. Due to the contour map being scaled to match those of the other two models, there is barely any discernible turbulence present through most of the subsurface at all. This indicates a much more laminar flow away from the surface. This is especially true in the case of $A^* = 0.002$. As forcing amplitude is increase, small regions of high turbulence begin to develop near the interface, due to surface break-up caused by wave over-turning and roof impacts. Higher turbulence only reaches the lower regions of the tank after being initially generated at the surface and then carried down. What really stands out is that the increase in local turbulence predicted by the `STB` is as a consequence of actual events. The other two

model formulations produce all-consuming regions of turbulence, regardless of what happens at the surface.

This reflects the observations made by Larsen and Fuhrman (2018) and Mayer and Madsen (2001), who demonstrated the unconditionally unstable nature of the standard two-equation models, resulting in the over-prediction of turbulence in near-potential flow regions with finite strain beneath the free surface. For sloshing flows in tanks that are closed systems, this effect is clear.

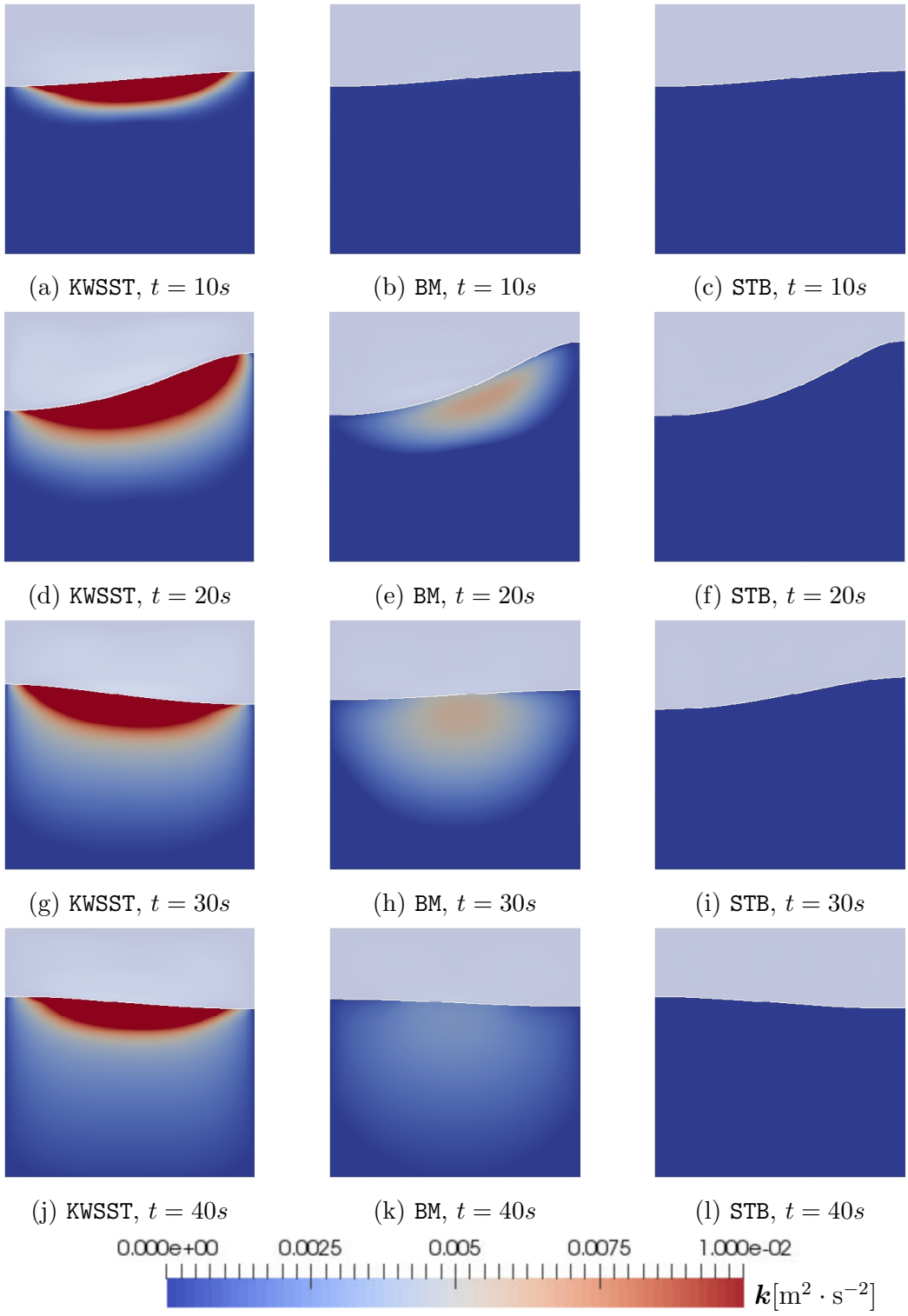

(a) KWSST, $t = 10s$ (b) BM, $t = 10s$ (c) STB, $t = 10s$

(d) KWSST, $t = 20s$ (e) BM, $t = 20s$ (f) STB, $t = 20s$

(g) KWSST, $t = 30s$ (h) BM, $t = 30s$ (i) STB, $t = 30s$

(j) KWSST, $t = 40s$ (k) BM, $t = 40s$ (l) STB, $t = 40s$

Figure 5.24: Turbulent kinetic energy contours at time $t = 10, 20, 30, 40$s, $\boldsymbol{\omega^* = 1}$, $\boldsymbol{A^* = 0.002}$

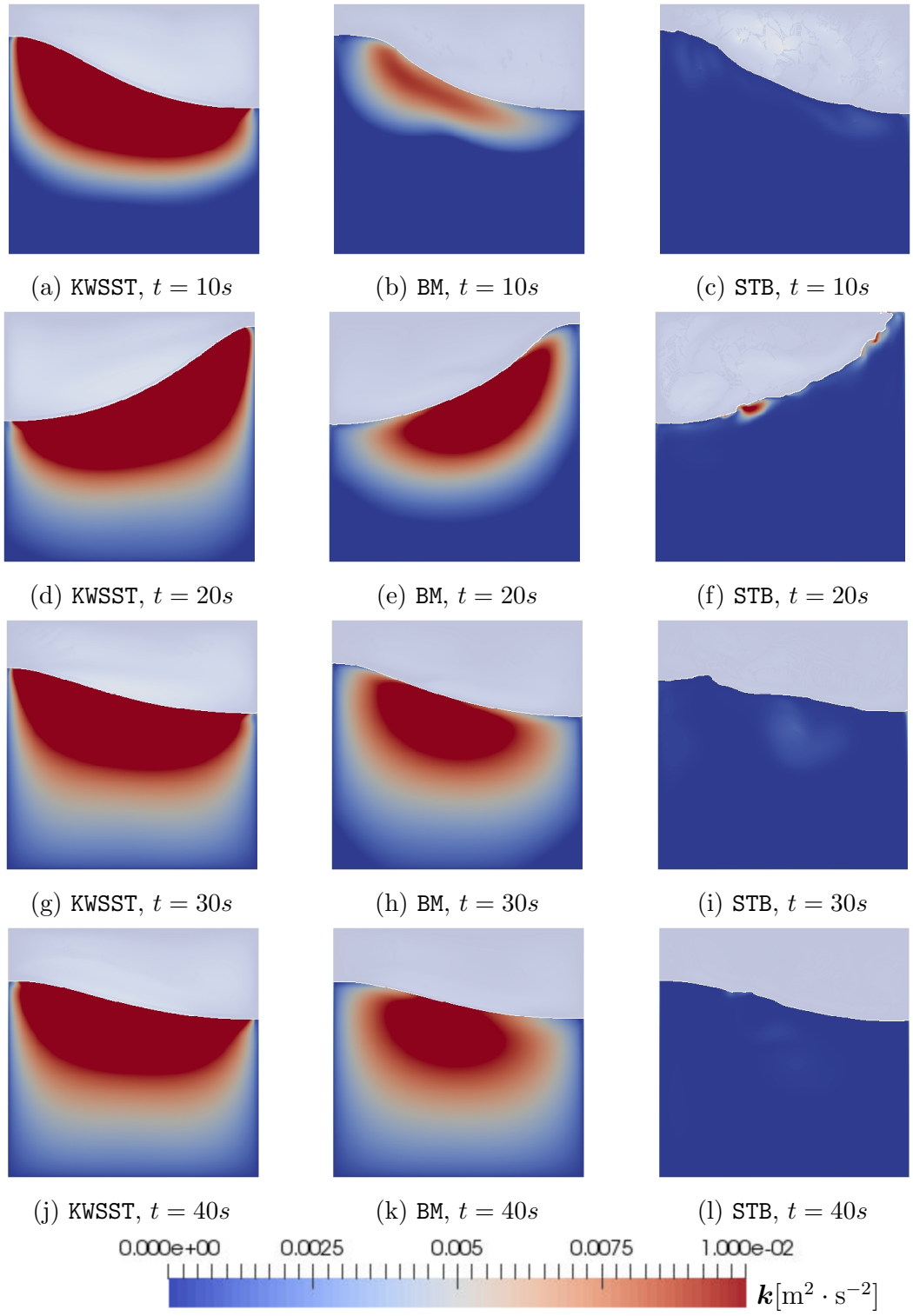

(a) KWSST, $t = 10s$ (b) BM, $t = 10s$ (c) STB, $t = 10s$

(d) KWSST, $t = 20s$ (e) BM, $t = 20s$ (f) STB, $t = 20s$

(g) KWSST, $t = 30s$ (h) BM, $t = 30s$ (i) STB, $t = 30s$

(j) KWSST, $t = 40s$ (k) BM, $t = 40s$ (l) STB, $t = 40s$

Figure 5.25: Turbulent kinetic energy contours at time $t = 10, 20, 30, 40$s, $\boldsymbol{\omega^* = 1}$, $\boldsymbol{A^* = 0.01}$

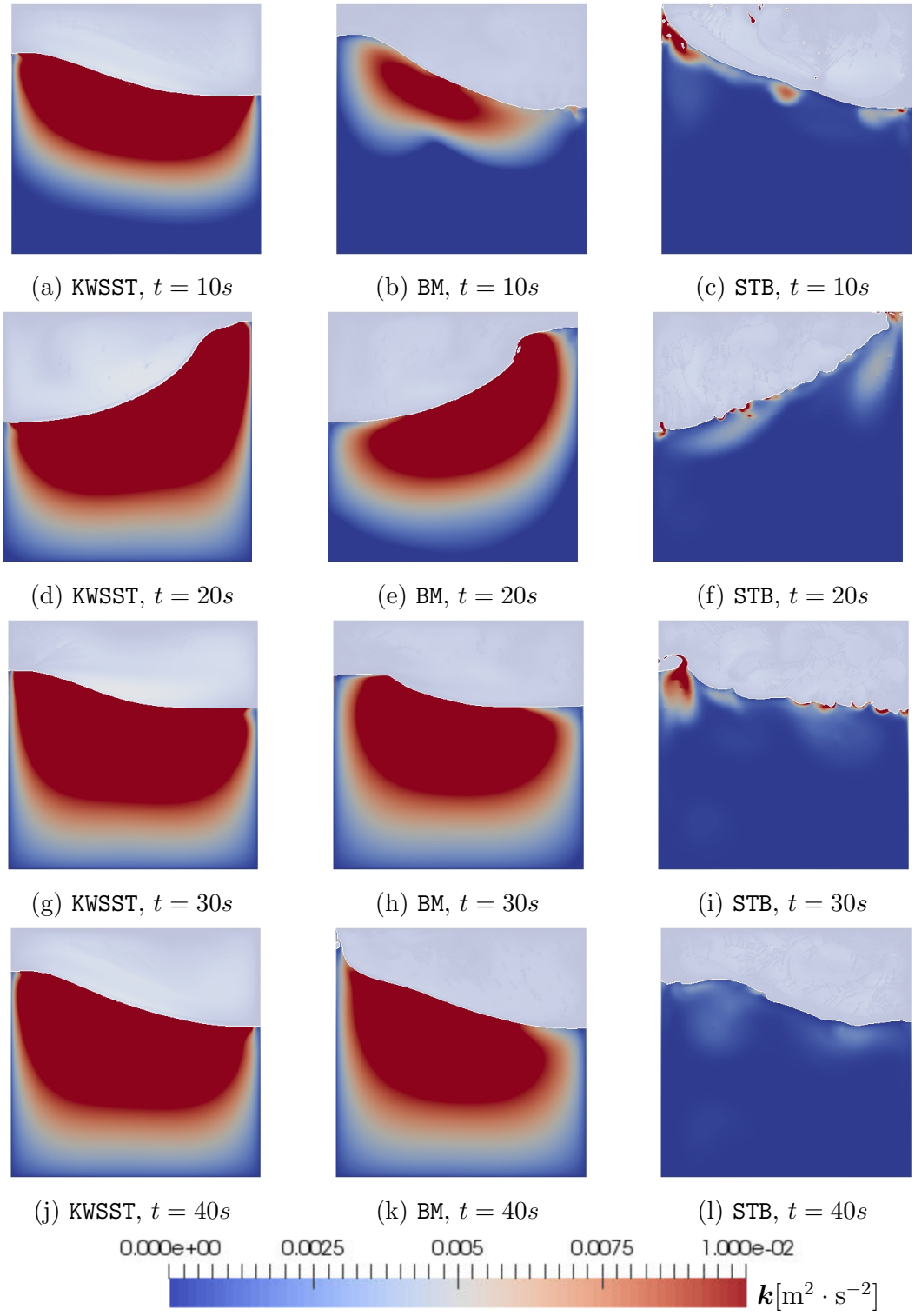

(a) KWSST, $t = 10s$ (b) BM, $t = 10s$ (c) STB, $t = 10s$

(d) KWSST, $t = 20s$ (e) BM, $t = 20s$ (f) STB, $t = 20s$

(g) KWSST, $t = 30s$ (h) BM, $t = 30s$ (i) STB, $t = 30s$

(j) KWSST, $t = 40s$ (k) BM, $t = 40s$ (l) STB, $t = 40s$

Figure 5.26: Turbulent kinetic energy contours at time $t = 10, 20, 30, 40$s, $\boldsymbol{\omega^* = 1}$, $\boldsymbol{A^* = 0.02}$

Eddy viscosity in the water

Boussinesq-type turbulence models are often quite elaborate in their formulation, with transport equations completed by an array of closure constants. Ultimately though, their success is dependent on the output of one parameter — eddy viscosity. As a reminder, we will re-state the formulation of eddy viscosity calculation for each model. The `BM` and `KWSST` models differ in the formulation of the k equation, but calculate ν_T in the same way fashion:

$$\nu_T = \frac{a_1 k}{\max(a_1\omega, F_2\sqrt{p_0})}, \tag{5.8}$$

where F_2 is a blending function, $a_1 = 0.31$ is a closure constant and $p_0 = 2S_{ij}S_{ij}$. The `STB` model utilises the exact same k and ω-equations as the `BM` model, but includes an extra 'stress-limiting' term in the denominator of the ν_T calculation so as to limit the eddy viscosity in regions of near-potential flow:

$$\nu_T = \frac{a_1 k}{\max\left(a_1\omega, F_2\sqrt{p_0}, \boxed{a_1\lambda_2\frac{\beta}{\beta^*\alpha}\frac{p_0}{p_\Omega}}\omega\right)}, \tag{5.9}$$

where $p_\Omega = 2\Omega_{ij}\Omega_{ij}$, β, β^* and α are model closure constants and λ_2 is a tunable constant taken to be 0.05 here. Larsen and Fuhrman (2018) demonstrate that so long as $\frac{p_\Omega}{p_0} \leq \lambda_2$, the model is formally stable, and thus erroneous over-production of turbulence is prevented.

The `BM` and `STB` models were both developed in response to observed over-production of turbulence in free surface flows. This problem has been found to be detrimental in predicting flow scenarios with wave propagation due to the resultant overly-dissipative flow field causing unnatural damping. Implicitly, we have already seen the evidence of extra damping in **Fig.** 5.15 as the `KWSST` model, followed

closely by the BM model, consistently and systematically predicted a reduced sloshing response to tank motions over a range of amplitudes relative to the STB formulation.

Our overall aim is to accurately predict thermal mixing in the subsurface of sloshing flows. It is the eddy viscosity that we use to directly calculate the turbulent thermal diffusivity via the gradient diffusion hypothesis:

$$-\rho\overline{u_i'T'} = \kappa_{\text{turb}}\left(\frac{\partial\bar{T}}{\partial x_i}\right) = \frac{\rho\nu_t}{Pr_t}\left(\frac{\partial\bar{T}}{\partial x_i}\right), \tag{5.10}$$

The heat flux across fluid layers due to turbulent eddy transport is modelled, and so needs to be underpinned be a reliable means of predicting local eddy diffusivity. Without that, thermal mixing in the subsurface cannot be predicted with any confidence.

Fig. 5.27 shows the time-averaged dimensionless eddy viscosity (or eddy viscosity ratio), $\nu_T^* = \nu_T/\nu$ in the water, plotted as a function of scaled tank depth for each of the 3 model formulations across a range of forcing amplitudes.

Once again, we have large qualitative and quantitative differences between the respective results of each model formulation. The BM and KWSST models predict significantly higher values for eddy viscoisty through the liquid depth. The depth-dependent profiles follow the same pattern as the k plots, with a smooth and diffuse increase from the tank base to the free surface - almost constant through the depth. In the case of $A^* = 0.002$ the eddy viscosity predicted by BM and KWSST is of an order of magnitude 4 times greater than that of STB. This represents a complete contrast in their characterisation of the flow field — from largely laminar to significantly turbulent.

This trend continues as the forcing amplitude is increased, although the magnitude of disparity close to the surface does reduce slightly. Not only that, we can again see that for the STB model, the high turbulence is restricted to the upper

regions of the flow — near the surface — and in the boundary layer at the very bottom of the tank.

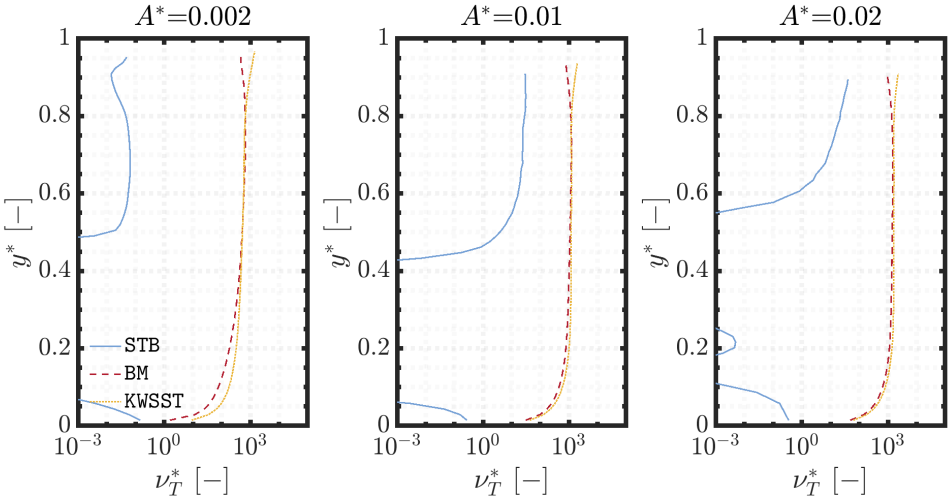

Figure 5.27: Time-averaged eddy viscosity ratio in the water, $\bar{\nu}_T^*$ vs distance from tank bottom, y^*, for turbulence models `STB`, `BM` & `KWSST`, with varying forcing amplitude, A

Fig. 5.27 shows only the data taken from samples along a line. Time-averaged, localised data can become distorted by local transient flow structures that may interact with the centre-line for some duration of the sampled run-time. Therefore, the full-field view of the eddy viscosity contours have been included in **Figs.** 5.28 & 5.29, taken at times $t = 10, 20, 30, 40s$. Again, we see the diffuse turbulent structures that grow to occupy most of the domain when deploying the `BM` and `KWSST` models. The `KWSST` eddy viscosity ratio contours also reveal one of the aspects that is fundamentally incorrect when using an incompressible turbulence model for stratified flows. The region of high eddy viscosity develops to form one large, continuous flow structure across both liquid and gas phases. In reality, this is non-physical, and goes against the fundamental nature of how turbulence interacts with the free surface in stratified flows (as discussed in **Chapter** 4). In **Fig.** 5.28, the `STB` model predicts no eddy viscosity of great enough magnitude so as to get picked up within range of the contour map, indicating primarily laminar flow.

For the $A^* = 0.002$ case in particular, we can see that despite large differ-

ences in turbulence levels, the motion of the free surface is almost identical. Minor differences develop at $A^* = 0.02$ — the bulk behaviour remains similar but small flow features at the surface begin to materialise when using the `STB` model. It is clear now that this fact is directly linked to lower effective viscosity in the liquid not damping out small scale flow structures. Again, recalling **Fig.** 5.15, the correlation is clear between subsurface turbulence and wave damping.

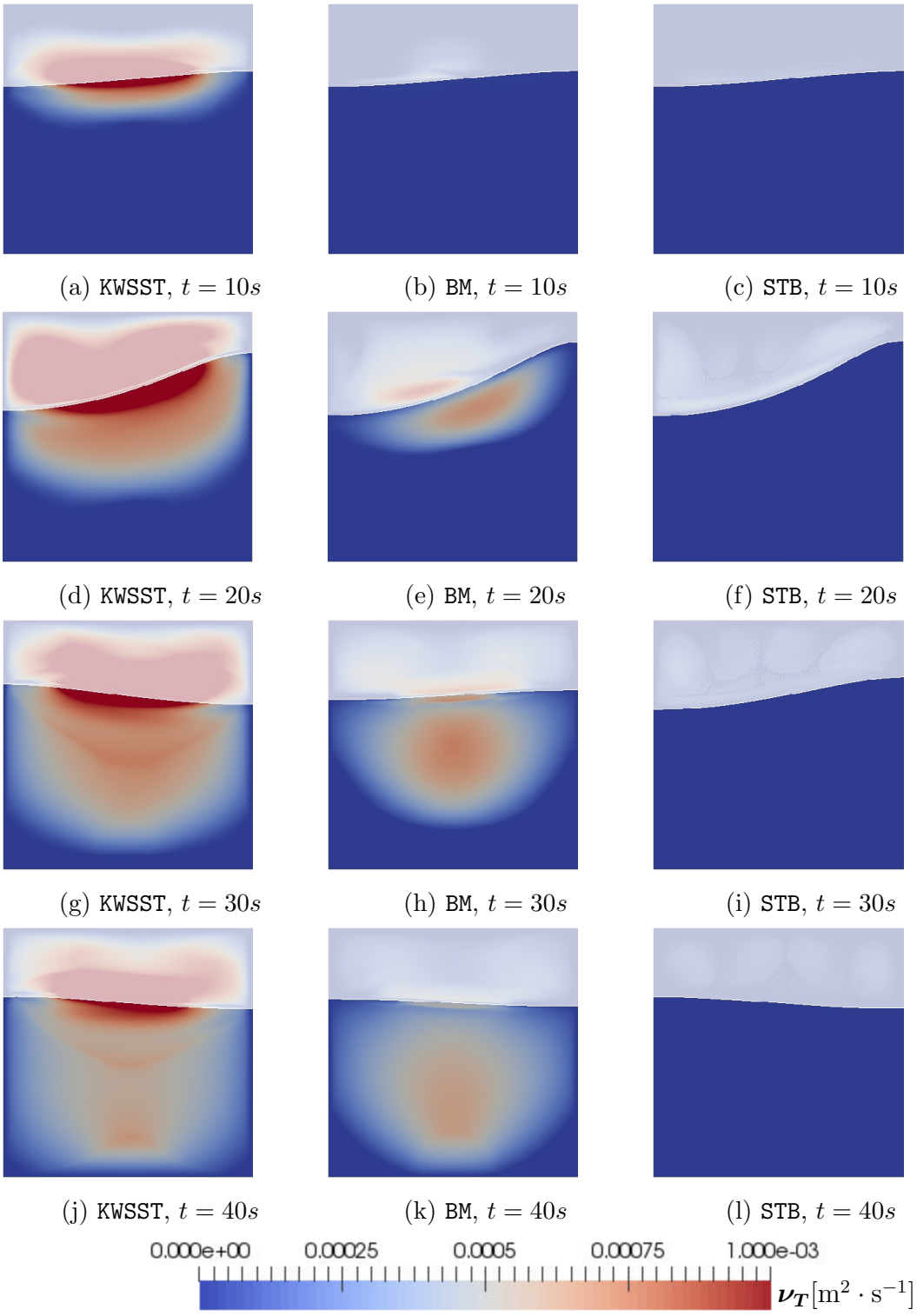

(a) KWSST, $t = 10s$ (b) BM, $t = 10s$ (c) STB, $t = 10s$

(d) KWSST, $t = 20s$ (e) BM, $t = 20s$ (f) STB, $t = 20s$

(g) KWSST, $t = 30s$ (h) BM, $t = 30s$ (i) STB, $t = 30s$

(j) KWSST, $t = 40s$ (k) BM, $t = 40s$ (l) STB, $t = 40s$

Figure 5.28: Kinematic eddy viscosity contours at time $t = 10, 20, 30, 40$s, $\boldsymbol{\omega^* = 1}$, $\boldsymbol{A^* = 0.002}$

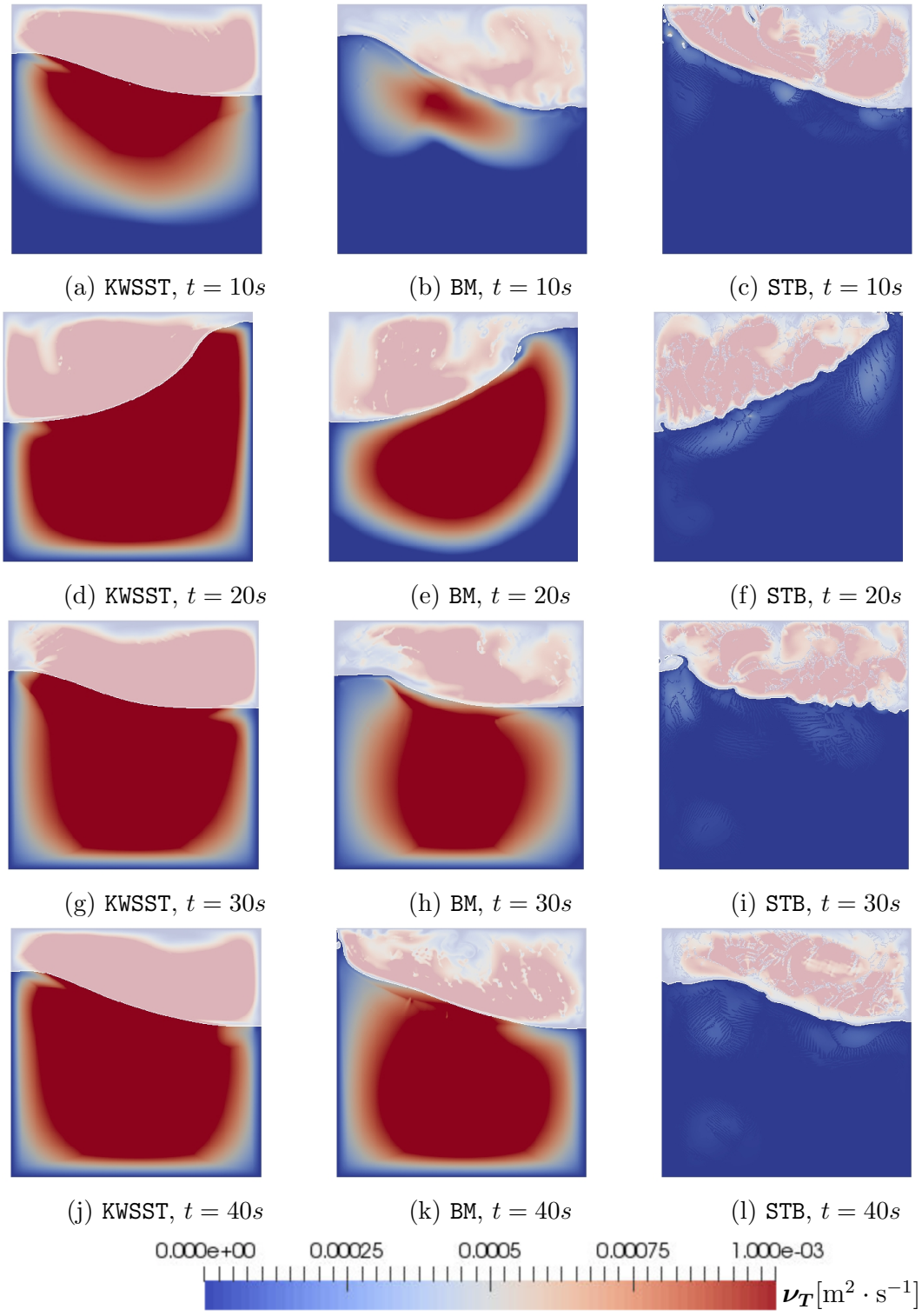

(a) KWSST, $t = 10s$ (b) BM, $t = 10s$ (c) STB, $t = 10s$

(d) KWSST, $t = 20s$ (e) BM, $t = 20s$ (f) STB, $t = 20s$

(g) KWSST, $t = 30s$ (h) BM, $t = 30s$ (i) STB, $t = 30s$

(j) KWSST, $t = 40s$ (k) BM, $t = 40s$ (l) STB, $t = 40s$

Figure 5.29: Kinematic eddy viscosity contours at time $t = 10, 20, 30, 40$s, $\boldsymbol{\omega^* = 1}$, $\boldsymbol{A^* = 0.02}$.

Fig. 5.30 shows the spatially averaged eddy viscosity ratio in the water, plotted as a function of time. Plotting with a log-scale on the vertical axis allows us to see clearly the numerous orders of magnitude with which the predicted eddy viscosity can differ, depending on the model. Both `KWSST` and `BM` predict very similar final results, and we can see that the ultimate state of turbulence within the subsurface is not as dependent on the forcing amplitude. They only really differ in the early stages of the simulation, when the inital growth of ν_T is somewhat faster for the `KWSST` model.

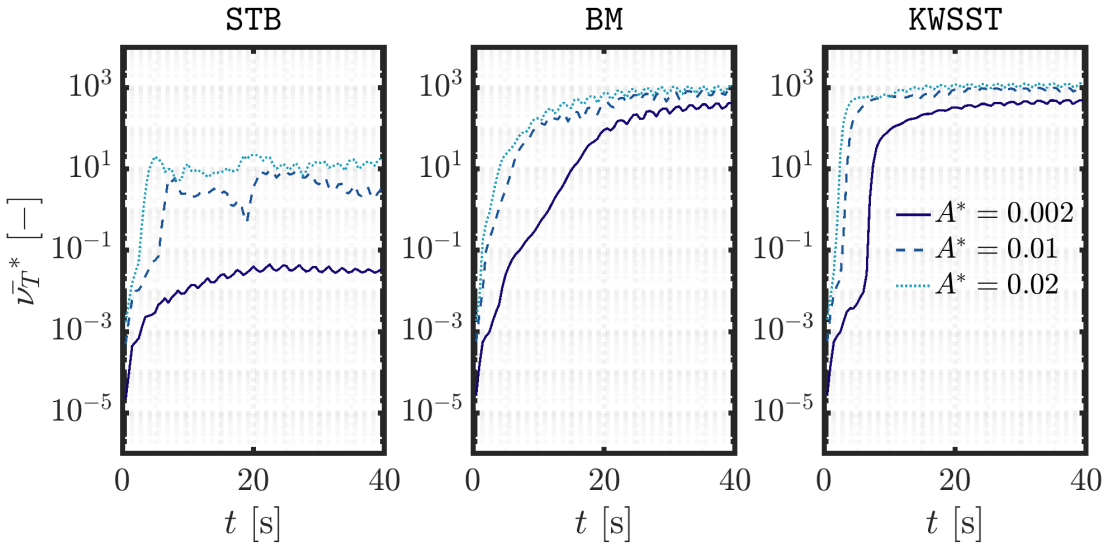

Figure 5.30: Spatially averaged eddy viscosity ratio in the water, $\bar{\nu_T^*}$ vs time, t, for turbulence models `STB`, `BM` & `KWSST`, with varying forcing amplitude, A^*.

How does this compare with results generated in `Fluent`?

To check that these observations likely apply to commercial codes, the `OpenFOAM` predictions of eddy viscosity in the subsurface are compared to some results generated in `Fluent`. The `Fluent` simulation is set-up using the $k-\omega$ SST model, utilising the fully compressible formulation as standard. No buoyancy source term, interface damping or stress limiting features are included, and so we now have a 4th variation of the $k-\omega$ SST model with which to compare results. The CICSAM (Ubbink and Issa, 1999; Wacławczyk and Koronowicz, 2008), scheme is used to discretise the advection term in the volume fraction equation. The `Fluent` results match up very

closely to the BM model results generated in OpenFOAM. This suggests that if indeed the unstable nature of two-equation models is detrimental to predicting subsurface turbulence in sloshing flows at resonance, then this is likely a widespread issue.

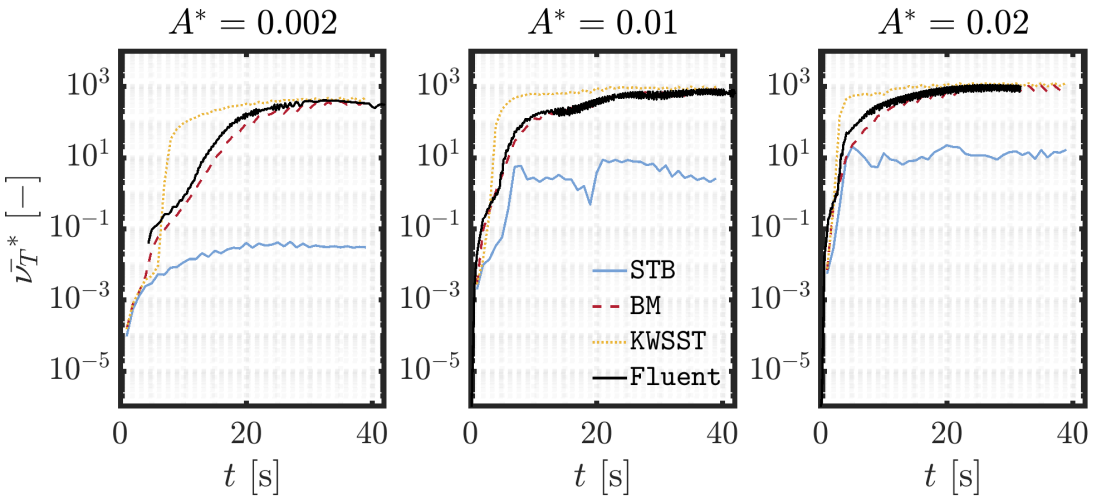

Figure 5.31: Spatially averaged eddy viscosity in the water, $\bar{\nu}_T^*$ vs time, t, for turbulence models STB, BM & KWSST, with varying forcing amplitude, A^*.

Eddy viscosity in the air

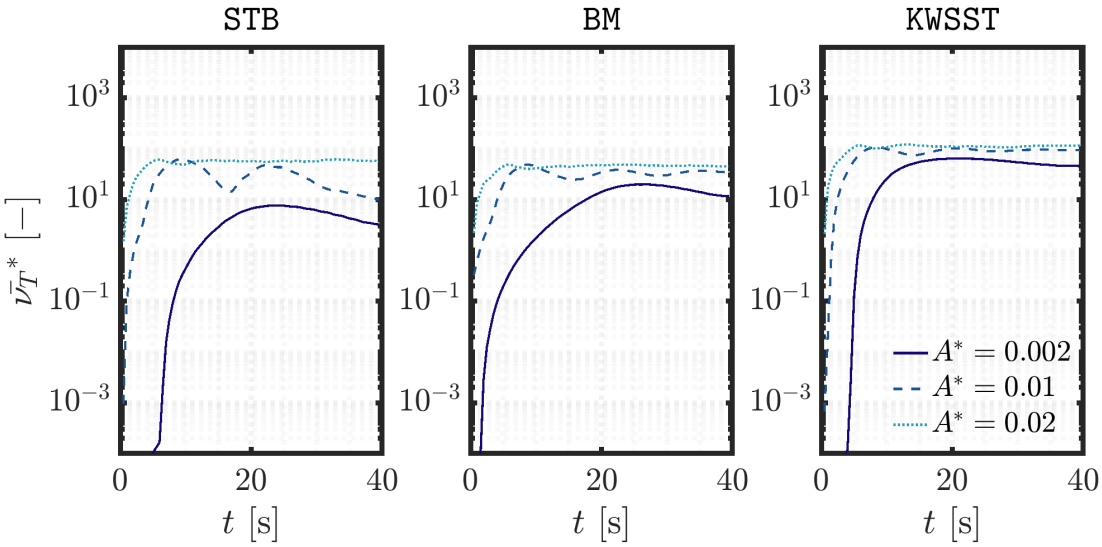

Figure 5.32: Spatially averaged eddy viscosity in the **air**, $\bar{\nu}_T^*$ vs time, t, for turbulence models STB, BM & KWSST, with varying forcing amplitude, A^*.

For completion we will now look at the effects of turbulence model formulation on the prediction of eddy viscosity in the air. **Fig.** 5.32 shows that unlike in the water,

we see very similar growth profiles across the board. The stress-limiting feature of the STB model is designed to become active only in regions where the flow is very weakly rotational (near potential flow), such as is the orbital motion beneath water waves. Contrary to the analysis of the subsurface, that we now have great similarities in prediction of turbulence in the air is not a surprise. In fact, this indicates that the stress-limiting term, which serves to mitigate erroneous, exponential growth in turbulence, is becoming active only in the scenarios and flow regions for which it was intended — not in flow situations of high turbulence and vorticity.

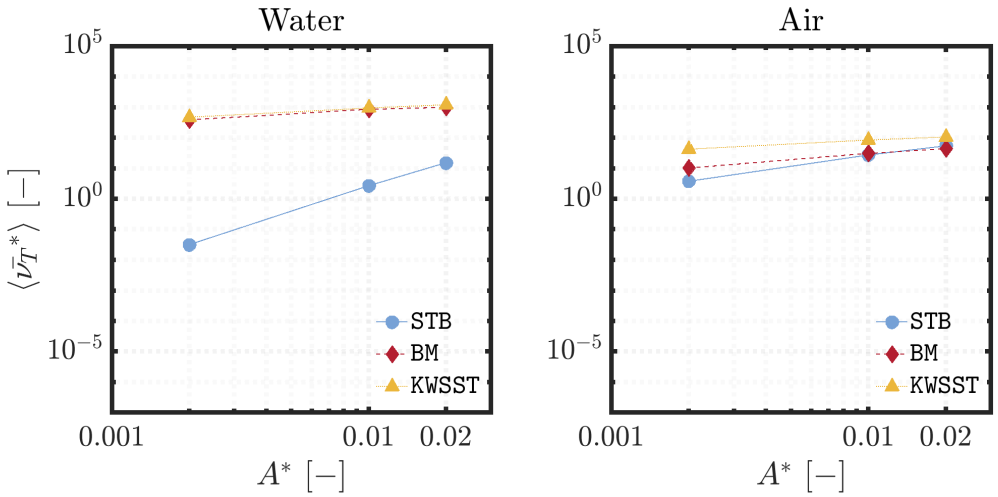

Figure 5.33: Spatially and temporally averaged eddy viscosity in the **water** (left) and **air** (right), $\bar{\nu}_T^*$ vs time, t, for turbulence models STB, BM & KWSST, with varying forcing amplitude, A^*.

Finally **Fig.** 5.33 shows a time-average of the final $5s$ of the spatially-averaged eddy viscosity ratio for each of the simulations as a function of forcing amplitude, for both air and water.

Water turbulence, as predicted by KWSST and BM is not highly dependent on forcing amplitude. Given the corresponding increase in wave response that comes with increased forcing amplitude at resonance, and the added effects of roof impacts, spray formation and wave breaking events (all of which we would expect to be significant 'turbulence generators') that feature in the $A^* = 0.02$ case, this is a surprising result. This observation further supports the notion that these models

produce turbulence in an unstable manner, and not in a way that reflects the true nature of the flow. Deploying the `STB` formulation is much more sensitive to forcing amplitude. Turbulence in the air is much less sensitive to which model formulation is used.

5.5 Interface turbulence damping sensitivity

Wall-like turbulence damping at the interface supplied varying degrees of success in **Chapter** 4, depending on the observable. Augmenting the `STB` and `BM` model formulations by including the damping function at the interface allowed good agreement with the experiments in the air to be realised, with mixed results in the subsurface. Most of the benefits came in improved air flow capturing; the `STB` model in particular yielded good predictions of turbulent quantities in the water without any need for modifications at all. This was found to be true over a range of flow scenarios.

We will now assess the impact of applying Egorov's damping function at the free surface of sloshing flows. The matrix of simulations performed in the following analysis is listed in 5.10. As with **Chapter** 4, each model will be run with 3 values for damping coefficient, $B = 0, 50, 100$, with $B = 0$ representing the absence of damping. These will be performed at two forcing amplitude: $A^* = 0.002, 0.02$.

Damping coefficient, $B =$	0	50	100
`STB`	✓	✓	✓
`BM`	✓	✓	✓
`KWSST`	✓	✓	✓

Table 5.10: Matrix of simulations demonstrating each simulation combination of turbulence model and turbulent damping at the interface.

5.5.1 Free surface response

Figures 5.34 & 5.35 show wave response amplitudes at the wall for each of the model formulations and damping coefficients. For the $A^* = 0.002$ case, increasing the damping coefficient, B has no effect at all on the behaviour of the `STB` model, whereas the wave response amplitude is slightly increased for `BM`. Interestingly, in **Table** 5.11 that increasing the damping coefficient for `BM` causes the predicted η_{RMS} to match that of `STB` exactly.

Increasing the forcing amplitude to $A^* = 0.02$ (**Fig.** 5.35) results in a higher degree of sensitivity to damping coefficient. This is the case for both model formulations. The differences seen in the time-series wave amplitude data are most likely due to the more complex flow caused by roof impacts, and how that is affected by the interfacial damping. However, the bulk response characteristics are maintained and the overall effect is minimal.

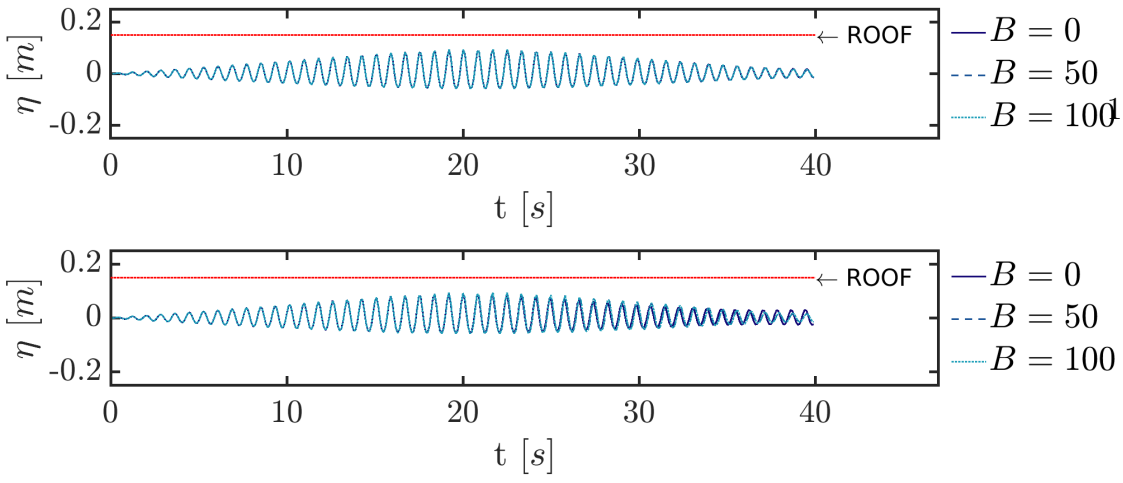

Figure 5.34: Wave amplitude, η, at the wall vs. time, for models `STB` (top) and `BM` (bottom), with varying damping coefficient B. Forcing amplitude, $\boldsymbol{A^* = 0.002}$.

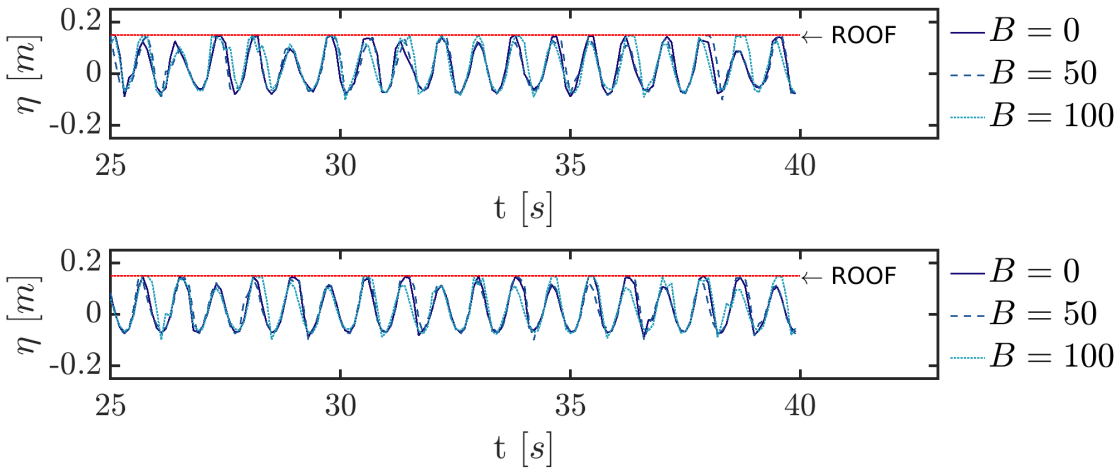

1

Figure 5.35: Wave amplitude, η, at the wall vs time, for models STB (top) and BM (bottom), with varying damping coefficient B. Forcing amplitude, $\boldsymbol{A^* = 0.02}$.

-	$\boldsymbol{A^* = 0.002}$				$\boldsymbol{A^* = 0.02}$			
$\boldsymbol{B =}$	0	50	100	-	0	50	100	-
Model	$\boldsymbol{\eta_{\mathrm{RMS}}[\times 10^{-2} m]}$			**Variation [%]**	$\boldsymbol{\eta_{\mathrm{RMS}}[\times 10^{-2} m]}$			**Variation [%]**
STB	3.67	3.68	3.68	0.17	8.39	8.06	8.26	2.01
BM	3.49	3.68	3.68	3.04	8.00	8.10	8.20	1.24

Table 5.11: RMS amplitude at the wall, η_{RMS} for BM, STB with increasing values of damping coefficient, B. Coefficient of variation is calculated for each model/amplitude combination data set.

5.5.2 Subsurface kinematics

The RMS velocity profiles reveal that for the case $A^* = 0.002$, the STB model produces subsurface motions that are independent of damping coefficient. The BM formulation, with $B = 0$ initially produces a much smoother profile for $U_{y,\mathrm{RMS}}$ through the depth, but adding damping at the interface moves it towards matching the STB predictions. Two distinct regions can now be seen, with a region from $y^* = 0.4 \rightarrow 1$ exhibiting higher energy flow in the vertical direction. The activation of the damping function is resulting in a locally less dissipative flow in which subsurface transient flow structures are allowed to develop more freely.

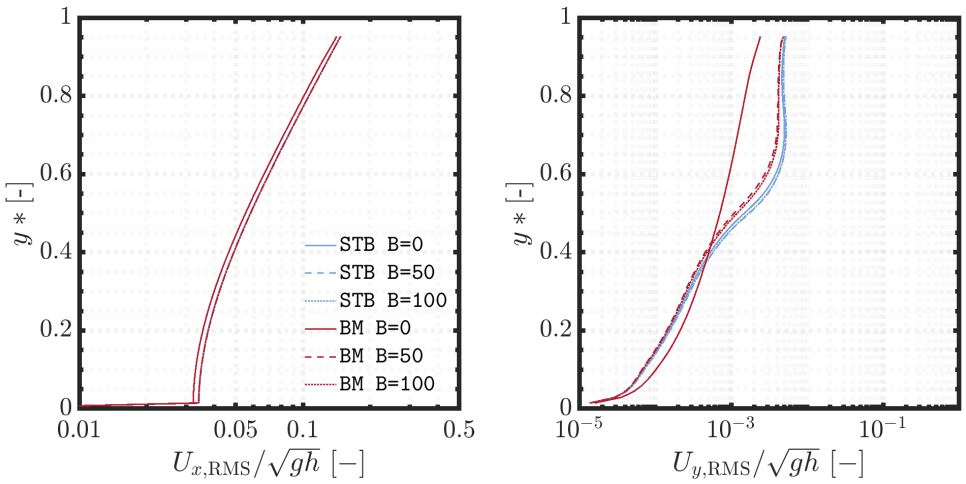

Figure 5.36: $U_{x,RMS}$ (co-axial to the direction of tank motion) and $U_{y,RMS}$ vs non-dimensional distance from the tank bottom (scaled to height of free surface), $y^* = y/h_{f.s.}$, $\boldsymbol{A^* = A/L_x = 2 \times 10^{-3}}$.

An ten-fold increase in forcing amplitude to $A^* = 0.02$, which features more complex flow phenomena, shows that the damping function at the surface leads to a slight increase in vertical velocity through the liquid depth. Interestingly, the vertical motions at the base of the tank are increased for the `STB` results by increasing damping coefficient. The reason for this is not clear. Motions in the horizontal are almost completely independent of the model/damping formulation.

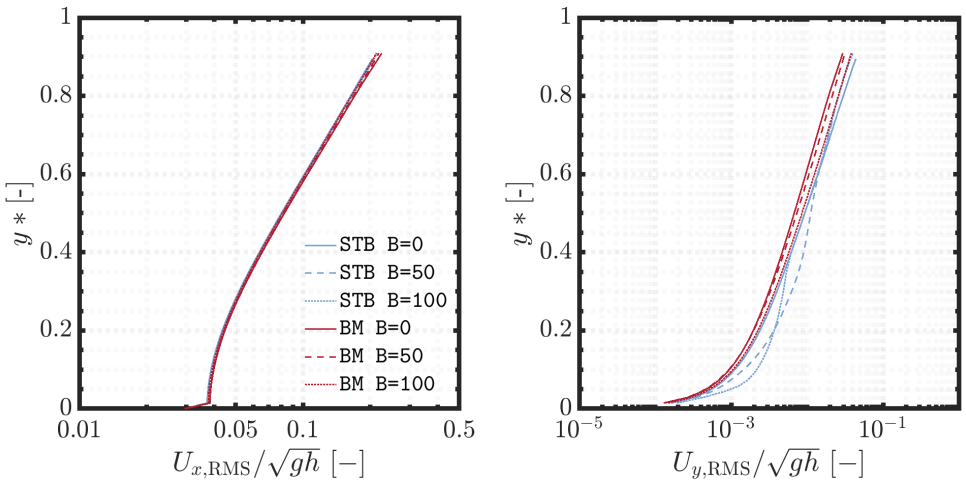

Figure 5.37: $U_{x,RMS}$ (co-axial to the direction of tank motion) and $U_{y,RMS}$ vs non-dimensional distance from the tank bottom (scaled to height of free surface), $y^* = y/h_{f.s.}$, $\boldsymbol{A^* = A/L_x = 2 \times 10^{-2}}$.

5.5.3 Turbulence in the subsurface (and in the air)

Eddy viscosity in the water

Fig. 5.38 shows the growth of the mean eddy viscosity within the subsurface region for each of the simulations for forcing amplitude $A^* = 0.002$. Increasing the damping coefficient has absolutely no effect when applied in conjunction with the `STB` model. For the `BM` formulation, the evolution of the turbulent flow field is changed considerably. After $t \approx 5s$, the time-series data diverges for the damped and undamped cases. The $B = 50$ and $B = 100$ cases yield the exact same behaviour — turbulence increasing more slowly and converging on a quasi-steady state at a level more than an order of magnitude lower than the case without damping.

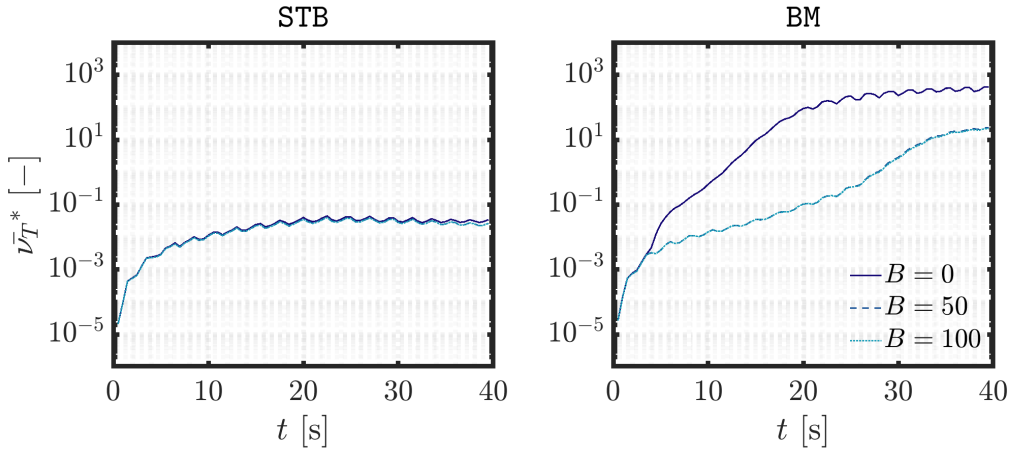

Figure 5.38: Spatially averaged eddy viscosity ratio in the **water**, $\bar{\nu_T^*}$ vs time, t, for turbulence models `BM` & `STB`, with varying damping coefficient, B. $\boldsymbol{A^* = 0.002}$.

Again, as the $A^* = 0.02$ flow is more complex, so too are the results and dependencies. This time there is some difference in the `STB` results, occurring at $t = 5s$, in the immediate aftermath of the first roof impact. For the undamped case, this a major point at which eddy viscosity jumps to a higher level which is maintained for the remainder of the simulation. Ultimately, the same levels of eddy viscosity are achieved (and sometimes surpassed) even with damping.

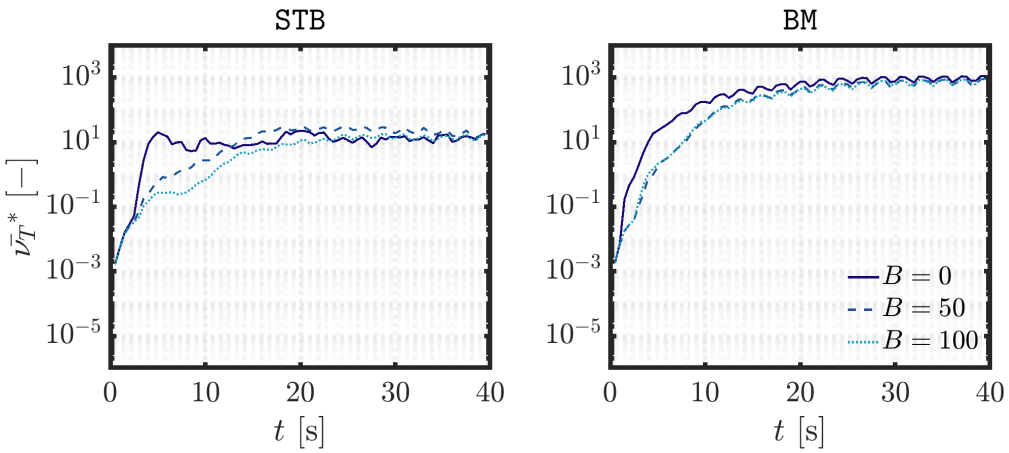

Figure 5.39: Spatially averaged eddy viscosity ratio in the **water**, $\bar{\nu}_T^*$ vs time, t, for turbulence models `BM` & `STB`, with varying damping coefficient, B. $\boldsymbol{A^* = 0.02}$.

Undesirable side-effects of deploying the Egorov's damping function in sloshing flows

The clear effects of the damping function being an active participant in events involving wave breaking illuminate what is perhaps problematic when applying it in the modelling of sloshing flows. The damping function becomes active as waves break and the free surface becomes disrupted — a larger percentage of the domain now occupied by regions of local volume fraction, $0 < \alpha < 1$. For moments of wave-breaking, this is exactly not what would be intended, when in fact this very phenomena should be a major source of turbulence *generation*. The damping function is intended to impose wall-like turbulence dissipation at the interface, not get mixed up with the complex flow structures involved in wave-breaking.

Fig. 5.40 shows the eddy viscosity contours of the `BM` model simulations at times $t = 5, 10, 15$s (top to bottom) and with damping coefficients $B = 0 \rightarrow 100$ (left to right.) The first thing to notice is how the eddy viscosity levels are slower to develop in the subsurface with increased damping. Eddy viscosity is clearly also much lower in the air. Looking more closely however, we can see more problematic side-effects of the damping function in the post wave-breaking environment. **Fig.** 5.41 shows magnified areas of **Figures** 5.40f & 5.40i, revealing small 'dead-zones' in

which turbulence is being artificially suppressed. Viewing videos of the flow confirms that these emerge as a legacy of small bubbles penetrating the flow in the aftermath of wave-breaking. This triggers the damping function, which in turns creates these lingering regions in which turbulence is being destroyed in a non-physical manner.

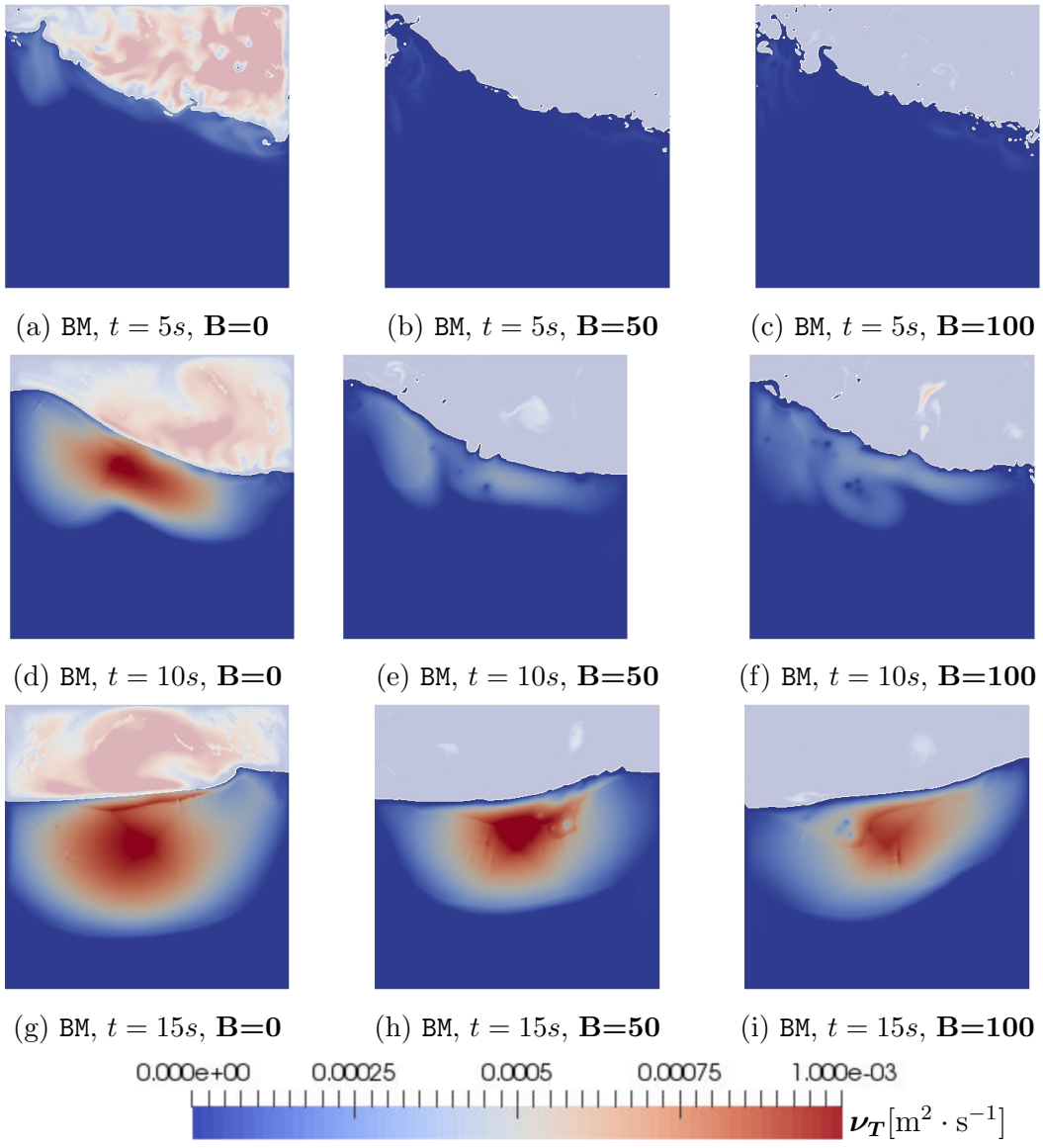

(a) BM, $t = 5s$, **B=0** (b) BM, $t = 5s$, **B=50** (c) BM, $t = 5s$, **B=100**

(d) BM, $t = 10s$, **B=0** (e) BM, $t = 10s$, **B=50** (f) BM, $t = 10s$, **B=100**

(g) BM, $t = 15s$, **B=0** (h) BM, $t = 15s$, **B=50** (i) BM, $t = 15s$, **B=100**

Figure 5.40: Kinematic eddy viscosity contours at time $t = 10, 20, 30, 40$. $\boldsymbol{\omega^* = 1}$, $\boldsymbol{A^* = 0.002}$.

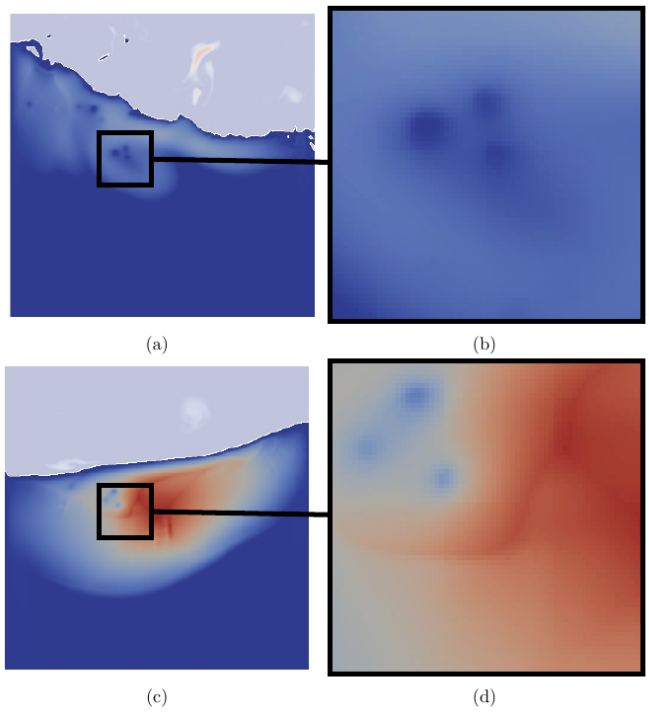

Figure 5.41: Low-turbulence regions, a legacy of interface damping becoming active during wave-breaking at times $t = 5, 10s$ as seen previously in **Fig.** 5.40.

Eddy viscosity in the air

The damping function has a considerable effect on the turbulence in the air for both models. **Fig.** 5.42 shows that for each model-amplitude combination, the mean eddy viscosity in the air is reduced by orders of magnitude throughout the run-time. Again, it is unclear how physically realistic the effect of turbulence damping is in the air — especially when its activation is triggered by the formation of spray and droplets following wall impacts.

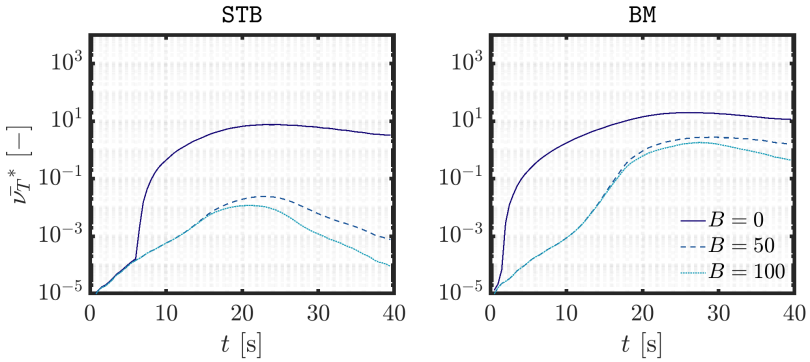

(a) $\boldsymbol{A^* = 0.002}$

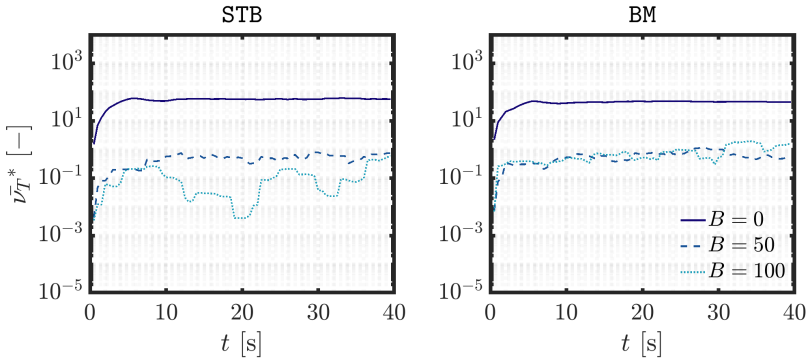

(b) $\boldsymbol{A^* = 0.02}$

Figure 5.42: Spatially averaged eddy viscosity ratio in the **air**, $\bar{\nu}_T^*$ vs time, t, for turbulence models `BM` & `STB`, with varying damping coefficient, B.

Summary of results

Fig. 5.43 includes the time-averaged mean eddy viscosity for each of the models in the air and water as a function of damping coefficient over the last $5s$ of the simulation ($t = 35 \rightarrow 40s$). Turbulence is reduced in the water for the `BM` $A^* = 0.002$

simulations by introducing turbulence damping at the interface. For each of other cases, mean eddy viscosity in the subsurface is not affected with any significance. Prediction of turbulence in the air is more sensitive to damping coefficient. This corresponds to similar findings in **Chapter** 4.

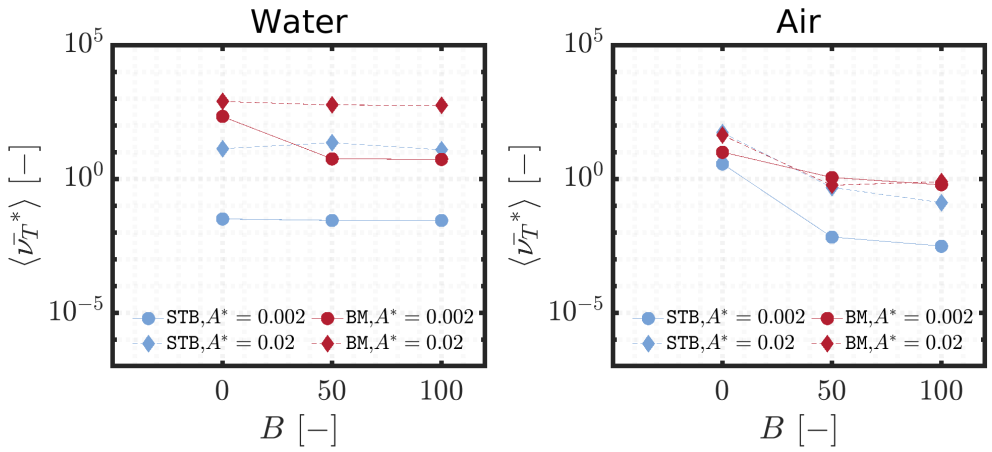

Figure 5.43: Spatially averaged eddy viscosity in the **air**, $\bar{\nu}_T^*$ vs time, t, for turbulence models `BM` & `STB`, with varying damping coefficient, B. $\boldsymbol{A^* = 0.02}$.

5.6 Conclusions

What do these results tell us about the `KWSST` formulation?

The issues when using the incompressible formulation of the $k-\omega$ SST to model stratified flows have been highlighted in the literature, and further confirmed in **Chapter** 4 when comparing it's performance to the experiments.

It has been useful to include this model in this chapter to demonstrate that despite its inefficiencies in accurately predicting turbulence in the subsurface, examining other parameters such as wave response aren't so erroneous as to become instantly suspicious when examining sloshing flows. The dissipative nature of the model that results in wave damping might be clear to see for flow scenarios in which waves are propagated over long distances (with noticeable non-physical decay). In other scenarios, this might go totally unnoticed. In sloshing flows, this dissipation

is not enough to cause a greatly diminished response - particularly at resonance and when the kinetic energy of the system is continually replenished by tank motion.

Despite this, if the user is aiming to deploy a VOF model to simulate a process involving subsurface mixing of scalars, particularly beneath free surfaces that are dynamic, the results can be affected enormously. Again, relating eddy viscosity to turbulent thermal diffusivity as:

$$\kappa_{\text{turb}} = \frac{\rho_0 \nu_t}{Pr_t}, \tag{5.11}$$

where Pr_t is the turbulent Prandtl number, and taking the example case of sloshing at $A^* = 0.002$. The average turbulent thermal diffusivity throughout the subsurface would be $\approx 10,000$ times greater when deploying the `KWSST` and `BM` models compared to the `STB` formulation.

And what of the compressible, buoyancy-modified `BM` model?

The buoyancy-modified model `BM`, which is formulated to be fully compressible has been found to perform very similarly to the `KWSST` model in predicting sloshing-induced turbulence. There are certainly some differences — the buoyancy source term in the k-equation does it's job. Turbulence is prevented from being diffused across the interface in a non-physical manner. However, suppressing turbulence at the interface itself does not prevent the exponential growth of eddy viscosity in the subsurface overall. Comparison with the fully compressible `Fluent` model confirms this. In **Chapter** 4, we saw that without interface damping, `BM` over-predicted eddy viscosity beneath the subsurface. Figures 5.28 & 5.29 clearly show the way in which the excessive turbulence generated just below the interface diffuses itself throughout the liquid depth. This continues up to the point that turbulence away from the free surface — in far less energetic regions of the flow — are just as (and sometimes

more) turbulent than in the near-surface region.

Overall assessment of models

For the cases in this chapter, which correspond to 'finite-depth' sloshing at resonance, it was found that the prediction of bulk free surface response is only weakly sensitive to the turbulence model formulation used. For the models without an added stabilising feature, a greatly increased eddy viscosity in the water resulted in a smoother surface profile. The `STB` model allowed more small flow features to develop at the interface, particularly at higher forcing amplitudes, with more transient behaviour and non-linearities picked up by the Fourier analysis as a result.

The biggest takeaway is how sensitive the generation of subsurface turbulence is to the model formulation. Despite only small changes in wave response amplitude, eddy viscosity levels were found to vary by up to 4 orders of magnitude. The stabilised model `STB` was found to be much more robust and accurate in matching the experimental measurements of eddy viscosity in the water over a range of flow configurations as reported by Fabre et al. (1987). Furthermore, Larsen and Fuhrman (2018) and Larsen et al. (2020) were able to demonstrate much improved results in matching experimental turbulence measurements of spilling and plunging waves. The differences were found to be even more profound when applying the model to sloshing flows.

Damping at the interface causes a large reduction of turbulence in the air. In **Chapter** 4, we found that interface damping allowed for stronger agreement with the experimental data, and so this reduction in eddy viscosity may be a fair reflection of the physics. However, we have also highlighted that interface damping is inappropriate for flows in which turbulence generation is strongly influenced by wave-breaking. In these instances, the way in which the damping function is applied means that turbulence is in fact suppressed during wave-breaking processes. When

used in conjunction with the STB model, interface damping was found to have no influence on subsurface turbulence.

Therefore, the STB model (without damping) can be viewed as being far more reliable for modelling sloshing over a range of conditions. This model will be used throughout the following work in this thesis.

A note on the need for further experimental measurements

The work in this chapter highlights the sensitivities when it comes to predicting turbulence in sloshing flows. To make judgements of best practice we have needed to rely on experimental data of similar flow scenarios, mathematical arguments, comparisons to high fidelity simulations and intuitive reasoning. Unfortunately, turbulence measurements for unsteady free surface flows are rare. The fact that so many recent publications have relied on benchmark data sets published in the 80's (Fabre et al., 1987) and 90's (Ting and Kirby, 1994) highlight the rarity at which good quality data is produced. The reason for this is no doubt the difficulty in acquiring reliable and repeatable data in the subsurface of flows that are globally unsteady.

In **Chapter** 3, the numerical model was validated in predicting the global free surface response over a range of scenarios with experimental sloshing data. To make a more robust case for a turbulence modelling strategy, we would hope to do the same. It is highly recommended that future work within the field of sloshing is focussed on producing quality data for calibrating turbulence models.

Chapter 6

Development of incompressible OpenFOAM solver for multiphase flows with heat transport

6.1 Introduction

In the next phase of the thesis, thermal mixing in liquids beneath the free surface will be investigated. From conversations with the fuel system team at BAE Systems, warm fuel typically recirculates back into tanks at around $+10°C$ above the mean temperature of the fuel within. Thus, due to the relatively low temperature variations and low liquid compressiblity, the Boussinesq approximation will be used. As this is not a native feature included in `interFoam` (a fully compressible `compressibleInterFoam` is available), the model will need to be extended. The Boussinesq approximation is often used for modeling flows involving natural convection, in which small temperature perturbations can lead to the development of buoyancy-driven flow patterns. Density is assumed constant except for in gravity terms, where which density is approximated as a linear function of temperature

change relative to some reference temperature:

$$(\rho_v - \rho_0)g = -\rho_0 g\beta[T - T_0], \tag{6.1}$$

where ρ_0 is the nominal reference density, ρ_v is the temperature-dependent density, T_0 is the reference temperature and β is the thermal expansion coefficient.

Limits of the Boussinesq approximation

In reality, the density of water (at constant pressure) varies as a non-linear function of temperature, but weakly enough such that this can be neglected for small temperature perturbations. Further errors are introduced by assuming constant density in the non-gravitational terms in the momentum equation. These grow proportionally to an increase in temperature difference:

$$\frac{\rho_v - \rho_0}{\rho_0} \approx \beta(T - T_0) \tag{6.2}$$

We can use the approximation with minimal errors provided that $\beta(T - T_0) \ll 1$. **Fig.** 6.1 shows the thermal expansion ratio of water and air plotted as a percentage vs. temperature variation about the reference temperature, $T - T_0$. For water, based on a coefficient of thermal expansion of $\beta_{\text{water}} = 0.2 \times 10^{-3}$ we can see that for values of up to $T - T_0 \approx 50K$, the thermal expansion is small: $\beta(T - T_0) \lessapprox 1\%$. Air has a thermal expansion coefficient 18.5 times larger, $\beta_{air} = 3.7 \times 10^{-3}$ and so this limit is approached at $T - T_0 \approx 3K$.

To assess whether these limits are appropriate to our requirements we must take into consideration a few things. The dynamic coupling between water and air is weak, owing to the large density ratio. This is particularly true when the interface length scales are large such as with sloshing flows. Therefore, any undue error in the

modelling of buoyancy-induced motions in the air will have little effect on the liquid motion. Furthermore, the focus on this research is concerned primarily with thermal mixing internal to the liquid component of sloshing flows. Assuming the liquid is water, we have already demonstrated that errors within the subsurface are tolerable provided the temperature variations remain low. Kerosene type jet fuels have a higher thermal expansion coefficient than water, at $\beta_{kerosene} = 0.99 \times 10^{-3}$, which is more restrictive in terms of using the Boussinesq approximation, with a limit of $\Delta T \approx 10K$. However, the thermal expansion coefficient of kerosene is constant over a wide range of temperatures, which makes a linear approximation more valid. In the chapter concerning thermal mixing that follows, the maximum temperature varation in the water relative to T_0 is limited to $T - T_0 \leq 8K$.

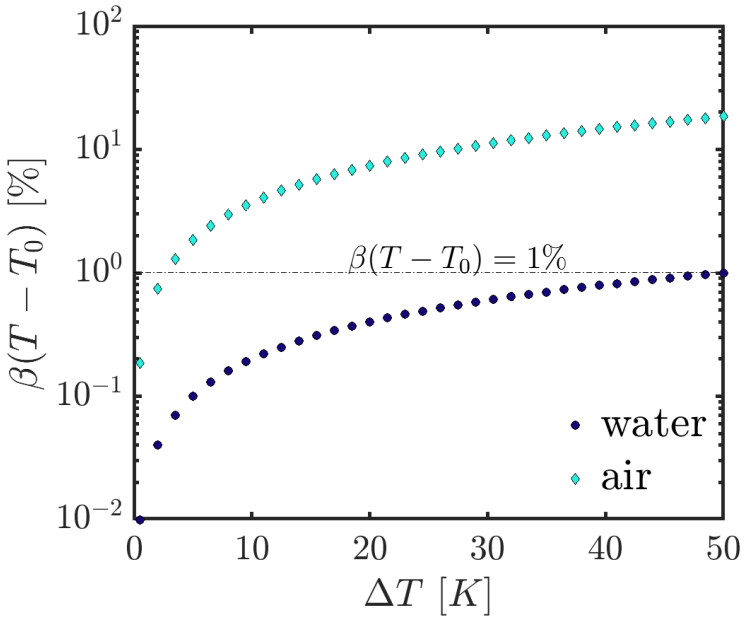

Figure 6.1: Thermal expansion, $\beta(T - T_0) = (\rho - \rho_0)/\rho_0$, as a percentage, vs temperature change ΔT. The dot-dashed line represents $\beta(T - T_0) \approx 1\%$

Heat transport across the free surface will not greatly affect the thermal mixing rates in the liquid. Assuming a closed system, with adiabatic walls, heat transfer between the liquid and gas phase will occur at the interface only:

$$\dot{Q}_{\text{air}} = -\dot{Q}_{\text{water}}, \tag{6.3}$$

where $\dot{Q}_i$ is the rate of change of internal heat energy per i^{th} fluid phase, which is calculated as:

$$\dot{Q}_i = m_i c_{p,i} \dot{\Delta} \bar{T}_i, \tag{6.4}$$

where m_i is the total mass of each phase, $c_{p,i}$ is the specific heat capacity, and the term $\dot{\Delta}\bar{T}$ is the rate of change of mean temperature for each fluid phase. Assuming that at some time $t \to \infty$, regardless of the initial condition of the system, the temperature field will evolve towards some well mixed homogeneous thermal state such that $\bar{T}_{f,\text{water}} = \bar{T}_{f,\text{air}}$, the total change in mean temperature for each phase will be of the ratio:

$$\frac{(\bar{T}_f - \bar{T}_{in})_{\text{air}}}{(\bar{T}_f - \bar{T}_{in})_{\text{water}}} = \frac{m_{water} c_{p,water}}{m_{air} c_{p,air}}. \tag{6.5}$$

Given that $m_i = \rho_i V_i$, $\rho_{water}/\rho_{air} \approx 1000$ and $c_{p,water}/c_{p,air} \approx 4$, then

$$\frac{(\bar{T}_f - \bar{T}_{in})_{\text{air}}}{(\bar{T}_f - \bar{T}_{in})_{\text{water}}} \approx 4000 \frac{V_{\text{water}}}{V_{\text{air}}}. \tag{6.6}$$

where $\bar{T}_{f,i}$ is the mean final temperature of each phase, $\bar{T}_{in}$ is the initial mean temperature, and V_i is the total volume of each phase. That is to say assuming some original unmixed, well ordered state such that at $t = 0$, $\bar{T}_{\text{water}} \neq \bar{T}_{\text{air}}$, and then as $t \to \infty$, $\bar{T}_{\text{water}} = \bar{T}_{\text{air}}$ and assuming that the volume of each phase is of the same order of magnitude, then the total change in mean temperature in the air is several orders of magnitude greater than that of the water.

For modelling fuel tanks with more complex physics e.g. large temperature variations, pressurised air, vapour modeling or phase change and interfacial mass transfer then a fully compressible model would be recommended.

6.2 Mathematical model

To summarise the model, we will restate the equations of `interFoam` along with those that have been added in order to extend the model. For the sake of brevity, only the meanings of new terms/equations will be discussed. The reader can refer back to **Chapter** 3 for a detailed explanation of the `interFoam` model equations.

The transport equation for the phase volume fraction is as follows:

$$\frac{\partial \alpha}{\partial t} + \nabla \cdot (\boldsymbol{u}\alpha) + \nabla \cdot \{\boldsymbol{u_c}\alpha(1-\alpha)\} = 0, \tag{6.7}$$

where:

$$\boldsymbol{u_c} = C_\alpha |\boldsymbol{u}| \frac{\nabla \alpha}{|\nabla \alpha|}. \tag{6.8}$$

The mass and momentum equations read as:

$$\nabla \cdot \boldsymbol{u} = 0, \tag{6.9}$$

$$\frac{\partial (\rho_0 \boldsymbol{u})}{\partial t} + \nabla \cdot (\rho_0 \boldsymbol{u}\boldsymbol{u}) = -\nabla p^* + (\boldsymbol{g} \cdot \boldsymbol{h})\nabla(\rho_v) + \nabla \cdot \boldsymbol{\tau} + \rho_0 \boldsymbol{f_b}, \tag{6.10}$$

where $p^* = p - \rho_v \boldsymbol{g} \cdot \boldsymbol{h}$ is the reduced pressure, ρ_0 is the reference density and ρ_v is the temperature-dependent variable density, calculated as a function of temperature difference:

$$\rho_v(\boldsymbol{x}, t) = \rho_0[1 - \beta(T(\boldsymbol{x}, t) - T_0)], \tag{6.11}$$

where T and T_0 are the instantaneous local and reference temperature respectively and β is thermal expansion coefficient. $\boldsymbol{f_b}$ is the body force due to surface tension:

$$\mathbf{f}_b = \sigma\kappa\nabla\alpha, \tag{6.12}$$

Heat transport is governed by the advection-diffusion equation for temperature:

$$\frac{\partial}{\partial t}(\rho_0 T) + \nabla \cdot (\rho_0 \boldsymbol{u} T) = \nabla \cdot (\kappa_{\text{eff}} \nabla T). \tag{6.13}$$

The effective thermal diffusivity κ_{eff} is the sum of the contributions of molecular diffusivity (a material property) and turbulent thermal diffusivity, which accounts for the transport of heat by unresolved eddies:

$$\kappa_{\text{eff}} = \kappa + \kappa_{\text{turb}}, \quad \kappa = \frac{\rho_0 \nu}{Pr}, \quad \kappa_{\text{turb}} = \frac{\rho_0 \nu_t}{Pr_t}, \tag{6.14}$$

where Pr is the Prandtl number:

$$Pr = c_p \mu / k, \tag{6.15}$$

and c_p is the specific heat capacity, k is thermal diffusivity and Pr_t is the turbulent Prandtl number. Each of these parameters are set to be constant. Turbulent thermal conductivity, κ_{turb} represents the contribution of heat flux due to eddy transport across gradients, which similarly to momentum is correlated to the

eddy viscosity via the gradient-diffusion hypothesis:

$$-\rho\overline{u_i'T'} = \kappa_{\text{turb}}\left(\frac{\partial\bar{T}}{\partial x_i}\right) = \frac{\rho_0\nu_t}{Pr_t}\left(\frac{\partial\bar{T}}{\partial x_i}\right), \tag{6.16}$$

where $\bar{T}$ is the Reynolds-average temperature, T' is the turbulent temperature fluctuation and u_i' is the turbulence velocity fluctiation in each spatial dimension. The overbar on T is excluded from **Eq.** 6.13, to avoid confiusion with mean bulk temperature referred to in **Eq.** 6.5.

Material properties are calculated as a linearly interpolated function cell volume fraction:

$$\rho_0(\boldsymbol{x},t) = \alpha\rho_1 + (1-\alpha)\rho_2, \tag{6.17}$$

$$\mu(\boldsymbol{x},t) = \alpha\mu_1 + (1-\alpha)\mu_2, \tag{6.18}$$

$$\kappa(\boldsymbol{x},t) = \alpha\frac{\rho_1\nu_1}{Pr_1} + (1-\alpha)\frac{\rho_2\nu_2}{Pr_2}. \tag{6.19}$$

Turbulent thermal diffusivity, which is a feature of the flow rather than being a material property is calculated in the same way:

$$\kappa_{turb}(\boldsymbol{x},t) = \alpha\frac{\rho_1\nu_{T,1}}{Pr_{T,1}} + (1-\alpha)\frac{\rho_2\nu_{T,2}}{Pr_{T,2}}. \tag{6.20}$$

The thermal expansion coefficient is given by:

$$\beta = -\frac{1}{\rho_0}\frac{\partial\rho}{\partial T}, \tag{6.21}$$

and is calculated as a mass-weighted linear-approximation in each control volume as follows:

$$\beta(\boldsymbol{x}, t) = \frac{1}{\rho_0}(\alpha\rho_1\beta_1 + (1-\alpha)\rho_2\beta_2)). \tag{6.22}$$

The transport and thermophysical properties adopted for each phase for the remainder of the thesis are as follows, and will remain unchanged throughout:

-	$c_p[\mathrm{J}\cdot\mathrm{kg}^{-1}]$	$\beta[\mathrm{K}^{-1}]$	$Pr[-]$	$Pr_\mathrm{t}[-]$	$\rho[kg\cdot m^{-3}]$	$\nu[m^2\cdot s^{-1}]$
Water	4×10^3	0.2×10^{-3}	0.7	0.7	1×10^3	1×10^{-6}
Air	1×10^3	3.7×10^{-3}	7	0.7	1	1.5×10^{-5}

Table 6.1: List of material properties

6.2.1 Library for calculating thermal and transport properties of mixture

`OpenFOAM` solvers each call upon a number libraries at runtime, when access to some physical model/utility is needed e.g. `interFoam` calls function utilities contained within the `immiscibleIncompressibleTwoPhaseMixture` library to calculate the mixture properties ν, ρ. Access to the volume fraction field, $\alpha(\boldsymbol{x}, t)$ allows functions contained within the library to calculate and return values for the mixture properties based on local volume fraction in each cell.

This library is customised in order to extend the same utility to allow the determination of thermophysical mixture properties at runtime using **Eqs.** 6.19, 6.20 & **Eq.** 6.22. Thermodynamic values are read from the `transportProperties` dictionary, along with the reference temperature T_0.

6.3 Summary

In this chapter, a mathematical frame work for introducing heat transfer has been introduced, using the Boussinesq approximation. This is implemented in `OpenFOAM` as an extension of the `interFoam` solver, with updated libraries for interpolating thermal properties as a function of local volume fraction. In previous chapters, aspects of interface capturing and prediction of subsurface turbulence have been rigorously tested. In **Chapter** 7, the extended model will be used to investigate thermal mixing in free surface flows.

Chapter 7

Sloshing and thermal mixing

7.1 Introduction

In **Chapter** 3, the computational model was validated in predicting isothermal sloshing over a range of challenging conditions. In **Chapters** 4 & 5, various turbulence modelling strategies were identified and tested for their ability to accurately predict eddy viscosity beneath the free surface. The stabilised $k-\omega$ SST model (Larsen and Fuhrman, 2018), was identified as being the most robust over a range of scenarios. With confidence that turbulence in the subsurface is being properly captured, and having extended the solver to account for heat transport in **Chapter** 6, in this chapter the role of sloshing and thermal mixing is investigated. To do so, a nominal, illustrative test case is set up for use throughout the remainder of the chapter. This will allow the study of:

- Natural convection-driven thermal mixing of buoyant, hot blobs of fluid in partially filled static tanks
- Thermal mixing in moving tanks. More specifically, the exploration of:
  - Sloshing response characteristics over a wide range of parameters

- Influence of fill height and sloshing regime on subsurface thermal mixing
- Influence of forcing amplitude and frequency (and corresponding wave mode shapes) on subsurface thermal mixing
- The competing forces of natural convection and slosh-induced fluid motions
- Subsurface turbulence

7.2 Thermal mixing in a static tank

7.2.1 Baseline test case

As a preliminary step towards introducing thermal aspects to sloshing, mixing through natural convection in a static tank is investigated. This will be useful in order to establish a static 'baseline' with which to quantitatively assess the enhancement of mixing incurred by introducing sloshing motions. Secondly, we will be able to demonstrate the effects of varying the initial temperature perturbation on how the subsurface thermal flow field evolves when driven by buoyancy alone. The static mixing case will also serve as an opportunity to perform a mesh-independence study and ensure that the predicted mixing rates are not affected by grid resolution.

The initial condition for our test case will be that of a hot blob of liquid situated at an initial state of rest, enveloped by a body of cool liquid (**Fig.** 7.1), with similarly cool air situated above the interface.

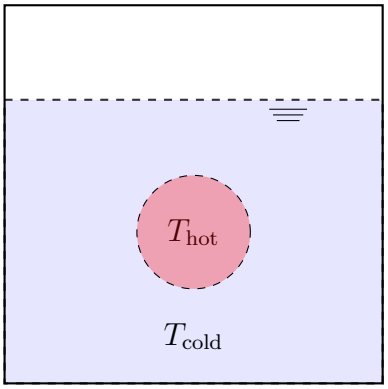

Figure 7.1: Tank with initial thermal conditions

Why a hot blob?

This initial condition is a well-ordered, un-mixed state. The hot blob represents a thermal instability relative to the horizontal fluid layer, and has a clear mechanism through which to self-mix via buoyancy-driven flow. The fact that this potential

is already built into the system means we can generate a useful baseline case of self-mixing, before later looking at how the thermal mixing process is enhanced by sloshing. Admittedly, a system in which a hot blob of fluid were to spontaneously appear is not likely in reality. However it is certain that within the wider context of applications such as partially filled fuel tanks, un-mixed regions of thermal variation will develop within. In such a case, the combined effects of forced and natural convection, molecular thermal diffusion and slosh-induced motions will all contribute towards the mixing process. This test case set-up represents something of a 'numerical experiment' to help extract an understanding of how these forces compete, and how that might vary as a consequence of input parameters such as temperature difference ΔT, forcing frequency ω^*, forcing ampltiude A^* and fill height ratio h_{fs}/L_x.

As a first step towards modelling very complex systems involving all of the above, forced convection — shear-mixing layers from inlets and slosh-induced motions — have been eliminated. In the next section of this chapter the level of complexity within the system will be increased by introducing tank motion.

7.2.2 Numerical model

The custom `OpenFOAM` solver described in **Chapter** 6 is used throughout this chapter. For the LES simulations, the Smagorinsky sub-grid model (`LES`) is used and for all RANS simulations the stabilised $k-\omega$ SST model (`STB`) is deployed.

Initial and boundary conditions

As the flow is initially at rest, the velocity field is set to zero at $t = 0$. The initial volume fraction and temperature fields are defined using the `setFields` utility in `OpenFOAM`. The tank is filled to a height, $h_{\text{fs}} = 0.35$. The hot blob's diameter is set to be one half of the fill height $D_{\text{hot}} = h_{\text{fs}}/2$. The initial background temperature is

set at $T_{\text{cold}} = 300K$, and will remain so throughout. The initial temperature of the hot blob of fluid will be an input parameter, changed in order to vary the strength of buoyancy in driving the mixing.

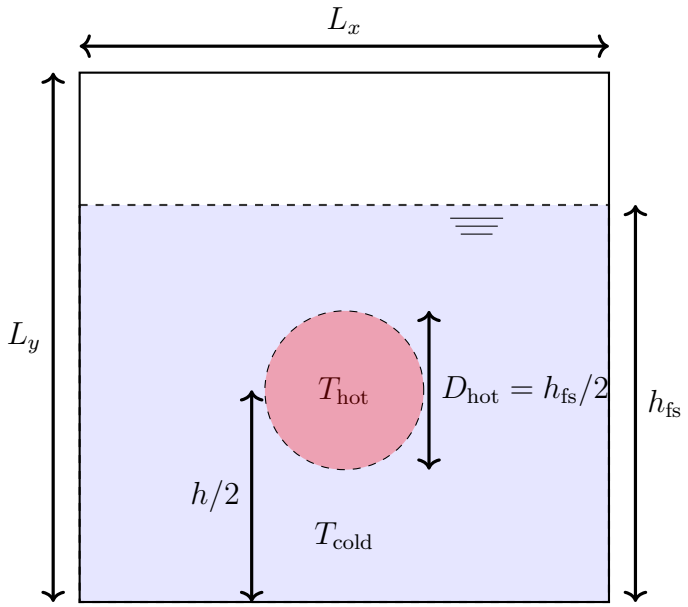

Figure 7.2: Tank with initial thermal conditions. $L_x = L_y = 0.5m$. $T_{\text{cold}} = 300K$. h_{fs} and T_{hot} are case dependent.

The model boundary conditions remain the same as in **Section** 3.5.2 with the addition of a temperature condition. Adiabatic walls are imposed in order to eliminate heat flux and preserve thermal energy within the domain. A limited version of the `vanLeer` scheme is used for discretising the temperature advection term.

7.2.3 Dimensionless groups

Thermal mixing in sloshing flows features various competing physical processes. In order to characterise the relative importance and expected contribution from each process we will state some of the key dimensionless groups.

Grashof Number

The Grashof number approximates the balance of buoyancy and viscous forces:

$$Gr = \frac{g\beta\Delta T L^3}{\nu^2}, \tag{7.1}$$

where $\Delta T = (T_{\text{hot}} - T_{\text{cold}})$ is the temperature difference between the two layers, β is the thermal expansion coefficient, and L is the characteristic length scale. Here L is taken to be the initial hot region diameter D_{hot}. As Grashof number is increased, the flow is likely to become more turbulent.

Rayleigh Number

The Rayleigh number describes the balance of buoyancy and thermal conduction in driving heat transport. High Rayleigh number indicates buoyant flow. Below a critical Rayleigh number, thermal instabilities fail to initiate, and so heat transfer is governed my molecular diffusion. The Rayleigh number is closely related to the Grashof and Prandtl numbers and can be expressed as follows:

$$Ra = \frac{g\beta\Delta T L^3}{\nu\kappa} = GrPr \tag{7.2}$$

where κ is thermal diffusivity.

Reynolds Number

The balance of inertial and viscous forces in fluids is described by the Reynolds number, which usually takes the form:

$$Re = \frac{UD}{\nu}, \tag{7.3}$$

where U and D are the characteristic velocity and length scales respectively.

Reynolds number is an important parameter, relevant to most fluid flows. Its use in predicting turbulence is well-defined for a variety of flow types. However, for sloshing it is not very well defined. For the majority of fluid flows, it is straightforward to calculate the Reynolds number by identifying some characteristic scale for both length and velocity. The length scale is usually defined by geometric features of the flow.

For sloshing flows, we can simply take the characteristic length scale to be either the tank fill height, h_{fs} or length, L_x. Choosing a velocity scale is less obvious, as the fluid response is heavily influence by the forcing parameters. Its exact nature cannot necessarily be known a priori. Fluid slosh at resonance for example, is likely to feature higher velocities than away from resonance. The only parameter directly influencing this is forcing frequency. Decreasing or increasing the frequency away from resonance, will both reduce the sloshing response, thus making it a difficult parameter to use for defining velocity scales.

For shallow-water sloshing flows, the characteristic velocity is sometimes taken as the wave celerity/bore speed $U = \sqrt{gh_{fs}}$ (Colagrossi et al., 2008). However, this is problematic in that it totally neglects to include the effects of excitation amplitude (and subsequently wave response amplitude)

Richardson Number

The Richardson number is a measure of the relative influence of natural and forced convection in a non-isothermal flow, expressed as follows:

$$Ri = \frac{g\beta\Delta TL}{U^2} = \frac{Gr}{Re^2}, \tag{7.4}$$

where U is again some characteristic velocity of the flow. Richardson number can also be expressed in terms of Grashof and Reynolds numbers. The challenges associated with defining an appropriate velocity scale means Richardson number is similarly difficult to define for sloshing flows.

7.2.4 Grid resolution study

A mesh study is performed for the purpose of ensuring that the rate of thermal mixing is not strongly affected by the mesh resolution. The results from both RANS and LES turbulence modelling strategies will be presented. Results are considered from the simulations listed in **Table** 7.1. Mesh resolution of up to $n_i = 800$ was generated for the 2D `STB` models. This was limited to $n_i = 500$ for the 3D cases due to computational expense.

Ultimately the overall aim of this chapter is to run a comprehensive parameter study, involving a large array of transient simulations. The only was to feasibly do this is by restricting the simulations to 2D. Transient 3D simulations over long run-times are extremely computationally expensive when considering processing and storage requirements. This is especially true for meaningful LES simulations, which have impose greater demands on mesh resolution than RANS models. Therefore, 3D simulations will only be run for the static cases, as a way of evaluating the limits of 2D modelling of thermal mixing.

Grid, $n_i =$	100	200	400	500	600	800
2D STB	✓	✓	✓	✓	✓	✓
3D STB	✓	✓	✓	✓		
3D LES	✓	✓	✓	✓		

Table 7.1: Matrix of simulations: combinations of 3D/2D model and grid resolutions

Mixing criteria

As a way of assessing how 'well mixed' the system has become relative to the initial un-mixed condition, variation of the temperature field is tracked through time. First, the coefficient of temperature variation is calculated:

$$V(t) = \frac{\sigma_T(t)}{\mu_T(t)}, \tag{7.5}$$

where σ_T and μ_T are the standard deviation and mean value of the temperature field. This is then normalised to the initial value of V at $t = 0$:

$$V^*(t) = \frac{V(t)}{V_0}. \tag{7.6}$$

As only a small fraction of the heat contained within the water will be lost to the air, the mean temperature in the subsurface might reasonably be assumed to be constant in a closed system such as this. Nonetheless, this is re-calculated and updated at each time-step.

2D thermal mixing in a static tank

Fig. 7.3 shows the evolution of the thermal flow field with an initial temperature perturbation $T_{\text{hot}} - T_{\text{cold}} = 10K$ for the `2D STB` simulation at 4 snapshots in time, $t = 10, 20, 30, 40s$ on 3 grids $n_i = 200, 400, 500$. The flow structures formed by the initial thermal instability quickly evolve to be quite complex. As the free surface is approached, the convection path of the thermal separates into a symmetrical structure featuring two counter-rotating vortices.

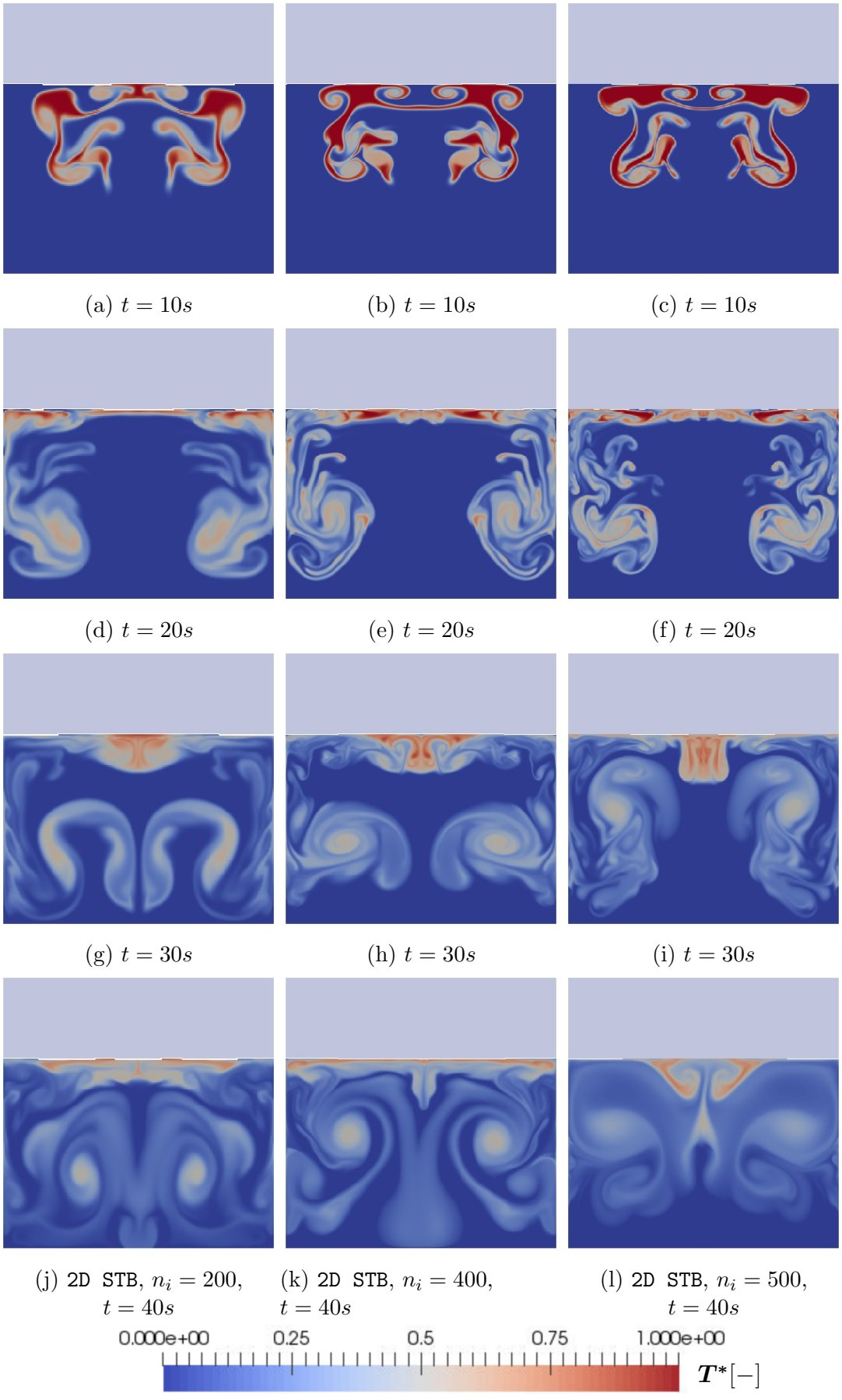

(a) $t = 10s$ (b) $t = 10s$ (c) $t = 10s$

(d) $t = 20s$ (e) $t = 20s$ (f) $t = 20s$

(g) $t = 30s$ (h) $t = 30s$ (i) $t = 30s$

(j) `2D STB`, $n_i = 200$, $t = 40s$ (k) `2D STB`, $n_i = 400$, $t = 40s$ (l) `2D STB`, $n_i = 500$, $t = 40s$

Figure 7.3: Contours of temperature in the range $T^* = (T - T_{\text{cold}})/(T_{\text{hot}} - T_{\text{cold}}) = 0 \rightarrow 1$, with varying grid resolutions for the 2D `STB` simulations From top to bottom: snapshots at times $t = 10, 20, 30, 40$s

The conversion of the potential energy initially contained within the thermal into kinetic energy allows much of the hot liquid to be transported across the underside of the interface, along the side walls and back down towards the base of the tank. After some time, most of the energy contained within these vortices dissipates, simultaneously creating a mechanism through which thermal mixing can occur on increasingly small scales. Not all heat is carried within these vortical structures. Some of the hot fluid becomes trapped at the surface by a break-off of two secondary vortices. This results in a region of stable buoyant warmer water idling beneath the free surface. This warm layer of water possesses its own method of dissipating heat — plumes are formed at the interface, convecting small amounts of heat away into the air above.

At $t = 10s$ there is already a divergence in the shape of developed flow structures across each of the grids shown in **Fig.** 7.3. The macroscopic behaviour, as just described is broadly similar, although the primary vortices have a tendency to take up different positions as the grid resolution is adjusted. Snapshots of the flow at $t = 40s$ (**Fig.** 7.4) for each of the grids show this trend is continued as the grid is refined even further up to an extremely fine resolution of $n_i = 800$. It would appear that mapping a circular topology (hot blob) on to a Cartesian grid can cause small deviations in the initial shape of the thermal. These small differences can propagate and grow through time, resulting in noticeable behavioural changes.

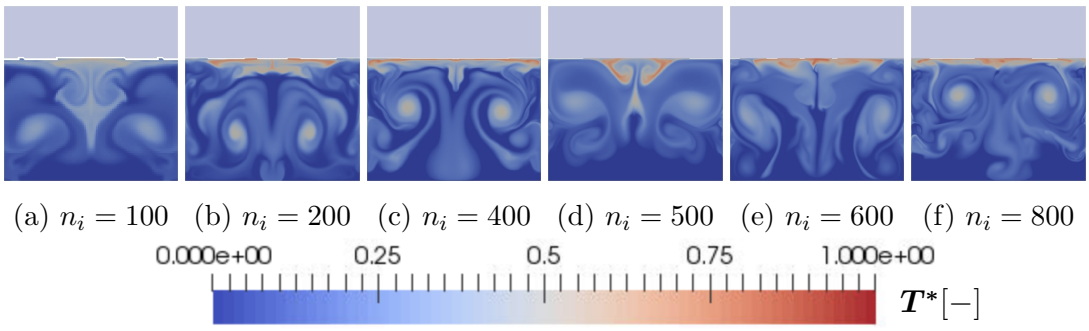

(a) $n_i = 100$ (b) $n_i = 200$ (c) $n_i = 400$ (d) $n_i = 500$ (e) $n_i = 600$ (f) $n_i = 800$

Figure 7.4: Contours of temperature in the range $T^* = (T - T_{\text{cold}})/(T_{\text{hot}-T_{\text{cold}}}) = 0 \rightarrow 1$, with varying grid resolutions for the 2D `STB` simulations at time, $t = 40s$

The overall effect of global mixing within the water is also found to be

quite mesh-sensitive. **Fig.** 7.5 shows the decrease in normalised variation of the temperature field, V^* as a function of time for each grid. The variation curve is characterised by an initial increase in mixing rate as the temperature field becomes rearranged by convective motions. This is followed by a period of linear decrease in variation until the rate of mixing begins to decay as the process becomes dominated by diffuse mixing on smaller scales. The overtly diffusive nature of the two most coarse grids predict a faster rate of initial mixing. The mixing curves for grids with resolution of $n_i = 400$ and finer all fall within a narrow range, without ever totally collapsing onto a fully converged solution. After a time $t = 40s$, the temperature field variation is in very close agreement for each grid.

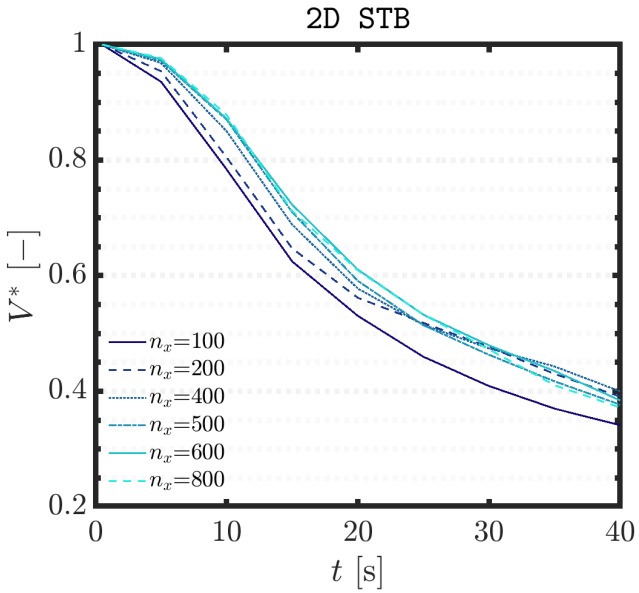

Figure 7.5: Normalised temperature variation, V^* vs time, t for model `STB` in 2D with increasing grid resolution.

3D thermal mixing in a static tank

The scaled temperature variation curves for the 3D simulations present the same profile as in the 2D model. The coarse grids in each case again produce a faster rate of mixing, with the two finer grids converging to within a narrow range through the $40s$ run-time.

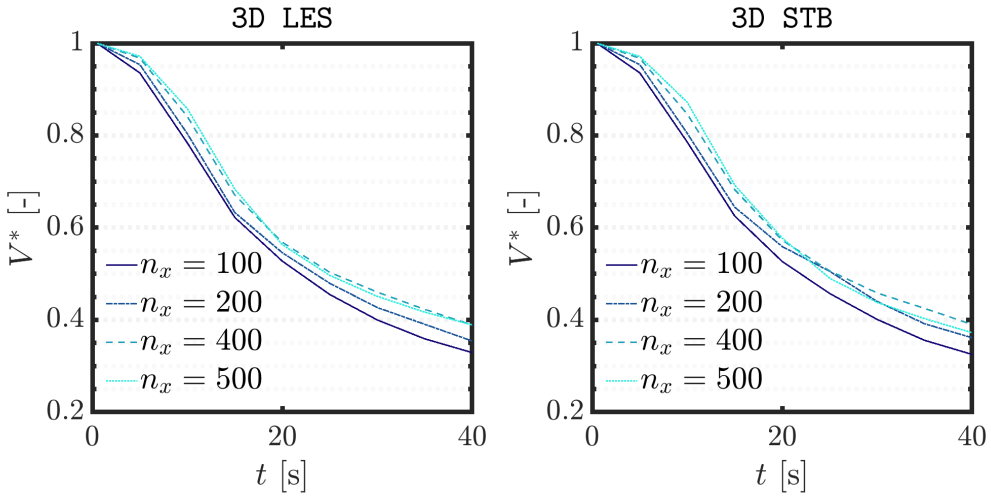

Figure 7.6: Normalised temperature variation, V^* vs time, t for models `STB` and `LES` in 3D with increasing grid resolution.

Figures 7.7 & 7.8 show the evolution of the temperature field for each model. The jump from $n_i = 200 \rightarrow n_i = 400$ results in more complex behaviour to occur. The counter-rotating vortices now have a tendency to break up into a number of smaller distinguishable rotating structures at $t = 10$s. The `LES` simulations are expected to be more grid-sensitive. Unlike RANS, increasing the mesh resolution in LES simulations effectively alters the mathematical model, as the spatial filter is decreased with each refinement step. Increasing resolution allows finer structures to be resolved, with only the turbulence on sub-grid scales being modelled. This is evident when comparing with the `3D STB` results. Looking at $t = 40s$ we can see that unlike in the `LES` simulations, an increase in grid resolution does not lead to finer turbulent flow structures to develop as the primary vortices begin to dissipate their energy.

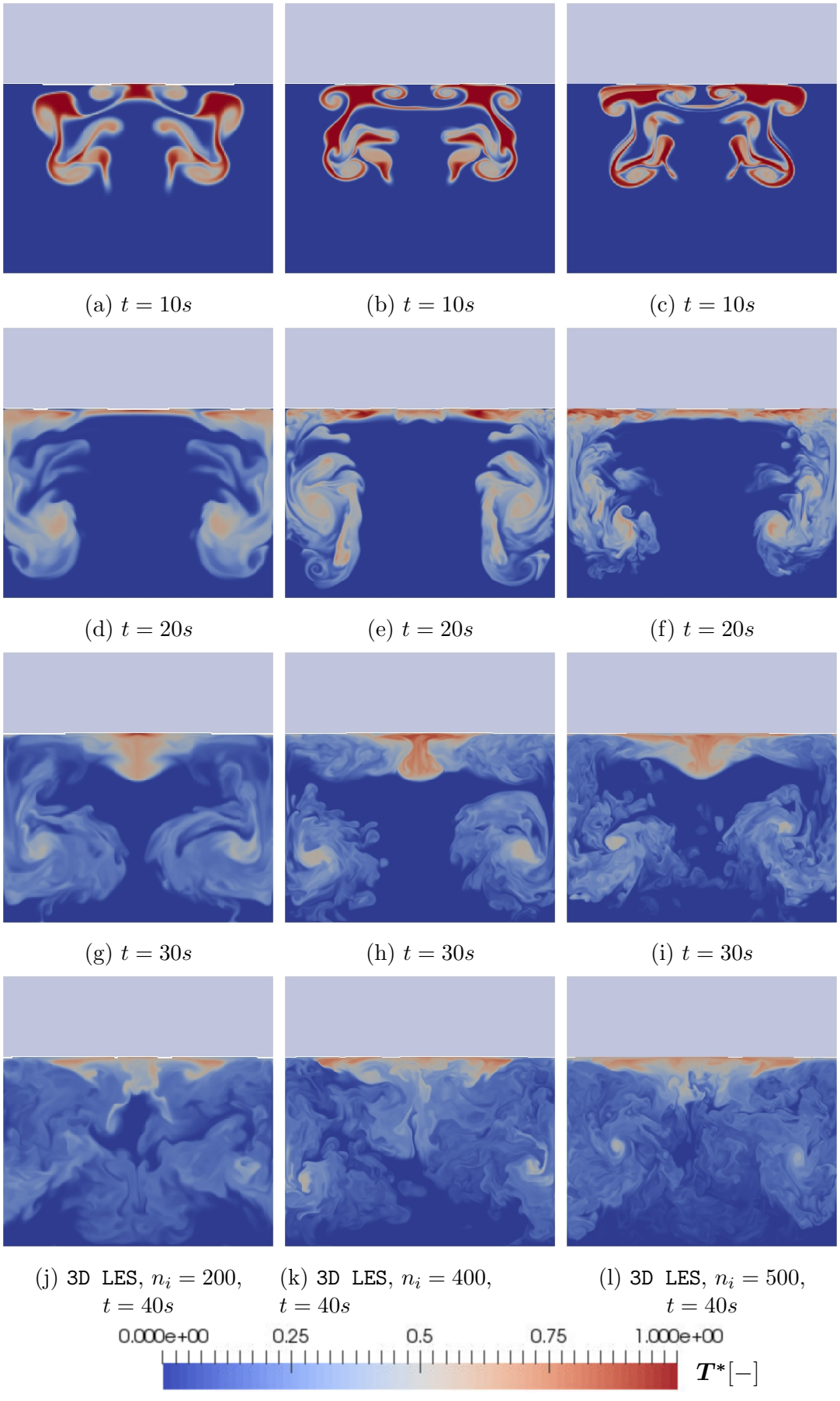

(a) $t = 10s$ (b) $t = 10s$ (c) $t = 10s$

(d) $t = 20s$ (e) $t = 20s$ (f) $t = 20s$

(g) $t = 30s$ (h) $t = 30s$ (i) $t = 30s$

(j) `3D LES`, $n_i = 200$, $t = 40s$ (k) `3D LES`, $n_i = 400$, $t = 40s$ (l) `3D LES`, $n_i = 500$, $t = 40s$

Figure 7.7: Contours of scaled temperature, $T^* = (T - T_{\text{cold}})/(T_{\text{hot}} - T_{\text{cold}})$ in the range $0 \rightarrow 1$, with vary grid resolutions for the `3D LES` simulations.

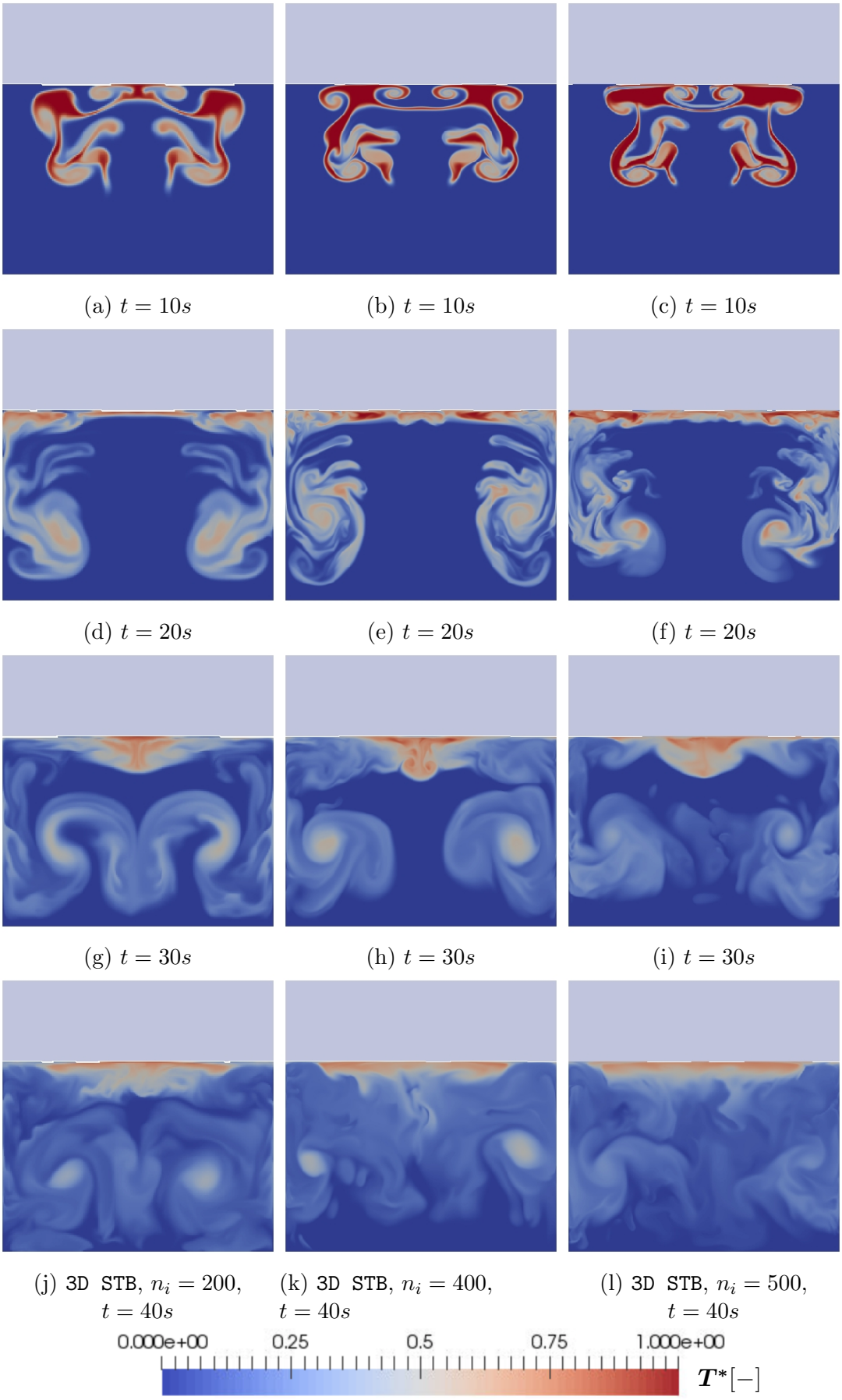

(a) $t = 10s$ (b) $t = 10s$ (c) $t = 10s$

(d) $t = 20s$ (e) $t = 20s$ (f) $t = 20s$

(g) $t = 30s$ (h) $t = 30s$ (i) $t = 30s$

(j) `3D STB`, $n_i = 200$, $t = 40s$ (k) `3D STB`, $n_i = 400$, $t = 40s$ (l) `3D STB`, $n_i = 500$, $t = 40s$

Figure 7.8: Contours of scaled temperature, $T^* = (T - T_{\text{cold}})/(T_{\text{hot}-T_{\text{cold}}})$ in the range $0 \rightarrow 1$, with varying grid resolutions for the `3D STB` simulations.

A comparison of 2D and 3D results

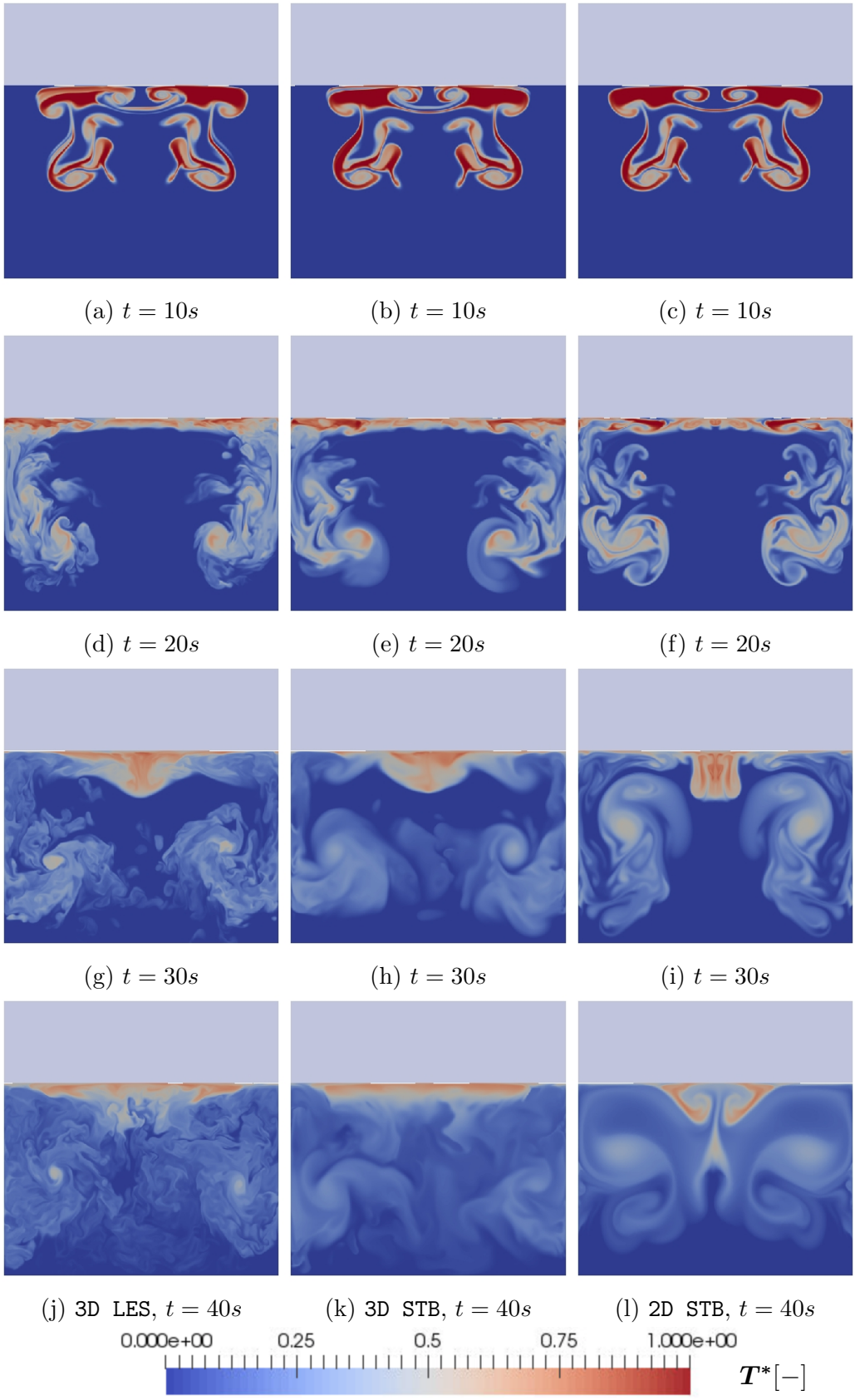

(a) $t = 10s$ (b) $t = 10s$ (c) $t = 10s$

(d) $t = 20s$ (e) $t = 20s$ (f) $t = 20s$

(g) $t = 30s$ (h) $t = 30s$ (i) $t = 30s$

(j) `3D LES`, $t = 40s$ (k) `3D STB`, $t = 40s$ (l) `2D STB`, $t = 40s$

Figure 7.9: Contours of scaled temperature, $T^* = (T - T_{\text{cold}})/(T_{\text{hot}-T_{\text{cold}}})$ in the range $0 \rightarrow 1$. From left to right, `3D LES`, `3D STB`, `2D STB`. From top to bottom: snapshots at times $t = 10, 20, 30, 40$s

Fig. 7.9 shows temperature contours at equivalent time intervals for each of the 3 models with grid resolution $n_i = 500$. At each time interval the differences become more clear. In the `2D STB`, without a third dimension in which to break down, the primary vortices begin to interact with the hot fluid at the surface, forming a further secondary structure which is not present in the 3D simulations. At $t = 40s$ the temperature field is much more smooth and diffuse than in the 3D models. Overall, the development of flow structures between the `3D STB` and `LES` models are actually very similar. The main difference is the process by which the pair of counter-rotating vortices break down. The `LES` simulation is resolving transients on much smaller length scales, and so mixing is taking place as eddies rotate, stretch, break up and dissipate. The `3D STB` simulation is instead modelling this process via a local increase in eddy viscosity in those turbulent regions, and so temperature gradients are more locally smooth and diffuse.

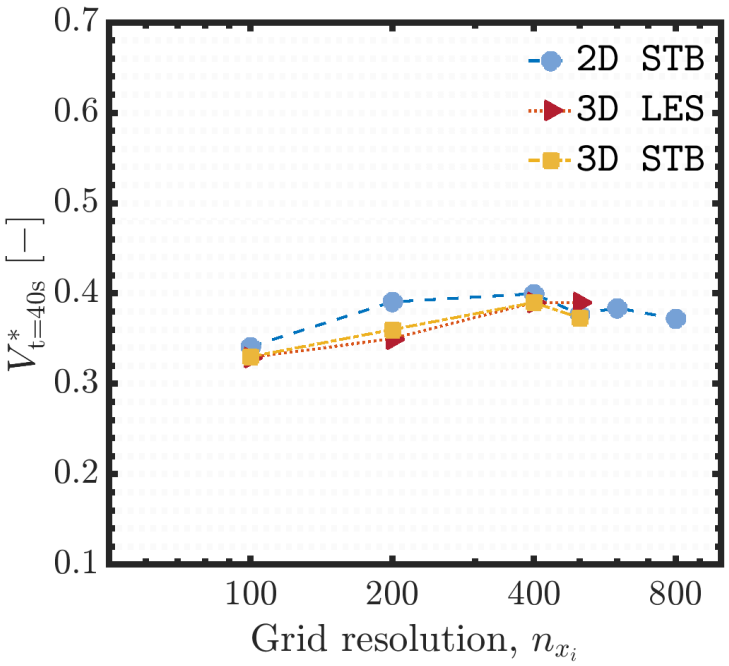

Figure 7.10: Scaled coefficient of temperature variation, $V^*_{t=40}$ at time $t = 40$ vs grid resolution

Using the variation of temperature at $t = 40s$ as a metric, we can make a formal decision about a suitable grid with which to proceed with. As was apparent

in the variation-time curves, the coarse grids ($n_i = 100, 200$) consistently produce a lower variation in the temperature field at $t = 40s$. For grids $n_i = 400$ and finer, reasonably good convergence is found for each of the models. **Table** 7.2 shows that for the `2D STB` model, the prediction of $V^*_{t=40s}$ keeps changing with each mesh refinement, but within a fairly narrow range of $V^*_{t=40s} = 0.0.372 \rightarrow 0.399$. This is in good agreement with both of the fine resolution `3D STB & LES` models. To achieve a balance of accuracy and computational economy, all simulations for the remainder of this chapter will use the $n_i = 500$ grid.

$n_i =$	100	200	400	500	600	800
Model	$\boldsymbol{V^*_{t=40}}$ [-]					
`3D LES`	0.329	0.356	0.390	0.390	-	-
`3D STB`	0.350	0.380	0.390	0.373	-	
`2D STB`	0.341	0.390	0.399	0.376	0.384	0.372

Table 7.2: Scaled temperature variation, V^* measured at simulation time $t = 40$s, $V^*_{t=40}$ for 3D `LES`, 2D & 3D `STB` with increasing grid resolution, n_i.

7.2.5 Effects of temprature perturbations on purely buoyancy-driven mixing

Buoyancy scaling

For the buoyancy-driven component of the flow — which in the static case we are looking at is the primary mechanism driving thermal mixing — we can establish a time-scale:

$$t_{\text{buoy}} \propto \left(\frac{L}{g\beta\Delta T}\right)^{\frac{1}{2}} \propto \left(\frac{L^4}{\nu^2 Gr}\right)^{\frac{1}{2}}. \tag{7.7}$$

The Grashof number is a function of the length scale of the thermal instability and the temperature difference between the hot and cold fluids. In this section will we vary the Grashof number only by altering the initial temperature

perturbation, so that the buoyancy time-scale changes as:

$$t_{\text{buoy}} \propto \frac{1}{\sqrt{Gr}} \propto \frac{1}{\sqrt{\Delta T}}. \tag{7.8}$$

We can then define a non-dimensional time scaled to buoyancy as:

$$t_b^* = \frac{t}{t_{\text{buoy}}} = t\Big(\frac{g\beta\Delta T}{L}\Big)^{\frac{1}{2}}. \tag{7.9}$$

It is expected then, that with increasing temperature (and hence Grashof number), the time scales taken for convective mixing to take place will decrease with an inverse square root proportionality to the initial temperature difference.

Thermal mixing

To test this, simulations with 3 temperature perturbations are run, with initial thermal conditions and corresponding Grashof number listed in **Table** 7.3.

Case #	**1**	**2**	**3**
ΔT [K]	1	4	16
Gr [–]	1.1×10^7	4.35×10^7	1.75×10^8

Table 7.3: Temperature perturbations and Grashof number for each case

In **Fig.** 7.11a we can see that indeed as expected, increasing the initial temperature perturbation increases the rate of thermal mixing. Plotting temperature variation as a function of the buoyancy time-scale, t_b^* in **Fig.** 7.11b reveals that the assumption of scaling holds well, with only a slight increase in mixing rate with Grashof number. The flow becomes increasingly turbulent as buoyancy dominated viscous effects, which in turn enhances mixing. **Fig.** 7.13 illustrates the flow similarities when factoring the buoyancy time scales.

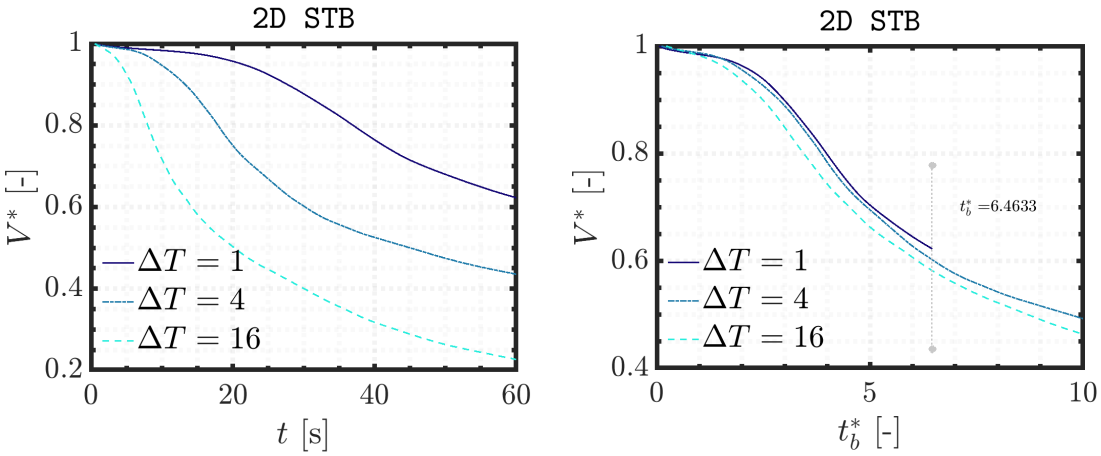

(a) V^* vs t (b) V^* vs t_b^*

Figure 7.11: Normalised temperature variation of the temperature field, V^* vs real time, t (left) and buoyancy-scaled time t_b^* (right).

A comparison of 2D STB, 3D STB and 3D LES results is shown in **Fig.** 7.12. Measuring the scaled temperature variation, V^* at time $t = 60s$ shows strong agreement at lower Grashof numbers. The 2D STB model predicts slightly faster mixing for the simulation with highest Grashof number.

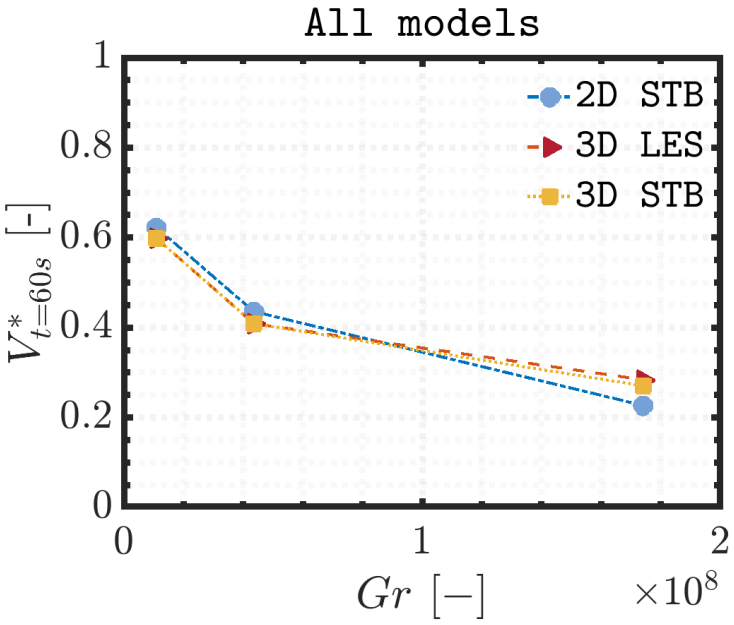

Figure 7.12: Comparison of the normalised variation of the temperature field after $60s$ vs Grashof number for 3D LES simulations, 2D & 3D STB simulations.

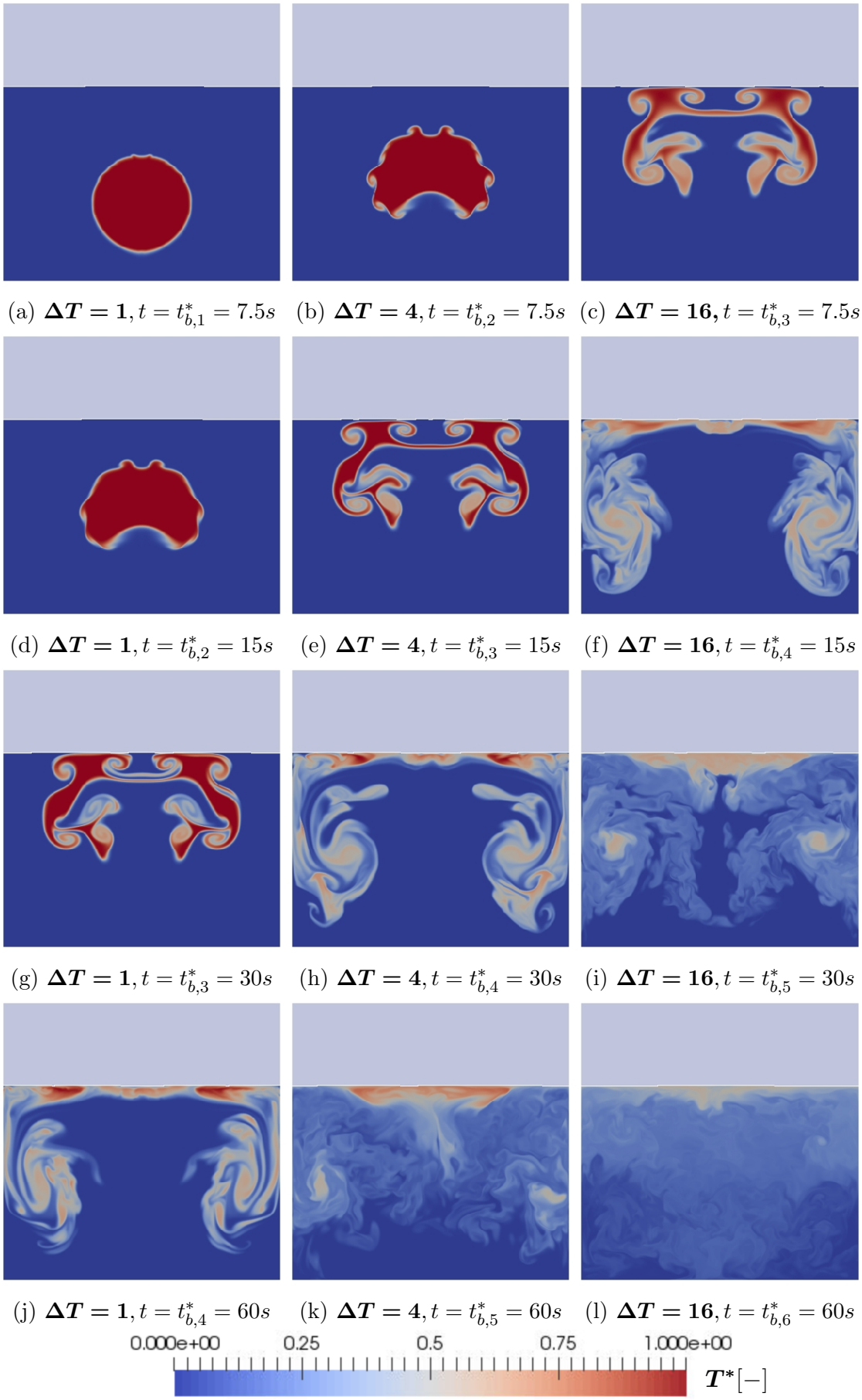

(a) $\boldsymbol{\Delta T = 1}, t = t^*_{b,1} = 7.5s$ (b) $\boldsymbol{\Delta T = 4}, t = t^*_{b,2} = 7.5s$ (c) $\boldsymbol{\Delta T = 16}, t = t^*_{b,3} = 7.5s$

(d) $\boldsymbol{\Delta T = 1}, t = t^*_{b,2} = 15s$ (e) $\boldsymbol{\Delta T = 4}, t = t^*_{b,3} = 15s$ (f) $\boldsymbol{\Delta T = 16}, t = t^*_{b,4} = 15s$

(g) $\boldsymbol{\Delta T = 1}, t = t^*_{b,3} = 30s$ (h) $\boldsymbol{\Delta T = 4}, t = t^*_{b,4} = 30s$ (i) $\boldsymbol{\Delta T = 16}, t = t^*_{b,5} = 30s$

(j) $\boldsymbol{\Delta T = 1}, t = t^*_{b,4} = 60s$ (k) $\boldsymbol{\Delta T = 4}, t = t^*_{b,5} = 60s$ (l) $\boldsymbol{\Delta T = 16}, t = t^*_{b,6} = 60s$

Figure 7.13: Flow similarity when scaled to buoyancy time-scale, illustrated by scaled temperature, $T^* = (T - T_{\text{cold}})/(T_{\text{hot}} - T_{\text{cold}})$ in the range $0 \rightarrow 1$, for the 3D LES simulations with initial temperature difference of $\boldsymbol{\Delta T = 1, 4, 16K}$.

7.3 Parametric study of sloshing and thermal mixing in a tank subject to linear harmonic sway motions

Having established a baseline for thermal mixing beneath the free surface in a stationary tank, we now introduce tank motion and study the effects of sloshing on thermal mixing. This section of the chapter is structured as follows:

1. The parameter space chosen for each of the varying sloshing and thermal conditions is presented.
2. The free surface response and behaviour characteristics is analysed for sensitivity to the forcing conditions and liquid depth ratio.
3. The effect of sloshing on thermal mixing in the subsurface is assessed both qualitatively and quantitatively

7.3.1 Parameters

Sloshing parameters

In addition to varying the initial temperature perturbation, where $\Delta T = \{1, 4, 16\}$, as was done in the static tank cases, we will sweep through the key forcing and geometric parameters that influence sloshing.

Forcing amplitude, A^* will sweep through 5 points across a range covering 2 orders of magnitude: $A^* = \{2 \times 10^{-4}, 1 \times 10^{-3}, 2 \times 10^{-3}, 1 \times 10^{-2}, 2 \times 10^{-2}\}$. This takes us through a variety of response behaviours: from negligible surface disturbance through to gentle wave generation and on to violent sloshing and wave over-turning as forcing amplitude is steadily increased.

Forcing frequency, ω^* will sweep through frequencies corresponding to the first 4 natural modes predicted by linear theory, ω_n where $n = \{1, 2, 3, 4\}$. As a reminder, we will restate the dispersion relation from which these natural frequencies are calculated:

$$\omega_n = \sqrt{\left(\frac{ng\pi}{L_x}\right)\tanh\left(\frac{nh_{\text{fs}}\pi}{L_x}\right)}. \tag{7.10}$$

Fill height ratio is varied through a range of 3 values, $h_{\text{f.s.}}/L_x = \{0.15, 0.3, 0.7\}$. Each fill height is chosen to target a certain regime: $h_{\text{f.s.}}/L_x = 0.7$ corresponds to 'finite depth/deep' sloshing with standing waves and roof impacts at high amplitude excitations; $h_{\text{f.s.}}/L_x = 0.3$ falls within the 'intermediate' sloshing regime, without roof impacts and $h_{\text{f.s.}}/L_x = 0.15$ corresponds to shallow water sloshing in which travelling waves are generated at the first natural frequency. For the rest of this chapter, these will be referred to as the 'deep', 'intermediate' and 'shallow' fill cases.

As we can see from **Eq.** 7.10, the frequency corresponding to each mode, amongst other things is a function of the fill height ratio h_{fs}/L_x. Therefore, each fill height has its own unique set of modal frequencies. These are listed in **Table** 7.4.

Fill height	$\boldsymbol{\omega_1}$ $[rad/s]$	$\boldsymbol{\omega_2}$ $[rad/s]$	$\boldsymbol{\omega_3}$ $[rad/s]$	$\boldsymbol{\omega_4}$ $[rad/s]$
Deep, $\boldsymbol{h_{\text{fs}}/L_x = 0.7}$ $[-]$	7.76	11.10	13.60	15.70
Intermediate, $\boldsymbol{h_{\text{fs}}/L_x = 0.3}$ $[-]$	6.74	10.85	13.55	15.69
Shallow, $\boldsymbol{h_{\text{fs}}/L_x = 0.15}$ $[-]$	5.230	9.52	12.81	15.34

Table 7.4: List of modal frequencies for the first 4 modes at each fill height.

Buoyancy parameters

As for the size and location of the hot blob at time $t = 0$, referring back to **Fig.** 7.2, the bubble of hot liquid is initially centred at the mid-point of the tank width and liquid depth, with diameter $D_{\text{hot}}/h_{\text{fs}} = 0.5$. This means that a reduction in fill height results in a smaller hot blob, and hence a relatively less buoyant (with less

potential energy) initial condition due to the reduced buoyancy length scale.

Fig. 7.14 shows the Grashof number and Rayleigh number plotted as a function of initial temperature difference for each fill height. We can see that lowering the fill ratio reduces the buoyancy contribution. The diffusive (viscosty and molecular thermal conduction) contributions remain unaltered by the geometry changes, thus shifting the balance further towards the diffusive scales.

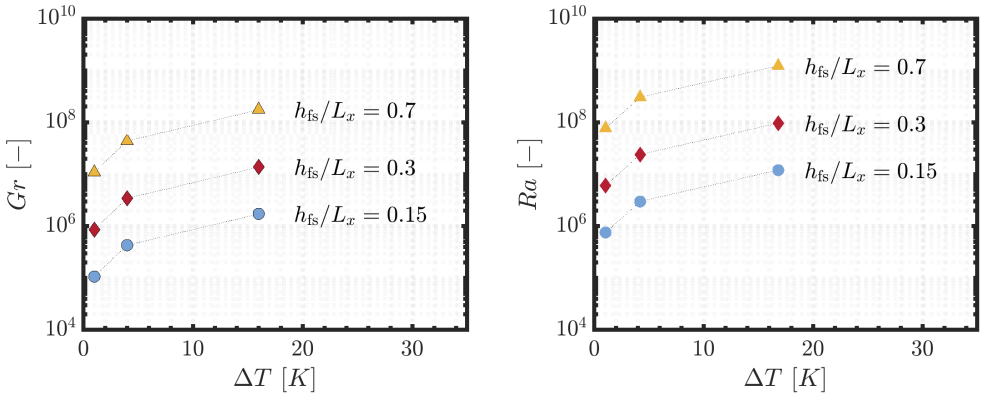

Figure 7.14: Grashof number and Rayleigh number plotted as a function of temperature difference, ΔT between hot and cold fluids regions.

Summary of parameters

The parameters and values taken for each is summarised as follows:

- **3 initial temperature conditions:** $\Delta T = \{1, 4, 16\}$.
- **4 forcing frequencies:** $\omega^* = \omega_n/\omega_1$, where $n = \{1, 2, 3, 4\}$.
- **5 forcing amplitudes:** $A^* = A/L_x = \{2 \times 10^{-4}, 1 \times 10^{-3}, 2 \times 10^{-3}, 1 \times 10^{-2}, 2 \times 10^{-2}\}$.
- **3 fill height ratios:** $h_{\mathrm{fs}}/L_x = \{0.15, 0.3, 0.7\}$

Summary of simulations

The numerical model is set up with the same boundary conditions, initial conditions, solver settings and numerical schemes as in the previous section. Tank motion is limited to pure sway (as depicted in **Fig.** 5.2). Each simulation is allowed to run for a total of $60s$, with field data sampled once every $0.5s$. A matrix of parameter combinations and the corresponding simulations is listed in **Table** 7.5, with a total of 180 simulations.

In terms of computing time, the number of CPU hours per simulation varied greatly depending on the parameters. For low amplitude cases, simulating 60s of sloshing was achievable within a range of 32-128 CPU hours on a 16-core machine. For high amplitude cases — in particular those involving tank forcing frequencies that generated a violent surface response — in excess of 1000 CPU hours was sometimes required for particularly tricky cases. These would often involve a high degree of free surface breakup, leading to challenging convergence conditions and small time-steps.

$A^* =$	2×10^{-4}				1×10^{-3}				2×10^{-3}				1×10^{-2}				2×10^{-2}			
$n =$	1	2	3	4	1	2	3	4	1	2	3	4	1	2	3	4	1	2	3	4
ΔT	$h_{\mathrm{fs}}/L_x = 0.7$																			
1	✓	✓	✓	✓	✓	✓	✓	✓	✓	✓	✓	✓	✓	✓	✓	✓	✓	✓	✓	✓
4	✓	✓	✓	✓	✓	✓	✓	✓	✓	✓	✓	✓	✓	✓	✓	✓	✓	✓	✓	✓
16	✓	✓	✓	✓	✓	✓	✓	✓	✓	✓	✓	✓	✓	✓	✓	✓	✓	✓	✓	✓
	$h_{\mathrm{fs}}/L_x = 0.3$																			
1	✓	✓	✓	✓	✓	✓	✓	✓	✓	✓	✓	✓	✓	✓	✓	✓	✓	✓	✓	✓
4	✓	✓	✓	✓	✓	✓	✓	✓	✓	✓	✓	✓	✓	✓	✓	✓	✓	✓	✓	✓
16	✓	✓	✓	✓	✓	✓	✓	✓	✓	✓	✓	✓	✓	✓	✓	✓	✓	✓	✓	✓
	$h_{\mathrm{fs}}/L_x = 0.15$																			
1	✓	✓	✓	✓	✓	✓	✓	✓	✓	✓	✓	✓	✓	✓	✓	✓	✓	✓	✓	✓
4	✓	✓	✓	✓	✓	✓	✓	✓	✓	✓	✓	✓	✓	✓	✓	✓	✓	✓	✓	✓
16	✓	✓	✓	✓	✓	✓	✓	✓	✓	✓	✓	✓	✓	✓	✓	✓	✓	✓	✓	✓

Table 7.5: Matrix of simulations, cycling through parameter space, varying scaled amplitude $A^* = A/L_x$, Natural frequency mode n, temperature difference ΔT and fill height ratio $h^* = h_{\mathrm{fs}}/L_x$. 180 simulations in total.

7.3.2 Free surface response as a function of the sloshing parameters

In this subsection of the chapter we will focus on the behaviour of the free surface subject to various external excitations, exploring the characteristics and magnitude of response with respect to forcing frequency and amplitude, as well as fill height ratio. As in **Chapter** 5, we will record the predicted wave height at the wall, $\eta(x,t) = \eta(0,t)$ and plot as a function of time. We will also present isosurfaces of volume fraction representing the free surface to understand the characteristic wave shapes generated by each mode, and how that varies with increasing forcing amplitude. As a reminder, the characteristic wave shapes for the first 4 modes are expected to be akin to those plotted in **Fig.** 7.15.

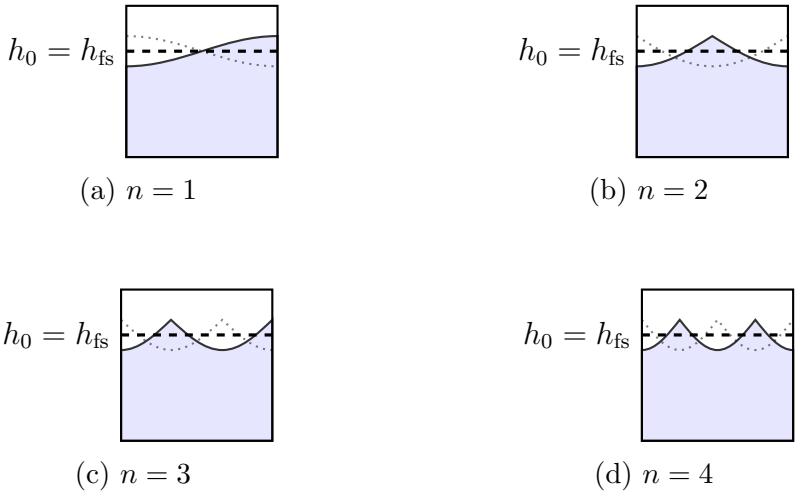

(a) $n = 1$ (b) $n = 2$

(c) $n = 3$ (d) $n = 4$

Figure 7.15: Sloshing modes at first four natural frequencies. Anti-symmetric mode shapes on the left; symmetric mode shapes on the right.

Wave response vs time. Forcing amplitude $A^* = 2 \times 10^{-4}$

Figs. 7.16, 7.17 & 7.18 show the free surface plotted as an isosurface of volume fraction, $\alpha = 0.5$. In these figures each column represents an excitation mode, $n = 1, 2, 3, 4$ and each row represents a sequential moment in time $t = t_1, t_2, t_3, t_4$, where $t_4 - t_1 < T_n$, and T_n is the harmonic time-period at each mode. That is to

say, each series of snapshots falls within a single period of oscillation. We can see that at such a small forcing amplitude, the wave response is very faint, although in **Fig.** 7.17 we can see some semblance of the beginnings of the characteristic wave profiles associated with the anti-symmetric odd modes $n = 1, 3$.

Fig. 7.19 shows the wall wave amplitude scaled to the initial free surface height, η/h_{fs} plotted as a function of oscillation periods, t/T in the interval $t/T = 40 \rightarrow 45$ for each of the modes and fill heights. Although still very small, it is clear that the odd modes $n = 1, 3$ are experiencing a much more noticeable disturbance than the even modes $n = 2, 4$. Due to the scaling of axes, the even modes look totally unresponsive. The amplitude for each time-series is almost symmetrical about $\eta = 0$ with a slight bias towards positive wave amplitudes, and they remain tightly in phase.

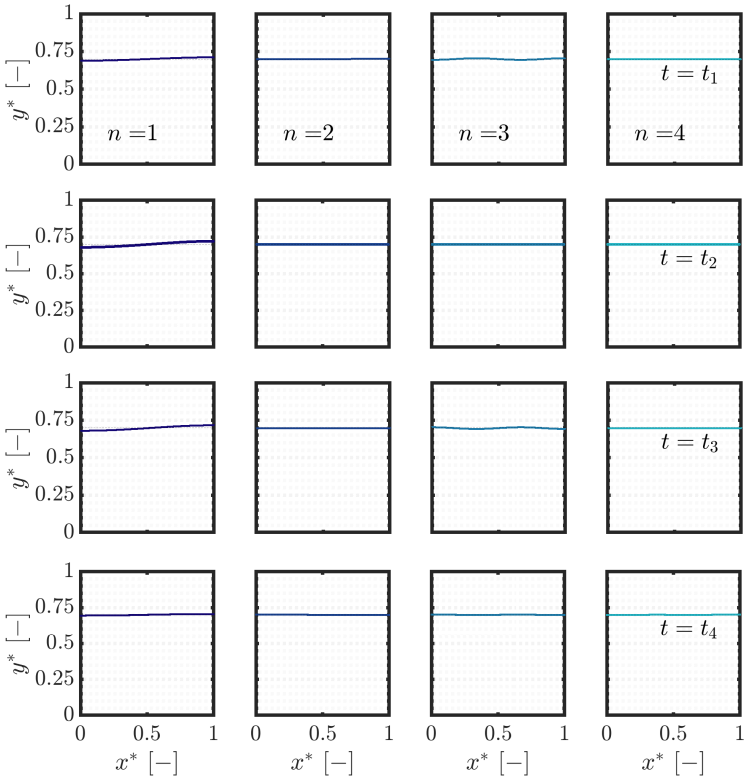

Figure 7.16: Illustration of free surface motion, with forcing amplitude $\boldsymbol{A^* = A/L_x = 2 \times 10^{-4}}$ and hill height ratio $\boldsymbol{h_{\text{fs}}/L_x = 0.7}$

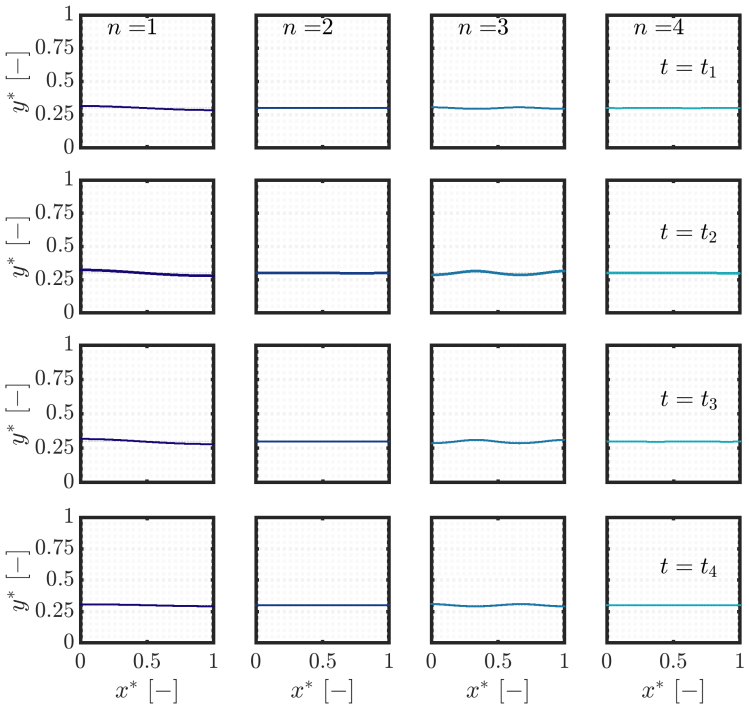

Figure 7.17: Illustration of free surface motion, with forcing amplitude $\boldsymbol{A^* = A/L_x = 2 \times 10^{-4}}$ and hill height ratio $\boldsymbol{h_{fs}/L_x = 0.3}$

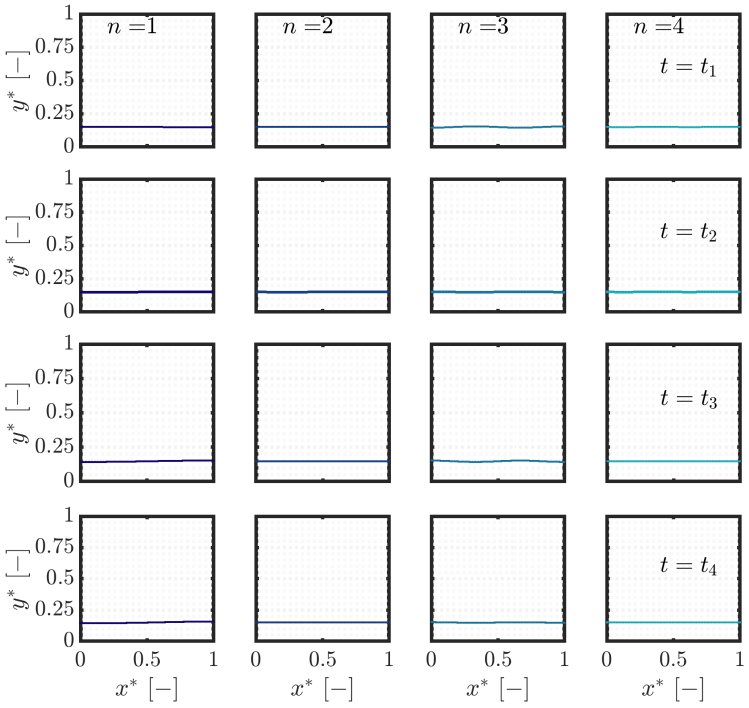

Figure 7.18: Illustration of free surface motion, with external forcing amplitude $\boldsymbol{A^* = A/L_x = 2 \times 10^{-4}}$ and hill height ratio $\boldsymbol{h_{fs}/L_x = 0.15}$

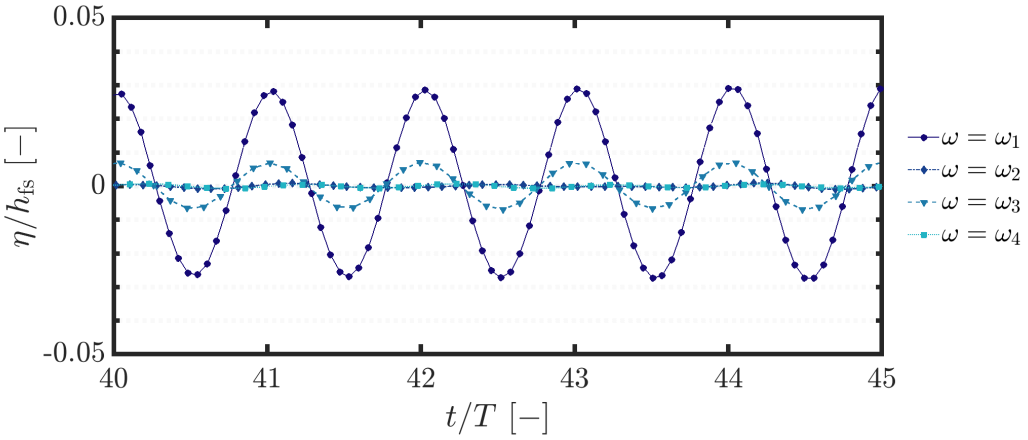

(a) $h_{\mathrm{fs}}/L_x = 0.7$

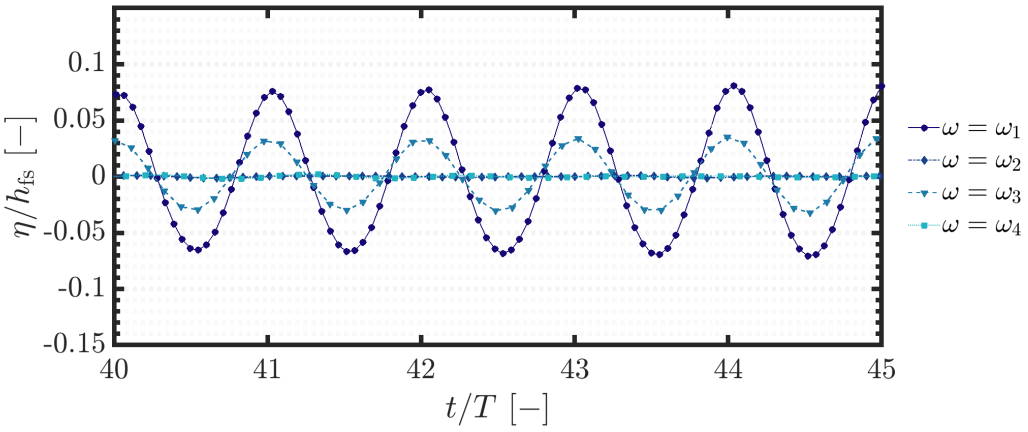

(b) $h_{\mathrm{fs}}/L_x = 0.3$

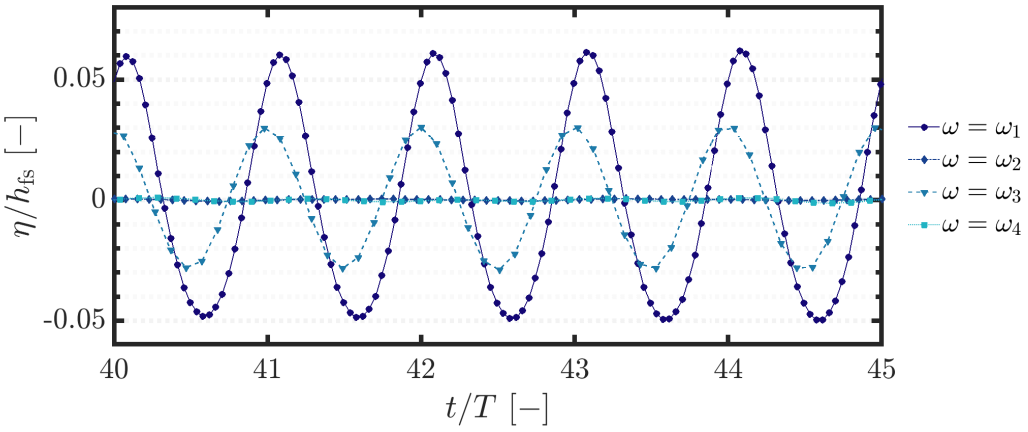

(c) $h_{\mathrm{fs}}/L_x = 0.15$

Figure 7.19: Scaled wave height at wall, η/h_{fs} plotted vs. number of simulated periods of oscillation $t^* = t/T$ for first four natural frequency modes ω_n where $n = 1, 2, 3, 4$, for the case in which the tank is subject to an external forcing amplitude of $\boldsymbol{A^* = A/L_x = 2 \times 10^{-4}}$

Wave response vs time. Forcing amplitude $A^* = 2 \times 10^{-3}$

Figs. 7.20, 7.21 & 7.22 show snapshots of the free surface in the tank undergoing external excitation with forcing amplitude $A^* = 2 \times 10^{-3}$. This represents a tenfold increase from the previous group of cases.

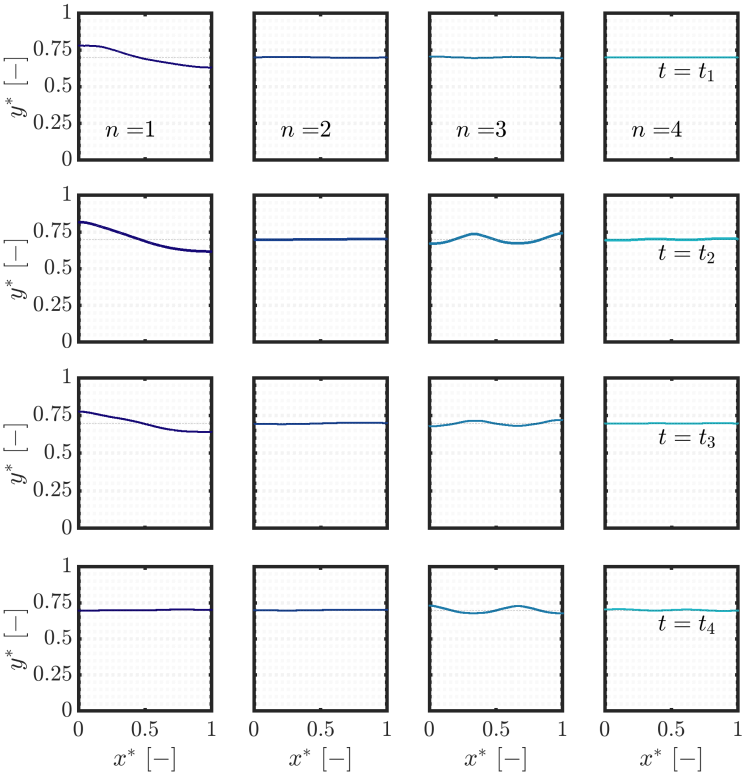

Figure 7.20: Illustration of free surface motion, with external forcing amplitude $\boldsymbol{A^* = A/L_x = 2 \times 10^{-3}}$ and hill height ratio $\boldsymbol{h_{fs}/L_x = 0.7}$

The $n = 1, 3$ mode shapes are now very clear, strongly resembling those from the experiments of Jin et al. (2014) shown in **Fig.** 3.10. Steep waves are formed as the waves rise and climb the tank walls for the $n = 1$ mode, although wave breaking and roof impacts are not yet a factor at this forcing amplitude. The $n = 1$ mode is starting to show variability in the characteristic behaviour of the wave motion depending on the fill height ratio. For the deep fill ratio, a standing wave has developed with an anti-node at each wall and a node located near the vertical centre-line of the tank. Surface motion in the shallow case — although not at all steep — is better described as a travelling wave. The intermediate filled tank seems

to represent a transition point between the two with a slightly less smooth interface than the deep tank.

This disparity in behaviour is more evident in **Fig.** 7.23, where we can see a clear difference in form between the wave amplitude-time curves. The deep fill case remains somewhat more symmetrical about $\eta/h_{\text{fs}} = 0$, whereas the magnitude of peaks relative to the wave-troughs have increased considerably for the shallower depth cases. This is due to the free surface now 'feeling' the base of the tank more so than at deeper filling levels. This matches the phenomenological description and observation made by Faltinsen and Timokha (2009) and others.

Interestingly, it is the $n = 3$ mode that incurs the largest wave response for the shallow depth case. The primary mode $n = 1$ dominates in deep sloshing, and even more so for the intermediate fill ratio (with positive wave amplitudes of magnitude exceeding that of the initial fill depth). In terms of characteristic mode shape, $n = 3$ is not as sensitive to the fill ratio regime as the primary mode, maintaining a similar wave profile at each of the fill heights.

At this forcing amplitude, the even, symmetrical modes still remain relatively unresponsive across each of the tanks.

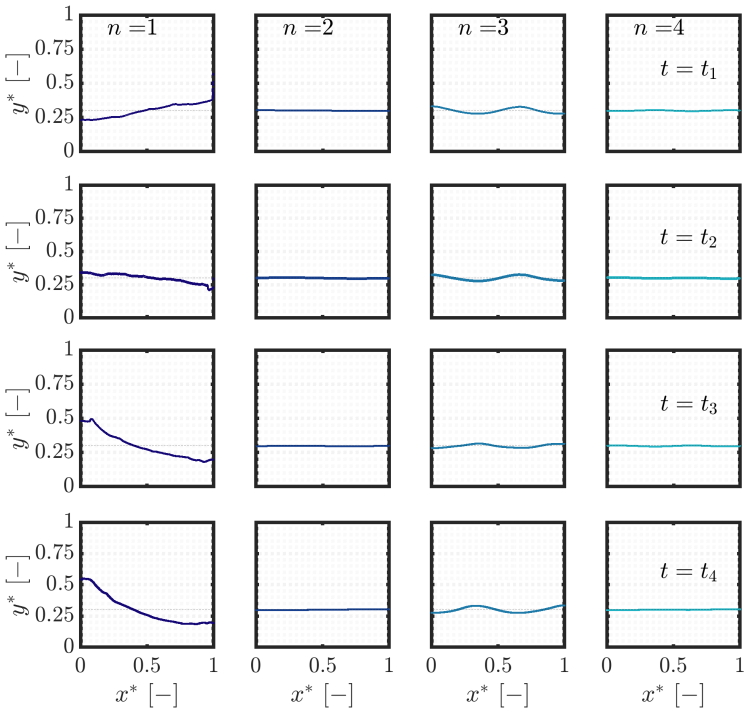

Figure 7.21: Illustration of free surface motion, with external forcing amplitude $\boldsymbol{A^* = A/L_x = 2 \times 10^{-3}}$ and hill height ratio $\boldsymbol{h_{fs}/L_x = 0.3}$

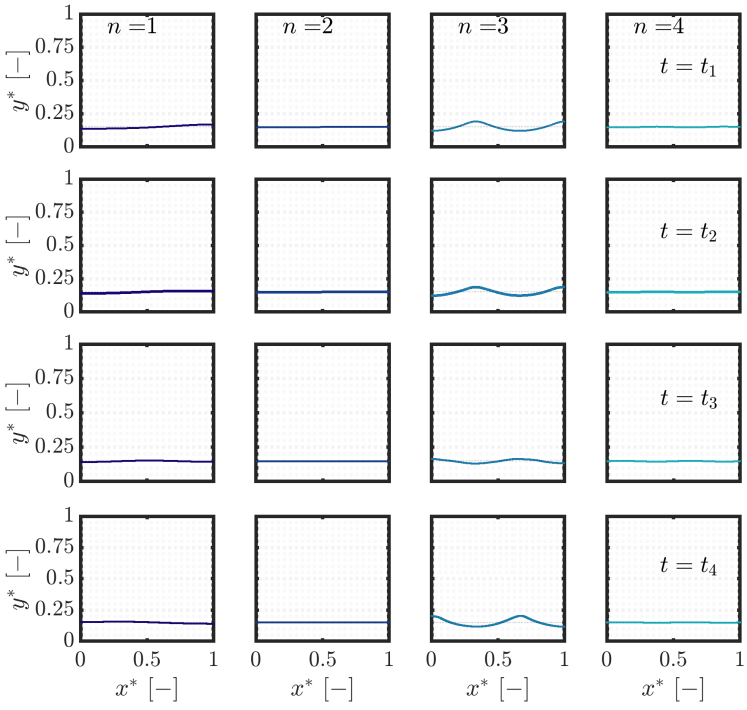

Figure 7.22: Illustration of free surface motion, with external forcing amplitude $\boldsymbol{A^* = A/L_x = 2 \times 10^{-3}}$ and hill height ratio $\boldsymbol{h_{fs}/L_x = 0.15}$

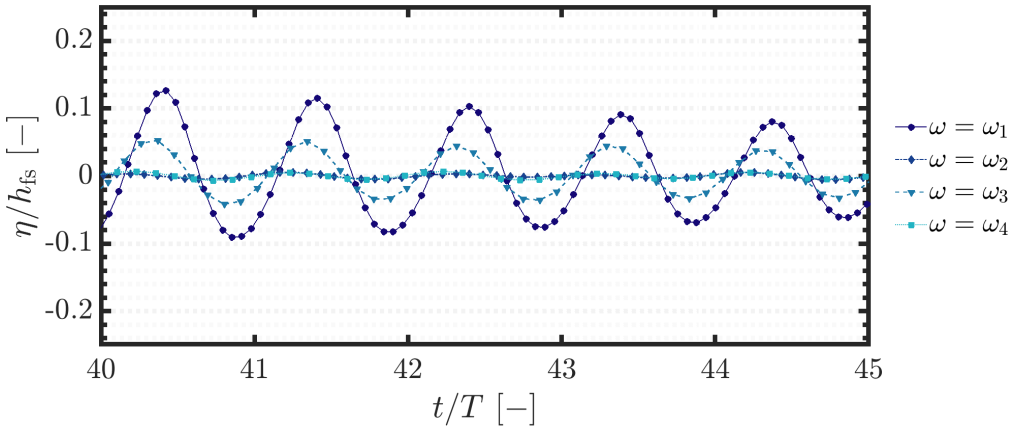

(a) $h_{\mathrm{fs}}/L_x = 0.7$

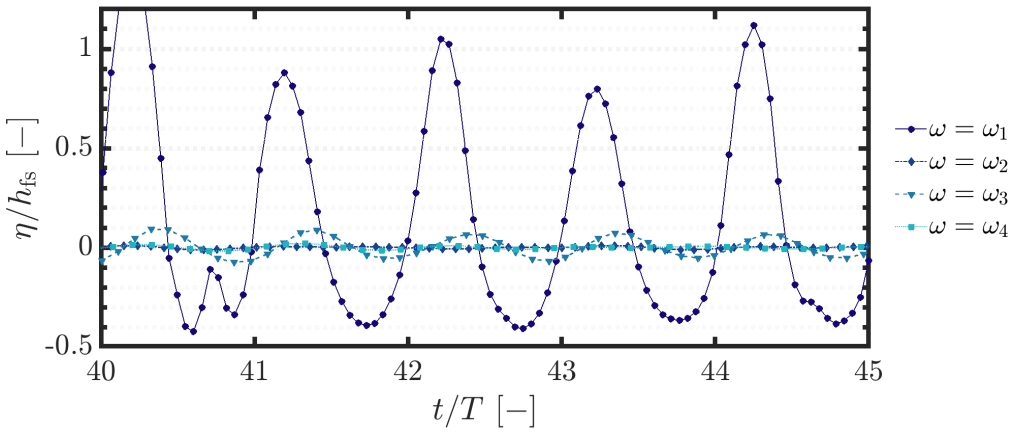

(b) $h_{\mathrm{fs}}/L_x = 0.3$

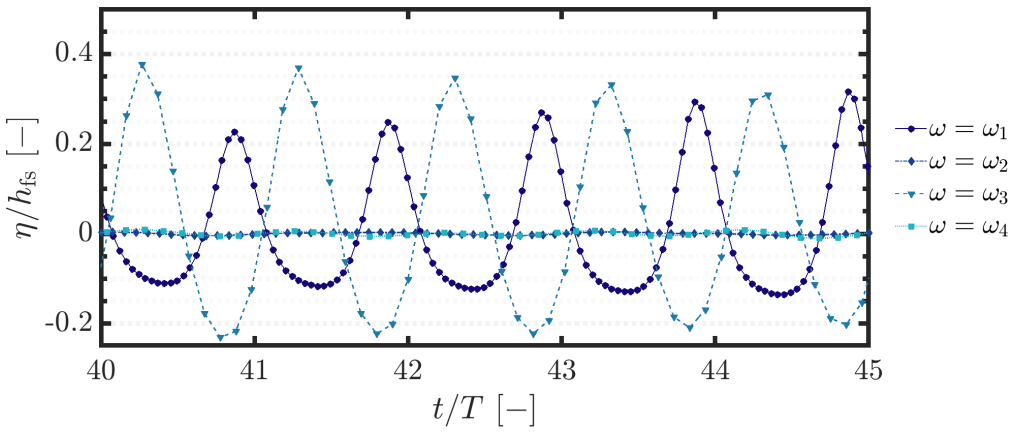

(c) $h_{\mathrm{fs}}/L_x = 0.15$

Figure 7.23: Scaled wave height at wall, η/h_{fs} vs number of simulated periods of oscillation $t^* = t/T$ for first four natural frequency modes ω_n where $n = 1, 2, 3, 4$, for the case in which the tank is subject to an external forcing amplitude of $\boldsymbol{A^* = A/L_x = 2 \times 10^{-3}}$

Wave response vs time. Forcing amplitude $A^* = 2 \times 10^{-2}$

Finally, free surface behaviour as a response to forcing with an amplitude of $A^* = 2 \times 10^{-2}$ is presented in **Figs.** 7.24, 7.25 & 7.26. Again, this is a ten-fold increase in forcing amplitude (and hence tank accelerations) on the previous set of cases. This represents the highest amplitude forcing considered throughout this research.

The sloshing response is now much more violent, with the onset of wave breaking for modes $n = 1, 3$ & 4. Wave response at the $n = 2$ mode which has been very weak at lower amplitudes has now become visibly more responsive. For the deep water $n = 1$ case, which corresponds to the nominal case set-up used in **Chapter** 5, roof impacts are now a feature.

For the intermediate fill height $n = 1$ case, the wave impacts on the side walls are strong enough to be causing droplets to spray up towards the tank roof. Further disruption to the free surface can be seen *after* impact as the liquid climbs steeply up the wall and becomes unstable.

The time-series response curves (**Fig.** 7.27) show much more eccentric behaviour, reflecting the more chaotic and violent nature of sloshing at higher forcing amplitudes. The $n = 1$ mode response peaks are much greater at the shallower fill heights than for the deep fill-ratio tank, with wave amplitudes of up to 2 times that of the initial fill height. This isn't possible for the deep fill tank which is restricted due to the roof. As the tank gets shallower, the troughs become wider for the $n = 1$ mode. The peaks get sharper and more intermittent as the shallow sloshing regime produces travelling waves that traverse the tank's length.

Wave-breaking for the higher modal frequencies $n = 3, 4$ is not restricted to interactions with the tank walls. The free surface can be seen overturning even at the tank's centre. This is due to the increased wave number $k_n = n\pi/L$. As n and subsequently k_n increase, the corresponding wavelength decreases, meaning

that for a given wave response amplitude, the surface waves are steeper. This is an important point — the likelihood of wave-breaking in sloshing flows is not simply a consequence of wave amplitude, but more critically wave steepness, which can be achieved at higher modal frequencies, even with a more modest wave height. Even the $n = 4$ symmetric mode shape, which typically exhibits less lateral motion and subsequently less forceful wall impacts can produce overturning waves.

This is particularly pertinent to our interest in thermal mixing, as it is likely that turbulence generated from wave-breaking will increase scalar mixing within the surf zone.

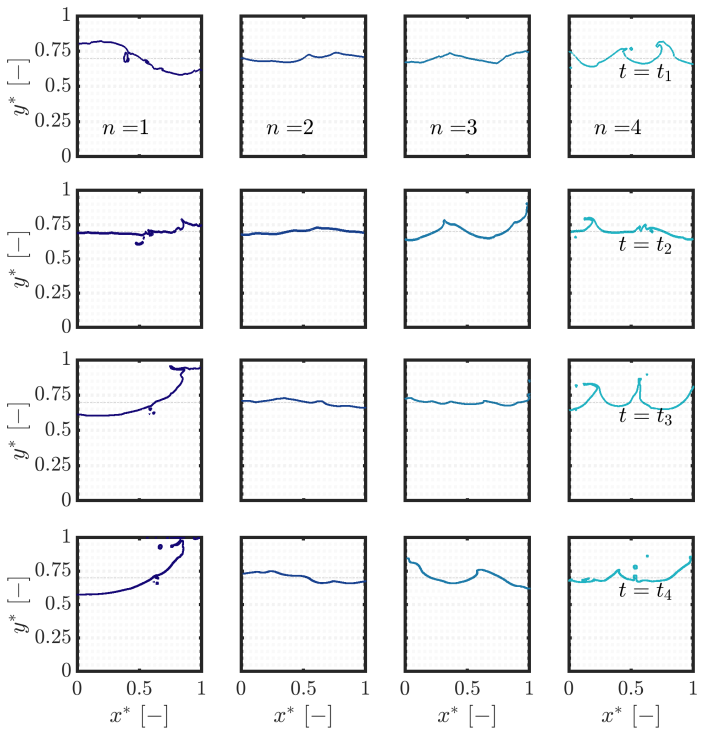

Figure 7.24: Illustration of free surface motion at 4 different times, each within a single oscillatory period, for each the 4 first natural frequency modes $\boldsymbol{n = 1, 2, 3, 4}$, with external forcing amplitude $\boldsymbol{A^* = A/L_x = 0.02}$ and hill height ratio $\boldsymbol{h_{fs}/L_x = 0.7}$

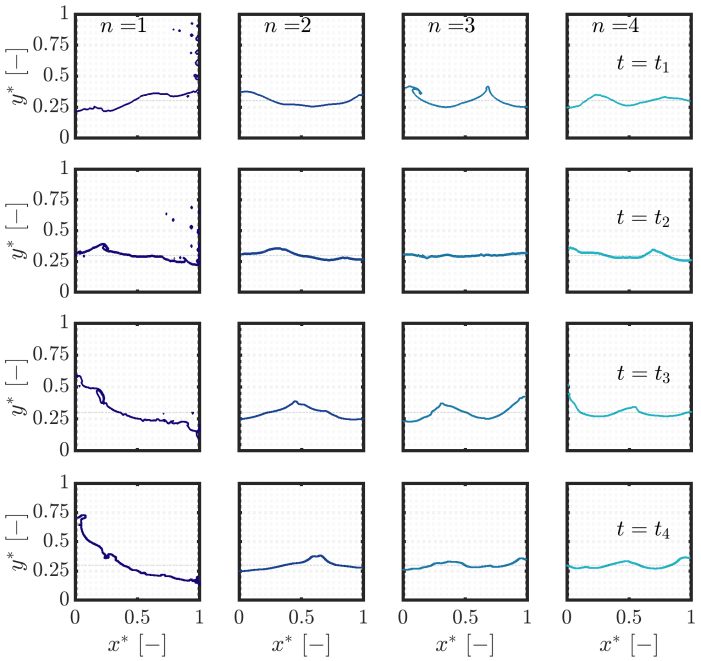

Figure 7.25: Illustration of free surface motion at 4 different times, each within a single oscillatory period, for each the 4 first natural frequency modes $\boldsymbol{n = 1, 2, 3, 4}$, with external forcing amplitude $\boldsymbol{A^* = A/L_x = 0.02}$ and hill height ratio $\boldsymbol{h_{fs}/L_x = 0.3}$

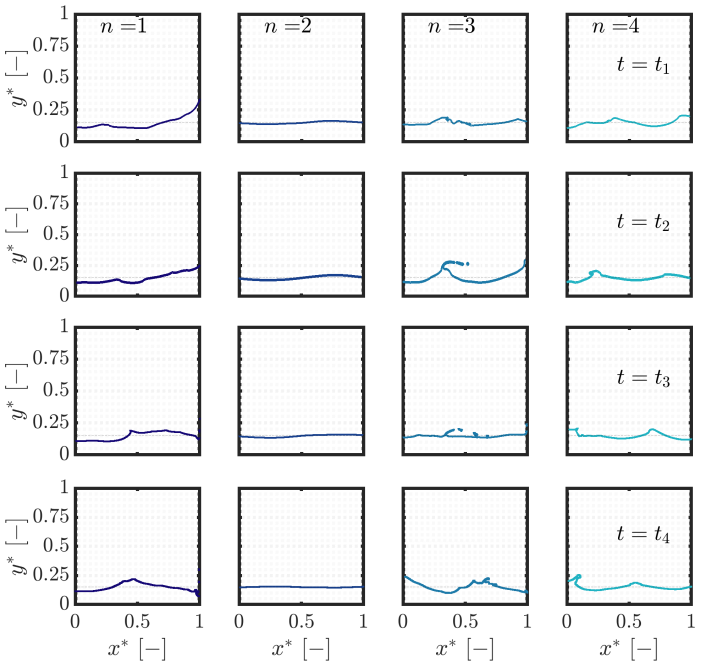

Figure 7.26: Illustration of free surface motion at 4 different times, each within a single oscillatory period, for each the 4 first natural frequency modes $\boldsymbol{n = 1, 2, 3, 4}$, with external forcing amplitude $\boldsymbol{A^* = A/L_x = 0.02}$ and hill height ratio $\boldsymbol{h_{fs}/L_x = 0.15}$

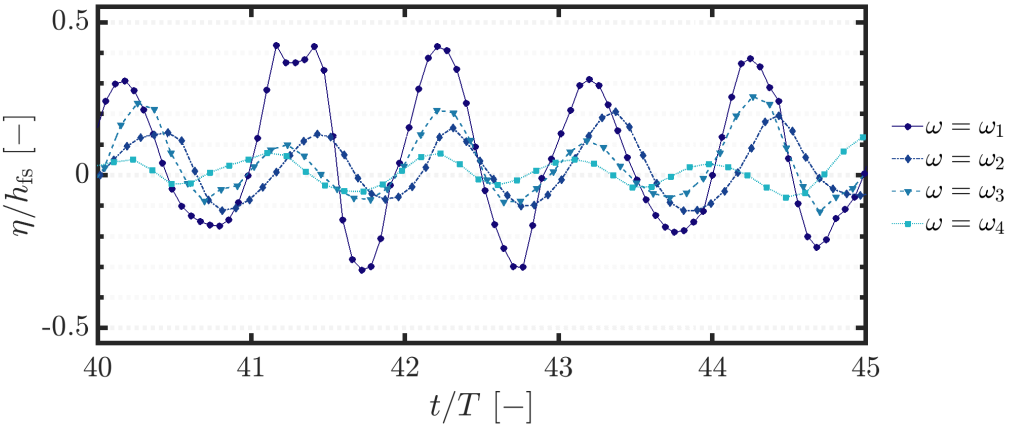

(a) $h_{\mathrm{fs}}/L_x = 0.7$

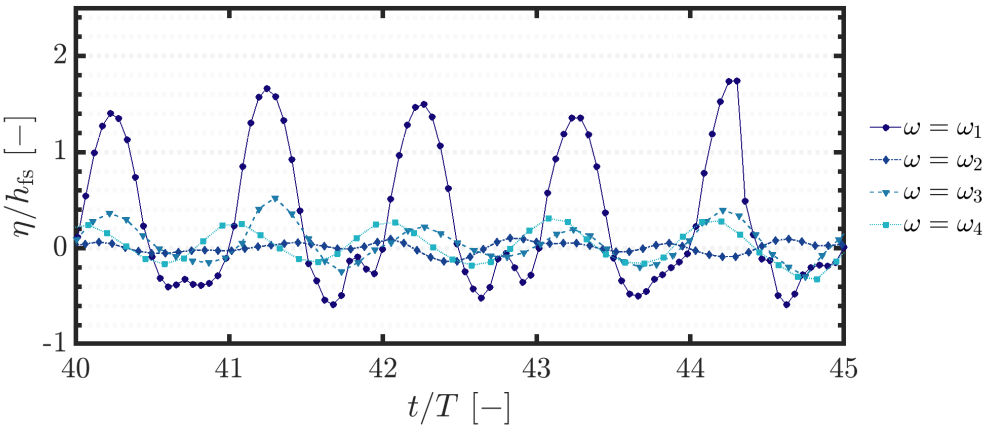

(b) $h_{\mathrm{fs}}/L_x = 0.3$

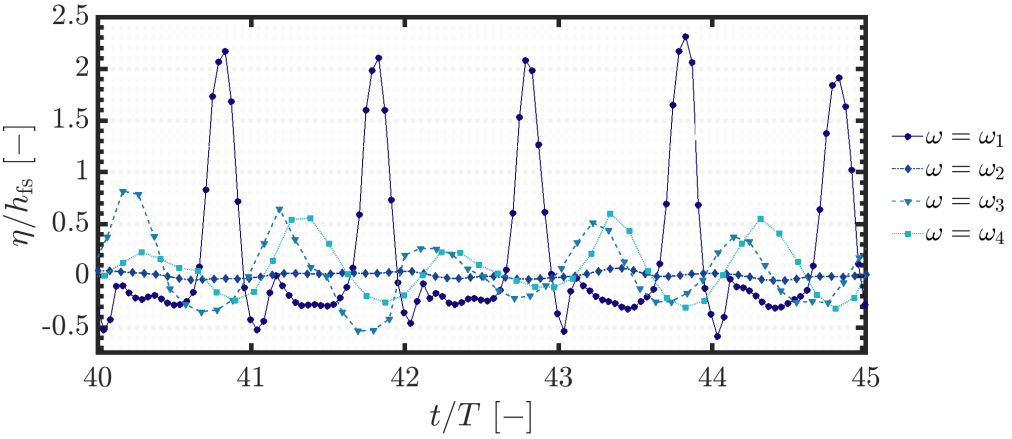

(c) $h_{\mathrm{fs}}/L_x = 0.15$

Figure 7.27: Scaled wave height at wall, η/h_{fs} vs number of simulated periods of oscillation $t^* = t/T$ for first four natural frequency modes ω_n where $n = 1, 2, 3, 4$, for the case in which the tank is subject to an external forcing amplitude of $\boldsymbol{A^* = A/L_x = 2 \times 10^{-2}}$

Free surface response across all amplitudes and frequencies

Response characteristics emerge from the system in a way that is very sensitive to fill height, frequency and amplitude of excitation. It has been found that the odd modes, i.e. the modes of excitations which produce anti-symmetric wave forms, $n = 1, 3$ generally illicit a greater wave response. This is true in particular at lower forcing amplitudes, and can be seen clearly in **Fig.** 7.28.

We can also see some convergence between the odd and even modes at higher forcing amplitudes — that is to say the even modes begin to 'catch up'. For the odd modes, the rate of increase in wave height with respect to forcing amplitude is quite steady at amplitudes higher than $A^* = 1 \times 10^{-3}$.

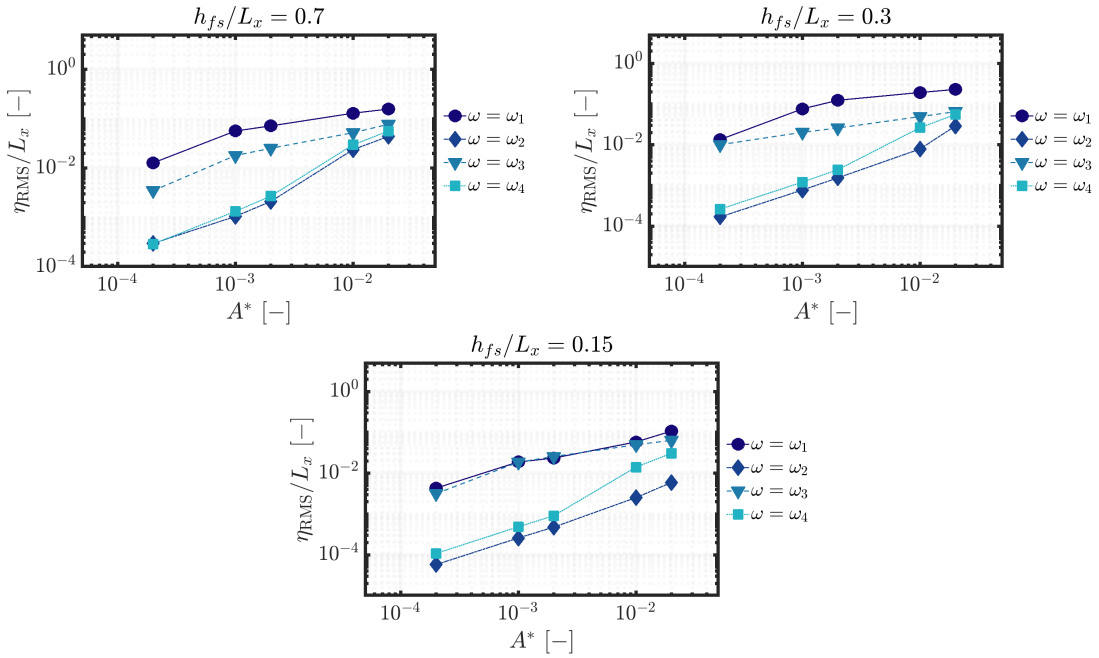

Figure 7.28: $\eta_{RMS}/h_{\mathrm{fs}}$ vs forcing amplitude A^* for each mode and fill height ratio.

For the even modes, particularly in the case of $n = 4$, there appears to be a point at which the rate of increase jumps at higher forcing amplitudes. To make matters even more complicated, this convergent behaviour between the odd and even modes fades somewhat as the fill height is decreased. The tank roof's presence will play some role in this, but more work would need to be done explore

this further.

Fig. 7.29 show the wave response-forcing amplitude curves this time with each sub-figure representing a corresponding mode. This allows direct comparison of the effects of fill height ratio. Close agreement is found between the even modes, while the odd modes show more variability. Other than to say that the deep fill case generally produces the weakest response when scaled to the initial fill depth, there doesn't seem to be a clear trend between fill height and wave response that applies across all frequencies.

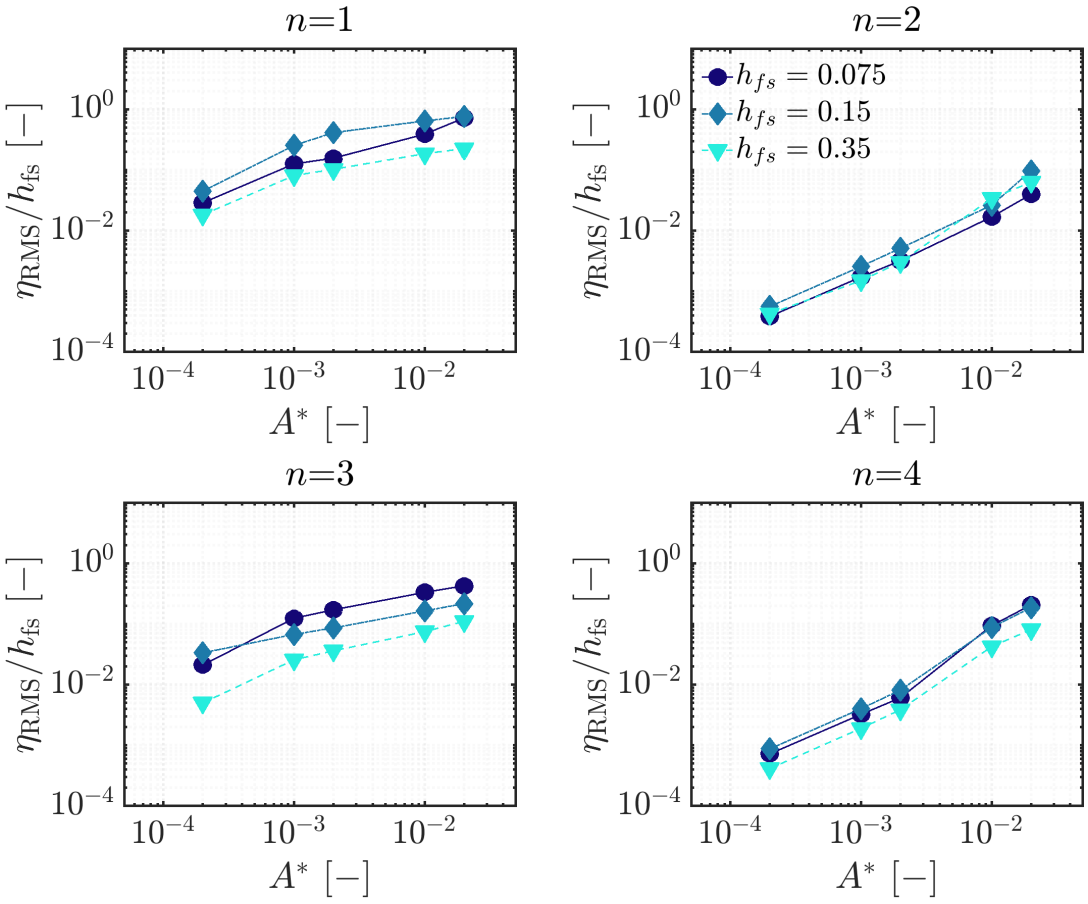

Figure 7.29: $\eta_{RMS}/h_{\mathrm{fs}}$ vs forcing amplitude A^* for each mode and fill height ratio.

7.3.3 Qualitative assessment of the influence of the sloshing parameters on thermal mixing

Having surveyed the characteristic dynamic response incurred by the sloshing parameters, we can move on to analyse how sloshing behaviours impact on thermal mixing within the liquid subsurface. The test case described in **Section** 7.2.1 has been set up to be inherently self-mixing. This allows us to focus on the balance of buoyancy and sloshing forces as they compete for primacy over the range of scenarios.

As we have such a wide parameter space — with 4 dependencies — we will start off by first looking at the weak sloshing cases (forcing amplitude $A^* = 2\times10^{-4}$). We will then sweep through in steps of increasing A^*. At each step we will discuss in a qualitative sense how mixing is affected by changes in the buoyancy, forcing amplitude, excitation frequency and fill height. We will then dig deeper, conducting a quantitative analysis of the relative enhancement of thermal mixing that can be achieved as a consequence of sloshing motions.

Thermal mixing within the liquid subsurface for low amplitude sloshing ($\boldsymbol{A^* = A/L_x = 2\times10^{-4}}$)

Figs. 7.30, 7.31 & 7.32 show how the temperature field evolves over time increments of $15s$ at $t = 15, 30, 45.60$s. In these figures, and throughout this section of the chapter we will show temperature contours relating only to the $\Delta T = 1$ initial condition, which is the least buoyant. Contours for the higher temperature conditions can be found in the appendix.

As we saw in the previous section, applying such a small forcing amplitude of $A^* = 2\times10^{-4}$ produces only a very minimal response from the free surface. Similarly to what was observed in the analysis of mixing in static tanks, the hot

blob rises towards the free surface and separates into symmetrical flow structures. The thermal is redirected laterally as it interacts with the free surface, with a small amount of heat lost to the air. For the shallow filled tanks, there is less potential built into the initial condition, and so the hot liquid is less able to circulate back down towards the tank's base.

The thermal flow fields are ever so slightly more diffuse for the odd modes, indicating that even very small wave motions can enhance thermal diffusion in the subsurface. However, these differences are so minor that we can say that in this regime the thermal mixing is fundamentally a buoyancy-driven process, and very much independent of the sloshing parameters.

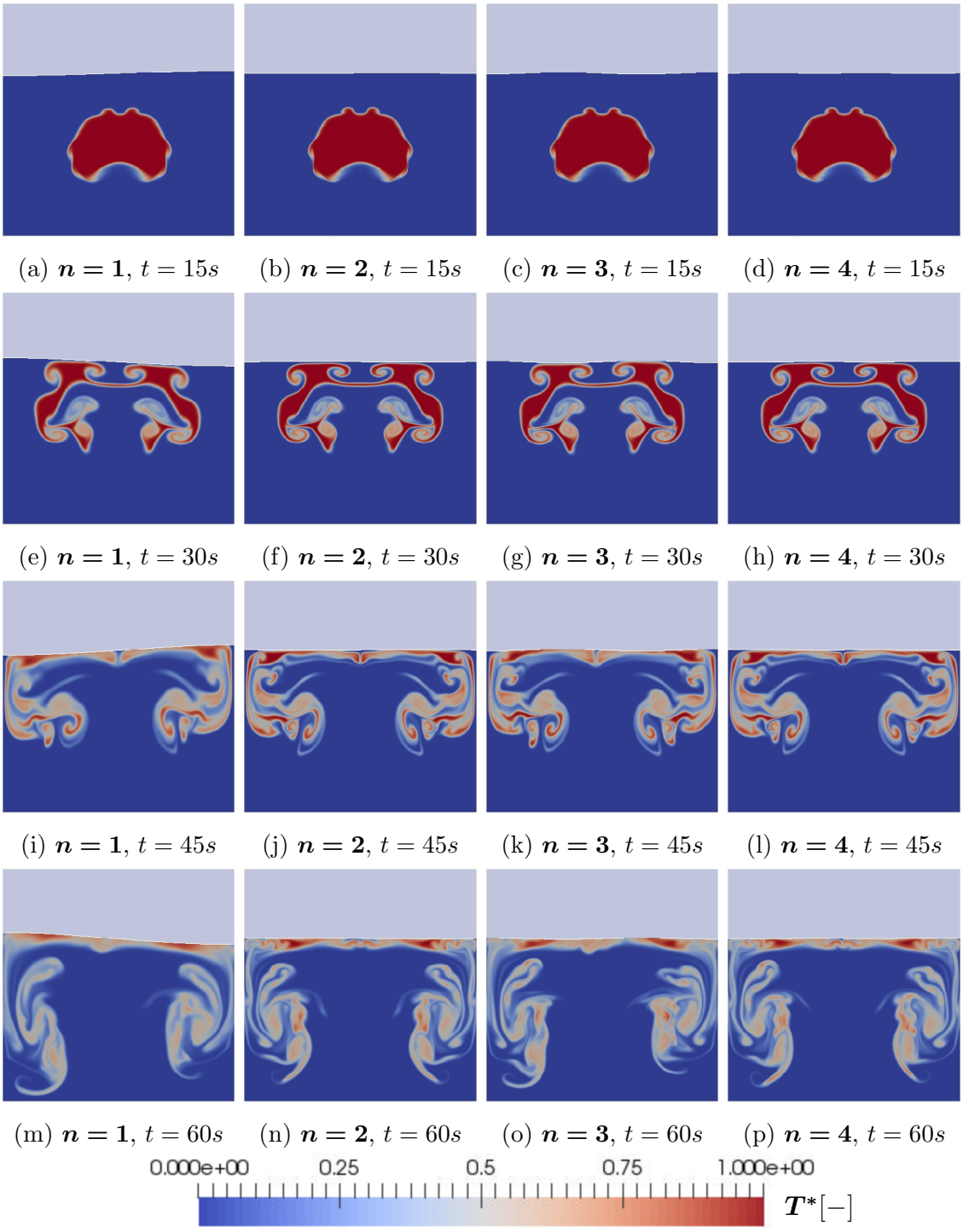

(a) $\boldsymbol{n = 1}$, $t = 15s$ (b) $\boldsymbol{n = 2}$, $t = 15s$ (c) $\boldsymbol{n = 3}$, $t = 15s$ (d) $\boldsymbol{n = 4}$, $t = 15s$

(e) $\boldsymbol{n = 1}$, $t = 30s$ (f) $\boldsymbol{n = 2}$, $t = 30s$ (g) $\boldsymbol{n = 3}$, $t = 30s$ (h) $\boldsymbol{n = 4}$, $t = 30s$

(i) $\boldsymbol{n = 1}$, $t = 45s$ (j) $\boldsymbol{n = 2}$, $t = 45s$ (k) $\boldsymbol{n = 3}$, $t = 45s$ (l) $\boldsymbol{n = 4}$, $t = 45s$

(m) $\boldsymbol{n = 1}$, $t = 60s$ (n) $\boldsymbol{n = 2}$, $t = 60s$ (o) $\boldsymbol{n = 3}$, $t = 60s$ (p) $\boldsymbol{n = 4}$, $t = 60s$

Figure 7.30: Scaled temperature, $T^* = (T - T_{\text{cold}})/(T_{\text{hot}} - T_{\text{cold}})$, for the first four modal frequencies, where $\boldsymbol{\Delta T = 1}$ and $\boldsymbol{h_{\text{f.s.}}/L_x = 0.7}$

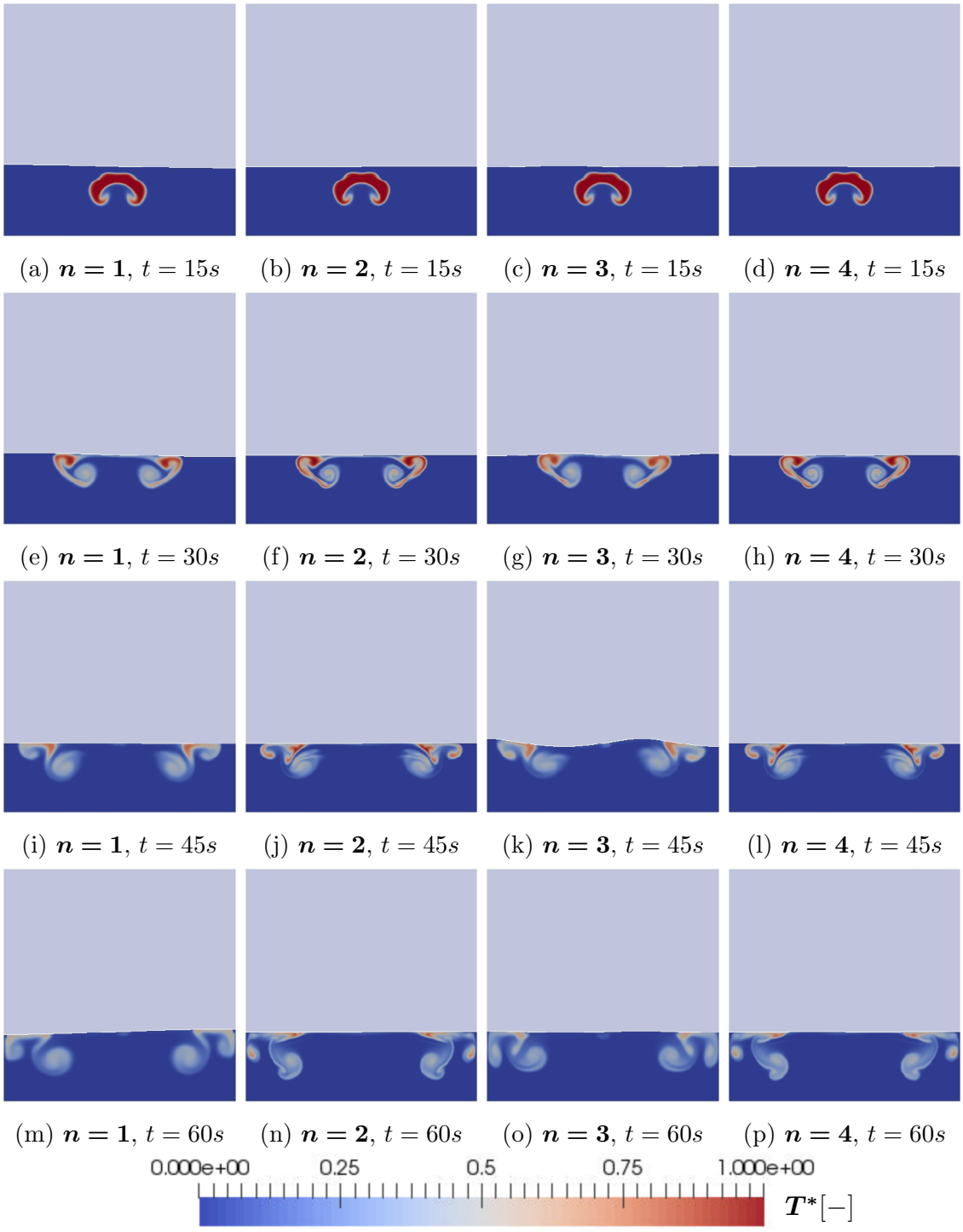

(a) $\boldsymbol{n = 1}$, $t = 15s$ (b) $\boldsymbol{n = 2}$, $t = 15s$ (c) $\boldsymbol{n = 3}$, $t = 15s$ (d) $\boldsymbol{n = 4}$, $t = 15s$

(e) $\boldsymbol{n = 1}$, $t = 30s$ (f) $\boldsymbol{n = 2}$, $t = 30s$ (g) $\boldsymbol{n = 3}$, $t = 30s$ (h) $\boldsymbol{n = 4}$, $t = 30s$

(i) $\boldsymbol{n = 1}$, $t = 45s$ (j) $\boldsymbol{n = 2}$, $t = 45s$ (k) $\boldsymbol{n = 3}$, $t = 45s$ (l) $\boldsymbol{n = 4}$, $t = 45s$

(m) $\boldsymbol{n = 1}$, $t = 60s$ (n) $\boldsymbol{n = 2}$, $t = 60s$ (o) $\boldsymbol{n = 3}$, $t = 60s$ (p) $\boldsymbol{n = 4}$, $t = 60s$

Figure 7.31: Scaled temperature, $T^* = (T - T_{\text{cold}})/(T_{\text{hot}} - T_{\text{cold}})$, for the first four modal frequencies, where $\boldsymbol{\Delta T = 1}$ and $\boldsymbol{h_{\text{f.s.}}/L_x = 0.3}$

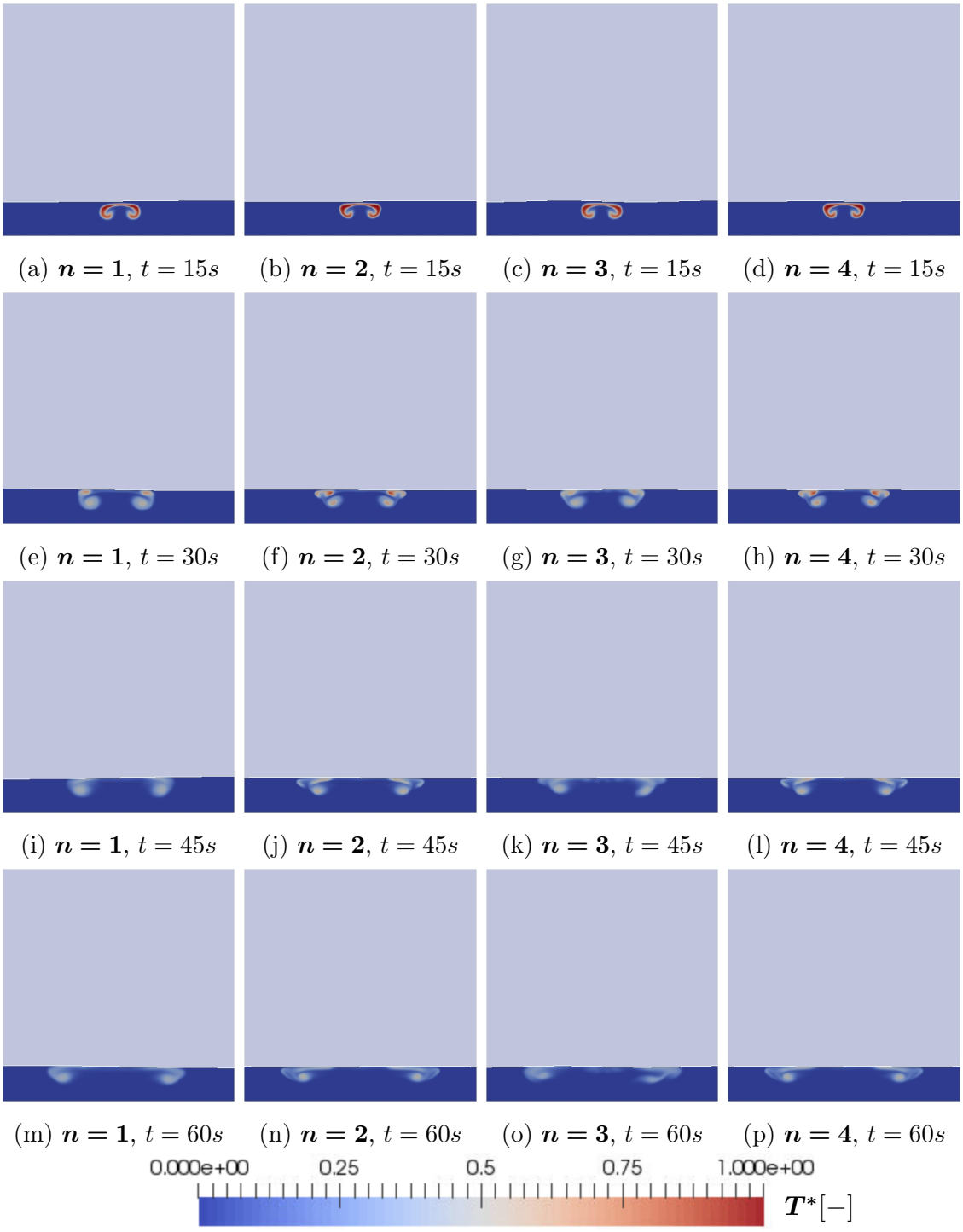

(a) $\boldsymbol{n = 1}$, $t = 15s$ (b) $\boldsymbol{n = 2}$, $t = 15s$ (c) $\boldsymbol{n = 3}$, $t = 15s$ (d) $\boldsymbol{n = 4}$, $t = 15s$

(e) $\boldsymbol{n = 1}$, $t = 30s$ (f) $\boldsymbol{n = 2}$, $t = 30s$ (g) $\boldsymbol{n = 3}$, $t = 30s$ (h) $\boldsymbol{n = 4}$, $t = 30s$

(i) $\boldsymbol{n = 1}$, $t = 45s$ (j) $\boldsymbol{n = 2}$, $t = 45s$ (k) $\boldsymbol{n = 3}$, $t = 45s$ (l) $\boldsymbol{n = 4}$, $t = 45s$

(m) $\boldsymbol{n = 1}$, $t = 60s$ (n) $\boldsymbol{n = 2}$, $t = 60s$ (o) $\boldsymbol{n = 3}$, $t = 60s$ (p) $\boldsymbol{n = 4}$, $t = 60s$

Figure 7.32: Scaled temperature, $T^* = (T - T_{\text{cold}})/(T_{\text{hot}} - T_{\text{cold}})$, for the first four modal frequencies, where $\boldsymbol{\Delta T = 1}$ and $\boldsymbol{h_{\text{f.s.}}/L_x = 0.15}$

Fig. 7.33 shows isosurfaces of $T^* = 0.1$, where $T^* = (T - T_{\text{cold}})/(T_{\text{hot}} - T_{\text{cold}})$ for two different initial temperature differences: $\Delta T = 1$ and $\Delta T = 16$ at equivalent buoyancy-scaled times t_b^*. In real time, this means the final row of figures are depicting isosurfaces from the $\Delta T = 1$ and $\Delta T = 16$ simulations at $t = 60s$ and $t = 7.5s$ respectively. Such close agreement between the isosurfaces when scaling to buoyancy time scales confirms that in this regime, thermal mixing is completely dominated by natural convection. Not only that, they are almost completely independent of excitation mode, further confirming that sloshing is making little difference to the development of flow structures in the subsurface.

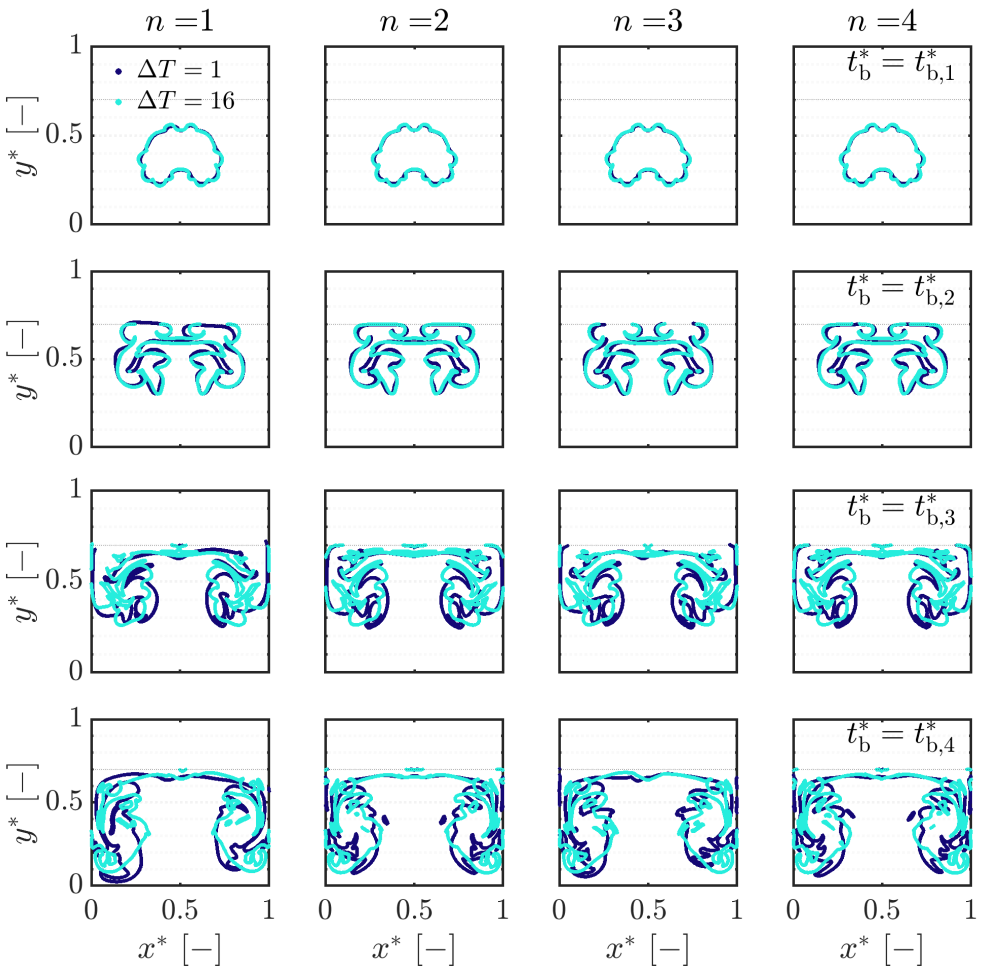

Figure 7.33: Isosurfaces of $T^* = 0.1$ at 4 equivalent scaled times, t_b^* at frequency modes $\boldsymbol{n = 1, 2, 3, 4}$, with external forcing amplitude $\boldsymbol{A^* = A/L_x = 2 \times 10^{-4}}$ and fill height ratio $\boldsymbol{h_{\text{f.s.}}/L_x = 0.7}$

Thermal mixing within the liquid subsurface for moderate amplitude sloshing ($A^* = A/L_x = 2 \times 10^{-3}$)

At a moderate forcing amplitude, we start to see sloshing play a more significant role for the $n = 1$ mode. Convective flow structures no longer develop in line with the other frequencies. For the deep (**Fig.** 7.34) and intermediate (**Fig.** 7.35) fill heights we can see the effects of turbulence from the surface disrupting the convective flow path. Recalling from **Fig.** 7.29 that at primary resonance, the intermediate fill tank yielded the greatest wave response relative to initial filling depth. **Figs.**7.35e & 7.35i show the process by which the liquid body is being stretched as the free surface expands and climbs the tank wall. These sloshing motions quickly result in a much more diffuse and homogeneous temperature profile beneath the surface. The $n = 3$ mode is now more active, although the temperature field is relatively less affected by surface motions than for the $n = 1$ mode. Temperature profiles for the even modes are almost identical to the weak sloshing cases we saw previously — buoyancy is still comfortably the dominating driver of mixing for the higher modes.

In the shallow tank (**Fig.** 7.36), only the $n = 3$ mode is producing enough of a dynamic response from the free surface to meaningfully affect the subsurface temperature field at this forcing amplitude.

For each of the tanks, the $n = 2$ mode is not generating enough surface motion to affect mixing at all.

In **Fig.** 7.37, we again use isosurfaces of $T^* = 0.1$ to check for deviations away from the buoyancy scaling in the deep tank. The $n = 1$ mode no longer share such close agreement. This suggests that for the deep tank at least, we are now entering a transitionary regime in which both sloshing and natural convection are of comparable importance. For the odd modes, there is another interesting development at the centre of the tank beneath the surface. Warm liquid is being carried down and away from the surface by some flow structure (see **Figs.** 7.37c

& 7.37d) that is growing over time. That this is less developed in the $\Delta T = 16$ isosurface confirms that these flow structures are not tied to the buoyancy time-scales and is instead generated by the action of the free surface motions.

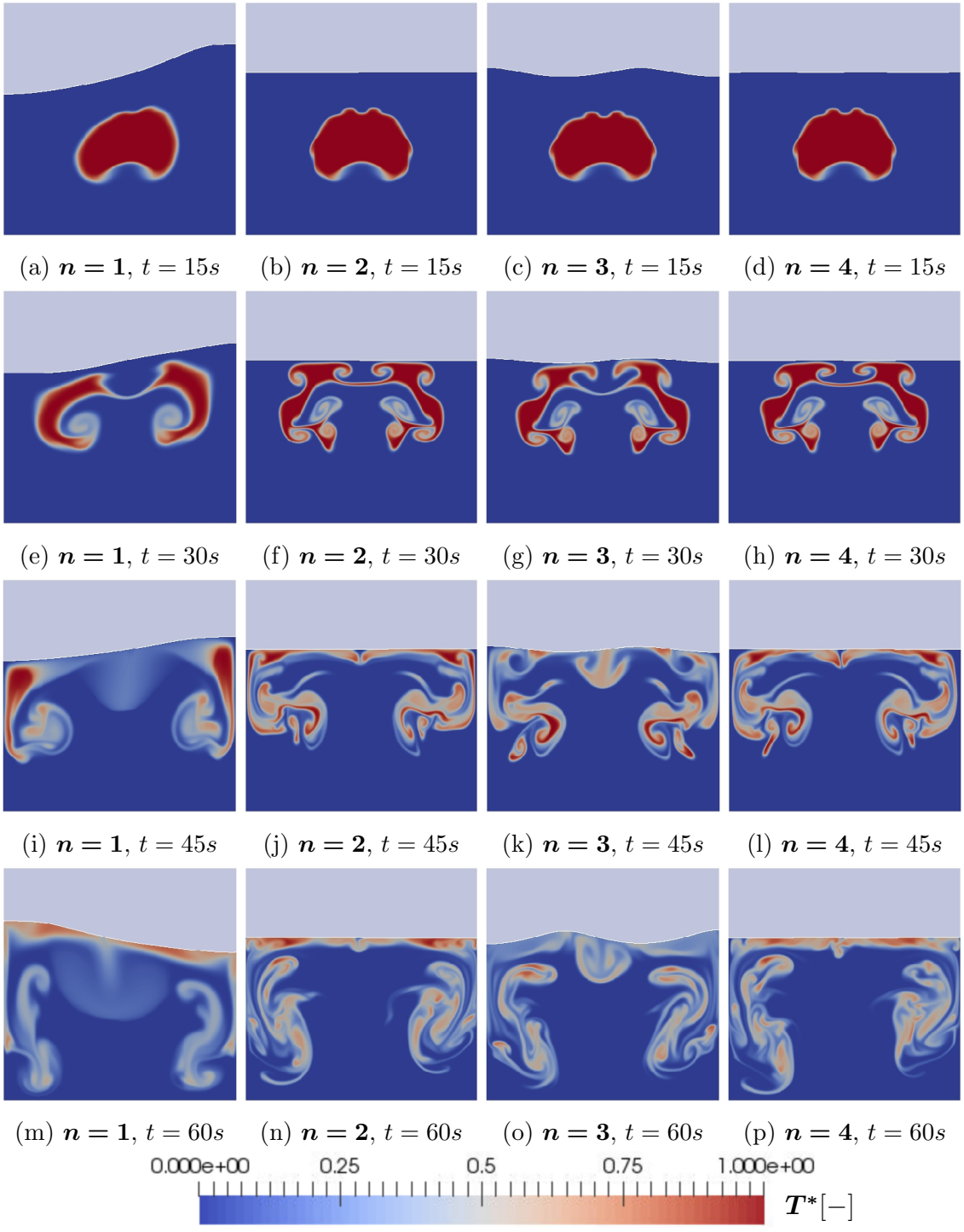

Figure 7.34: Scaled temperature, $T^* = (T - T_{\text{cold}})/(T_{\text{hot}} - T_{\text{cold}})$, for the first four modal frequencies, where $\boldsymbol{\Delta T = 1}$ and $\boldsymbol{h_{\text{f.s.}}/L_x = 0.7}$

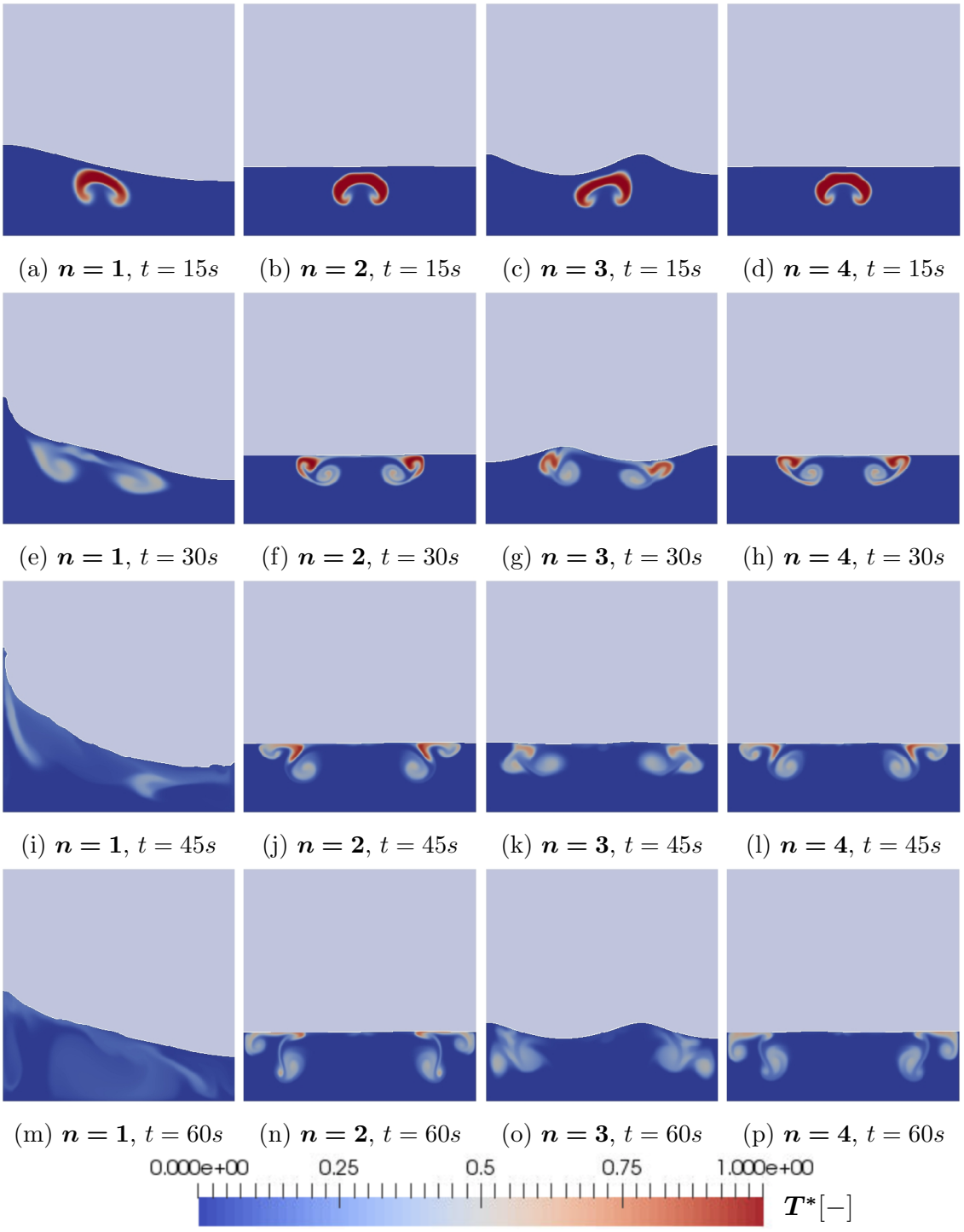

(a) $\boldsymbol{n = 1}$, $t = 15s$ (b) $\boldsymbol{n = 2}$, $t = 15s$ (c) $\boldsymbol{n = 3}$, $t = 15s$ (d) $\boldsymbol{n = 4}$, $t = 15s$

(e) $\boldsymbol{n = 1}$, $t = 30s$ (f) $\boldsymbol{n = 2}$, $t = 30s$ (g) $\boldsymbol{n = 3}$, $t = 30s$ (h) $\boldsymbol{n = 4}$, $t = 30s$

(i) $\boldsymbol{n = 1}$, $t = 45s$ (j) $\boldsymbol{n = 2}$, $t = 45s$ (k) $\boldsymbol{n = 3}$, $t = 45s$ (l) $\boldsymbol{n = 4}$, $t = 45s$

(m) $\boldsymbol{n = 1}$, $t = 60s$ (n) $\boldsymbol{n = 2}$, $t = 60s$ (o) $\boldsymbol{n = 3}$, $t = 60s$ (p) $\boldsymbol{n = 4}$, $t = 60s$

Figure 7.35: Scaled temperature, $T^* = (T - T_{\text{cold}})/(T_{\text{hot}} - T_{\text{cold}})$, for the first four modal frequencies, where $\boldsymbol{\Delta T = 1}$ and $\boldsymbol{h_{\text{f.s.}}/L_x = 0.3}$

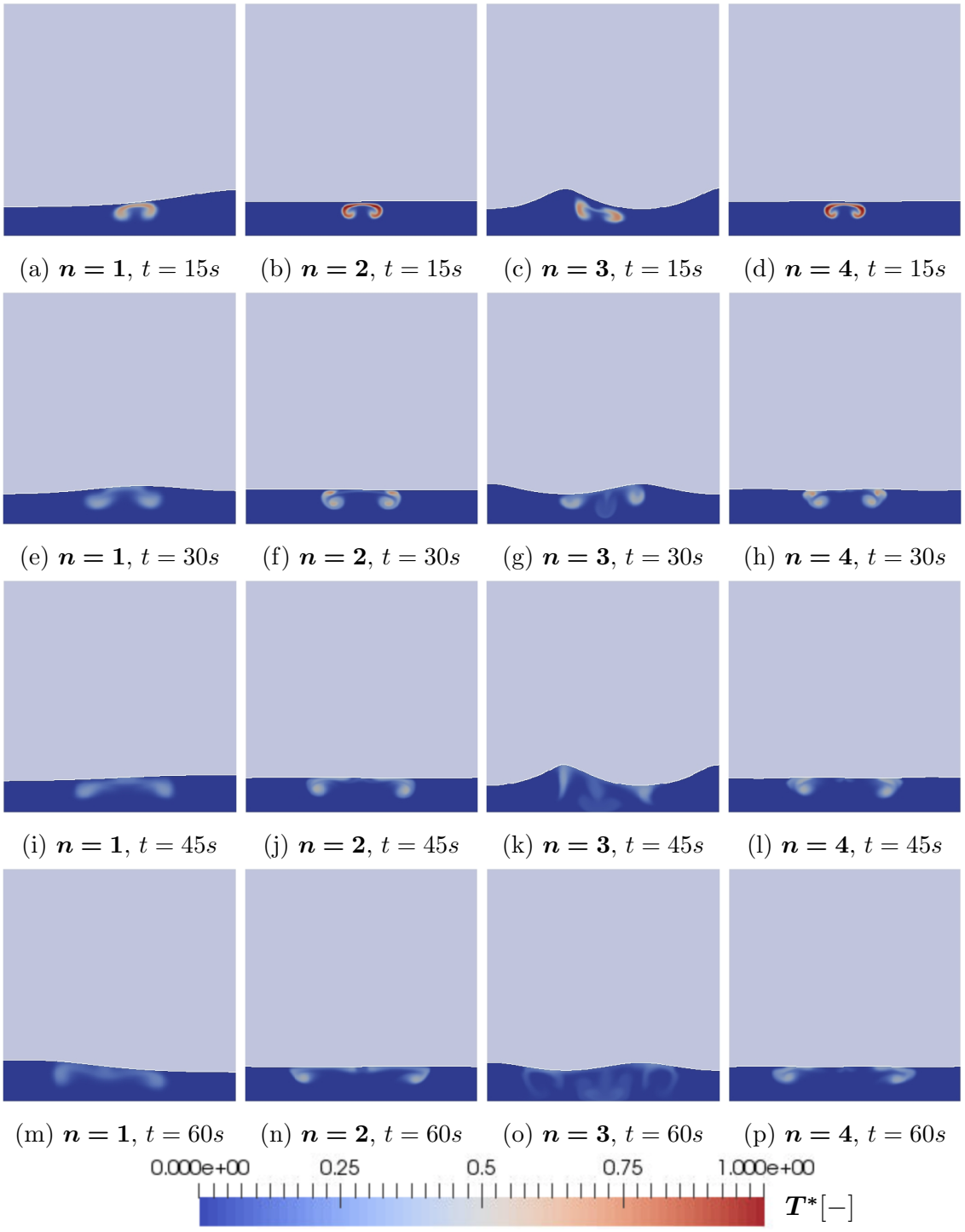

(a) $\boldsymbol{n = 1}$, $t = 15s$ (b) $\boldsymbol{n = 2}$, $t = 15s$ (c) $\boldsymbol{n = 3}$, $t = 15s$ (d) $\boldsymbol{n = 4}$, $t = 15s$

(e) $\boldsymbol{n = 1}$, $t = 30s$ (f) $\boldsymbol{n = 2}$, $t = 30s$ (g) $\boldsymbol{n = 3}$, $t = 30s$ (h) $\boldsymbol{n = 4}$, $t = 30s$

(i) $\boldsymbol{n = 1}$, $t = 45s$ (j) $\boldsymbol{n = 2}$, $t = 45s$ (k) $\boldsymbol{n = 3}$, $t = 45s$ (l) $\boldsymbol{n = 4}$, $t = 45s$

(m) $\boldsymbol{n = 1}$, $t = 60s$ (n) $\boldsymbol{n = 2}$, $t = 60s$ (o) $\boldsymbol{n = 3}$, $t = 60s$ (p) $\boldsymbol{n = 4}$, $t = 60s$

Figure 7.36: Scaled temperature, $T^* = (T - T_{\text{cold}})/(T_{\text{hot}} - T_{\text{cold}})$, for the first four modal frequencies, where $\boldsymbol{\Delta T = 1}$ and $\boldsymbol{h_{\text{f.s.}}/L_x = 0.15}$

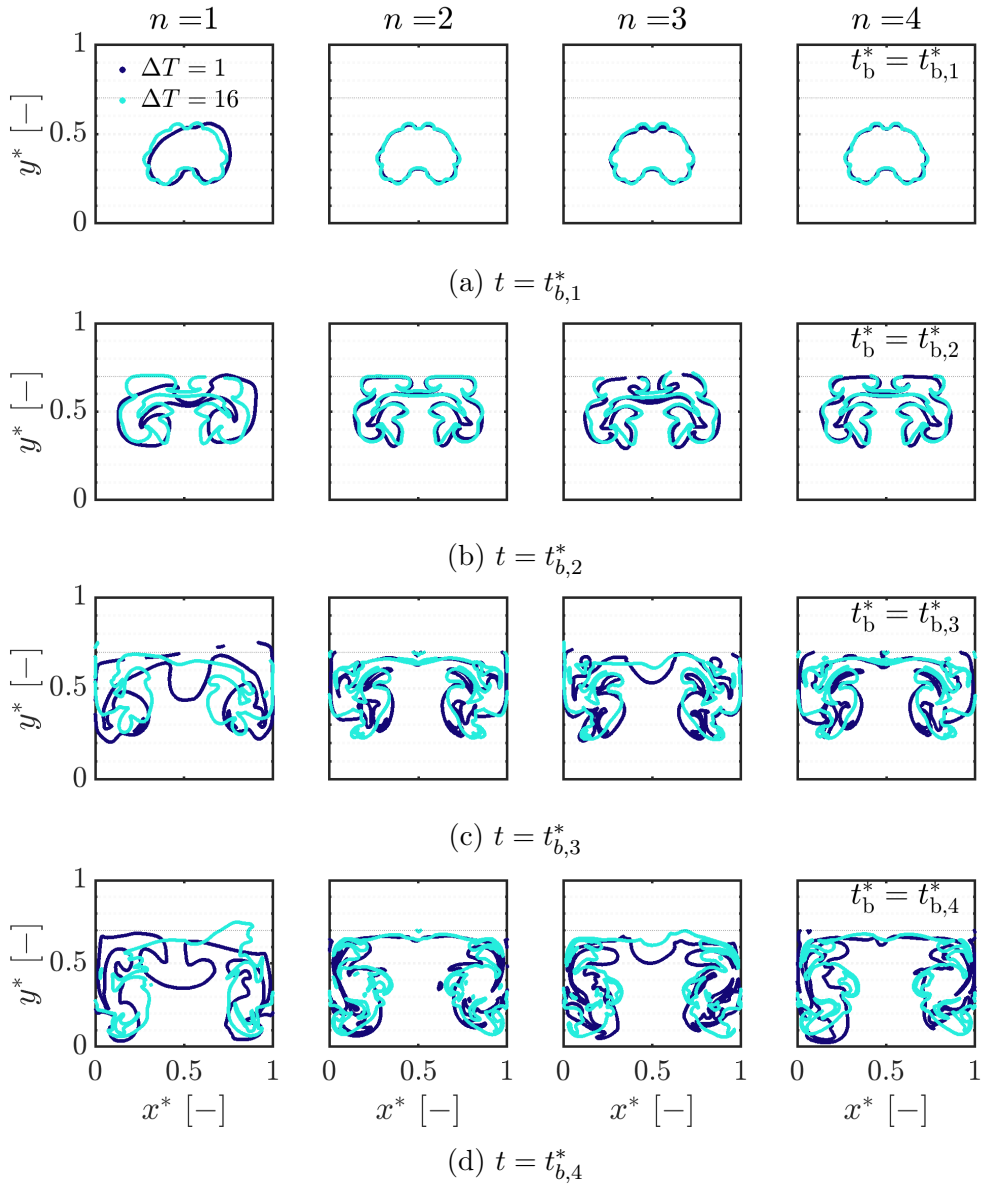

(a) $t = t^*_{b,1}$

(b) $t = t^*_{b,2}$

(c) $t = t^*_{b,3}$

(d) $t = t^*_{b,4}$

Figure 7.37: Isosurfaces of $T^* = 0.1$ at 4 equivalent scaled times, t^*_b at frequency modes $\boldsymbol{n = 1, 2, 3, 4}$, with external forcing amplitude $\boldsymbol{A^* = A/L_x = 2 \times 10^{-3}}$ and fill height ratio $\boldsymbol{h_{\text{f.s.}}/L_x = 0.7}$

Thermal mixing within the liquid subsurface for high amplitude sloshing ($A^* = A/L_x = 2 \times 10^{-2}$)

In tanks subjected to high amplitude excitations, thermal mixing is enhanced considerably. In the deep fill tank (**Fig.** 7.38), the thermal is twisted, stretched and broken up as the hot fluid ascends and interacts with the dynamic surface region. Heat is dissipated through the subsurface at a much quicker rate than at lower amplitudes. The role of sloshing is now an important contributor across all four modes. Interestingly, despite being much weaker at lower forcing amplitudes, excitation at the $n = 4$ mode is now matching the primary frequency in terms of it's effectiveness at enhancing mixing. Overturning waves are generating a highly turbulent surf zone beneath the surface.

Thermal mixing now occurs so quickly in the intermediate and shallow depth cases that in **Figs.** 7.39 & 7.40 we plot temperature contours only up to $t = 30s$ and $t = 20s$ respectively. Plotting contours after this would show nothing interesting due to the homogeneity of the temperature field

At shallower fill depths, when the tank is excited at the primary frequency $n = 1$, the hot fluid becomes stretched due to the large displacements experienced by the liquid as it sloshes laterally from side-to-side. Good examples of this can be seen in **Figs.** 7.39i & 7.40e which show the hot fluid far removed from the centre-line well before it has had the chance to ascend to the surface. With the exception of $n = 2$, thermal flow structures that were able to persist at lower excitation amplitudes are now broken up by the slosh-induced motions and enhanced diffusivity of the locally turbulent flow field. Again, the $n = 4$ modal is now shown to yield highly effective mixing properties.

Again, we use isosurfaces of $T^* = 0.1$ to demonstrate that at this forcing amplitude, the evolution of the temperature field has become firmly de-coupled from the buoyancy time-scales in the deep tank (**Fig.** 7.41).

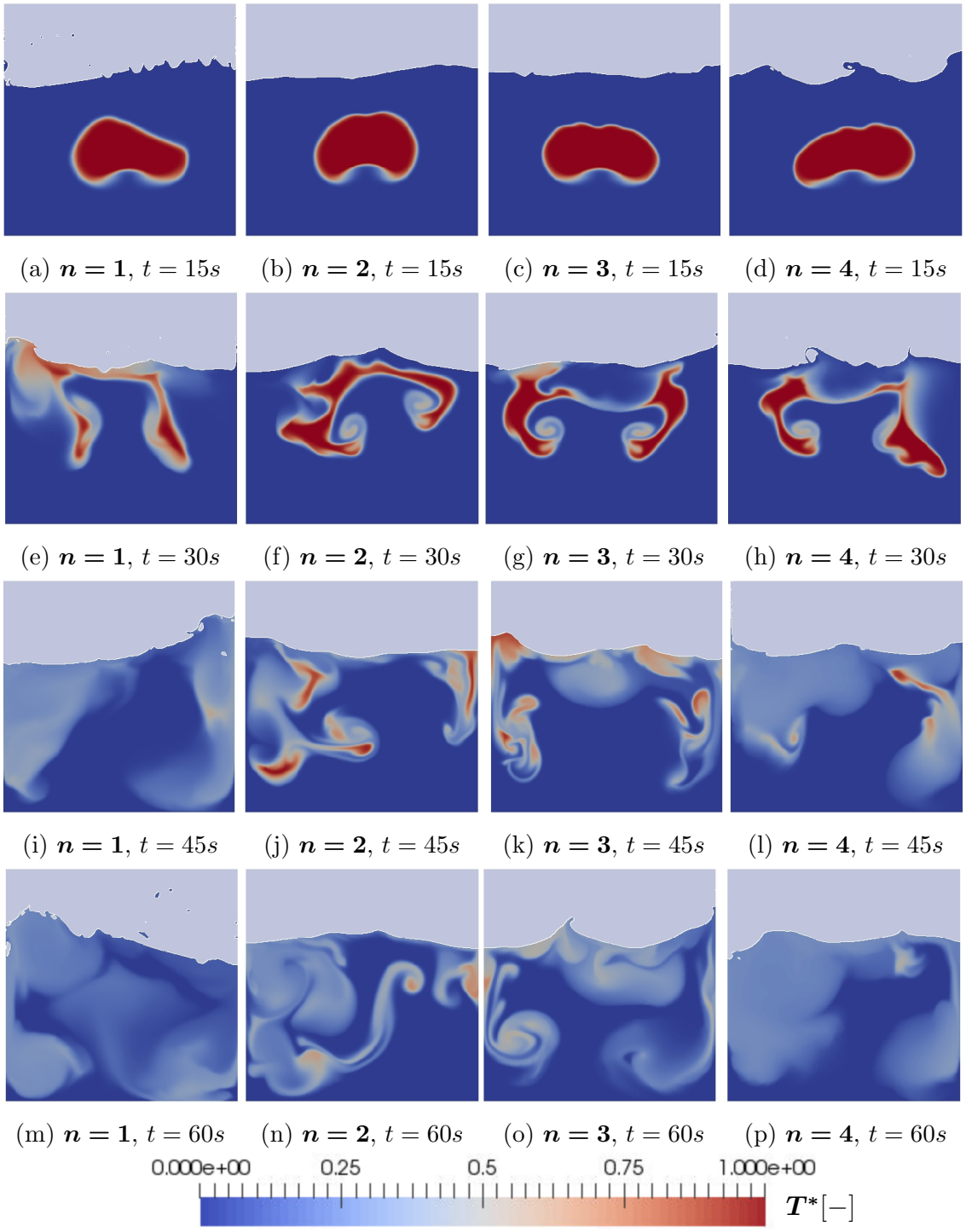

(a) $\boldsymbol{n = 1}$, $t = 15s$ (b) $\boldsymbol{n = 2}$, $t = 15s$ (c) $\boldsymbol{n = 3}$, $t = 15s$ (d) $\boldsymbol{n = 4}$, $t = 15s$

(e) $\boldsymbol{n = 1}$, $t = 30s$ (f) $\boldsymbol{n = 2}$, $t = 30s$ (g) $\boldsymbol{n = 3}$, $t = 30s$ (h) $\boldsymbol{n = 4}$, $t = 30s$

(i) $\boldsymbol{n = 1}$, $t = 45s$ (j) $\boldsymbol{n = 2}$, $t = 45s$ (k) $\boldsymbol{n = 3}$, $t = 45s$ (l) $\boldsymbol{n = 4}$, $t = 45s$

(m) $\boldsymbol{n = 1}$, $t = 60s$ (n) $\boldsymbol{n = 2}$, $t = 60s$ (o) $\boldsymbol{n = 3}$, $t = 60s$ (p) $\boldsymbol{n = 4}$, $t = 60s$

Figure 7.38: Scaled temperature, $T^* = (T - T_{\text{cold}})/(T_{\text{hot}} - T_{\text{cold}})$, for the first four modal frequencies, where $\boldsymbol{\Delta T = 1}$ and $\boldsymbol{h_{\text{f.s.}}/L_x = 0.7}$

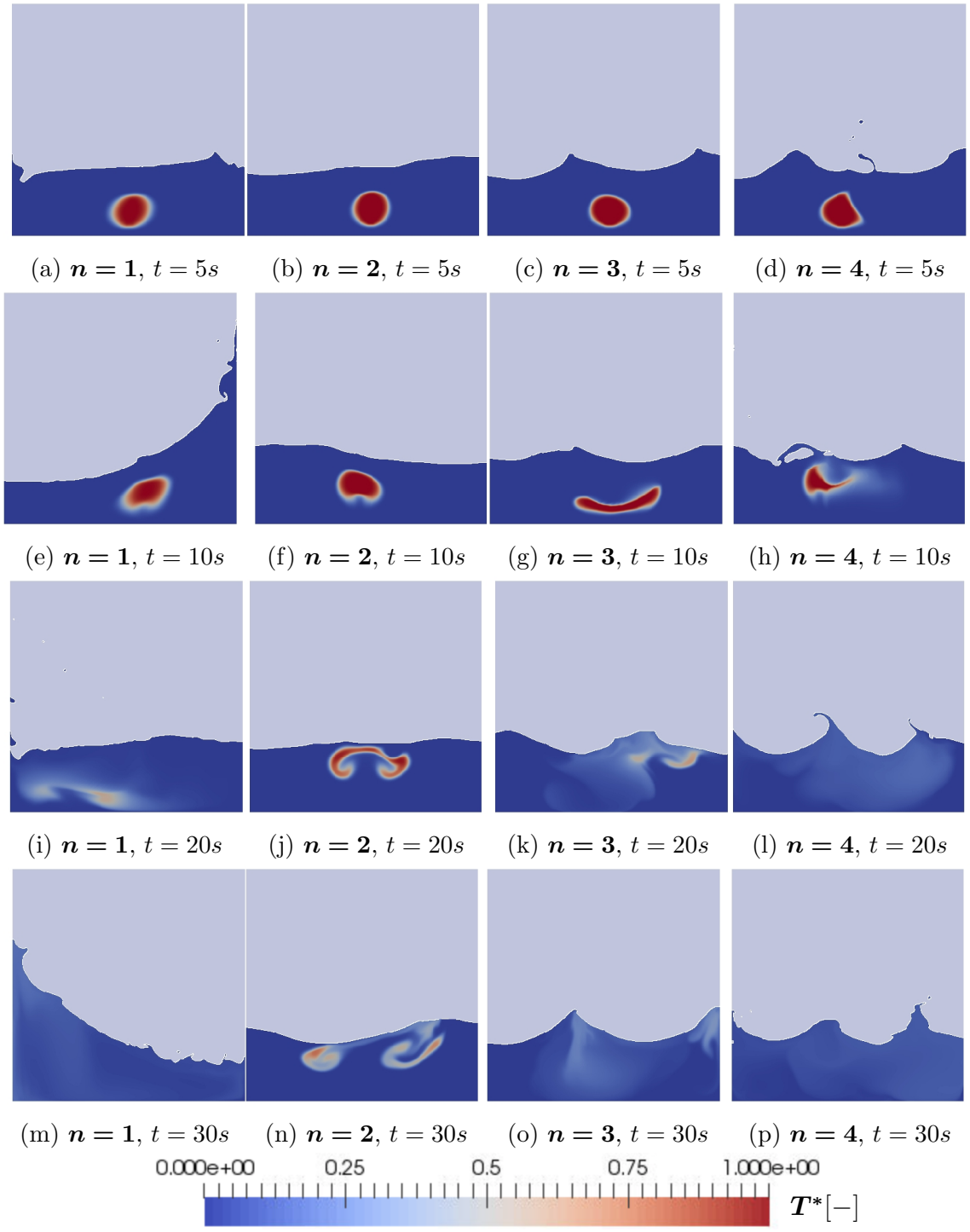

(a) $\boldsymbol{n = 1}$, $t = 5s$ (b) $\boldsymbol{n = 2}$, $t = 5s$ (c) $\boldsymbol{n = 3}$, $t = 5s$ (d) $\boldsymbol{n = 4}$, $t = 5s$

(e) $\boldsymbol{n = 1}$, $t = 10s$ (f) $\boldsymbol{n = 2}$, $t = 10s$ (g) $\boldsymbol{n = 3}$, $t = 10s$ (h) $\boldsymbol{n = 4}$, $t = 10s$

(i) $\boldsymbol{n = 1}$, $t = 20s$ (j) $\boldsymbol{n = 2}$, $t = 20s$ (k) $\boldsymbol{n = 3}$, $t = 20s$ (l) $\boldsymbol{n = 4}$, $t = 20s$

(m) $\boldsymbol{n = 1}$, $t = 30s$ (n) $\boldsymbol{n = 2}$, $t = 30s$ (o) $\boldsymbol{n = 3}$, $t = 30s$ (p) $\boldsymbol{n = 4}$, $t = 30s$

Figure 7.39: Scaled temperature, $T^* = (T - T_{\text{cold}})/(T_{\text{hot}} - T_{\text{cold}})$, for the first four modal frequencies, where $\boldsymbol{\Delta T = 1}$ and $\boldsymbol{h_{\text{f.s.}}/L_x = 0.3}$

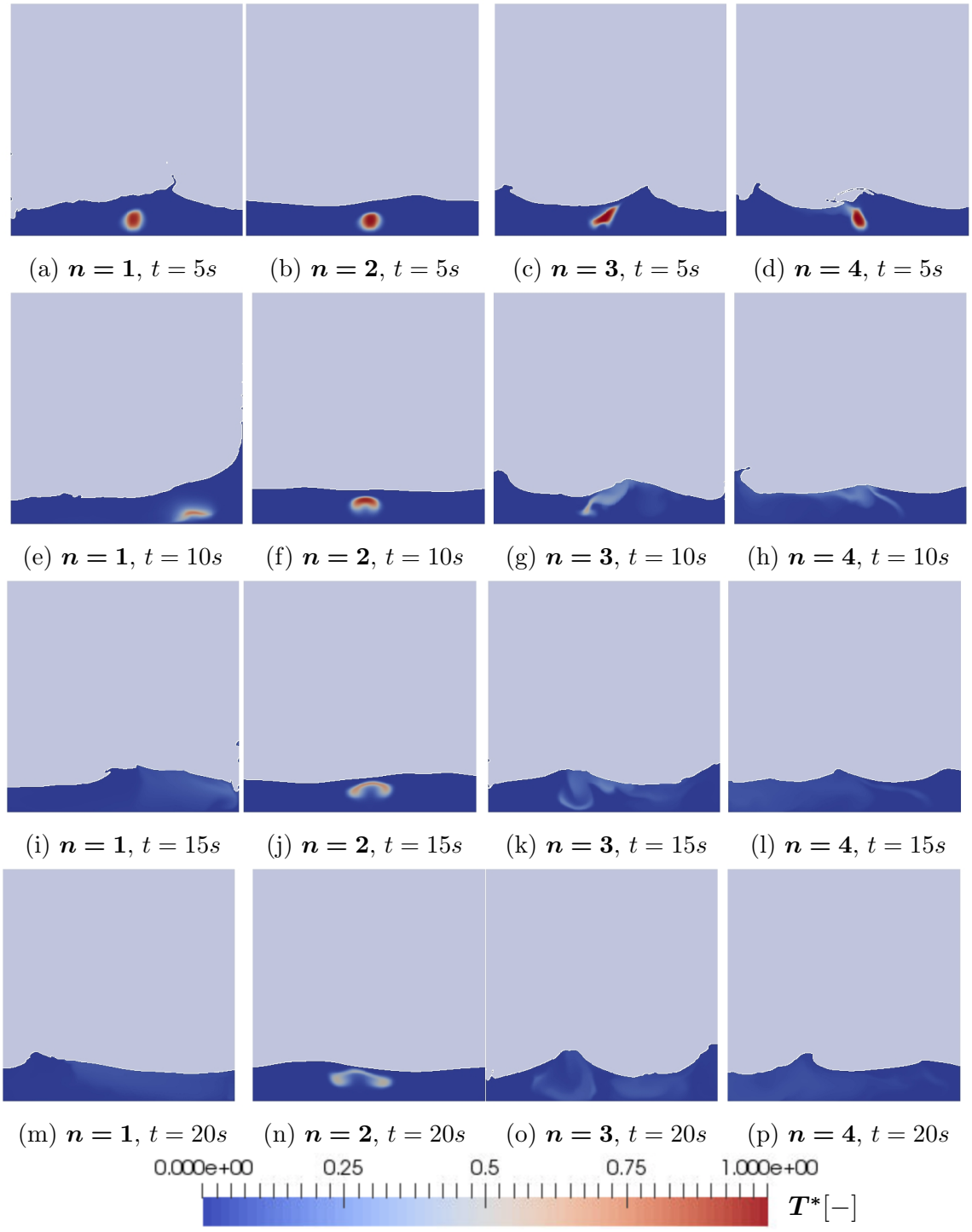

(a) $\boldsymbol{n = 1}$, $t = 5s$ (b) $\boldsymbol{n = 2}$, $t = 5s$ (c) $\boldsymbol{n = 3}$, $t = 5s$ (d) $\boldsymbol{n = 4}$, $t = 5s$

(e) $\boldsymbol{n = 1}$, $t = 10s$ (f) $\boldsymbol{n = 2}$, $t = 10s$ (g) $\boldsymbol{n = 3}$, $t = 10s$ (h) $\boldsymbol{n = 4}$, $t = 10s$

(i) $\boldsymbol{n = 1}$, $t = 15s$ (j) $\boldsymbol{n = 2}$, $t = 15s$ (k) $\boldsymbol{n = 3}$, $t = 15s$ (l) $\boldsymbol{n = 4}$, $t = 15s$

(m) $\boldsymbol{n = 1}$, $t = 20s$ (n) $\boldsymbol{n = 2}$, $t = 20s$ (o) $\boldsymbol{n = 3}$, $t = 20s$ (p) $\boldsymbol{n = 4}$, $t = 20s$

Figure 7.40: Scaled temperature, $T^* = (T - T_{\text{cold}})/(T_{\text{hot}} - T_{\text{cold}})$, for the first four modal frequencies, where $\boldsymbol{\Delta T = 1}$ and $\boldsymbol{h_{\text{f.s.}}/L_x = 0.15}$

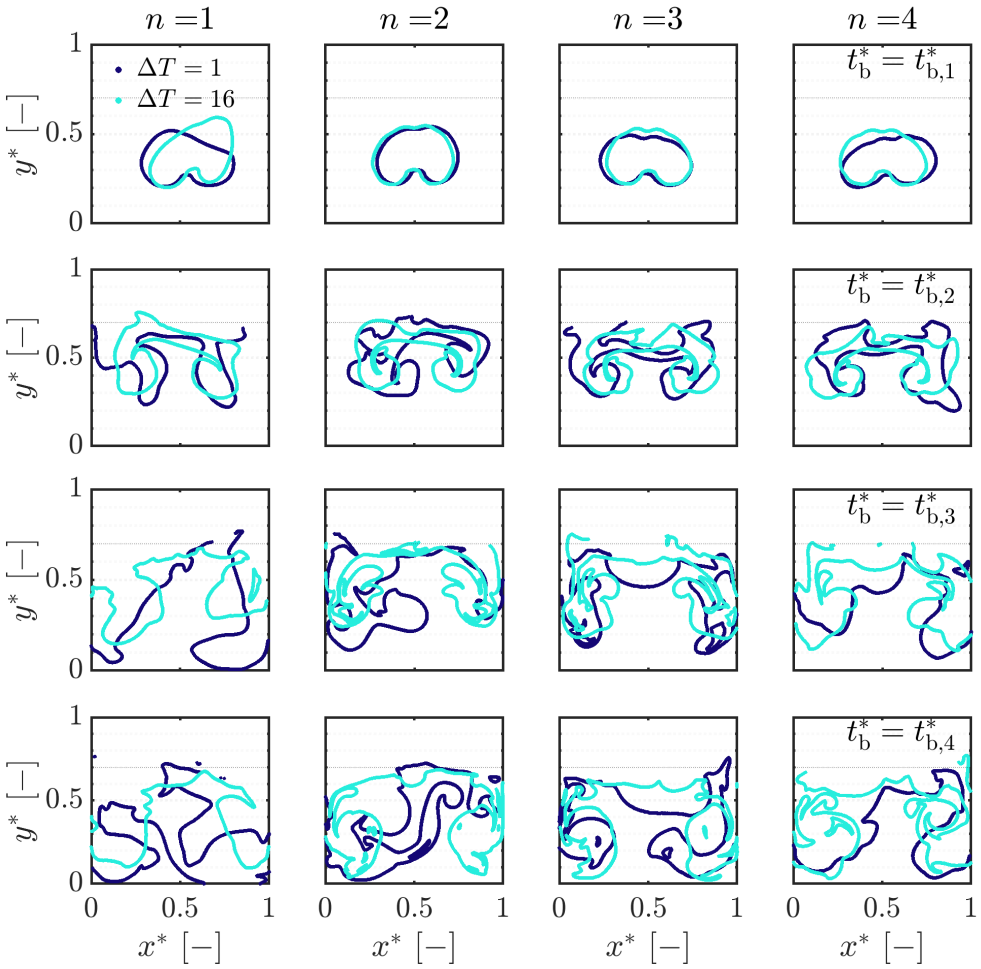

Figure 7.41: Isosurfaces of $T^* = 0.1$ at 4 equivalent scaled times, t_b^* at frequency modes $\boldsymbol{n = 1, 2, 3, 4}$, with external forcing amplitude $\boldsymbol{A^* = A/L_x = 2 \times 10^{-2}}$ and fill height ratio $\boldsymbol{h_{f.s.}/L_x = 0.7}$

7.3.4 Quantitative assessment of thermal mixing as a function of buoyancy, frequency and amplitude of excitation at different fill heights

Method of thermal mixing assessment

From a qualitative view-point, the shift in balance of sloshing and buoyancy-dominated mixing has been shown to be highly sensitive to the parameters. Now, we will undertake a quantitative analysis to help further understand these dependencies. In order to assess mixing rates we will use a two step process. The first step will be to simply take a crude measurement of the normalised coefficient of variation V^*, of the temperature field at time $t = 60s$, where:

$$V^*_{t=60} = \frac{V(t=60)}{V(t=0)}. \tag{7.11}$$

This gives us a measure of how uniform the subsurface temperature field has become after 60s relative to the variation inherent to the initial condition. To isolate and delineate just how much of that homogenisation is due to the sloshing contributions rather than through natural convection and diffusion, the final temperature field variation is then scaled to the baseline case of an equivalent static case in which thermal mixing is driven by natural convection and diffusion alone. This is done for each combination of fill height and initial temperature difference, and expressed as a mixing enhancement factor, E_{mix}. For example, for the fill height $h_{\text{fs}}/L_x = 0.15$ case with initial temperature difference of $\Delta T = 16$, each of the sloshing simulations with varying amplitude and frequency corresponding to that scenario will be scaled to the equivalent static tank case such that:

$$E_{\text{mix}} = \frac{V^*_{\text{t=60s,static}}}{V^*_{\text{t=60s,sloshing}}}. \tag{7.12}$$

This is done for two reasons. Firstly, increasing the initial temperature difference increases the potential energy of the system and so mixing through natural convection is inevitably faster. This factor is now eliminated by scaling to the equivalent static case for that temperature condition. Secondly, it also eliminates any factors that would unfairly differentiate each scenario e.g. the fact that as the initial filling height is reduced, due to the change in length scales, not only is the buoyancy reduced but so too is the distance between the initial position of the hot blob and the free surface. In this sense, we are trying as best possible to eliminate anything that is special about the initial conditions and instead reflect only what is special about the system's behaviour thereafter.

Limitations of the method

A limitation of this approach is that expressing the effectiveness of mixing through an 'enhancement factor' is undoubtedly sensitive to the time at which these measurements are taken. For sure we know that at $t = 0$, $V^*_{\text{static}}/V^*_{\text{sloshing}} = 1$. Through the action of molecular thermal diffusion alone, in a closed system with adiabatic walls, we can also be certain that as $t \to \infty$, $V^*_{\text{static}}(t)/V^*_{\text{sloshing}}(t) \to 1$. The enhancement factor might take any positive value at any time in between. Taking measurements at $t = 60s$ might seem like some arbitrary choice. However this was chosen so as to allow time for the system to evolve enough to be able to pull out some meaningful observations about the mixing process, but not so much time such that the temperature field has become well mixed and uniform regardless of the parameters. Despite this, these limitations are acknowledged.

Fig. 7.42 shows the normalised subsurface temperature variation at time $t = 60s$, plotted as a function of forcing amplitude. Each curve corresponds to an initial temperature difference, with each sub-figure corresponding to a modal frequency of excitation $\omega_n = \omega_1 \rightarrow \omega_4$. The two least buoyant temperature condition curves ($\Delta T = 1, 4$) behave quite similarly, which we will discuss first. We will focus on the $\Delta T = 16$ case separately as this scenario gives rise to some interesting behaviour.

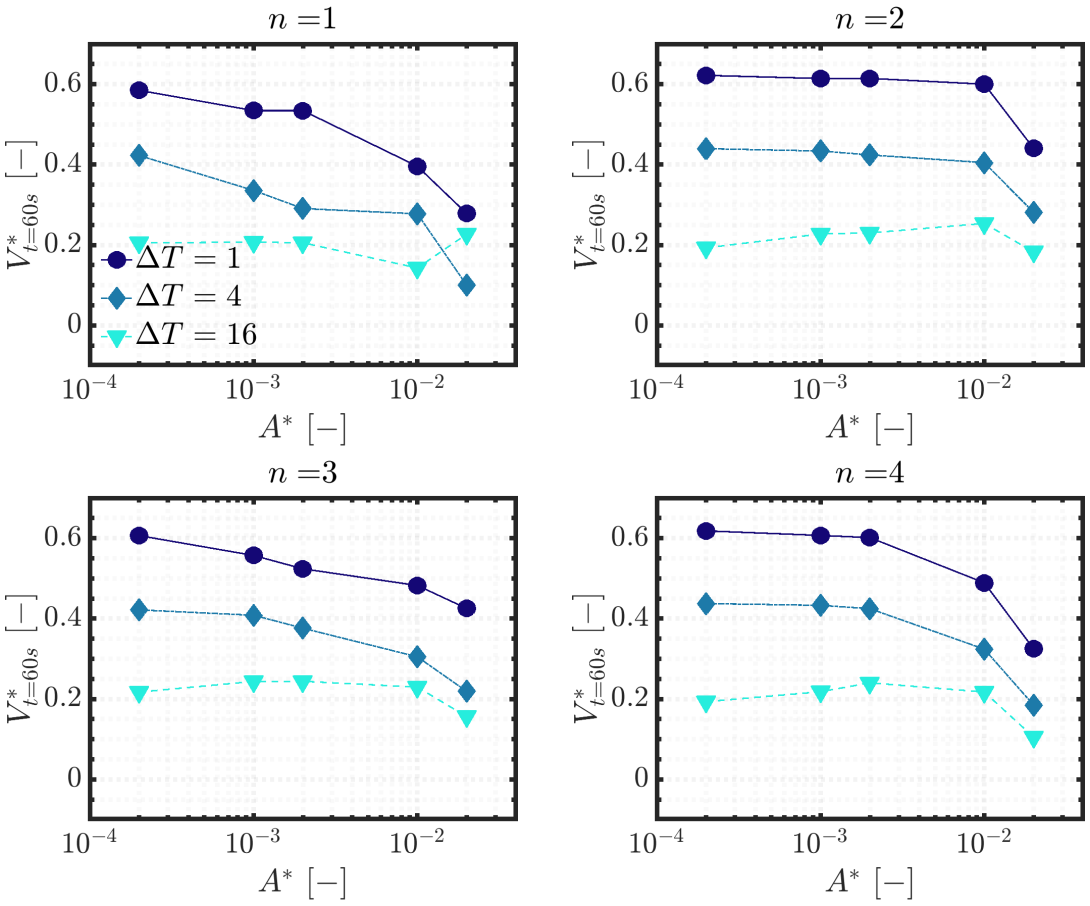

Figure 7.42: Variation of the temperature field, V^* at $t = 60s$, vs forcing amplitude A^*, with $h_{\text{fs}}/L_x = 0.7$

For $n = 1$, the curves descend together with an offset that converges slightly at high amplitudes. The off-set tells us that buoyancy is playing a significant role in the rate of mixing. That the curves are also steadily descending as a function of amplitude tells us that this is balanced by sloshing contributions as the forcing am-

plitude ramps up. The $n = 3$ curves follow similar but less steep profiles, suggesting a mixing rate slightly less sensitive to forcing amplitude.

For $n = 2$, the curves are again offset, but almost completely flat until reaching the maximum forcing amplitude where we finally see the mixing enhanced by sloshing motions. This tells us that for $n = 2$, the rate of mixing is completely driven by buoyancy up until only very high amplitude sloshing. This reflects the relatively weak free surface response that was consistently observed for this mode in the previous section. The $n = 4$ curves are similarly flat up until $A^* = 2 \times 10^{-3}$, at which point the sloshing begins to enhance mixing. Following on from the pattern that emerged when measuring wave response, this suggests a general trend in that the symmetric wave modes tend to produce inferior mixing conditions at lower forcing amplitudes in comparison to the anti-symmetric modes.

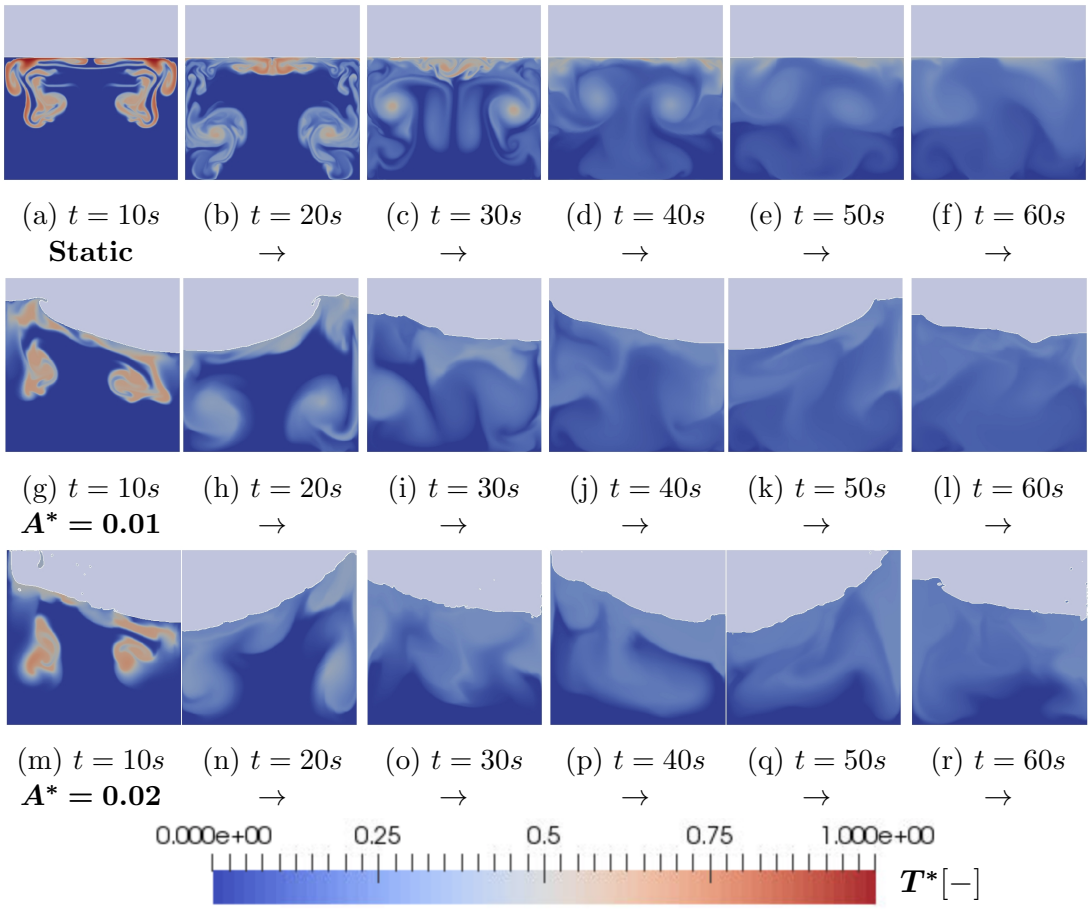

Figure 7.43: Temperature contours for the $\boldsymbol{n = 1}$ mode with initial temperature difference $\boldsymbol{\Delta T = 16}$

Now focussing on the most buoyant case, it is evident that the $\Delta T = 16$ curves in **Fig.** 7.42 behaves quite differently to the others. In particular, if we look at the data points for the $n = 1$ modal frequency, the greatest variation (i.e. least mixed) in the temperature field at $t = 60s$ actually occurs at the highest forcing amplitude. There is a significant jump in $V^*_{\mathrm{t=60s}}$ for the last two data points, which belies the fact that we are in fact doubling the forcing amplitude between each of those simulations. The other modes also show similar, if less extreme behaviour in that the mixing seems to be at times suppressed slightly with increased excitation amplitude. This is unexpected and certainly sounds counter-intuitive — so what is happening?

Fig. 7.43 shows the evolution of the temperature field at intervals of $\Delta t = 10s$ for the static tank and the two highest amplitude sloshing cases, $A^* = 0.01, 0.02$. Even without external excitation, the static tank does a fairly good job of self-mixing due to the amount of potential energy contained within the initial instability. With assistance from sloshing motions, the liquid temperature field in the $A^* = 0.01$ case is more homogeneous than for the static tank case. For the $A^* = 0.02$ case, we see a fairly large cold region (**Fig.** 7.43r) still present near the tank base after $60s$ has passed. This presents an interesting case in which it appears that interactions with the free surface are inhibiting the convective flow structures from distributing heat throughout the tank as effectively.

Presenting mixing rates for what is a 4D parameter space is challenging. In **Fig.** 7.44 we attempt to simultaneously tackle 3 of the 4 parameters by plotting a contour map to compliment **Fig.** 7.42 and help illustrate the relative sensitivities and inter-dependencies each parameter. Horizontal and vertical axes in each sub-figure represent the forcing amplitude and frequency mode respectively. Each row of sub-figures represents data from an initial temperature condition ($\Delta T = 1, 4, 16$). Sub-figures in the left column of contour maps are coloured by magnitude of $V^*_{\mathrm{t=60s}}$, while the plots in the right column are coloured by $log_{10}(E_{\mathrm{mix}})$. The colour-bars are

orientated such that in each case, dark blue represents faster mixing.

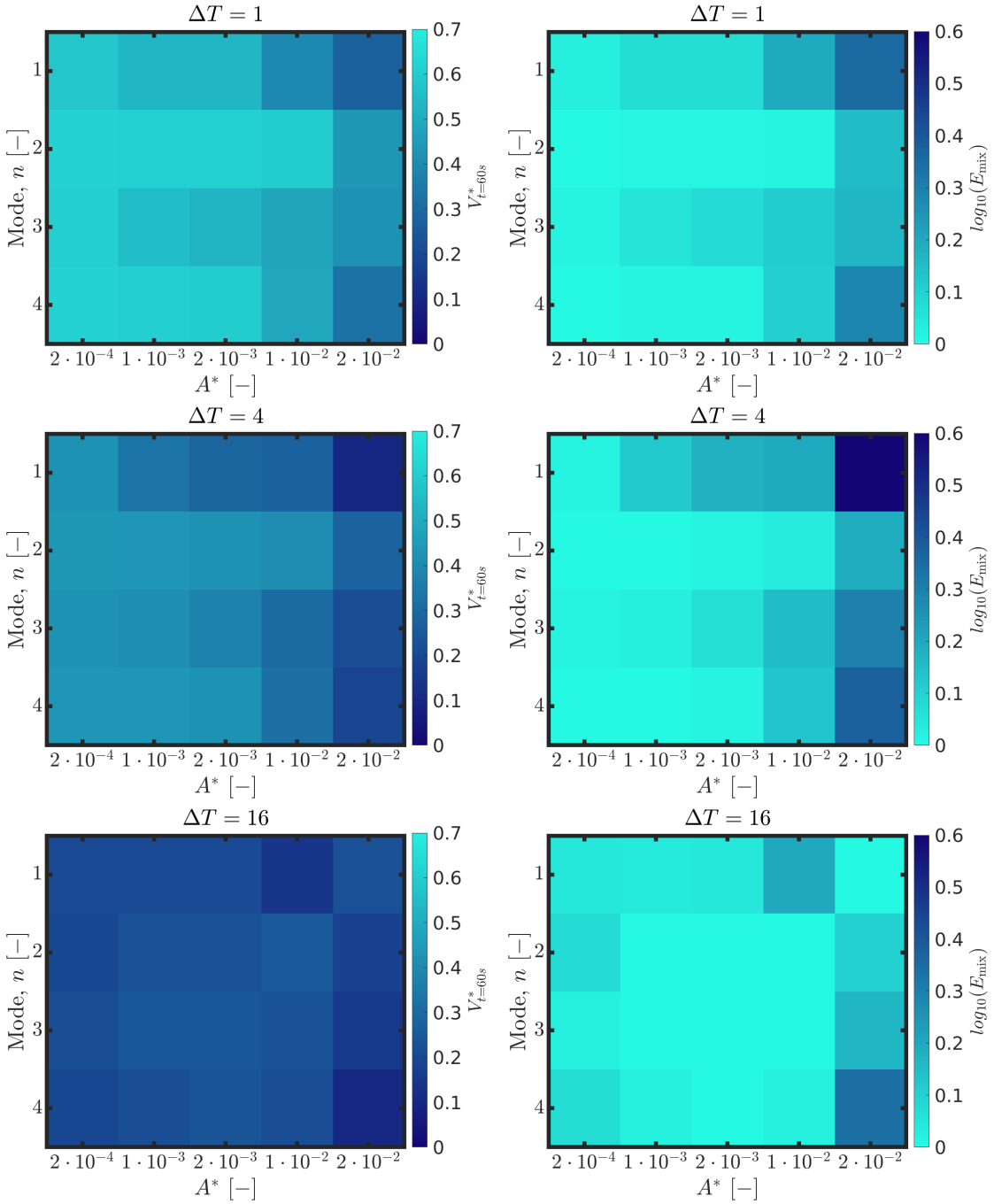

Figure 7.44: Thermal mixing maps. Left column contours represent variation of temperature field, V^* at $t = 60s$. Right column represents the mixing enhancement relative to the static base case, $A^* = 0$. Vertical and horizontal-axes represent forcing mode and amplitude respectively.

In particular, **Fig.** 7.44 helps us compare the sensitivity of mixing rate to amplitude, and how that varies with each mode. Except for the special case of $\Delta T = 16$ we see a clear pattern emerge. The enhanced mixing contribution from

sloshing becomes active at lower amplitudes for the anti-symmetric modes, with a steady increase in mixing rate — the primary mode $n = 1$ being dominant overall. Sloshing at the $n = 2$ mode only really has a meaningful effect at the highest amplitude, and even then it is the weakest in terms of accelerating the mixing process. Interestingly, the $n = 4$ mode starts off as a weak mixer but becomes more effective than the $n = 3$ mode at high forcing amplitudes.

Mixing is enhanced by sloshing slightly more at $\Delta T = 4$ than when $\Delta T = 1$. This is due to the hot fluid being convected more quickly towards the interface, where the dynamic surface effects help to locally dissipate heat faster than if the hot fluid remains at depth. This implies that the effects of sloshing on thermal mixing are highly dependent on the orientation of things, both in time and space. If thermal/scalar gradients occur away from the free surface then the effect of sloshing will not be as influential to the mixing process.

Thermal mixing in the intermediate fill tank, $h_{\text{f.s.}}/L_x = 0.3$

Fig. 7.48 shows $V^*_{\text{t=60s}}$ as a function of forcing amplitude for the intermediate fill height tank at each mode and initial temperature condition. Compared to the deep filled tank, thermal mixing for the $n = 1$ modal frequency is now much more heavily dominated by sloshing; the curves quickly converge and collapse on to each other even at an intermediate forcing amplitude. Furthermore, at $A^* = 1 \times 10^{-2}$ we've reached a point where $V^* \to 0$ as $t \to 60$, with the sloshing effects resulting in a temperature field more homogeneous than any of those achieved by sloshing in the deep fill cases. The $n = 3$ mode is firmly in the regime with significant contributions from both natural convection and sloshing motions as the curves decay at an offset that is slowly converging with increased amplitude.

As before, subjecting the tank to oscillations at the lowest symmetrical excitation mode $n = 2$ has little to no effect until becoming active only at the very

highest forcing amplitude. The $n = 4$ mode is interesting in that the mixing process makes a sharp transition from being clearly buoyancy-dominated to completely sloshing-dominated as the forcing amplitude ramps up. The translational regime for this frequency is clearly very narrow. As in the deep filled tank, the $n = 4$ mode overtakes the $n = 3$ mode at high amplitudes and becomes the superior mixer.

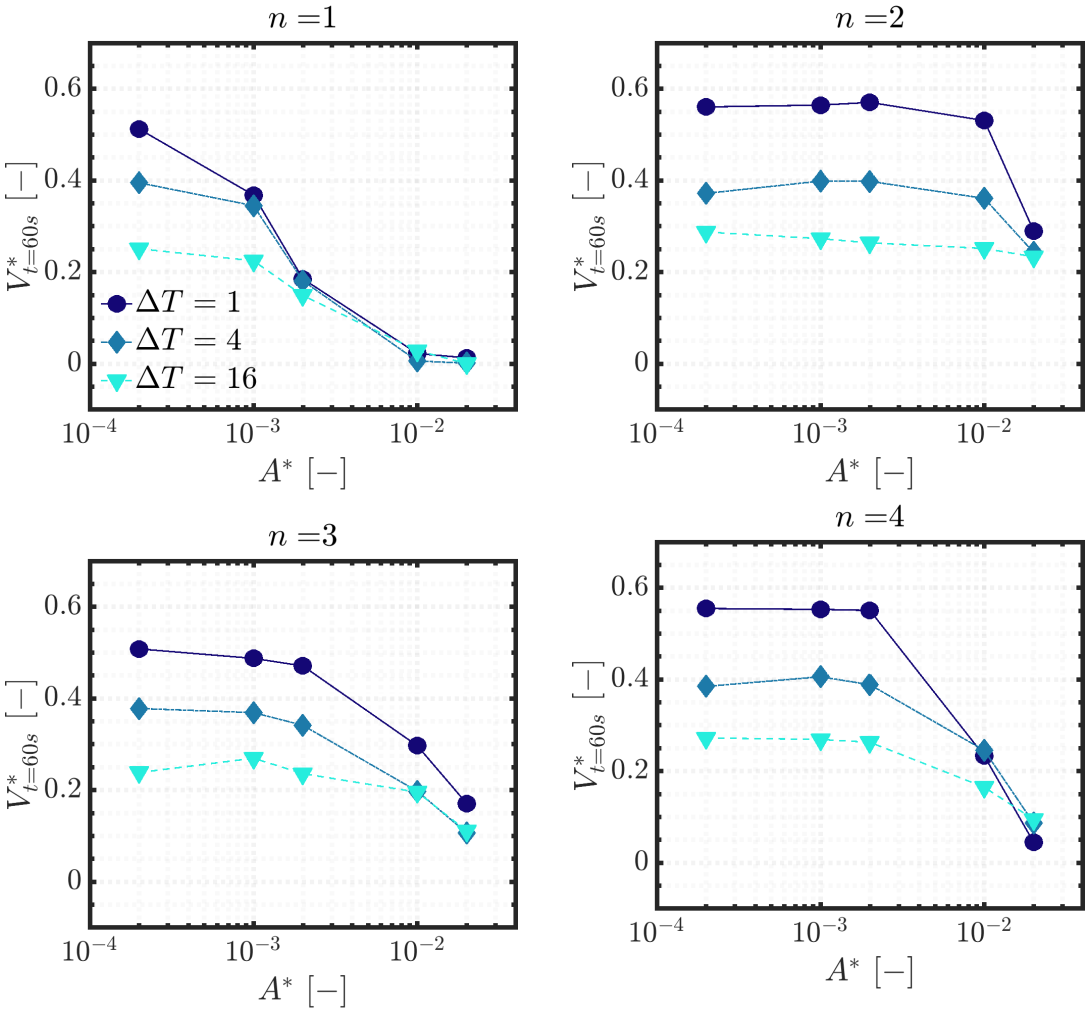

Figure 7.45: V^* at $t = 60s$, vs forcing amplitude A^*, with $h_{\text{fs}}/L_x = 0.3$

We can see from the snapshots in **Fig.** 7.46 that for the $n = 4$ mode, increasing the forcing amplitude to $A^* = 0.002 \rightarrow A^* = 0.02$ is causing a behavioural transition from a calm surface to one that becomes more active, eventually leading to wave profiles with steepness enough to over-turn at regular occurrence. Unlike for the $n = 1$ mode, overturning waves are not necessarily impact-related phenomena, easily occurring away from the walls. Heat concentrated in the hot blob beneath

the surface is quickly dissipated by turbulence as the waves break above.

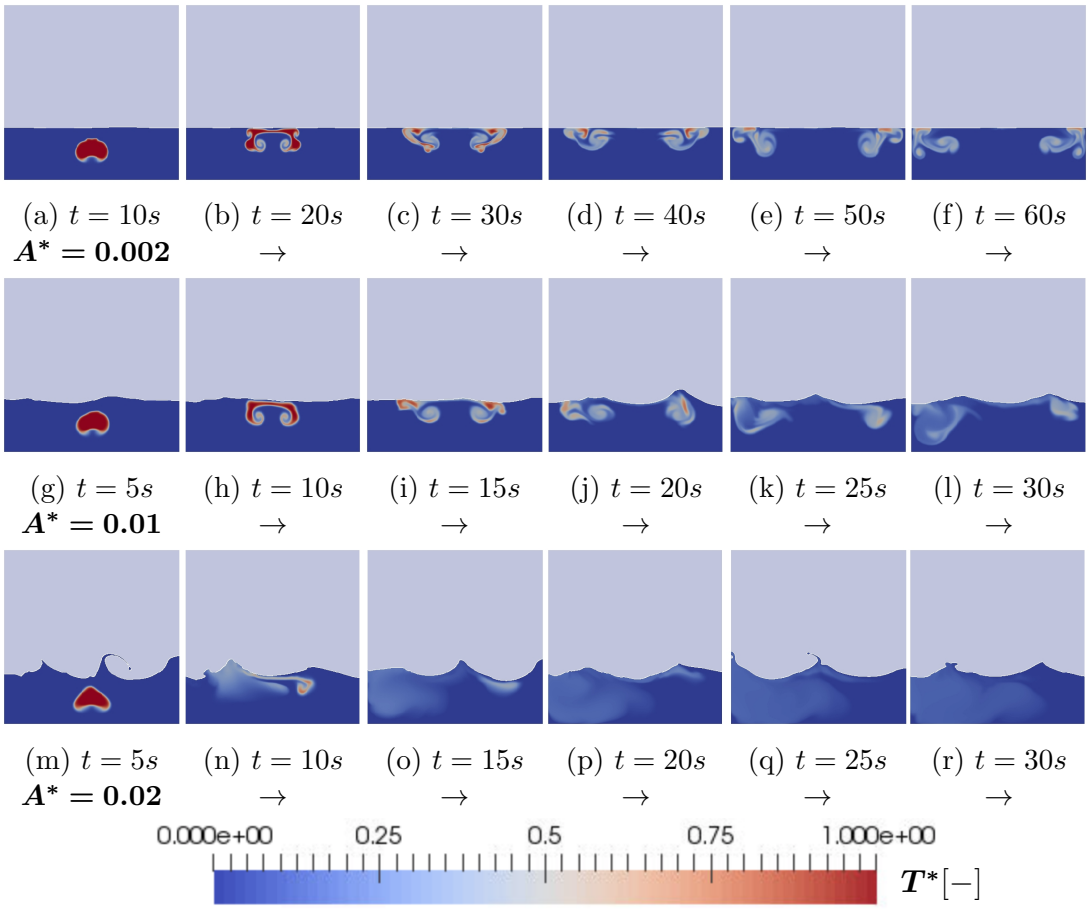

Figure 7.46: Temperature contours for the $\boldsymbol{n = 4}$ mode with initial temperature difference $\boldsymbol{\Delta T = 4}$

In **Fig.** 7.47 we can see a full view of how mixing is influenced by the parameters for the intermediate fill tank. The mixing maps are very similar to those for the deep fill tank. Again, odd anti-symmetric modes enhance mixing more effectively at lower amplitudes than even modes, with the $n = 4$ mode eventually becoming very effective as the forcing amplitude is increased. Overall, mixing is enhanced more by sloshing at this intermediate filling level than for the deep fill tank. The mixing enhancement colour-bar is now scaled to a maximum value of $log_{10}(E_{\text{mix}}) = 2.5$, compared to the maximum limit of $log_{10}(E_{\text{mix}}) = 0.6$ for the deep fill tank. This reflects the fact that for the $n = 1$, $A^* = 0.02$, $\Delta T = 4$ case, homogeneity of the thermal field is enhanced by a factor of $E_{\text{mix}} = 275$ relative to the static tank with same initial conditions. The equivalent case for the deep filled

tank enhanced the mixing by a factor or $E_{\text{mix}} = 4$ — some orders of magnitude lower. This suggests the sloshing dynamics in the intermediate flow regime produce conditions highly conducive to subsurface mixing.

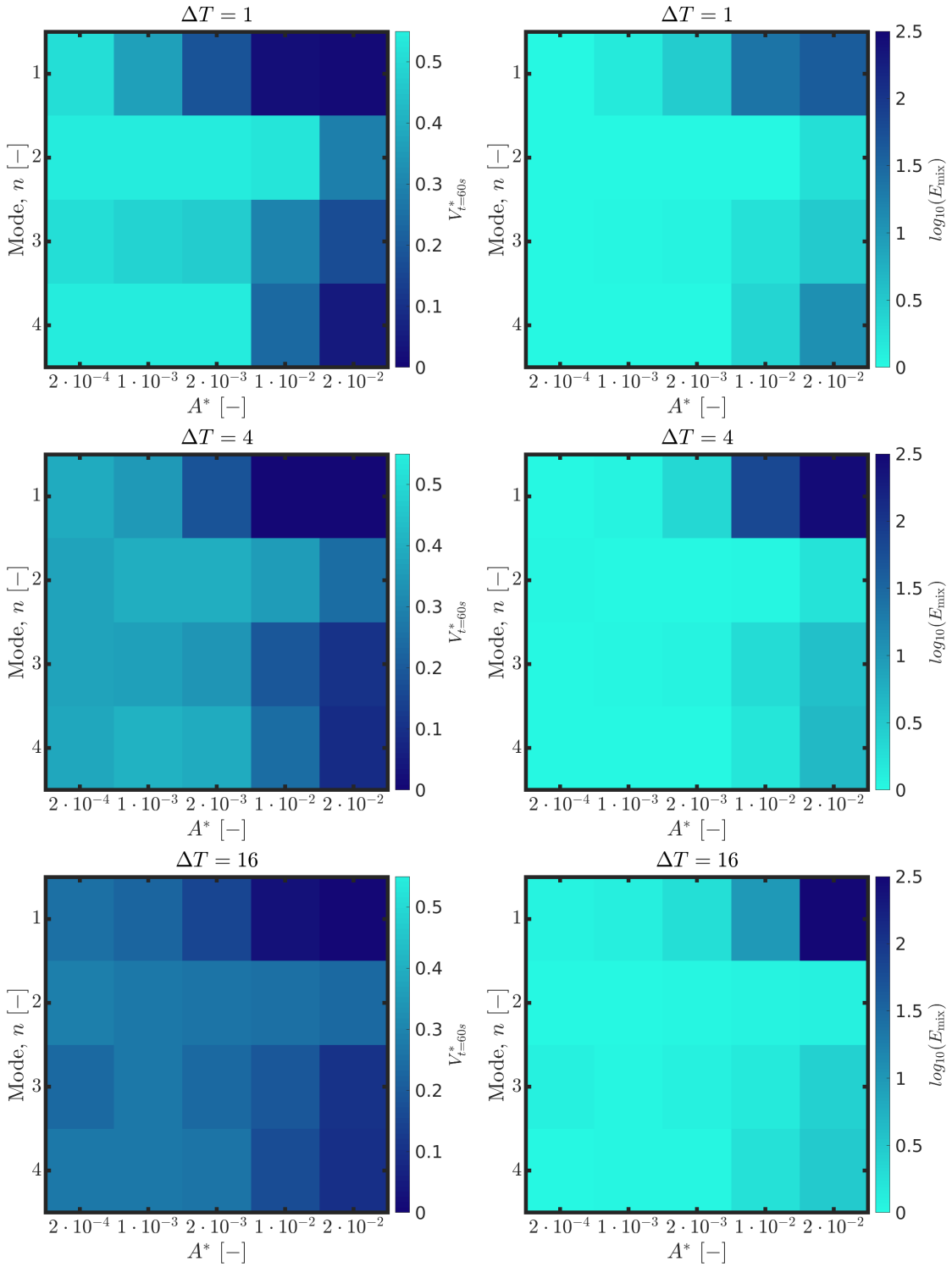

Figure 7.47: Thermal mixing maps. Left column contours represent variation of temperature field, V^* at $t = 60s$. Right column represents the mixing enhancement relative to the static base case, $A^* = 0$. Vertical and horizontal-axes represent forcing mode and amplitude respectively.

Thermal mixing in the shallow fill tank, $h_{\text{f.s.}}/L_x = 0.15$

As we go shallower once again, the mixing curves in **Fig.** 7.48 become even more congruent as the buoyancy-driven component of the mixing becomes weaker and less relevant. **Fig.** 7.29 showed us that this fill-height ratio is a special case in which the $n = 3$ wave response magnitude is similar to that of the primary natural frequency — even superior at lower forcing amplitudes. This is similarly reflected in the subsurface mixing rates. **Fig.** 7.49 shows the $n = 3$ mode giving greater thermal mixing enhancement at all but the highest forcing amplitude, with only $n = 1$ finally becoming superior. This bucks the trend of the deeper fill ratio tanks, where the first and fourth modal frequencies would consistently produce superior mixing conditions at the highest amplitude. Once again sloshing at the even, symmetric modes produces little mixing enhancement at low amplitudes, with the $n = 2$ mode producing very little effect even at the highest amplitude.

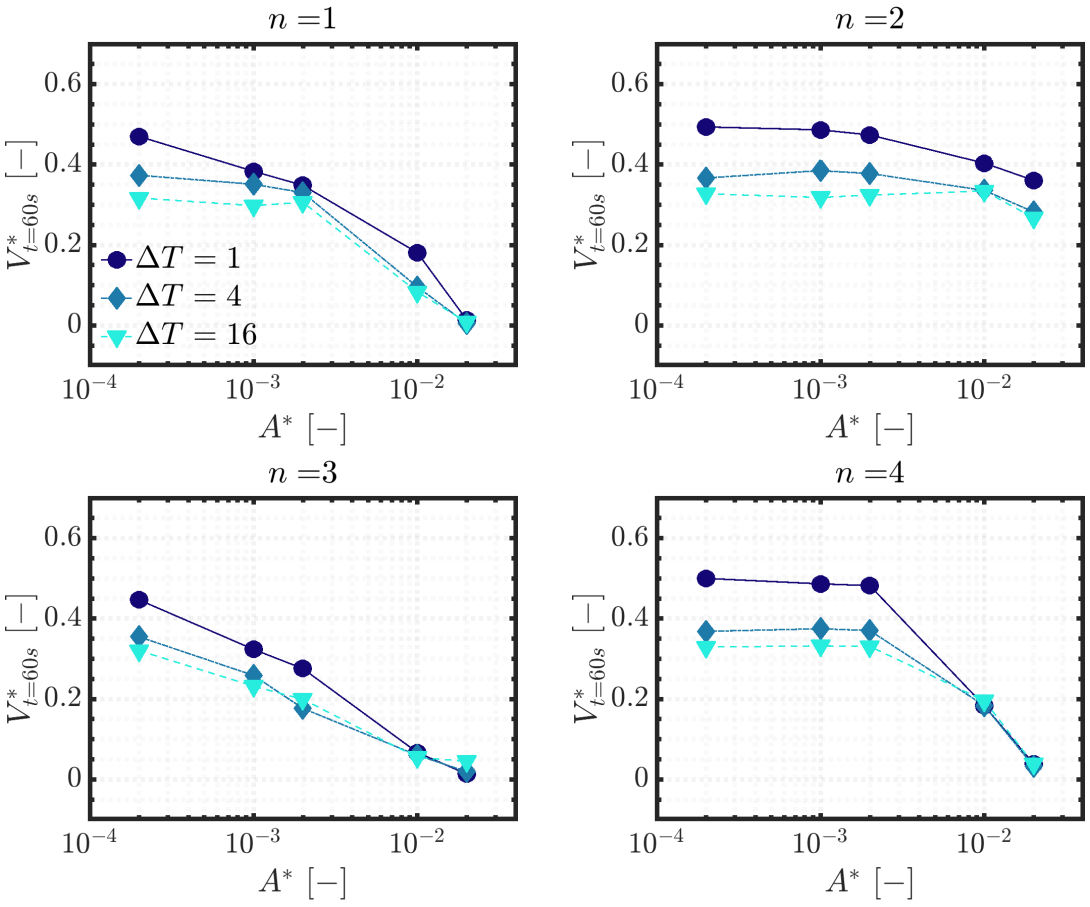

Figure 7.48: V^* at $t = 60s$, vs forcing amplitude A^*, with $h_{\text{fs}}/L_x = 0.15$

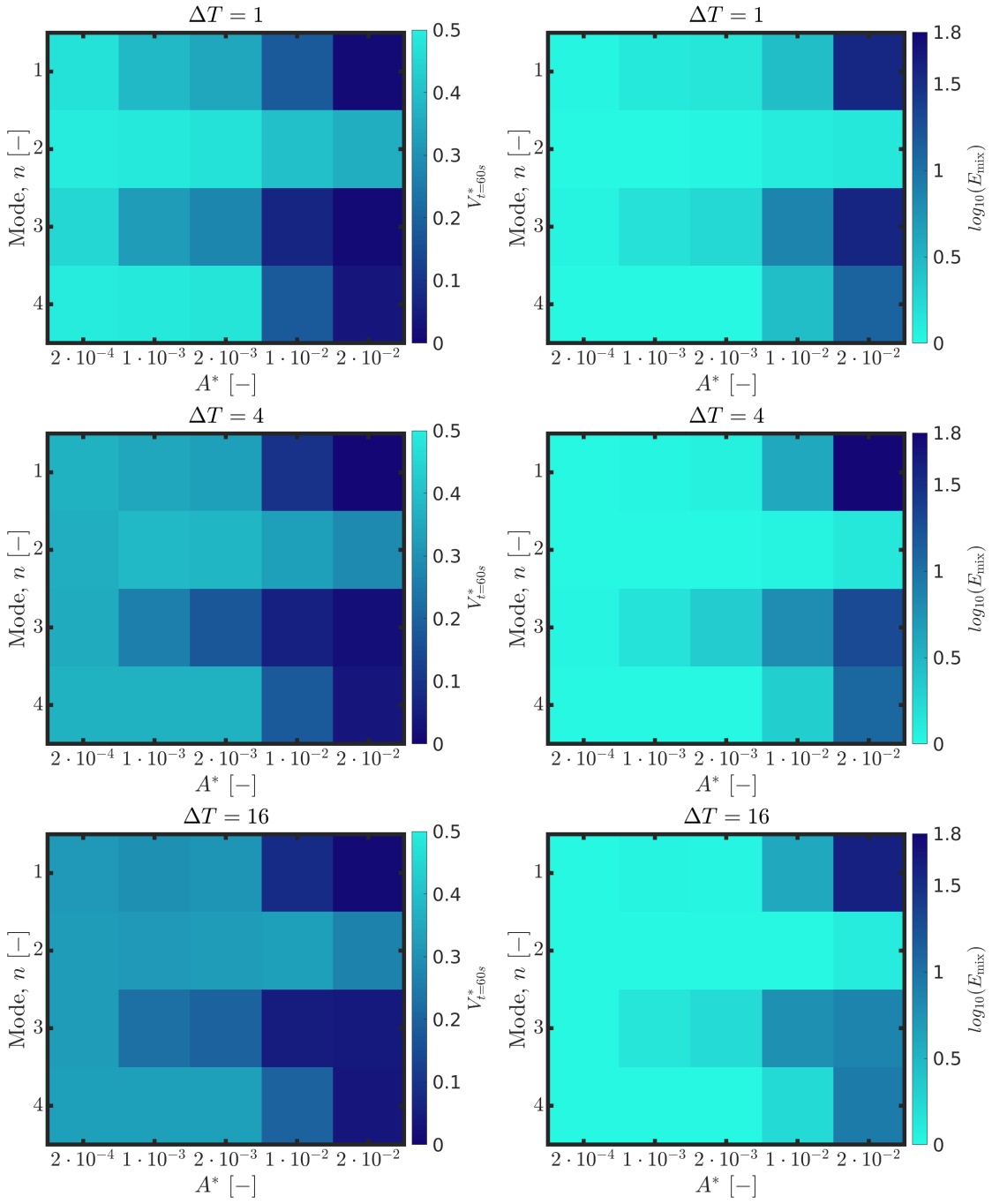

Figure 7.49: Thermal mixing maps. Left column contours represent variation of temperature field, V^* at $t = 60s$. Right column represents the mixing enhancement relative to the static base case, $A^* = 0$. Vertical and horizontal-axes represent forcing mode and amplitude respectively.

For each of the 3 initial temperature conditions, the mixing enhancement map is extremely similar, which contrasts with what we saw for the deep fill tank. Clearly, the buoyancy time-scales are too slow to compete as strongly with the effects of sloshing motions in the fluid. At such shallow depths, the wave profile for the

primary natural frequency has transitioned from a standing wave to a travelling wave.

The reduced liquid volume to surface ratio at shallower depths means that the internal fluid becomes more stretched as the interface deforms and elongates when climbing the tank walls. We see this effect demonstrated in **Fig.** 7.29. Steep, high amplitude waves do little to disturb the blob of hot fluid from its position at centre of the tank (**Fig.** 7.50a) for the deep fill tank. In the shallow tank, the hot blob of fluid is transported far from its initial position, being laterally displaced some distance towards the side wall of the tank (**Fig.** 7.50h). Little to no fluid within the tank is able to escape the actions of the dynamic free surface. In deep filled tanks, low energy regions away from the surface can remain relatively undisturbed. In **Fig.** 7.43r, after $60s$ of sloshing with violent surface motions, low-energy regions close to the tank base were observed to remain cold and un-replenished.

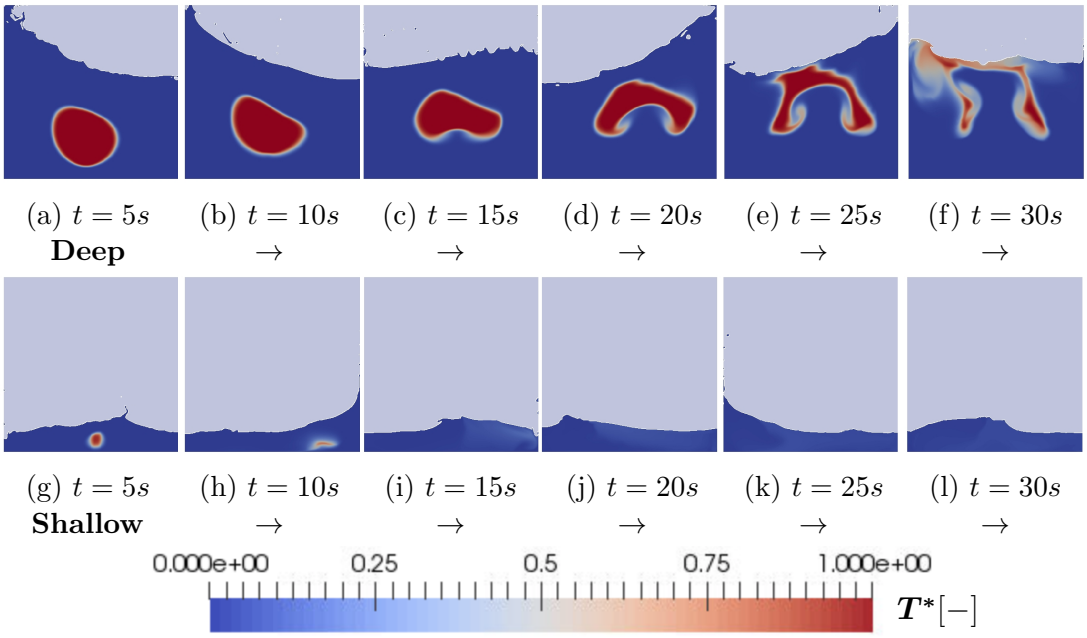

Figure 7.50: Temperature contours for the $\boldsymbol{n = 1}$ mode with initial temperature difference $\boldsymbol{\Delta T = 4}$

Turbulence in subsurface and its dependency on the parameters

Much of the work in **Chapters** 4 & 5 was focussed on identifying a robust way of predicting subsurface turbulence in multiphase flows. The anticipation was that correctly representing turbulence in the subsurface is critical to modelling scalar mixing in sloshing flows. Now we analyse the relationship between sloshing, mixing and turbulence, and how these phenomena are influenced by the parameters. **Fig.** 7.51 shows the mean subsurface eddy viscosity ratio, $\bar{\nu}_T^* = \bar{\nu_T}/\nu$ plotted as a function of forcing amplitude for each of the 4 modes and 3 temperature conditions for the deep fill tank.

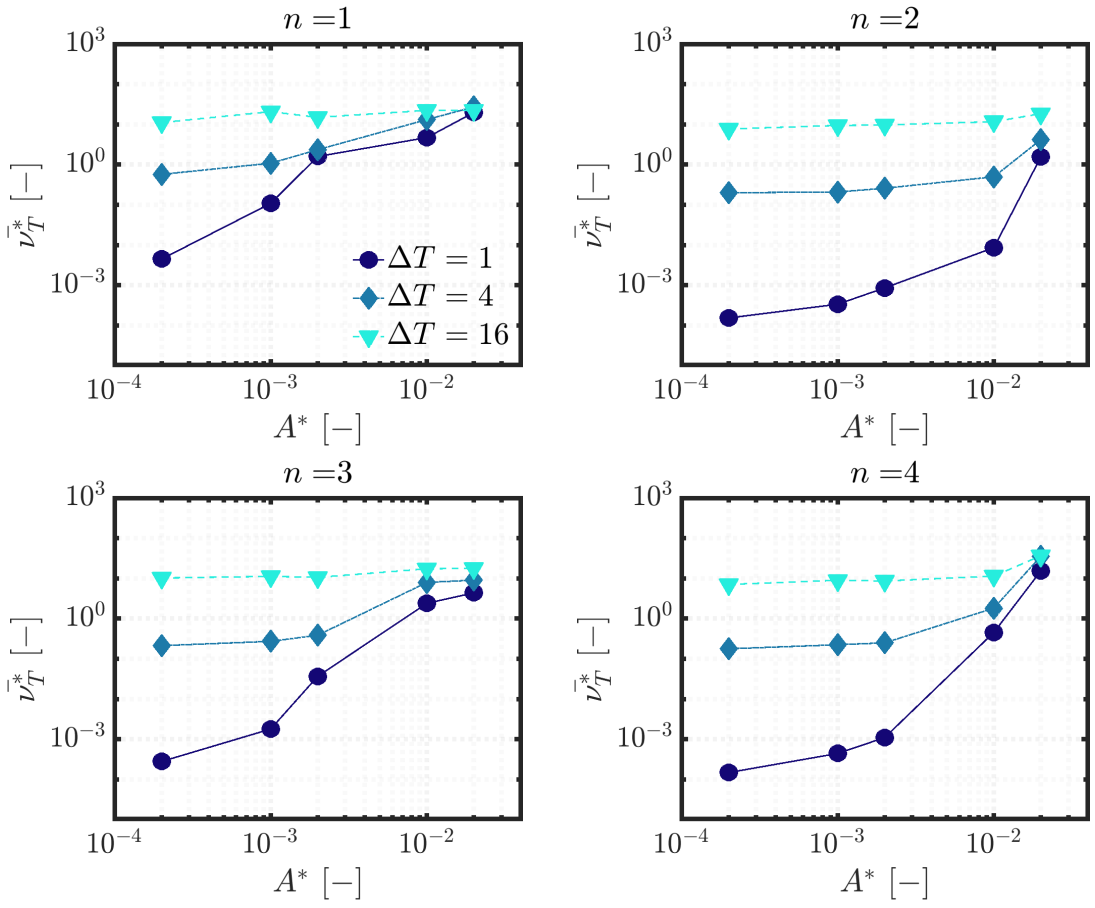

Figure 7.51: Mean liquid eddy viscosity ratio, $\bar{\nu}_T^*$ vs forcing amplitude, A^* at $t = 60s$, $h_{\text{fs}}/L_x = 0.7$

Mean eddy viscosity ratio above 0.1 indicates that on average the thermal diffusivity in the liquid subsurface is being significantly enhanced by turbulent

eddies. The limitation of this method of assessment is that it doesn't give us any information about localised turbulence. As with the temperature variation curves, we can broadly say that a flat curve indicates buoyancy-driven turbulence. Curves that collapse onto one other suggest sloshing motions to be the primary source for the onset of turbulence. Anything in between suggests we are in a regime where both are significant contributing factors. **Fig.** 7.51 shows that for the scenario $h_{\text{fs}}/L_x = 0.7$, $\Delta T = 16$, which has the highest Grashof number of any initial condition (see **Fig.** 7.14), the curve is flat and the levels of turbulence in the domain at $t = 60s$ are quite independent of forcing amplitude and frequency. On average the subsurface thermal diffusivity is dominated by turbulence, even without the additional contribution from sloshing. Eddy viscosity becomes more dependent on forcing amplitude as the buoyancy is decreased.

As we might expect at this point, the regime in which slosh-induced turbulence becomes more significant starts at lower amplitudes for the symmetrical modes. We can easily link this back to the similar sensitivities found in relating magnitude of wave response to the forcing amplitude in **Fig.** 7.28.

For the intermediate fill ratio tank, the reduced Grashof number of the initial thermal instability compared to the deep fill tank results in lower levels of convection-driven turbulence generation. **Fig.** 7.52 shows the mean eddy viscosity ratio in the subsurface at $t = 60s$. Compared to the eddy viscosity profiles in the deep filled tank **Fig.** 7.51 the curves are grouped more closely, meaning the subsurface turbulence is less dependent on buoyancy and more so on the contribution from sloshing. Eddy viscosity in the $n = 1$ case is almost completely independent of temperature across the 3 highest forcing amplitudes.

The $n = 4$ mode in particular make a sharp transition from primarily laminar to highly turbulent when increasing excitation amplitude from $A^* = 0.002 \rightarrow 0.01$. The sharp jump in response amplitude seen in **Fig.** 7.28 that leads to increased wave steepness and subsequent wave breaking has caused a large increase

in turbulence within the subsurface. Reflecting on the corresponding jump in mixing rates shown in **Fig.** 7.46, this illustrates the clear correlation between wave breaking, turbulence and thermal mixing.

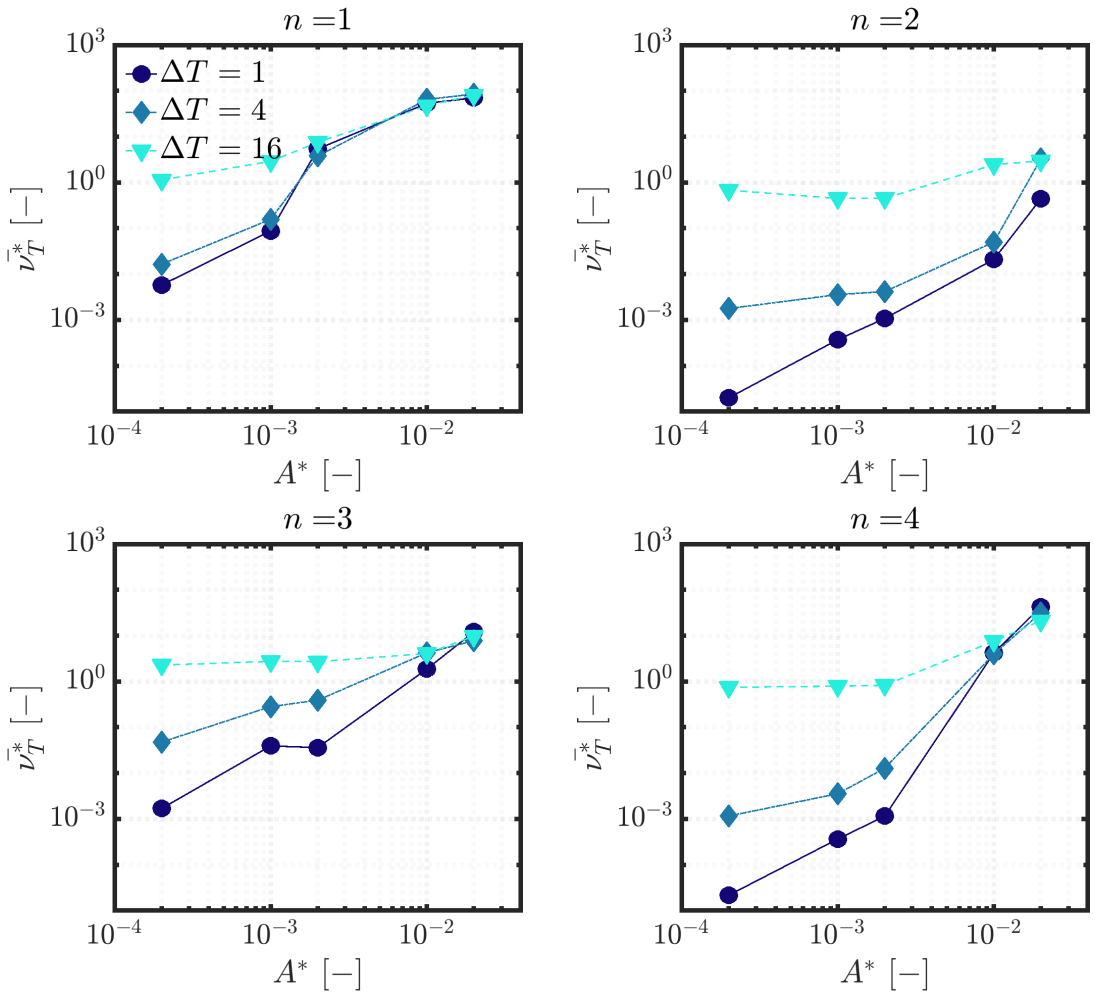

Figure 7.52: Mean liquid eddy viscosity ratio, $\bar{\nu}_T^*$ vs forcing amplitude, A^* at $t = 60s$, $h_{\text{fs}}/L_x = 0.3$

Turbulence in the shallow depth fill ratio tank show quite similar sensitivities to each of the parameters. There is very little dependence on temperature under excitations at the primary frequency, with the $\Delta T = 16$ case showing only slightly higher levels of turbulence at low forcing amplitudes. The $n = 2$ case remains quite laminar throughout the subsurface, with $\bar{\nu_T}$ failing to exceeding unity even at the highest amplitude. Both the $n = 1$ and $n = 4$ mode curves becoming increasingly steep as the interface begins to break up and generate high levels of turbulence at higher excitation amplitudes.

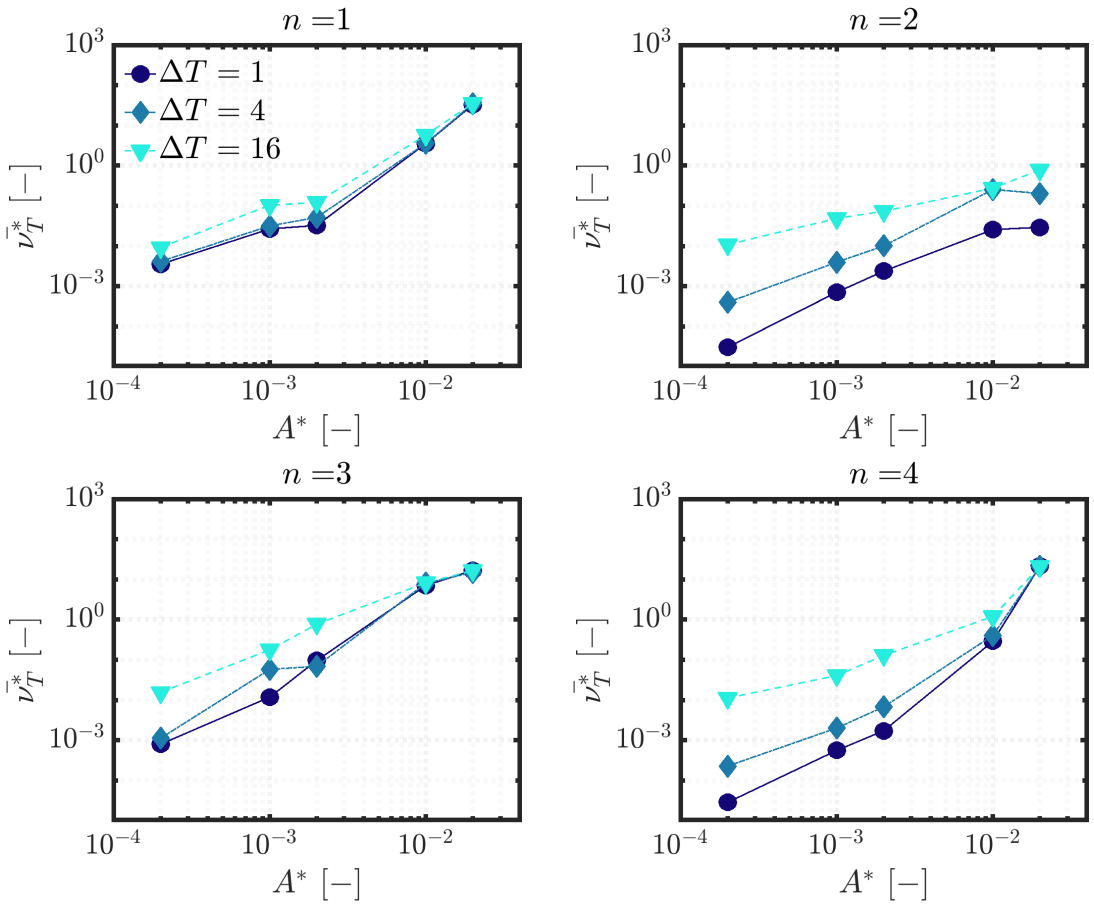

Figure 7.53: Mean liquid eddy viscosity ratio, $\bar{\nu}_T^*$ vs forcing amplitude, A^* at $t = 60s$, $h_{\text{fs}}/L_x = 0.15$

In **Fig.** 7.54 we plot data points from all 180 simulations to illustrate the relationship between turbulent eddy-viscosity in the subsurface and mixing enhancement. An additional dashed line is plotted to signify the point at which mean turbulent thermal diffusivity exceeds that of molecular conductivity. Recalling from **Chapter** 6 that effective thermal diffusivity is calculated as:

$$\kappa_{\text{eff}} = \kappa + \kappa_{\text{turb}}, \quad \kappa = \frac{\rho_0 \nu}{Pr}, \quad \kappa_{\text{turb}} = \frac{\rho_0 \nu_t}{Pr_t}. \tag{7.13}$$

Taking $Pr_t = 0.7$ and $Pr = 7$ for water, we can say that thermal eddy diffusivity, κ_{turb} is dominant when:

$$\frac{\rho_0 \nu_t}{Pr_t} > \frac{\rho_0 \nu}{Pr}, \tag{7.14}$$

or in terms of eddy viscosity ratio, when:

$$\nu_T^* = \frac{\nu_t}{\nu} > \frac{Pr_t}{Pr} = 0.1. \tag{7.15}$$

We can see in **Fig.** 7.54 this serves as a good threshold for predicting enhanced mixing for the deep and intermediate fill tanks. For the shallow tank, mixing becomes enhanced at lower levels of mean eddy-viscosity. This suggests that slosh-induced motions such as the stretching and displacements of the fluid body are also influential on heat transport in shallow sloshing, supplementing the enhanced mixing effects of turbulence.

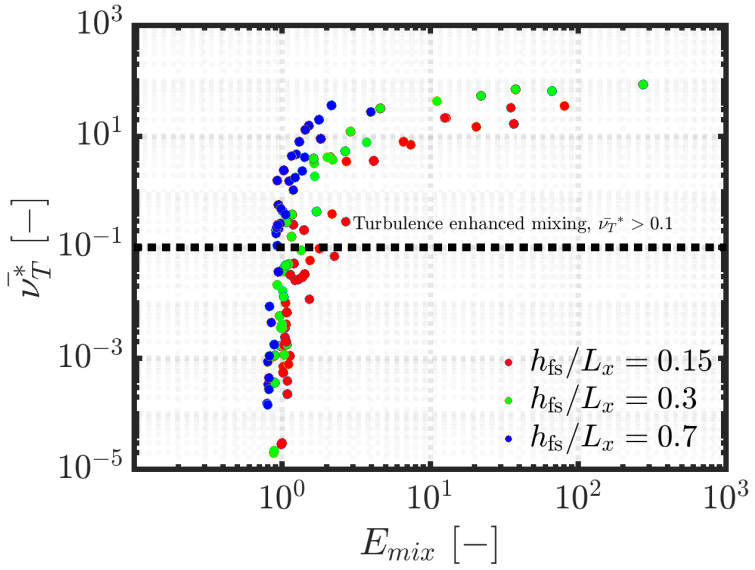

Figure 7.54: Mean liquid eddy viscosity ratio $\bar{\nu}_T^*$ vs mixing enhancement factor, E_{mix}. Data points are coloured by fill depth ratio.

7.4 Conclusions

7.4.1 Conclusions on free surface response to sloshing parameters

Sloshing response behaviour was systematically analysed over an extensive parameter space. This covered a range of forcing amplitudes and modal frequencies across 3 different fill-ratio based sloshing regimes, with 3 initial temperature conditions.

Broadly speaking, the anti-symmetrical modes were found to generate a much greater wave amplitude response than the symmetric modes. This is as expected, due to the lateral motions inherent to their mode shapes. The first modal frequency $n = 1$ was found to produce greatest wave response for the deep and intermediate fill tanks. In the shallow tank, the $n = 3$ mode was able to generate a superior response over a number of forcing amplitudes — a result not observed in literature so far as this author is aware. The result is likely due to increased interaction with the tank's base as the liquid depth becomes more shallow.

Across all configurations, the $n = 2$ mode was found to yield the weakest wave response amplitudes. This agrees with other observations made by Jung et al. (2015) and Jin et al. (2014) — in **Fig.** 3.9, neither the experiments or numerical model picked up any discernible increase in response when forcing was applied at the second natural frequency. The other symmetrical mode, $n = 4$ displayed quite different characteristics, being particularly sensitive to forcing amplitude.

7.4.2 Conclusions on thermal mixing

Intuition would tell us that sloshing a body of liquid should no doubt speed up the rate of mixing within. This was found to be true *most* of the time. The influence of sloshing on thermal mixing was found to be highly sensitive to the forcing parameters. Due to the sharp increases in response amplitude at resonance, and the variety in behavioural characteristics for different resonant modes, mixing is not increased proportionally to the amount of energy supplied to the system. The reality is far more complex.

Influence of forcing frequency and amplitude

Excitations at the anti-symmetric, odd natural frequency modes $n = 1, 3$ produced the strongest mixing characteristics at low forcing amplitudes — the lateral displacements involved in their characteristic behaviour produce greater surface response and hence more favourable mixing conditions. For most scenarios, the $n = 1$ mode induces superior mixing at the highest forcing amplitude considered.

The symmetric $n = 4$ mode produced comparably weak mixing at low forcing amplitudes. However, the steeper waves generated by the increased wave number resulted in a sharp jump in mixing capability as surface waves began to overturn, producing a highly turbulent surf zone in response to increased excitation. This feature allowed the $n = 4$ mode to produce superior mixing conditions to the $n = 3$ mode over a number of scenarios at high forcing amplitudes, despite a relatively weaker wave response amplitude. Symmetric modes are generally of less interest to engineers (Dodge et al., 2000). This is due to the perception that their oscillation do not shift the liquid CG enough to produce problematic forces/moments on the tank's structure or compromise stability. However, we have shown that the symmetrical $n = 4$ mode gives rise to some interesting behavioural characteristics that can have a considerable influence on subsurface mixing. Other than at the very

highest forcing amplitude, $n = 2$ mode offered no enhancement in mixing conditions relative to the static tank.

Influence of buoyancy

For hot blobs of liquid with a high Grashof number, the mixing is heavily influenced by buoyancy. Reducing the hot liquid's temperature resulted in the balance of competing buoyancy and sloshing forces to become very complex — much more dependent on the forcing parameters and sloshing regime. For tanks situated in recirculating fuel system, this suggests that the relative influence of sloshing on thermal mixing will be highly sensitive to both the amplitude and nature of sloshing response, as well as the buoyancy of incoming fuel.

A special case was uncovered in the deep tank, at $\Delta T = 16$, in which the rate of thermal mixing was actually inhibited by the sloshing motions. This was the most buoyant of all the cases considered, and so through natural convection alone, the thermal instability was able to quickly mix with the colder fluid in the tank. Interactions between the convective currents and the dynamic free surface region suppressed the hot fluid from circulating as effectively throughout the tank. Ultimately, the highest amplitude sloshing for the $n = 1$ mode produced worse mixing properties than the static tank. Other forcing mode/amplitude combinations demonstrated a similar outcome (see **Fig.** 7.44), in which mixing was not necessarily enhanced with an increase in excitation amplitude. In a more realistic fuel tank, in which we have a buoyant, heated fuel stream entering a cooler environment, it may be the case that in some scenarios sloshing motions can destructively interfere with the forced/natural convection flow patterns and reduce the rate of thermal mixing. The possibility of such scenarios should be targeted with experiments to confirm their existence.

Influence of fill height

Varying fill height ratio gives rise to sloshing regimes with unique characteristics. The most marked difference in characteristic behaviour is the transition from a standing wave to travelling waves at the primary frequency as fill height ratio is reduced. The fluid body at intermediate and shallow fill heights becomes much more stretched due to the increase in free surface area to liquid volume ratio. Furthermore, the flow is more highly influenced by non-linearities and viscous effects for shallower filled tanks.

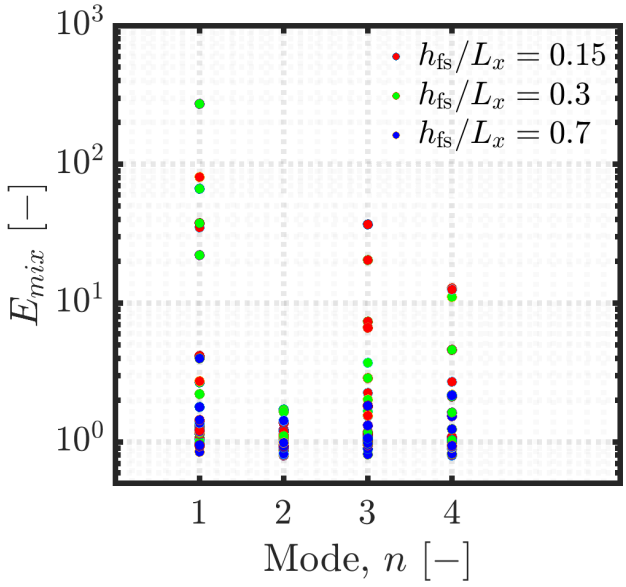

Figure 7.55: Mixing enhancement factor vs. forcing frequency mode. Data points are coloured by fill depth ratio.

Fig. 7.55 shows this results in a much higher mixing enhancement relative to the static tank. Maximum E_{mix} values for shallower tanks exceed the corresponding maximum values in deep tanks by some orders of magnitude across modes (with the exception of $n = 2$). This has some implications on thermal mixing inside aircraft fuel tanks. Firstly, even though they are compartmentalised by baffles and spars, aircraft wing tanks tend to have a low aspect ratio h_{fs}/L_x. Furthermore, as tanks become depleted (reduce in fill height ratio), transitions through sloshing regimes may occur. As such, a wide range of conditions might be experienced within a single

fuel tank through the duration of flight. Therefore, the mixing characteristics within will similarly vary accordingly.

Chapter 8

Conclusions

The aim of this research was to develop an understanding of the role sloshing plays in thermal mixing — a field of research which as of yet has received little attention. A numerical model was developed in `OpenFOAM`, with each aspect of its physical modelling capabilities critically analysed step-by-step. Establishing a model that properly accounts for subsurface turbulence has enabled the exploration of sloshing-driven mixing. An extensive and systematic sweep through the parameter space of sloshing and thermal conditions was undertaken. The degree to which sloshing is able to enhance thermal mixing was found to be highly sensitive to the forcing parameters.

To conclude this thesis, in this chapter a summary of the key findings is presented. This will be made on a chapter-by-chapter basis, highlighting the relevant contributions of this work. These findings will then be expanded upon, with discussion of the wider implications of the results. Lastly, some important remaining knowledge gaps will identified, leading to recommendations for future work.

8.1 Overview of key findings

8.1.1 Conclusions from Chapter 3: Modeling isothermal sloshing

In **Chapter** 3, a numerical framework for modelling isothermal sloshing flows was presented. `interFoam` — a finite-volume VOF solver with moving mesh capabilities — was coupled with the $k-\omega$ SST turbulence model and was validated as being suitable for modelling a variety of sloshing flows. This was tested across 3 sloshing regimes: shallow, intermediate and deep sloshing. The model was able to replicate time-varying single-point liquid depth and pressure probe measurements from the experimental data of Armenio and La Rocca (1996) and Chen et al. (2013a) with excellent agreement over a number of cases. The ability of `interFoam` to accurately predict resonance was tested over a range of excitation frequencies, including the first 3 natural modes $n = 1, 2, 3$. Again, its excellent performance in doing so was validated against the experiments of Jin et al. (2014). These studies confirmed the model's ability to capture sloshing in challenging conditions.

8.1.2 Conclusions from Chapters 4 & 5: Turbulence modelling in multiphase flows

Some of the pertinent challenges of modelling turbulence in stratified flows were presented in **Chapter** 4. A number of recent publications have highlighted the issues inherent to turbulence modelling in multiphase flows — in particular, two-equation RANS models and their tendency to over-predict turbulence beneath the free surface. Modified formulations of the $k-\omega$ SST models developed by Devolder et al. (2017) and Larsen and Fuhrman (2018) were tested against the benchmark experimental measurements of Fabre et al. (1987). These models were deployed in

combination with Egorov's interface damping function (Egorov et al., 2004), with improved results for turbulence in the air and shear stress at the interface. However, the damping model was found to decrease the accuracy of eddy-viscosity prediction beneath the free surface, making it less suitable for studying turbulence enhanced subsurface mixing.

In **Chapter** 5, it was demonstrated that the choice of $k-\omega$ SST formulation has a profound effect on the prediction of turbulence quantities in sloshing flows. Mean eddy viscosity in the subsurface was found to vary by up to 4 orders of magnitude at lower forcing amplitudes, depending on which model formulation was applied. For the models predicting high levels of eddy viscosity, response was damped very slightly as a result, with fewer transient flow structures developing in the near-surface region. Response amplitudes predicted by the stabilised $k-\omega$ SST model of Larsen and Fuhrman (2018) were found to agree closely with 3D LES simulations, when excited at the first natural frequency. Egorov's model for damping turbulence at the interface was found to be unsuitable for sloshing flows. False turbulence damping is introduced during free surface break-up, causing turbulent events such as wave-breaking to be improperly captured.

Given the relatively subtle effects of subsurface eddy viscosity levels on wave response, it is unsurprising that this aspect of modelling sloshing has gained little attention in the literature. For modelling subsurface mixing in sloshing flows, it is a critical consideration.

8.1.3 Conclusions from Chapter 7: Sloshing and thermal mixing

In **Chapter** 7, a comprehensive sweep through a wide parameter space was undertaken. Sloshing wave amplitudes and free surface mode shapes were studied in a tank subjected to resonant conditions, across a range of forcing amplitudes and the first

4 natural frequencies of the liquid. 3 fill heights were studied, corresponding to the deep, intermediate and shallow sloshing regimes. As expected, the anti-symmetric modes gave rise to the greatest wave response. The $n = 4$ mode was found to be very unresponsive at low forcing amplitudes, with a tendency to suddenly exhibit much more activity at higher forcing amplitudes. The increased wave number and corresponding mode shape at $n = 4$ causes steep surface waves to develop. The steepness of wave profiles resulted in an increased propensity for wave overturning, even away from the tank wall.

Thermal mixing of a hot blob of fluid was modelled in a static tank. This served as a baseline with which to compare the relative enhancement of thermal mixing due to liquid sloshing. In the absence of experimental data with which to validate thermal mixing beneath a free surface, LES simulations in a 3D tank were used to validate convection-driven mixing rates as predicted by the 2D RANS model. Despite differences in the developed flow patters, the overall macroscopic mixing tendencies were found to agree closely over a range of Grashof numbers. The limitations of the 2D modelling approach were also highlighted — demonstrating the difficulty of achieving a truly grid-independent solution for the transport of buoyant, convective flow structures in the subsurface.

The effects of sloshing on thermal mixing were assessed for sensitivity to the parameters both qualitatively and quantitatively. An enhancement factor was established as a metric in order to make a quantitative assessment of how mixing was enhanced relative to the stationary tank after a period of $60s$:

$$E_{\text{mix}} = \frac{V^*_{\text{t=60s,static}}}{V^*_{\text{t=60s,sloshing}}}. \tag{8.1}$$

At low forcing amplitudes, the subsurface flow field remained largely laminar and did not significantly increase the rate of mixing relative to the base-line static case. In general, the odd, anti-symmetric modes generated faster mixing across low

to intermediate forcing amplitudes due to the increased lateral liquid displacements.

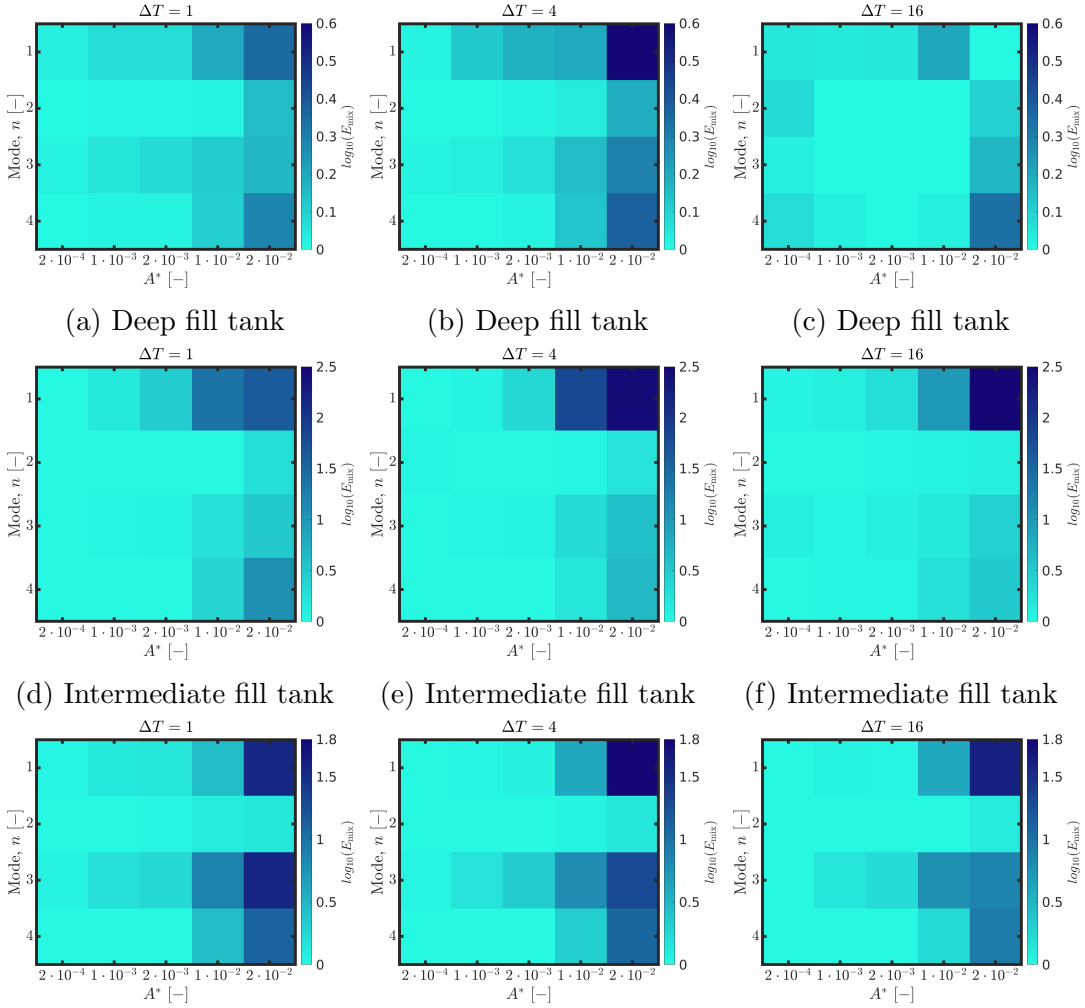

(a) Deep fill tank (b) Deep fill tank (c) Deep fill tank

(d) Intermediate fill tank (e) Intermediate fill tank (f) Intermediate fill tank

(g) Shallow fill tank (h) Shallow fill tank (i) Shallow fill tank

Figure 8.1: Thermal mixing enhancement maps, coloured by E_{mix}, for deep (top row), intermediate (middle row) and shallow (bottom row) tanks. Increase in initial temperature difference from left→right.

At higher amplitudes, sloshing motions were found to increase mixing rates but with a high degree of sensitivity to the modal forcing frequencies. Overall, mixing was enhanced most effectively by tank motions at the primary frequency. This was especially true for intermediate and shallow depth tanks. A reduced volume to free surface ratio, and a change in characteristic sloshing regime from standing to travelling waves resulted in a higher degree of stretching and distortion in the liquid. At high amplitudes, tank motions at the $n = 4$ modal frequency resulted in a sharp jump in mixing enhancement — the effects of regular wave-breaking producing a highly turbulent surf zone despite modest wave amplitudes compared

to the anti-symmetric mode surface profiles.

An interesting case was identified for the $\Delta T = 16$, deep filled tank (**Fig.** 8.1c) in which high amplitude sloshing under excitations at the primary modal frequency was found to suppress mixing. The interaction of convective currents with the dynamic surface region served to restrict the circulation of warmer fluid. Ultimately, this resulted in inferior thermal mixing after a period of $t = 60$s compared to the static tank.

8.2 Wider implications

Recalling our initial motivation for this work, in **Chapter** 1 we made reference to the way in which the internal workings of the fuel tank as a thermodynamic system are typically reduced to a lumped parameter within 1D thermal network models. Explicitly modelling the internal dynamics of a fuel tank is a computationally intensive procedure, and so the fuel temperature is often assumed to be uniform and directly proportional to the amount of heat absorbed from other subsystems.

This belies the complex nature of how mixing interacts with sloshing flows in partially filled containers. In this thesis, we have considered very basic scenarios — with a simple rectangular geometry and linear, periodic sway motions. And yet still, the system response yields a wide variety of behavioural characteristics. The sensitivity to the parameters, and the influence of resonance means that just a small change in excitation frequency has the potential to rapidly increase/decrease the rate of mixing within.

In reality, aircraft fuel systems are even more complicated. Tanks are not closed systems, but part of a larger fuel network — ever-evolving as fuel is extracted, recirculated and depleted. Some tanks may act as the recipients of multiple fuel streams, pumped in at varying temperatures. Furthermore, aircraft flight dynamics

cannot guarantee simple periodic motion. Fuel tanks can at times be subject to sudden and high-g accelerations. Sloshing can be driven by rolling, surging, stochastic or pulsating motions. Fuel can even be thrown violently around the tank during inversions. As we showed in **Chapter** 2, fuel tank geometries can take on elaborate forms to be fitted around other subsystems in tightly packed aircraft envelopes.

All this suggests the assumptions made about thermal mixing in fuel tanks must be challenged.

8.3 Future work

8.3.1 On turbulence modeling in free surface flows

Numerical CFD codes of various construction have reached a maturity such that they can be considered robust in accurately simulating a variety of complex flows involving free surfaces across scales. However, the results in this thesis and numerous examples from recent publications highlight the challenges that still exist in developing reliable turbulence models for stratified free surface flows.

We have demonstrated in this thesis just how sensitive the prediction of turbulence can be to modelling strategy. Without the ability to directly compare turbulence models to experimental data for sloshing flows, in this thesis we used 3D LES results and analogous experimental data to make judgement calls.

It is critical that future work is focussed on generating high quality characterisations of subsurface turbulence for the purposes of benchmarking. Phase-averaged measurements of turbulent quantities, in the spirit of the experiments of Ting and Kirby (1994), would be a good start.

8.3.2 On thermal mixing in sloshing flows

Experimental campaigns

As mentioned in **Chapter** 2, thermal mixing has rarely been considered in the study of sloshing flows. Research has been limited to a few cases, with very little in the way of a comprehensive data set with which to benchmark thermal models. Grotle et al. (2017) are one of the few to use experiments to validate their numerical model of thermal mixing due to sloshing. This was done by comparing experimental and numerical calculations of the macroscopic absolute air pressure drop within the tank. Validation was sought via an implicit effect on the thermodynamic response of the system, rather than a detailed comparisons of the temperature field.

Aly et al. (2020) recently used an SPH code to analyse mixed convection in a sloshing porous cavity with a nano-fluid, studying the effects of sloshing on Nusselt number. Their work is certainly interesting, and the effects of sloshing on heat transfer coefficients is ripe for investigation. However, their thermal model is validated only by comparisons to experimental temperature profiles from single-phase lid-driven cavity flow. Again, this highlights the scarcity of quality experimental data.

Given the variety of interesting observations with regards to sloshing and subsurface mixing that have been uncovered by the simulations in this thesis, a campaign of experiments is more than justified. Experiments focussing on measuring heat transfer in sloshing flows that can be used for benchmarking numerical models is highly recommended for future work.

Fuel tank design simulations

Having established a computational methodology for simulating sloshing and thermal mixing, this approach can be used as a design tool for more realistic tank designs. The next step is to include inlets/outlets to account for incoming/outgoing fuel streams. The effect of fuel jets entering the resident liquid body adds an extra dimension to the internal dynamics of the tank, which needs to be studied.

The numerical model described in this thesis will allow key design aspects such as internal geometry, thermal mixing, slosh mitigation, pump orientation and fuel gauging to be optimised without the need for experiments to analyse every design iteration.

Bibliography

Mol mitsui osk lines. https://www.mol.co.jp/. Accessed: 2022-01-02.

Abramson, H. N. 1966. The dynamics of liquids in moving containers. *NASA Report, SP*. **106**, pp. I960.

Abramson, H. N. and Garza, L. R. 1964. Some measurements of the effects of ring baffles in cylindrical tanks. *Journal of Spacecraft and Rockets*. **1**(5), pp. 560–562.

Abramson, H. N. and Ransleben Jr, G. E. 1960. Simulation of fuel sloshing characteristics in missile tanks by use of small models. *ARS Journal*. **30**(7), pp. 603–612.

Abramson, H. N. and Ransleben Jr, G. E. Some studies of a floating lid type device for suppression of liquid sloshing in rigid cylindrical tanks. Technical report, Southwest Reseach Institute, San Antonio, TX. USA, 1961.

Abramson, H. N., Martin, R., and Ransleben Jr, G. E. Application of similitude theory to the problem of fuel sloshing in rigid tanks. Technical report, Southwest Reseach Institute, San Antonio, TX. USA, 1958.

Abramson, H. N., Chu, W.-H., and Ransleben Jr, G. O. E. 1961a. Representation of fuel sloshing in cylindrical tanks by an equivalent mechanical model. *ARS Journal*. **31**(12), pp. 1697–1705.

Abramson, H. N., Chu, W.-H., and Garza, L. R. 1963. Liquid sloshing in spherical tanks. *AIAA Journal*. **1**(2), pp. 384–389.

Abramson, H. N. et al. Liquid sloshing in rigid cylindrical tanks under-going pitching motion. Technical report, Southwest Reseach Institute, San Antonio, TX. USA, 1961b.

Akyildız, H. and Ünal, N. E. 2006. Sloshing in a three-dimensional rectangular tank: numerical simulation and experimental validation. *Ocean engineering.* **33** (16), pp. 2135–2149.

Akyıldız, H., Ünal, N. E., and Aksoy, H. 2013. An experimental investigation of the effects of the ring baffles on liquid sloshing in a rigid cylindrical tank. *Ocean Engineering.* **59**, pp. 190–197.

Aly, A. M., Raizah, Z., and Sheikholeslami, M. 2020. Analysis of mixed convection in a sloshing porous cavity filled with a nanofluid using isph method. *Journal of Thermal Analysis and Calorimetry.* **139**(3), pp. 1977–1991.

Alyanak, E. J. and Allison, D. L. Fuel thermal management system consideration in conceptual design sizing. In *57th AIAA/ASCE/AHS/ASC Structures, Structural Dynamics, and Materials Conference*, pp. 0670, 2016.

Antuono, M., Bouscasse, B., Colagrossi, A., and Lugni, C. 2012. Two-dimensional modal method for shallow-water sloshing in rectangular basins. *Journal of Fluid Mechanics.* **700**, pp. 419–440.

Arai, M. 1984. Experimental and numerical studies of sloshing pressure in liquid cargo tanks. *Journal of the Society of Naval Architects of Japan.* **1984**(155), pp. 114–121.

Arai, M., Cheng, L.-Y., and Inoue, Y. 1992. 3d numerical simulation of impact load due to liquid cargo sloshing. *Journal of the Society of Naval Architects of Japan.* **1992**(171), pp. 177–184.

Armenio, V. and La Rocca, M. 1996. On the analysis of sloshing of water in rectangular containers: Numerical study and experimental validation. *Ocean Engineering.* **23**(8), pp. 705–739.

Armenio, V. and La Rocca, M. 1996. On the analysis of sloshing of water in rectangular containers: numerical study and experimental validation. *Ocean engineering*. **23**(8), pp. 705–739.

Bai, W., Liu, X., and Koh, C. 2015. Numerical study of violent lng sloshing induced by realistic ship motions using level set method. *Ocean Engineering*. **97**, pp. 100–113.

Battaglia, L., Cruchaga, M., Storti, M., D'Elía, J., Aedo, J. N., and Reinoso, R. 2018. Numerical modelling of 3d sloshing experiments in rectangular tanks. *Applied Mathematical Modelling*. **59**, pp. 357–378.

Botia-Vera, E., Souto-Iglesias, A., Bulian, G., and Lobovskỳ, L. Three sph novel benchmark test cases for free surface flows. In *5th ERCOFTAC SPHERIC workshop on SPH applications*, pp. 146–153, 2010.

Bouscasse, B., Colagrossi, A., Antuono, M., and Lugni, C. A classification of shallow water resonant sloshing in a rectangular tank. In *International Conference on Offshore Mechanics and Arctic Engineering*, volume 55430, pp. V009T12A049. American Society of Mechanical Engineers, 2013.

Brackbill, J. U., Kothe, D. B., and Zemach, C. 1992. A continuum method for modeling surface tension. *Journal of computational physics*. **100**(2), pp. 335–354.

Bradford, S. F. 2000. Numerical simulation of surf zone dynamics. *Journal of Waterway, Port, Coastal, and Ocean Engineering*. **126**(1), pp. 1–13.

Brown, S. A., Magar, V., Greaves, D. M., and Conley, D. C. 2014. An evaluation of rans turbulence closure models for spilling breakers. *Coastal Engineering Proceedings*. (34), pp. 5–5.

Cappello, J., Sauret, A., Boulogne, F., Dressaire, E., and Stone, H. A. 2015. Damping of liquid sloshing by foams: from everyday observations to liquid transport. *Journal of Visualization*. **18**(2), pp. 269–271.

Celebi, S. and Akyildiz, H. 2002. Nonlinear modelling of liquid sloshing in a moving rectangular tank. *Ocean Engineering*. **29**(12), pp. 1527–1553.

Chen, Y. and Xue, M.-A. 2018. Numerical simulation of liquid sloshing with different filling levels using openfoam and experimental validation. *Water*. **10**(12), pp. 1752.

Chen, Y.-H., Hwang, W.-S., and Ko, C.-H. 2007. Sloshing behaviours of rectangular and cylindrical liquid tanks subjected to harmonic and seismic excitations. *Earthquake engineering & structural dynamics*. **36**(12), pp. 1701–1717.

Chen, Z., Zong, Z., Li, H., and Li, J. 2013a. An investigation into the pressure on solid walls in 2d sloshing using sph method. *Ocean Engineering*. **59**, pp. 129–141.

Chen, Z., Zong, Z., Li, H. T., and Li, J. 2013b. An investigation into the pressure on solid walls in 2D sloshing using SPH method. *Ocean Engineering*. **59**, pp. 129–141.

Chiba, M., Murase, R., Kimura, R., Yamamoto, Y., and Komatsu, K. 2016. Experimental studies on the dynamic stability of liquid in a spherical tank covered with diaphragm under vertical excitation. *Journal of Fluids and Structures*. **61**, pp. 218–248.

Chu, W.-H. 1964. Fuel sloshing in a spherical tank filled to an arbitrary depth. *AIAA Journal*. **2**(11), pp. 1972–1979.

Colagrossi, A., Lugni, C., Greco, M., and Faltinsen, O. Experimental and numerical investigation of 2d sloshing with slamming. In *Proc. 19th Int. Workshop on Water Waves and Floating Bodies, Cortona, Italy*, 2004.

Colagrossi, A., Delorme, L., Colicchio, G., Souto-Iglesias, A., and Cercós-Pita, J. Reynolds number and shallow depth sloshing. In *3o ERCOFTAC SPHERIC Workshop on SPH Applications*, 2008.

Delorme, L., Colagrossi, A., Souto-Iglesias, A., Zamora-Rodriguez, R., and Botia-Vera, E. 2009. A set of canonical problems in sloshing, part i: Pressure field in forced roll—comparison between experimental results and sph. *Ocean Engineering.* **36**(2), pp. 168–178.

Devolder, B., Rauwoens, P., and Troch, P. 2017. Application of a buoyancy-modified k-ω sst turbulence model to simulate wave run-up around a monopile subjected to regular waves using openfoam®. *Coastal Engineering.* **125**, pp. 81–94.

Devolder, B., Troch, P., and Rauwoens, P. 2018. Performance of a buoyancy-modified k-ω and k-ω sst turbulence model for simulating wave breaking under regular waves using openfoam®. *Coastal Engineering.* **138**, pp. 49–65.

Didier, E., Neves, D., Martins, R., and Neves, M. 2014. Wave interaction with a vertical wall: Sph numerical and experimental modeling. *Ocean engineering.* **88**, pp. 330–341.

Dodge, F. T. et al. 2000. *The new" dynamic behavior of liquids in moving containers".* Southwest Research Inst. San Antonio, TX.

Egorov, Y., Boucker, M., Martin, A., Pigny, S., Scheuerer, M., and Willemsen, S. 2004. Validation of cfd codes with pts-relevant test cases. *5th Euratom Framework Programme ECORA project.* pp. 91–116.

Elhanafi, A., Fleming, A., Leong, Z., and Macfarlane, G. 2017. Effect of rans-based turbulence models on nonlinear wave generation in a two-phase numerical wave tank. *Progress in Computational Fluid Dynamics, an International Journal.* **17** (3), pp. 141–158.

Fabre, J., Masbernat, L., and Suzanne, C. 1987. Experimental data set no. 7: Stratified flow, part i: Local structure. *Multiphase Science and technology.* **3** (1-4).

Faitinsen, O. M. 1978. A numerical nonlinear method of sloshing in tanks with two-dimensional flow. *Journal of Ship Research.* **22**(03), pp. 193–202.

Faltinsen, O. 2017. Sloshing.

Faltinsen, O., Firoozkoohi, R., and Timokha, A. 2011. Steady-state liquid sloshing in a rectangular tank with a slat-type screen in the middle: Quasilinear modal analysis and experiments. *Physics of Fluids*. **23**(4), pp. 042101.

Faltinsen, O. M. and Timokha, A. N. 2001. An adaptive multimodal approach to nonlinear sloshing in a rectangular tank. *Journal of Fluid Mechanics*. **432**, pp. 167–200.

Faltinsen, O. M. and Timokha, A. N. 2009. *Sloshing*, volume 577. Cambridge university press Cambridge.

Faltinsen, O. M., Rognebakke, O. F., Lukovsky, I. A., and Timokha, A. N. 2000. Multidimensional modal analysis of nonlinear sloshing in a rectangular tank with finite water depth. *Journal of fluid mechanics*. **407**, pp. 201–234.

Fan, W. and Anglart, H. 2019. Progress in phenomenological modeling of turbulence damping around a two-phase interface. *Fluids*. **4**(3), pp. 136.

Fan, W. and Anglart, H. 2020. varrhoturbvof: A new set of volume of fluid solvers for turbulent isothermal multiphase flows in openfoam. *Computer Physics Communications*. **247**, pp. 106876.

Farhat, C., Chiu, E. K.-y., Amsallem, D., Schotté, J.-S., and Ohayon, R. 2013. Modeling of fuel sloshing and its physical effects on flutter. *AIAA journal*. **51**(9), pp. 2252–2265.

Fiebach, A., Schmeyer, E., Knotek, S., and Schmelter, S. Numerical simulation of multiphase flow in a vertically mounted venturi flow meter. In *Proceedings of the 17th international flow measurement conference FLOMEKO*, pp. 26–29, 2016.

Firouz-Abadi, R., Zarifian, P., and Haddadpour, H. 2014. Effect of fuel sloshing in the external tank on the flutter of subsonic wings. *Journal of Aerospace Engineering*. **27**(5), pp. 04014021.

Fox, D. W. and Kuttler, J. R. 1983. Sloshing frequencies. *Zeitschrift für angewandte Mathematik und Physik ZAMP.* **34**(5), pp. 668–696.

Frederix, E., Mathur, A., Dovizio, D., Geurts, B., and Komen, E. 2018. Reynolds-averaged modeling of turbulence damping near a large-scale interface in two-phase flow. *Nuclear Engineering and Design.* **333**, pp. 122–130.

Fulgosi, M., Lakehal, D., Banerjee, S., and De Angelis, V. 2003. Direct numerical simulation of turbulence in a sheared air–water flow with a deformable interface. *Journal of fluid mechanics.* **482**, pp. 319–345.

Gada, V. H., Tandon, M. P., Elias, J., Vikulov, R., and Lo, S. 2017. A large scale interface multi-fluid model for simulating multiphase flows. *Applied Mathematical Modelling.* **44**, pp. 189–204.

Gavory, T. and De Seze, P. Sloshing in membrane lng carriers and its consequences from a designer's perspective. In *The Nineteenth International Offshore and Polar Engineering Conference*. OnePetro, 2009.

Gingold, R. A. and Monaghan, J. J. 1977. Smoothed particle hydrodynamics: theory and application to non-spherical stars. *Monthly notices of the royal astronomical society.* **181**(3), pp. 375–389.

Gotoh, H., Khayyer, A., Ikari, H., Arikawa, T., and Shimosako, K. 2014. On enhancement of incompressible sph method for simulation of violent sloshing flows. *Applied Ocean Research.* **46**, pp. 104–115.

Green, M. D. and Peiró, J. 2018. Long duration sph simulations of sloshing in tanks with a low fill ratio and high stretching. *Computers & fluids.* **174**, pp. 179–199.

Grotle, E. L. 2018. Thermodynamic response enhanced by sloshing in marine lng fuel tanks: Experimental work and numerical modelling.

Grotle, E. L. and Æsøy, V. 2017. Numerical simulations of sloshing and the thermodynamic response due to mixing. *Energies.* **10**(9), pp. 1338.

Grotle, E. L., Bihs, H., and Æsøy, V. 2017. Experimental and numerical investigation of sloshing under roll excitation at shallow liquid depths. *Ocean Engineering*. **138**, pp. 73–85.

Ha, M., Kim, D., Choi, H. I., Cheong, C., and Kwon, S. H. 2012. Numerical and experimental investigations into liquid sloshing in a rectangular tank. *Advances in Wind and Structures*. pp. 609–735.

Hall, J., Rendall, T., Allen, C., and Peel, H. 2015. A multi-physics computational model of fuel sloshing effects on aeroelastic behaviour. *Journal of Fluids and Structures*. **56**, pp. 11–32.

Hanjalić, K. and Launder, B. E. 1972. A reynolds stress model of turbulence and its application to thin shear flows. *Journal of fluid Mechanics*. **52**(4), pp. 609–638.

Harlow, F. H. and Welch, J. E. 1965. Numerical calculation of time-dependent viscous incompressible flow of fluid with free surface. *The physics of fluids*. **8**(12), pp. 2182–2189.

Hinatsu, M. Experiments of two-phase flows for the joint research. In *Proc. SRITUHH mini-Workshop on Numerical Simulation of Two-Phase Flows, 2001*, pp. 12–19. Ship Research Institute, 2001.

Hirt, C. W. and Nichols, B. D. 1981. Volume of fluid (VOF) method for the dynamics of free boundaries. *Journal of Computational Physics*. **39**(1), pp. 201–225.

Hu, Z.-Q., Wang, S.-Y., Chen, G., Chai, S.-H., and Jin, Y.-T. 2017. The effects of lng-tank sloshing on the global motions of flng system. *International Journal of Naval Architecture and Ocean Engineering*. **9**(1), pp. 114–125.

Huang, H., Spadaccini, L. J., and Sobel, D. R. 2004. Fuel-cooled thermal management for advanced aeroengines. *J. Eng. Gas Turbines Power*. **126**(2), pp. 284–293.

Ibrahim, R. A. 2005. *Liquid sloshing dynamics: theory and applications*. Cambridge University Press.

Ibrahim, R. A. 2020. Assessment of breaking waves and liquid sloshing impact. *Nonlinear Dynamics*. **100**(3), pp. 1837–1925.

Jacobsen, N. G. 2011. A full hydro-and morphodynamic description of breaker bar development.

Jäger, M. 2019. *Fuel Tank Sloshing Simulation Using the Finite Volume Method*. Springer.

Jasak, H. and Weller, H. 1995. Interface tracking capabilities of the inter-gamma differencing scheme. *Department of Mechanical Engineering, Imperial College of Science, Technology and Medicine*.

Jin, H., Liu, Y., and Li, H.-J. 2014. Experimental study on sloshing in a tank with an inner horizontal perforated plate. *Ocean Engineering*. **82**, pp. 75–84.

Jin, H., Song, R., and Liu, Y. 2020. Sloshing motion in a real-scale water storage tank under nonlinear ground motion. *Water*. **12**(8), pp. 2098.

Jones, W. and Launder, B. E. 1972. The prediction of laminarization with a two-equation model of turbulence. *International journal of heat and mass transfer*. **15**(2), pp. 301–314.

Jung, J. H., Yoon, H. S., and Lee, C. Y. 2015. Effect of natural frequency modes on sloshing phenomenon in a rectangular tank. *International Journal of Naval Architecture and Ocean Engineering*. **7**(3), pp. 580–594.

Kuo, K. K.-y. and Acharya, R. 2012. *Fundamentals of turbulent and multiphase combustion*. John Wiley & Sons.

Lamb, H. 1924. *Hydrodynamics*. University Press.

Langton, R., Clark, C., Hewitt, M., and Richards, L. 2009. *Aircraft fuel systems*. John Wiley & Sons.

Larsen, B. E. and Fuhrman, D. R. 2018. On the over-production of turbulence beneath surface waves in reynolds-averaged navier–stokes models. *Journal of Fluid Mechanics*. **853**, pp. 419–460.

Larsen, B. E., van der Zanden, J., Ruessink, G., Fuhrman, D. R., et al. 2020. Stabilized rans simulation of surf zone kinematics and boundary layer processes beneath large-scale plunging waves over a breaker bar. *Ocean Modelling*. **155**, pp. 101705.

Lee, S. J., Kim, M., Lee, D., Kim, J., and Kim, Y. 2007. The effects of lng-tank sloshing on the global motions of lng carriers. *Ocean engineering*. **34**(1), pp. 10–20.

Li, B., Liu, H., and Zheng, S. 2018. Multidisciplinary topology optimization for reduction of sloshing in aircraft fuel tanks based on sph simulation. *Structural and Multidisciplinary Optimization*. **58**(4), pp. 1719–1736.

Li, Y.-l., Zhu, R.-c., Miao, G.-p., and Ju, F. 2012. Simulation of tank sloshing based on openfoam and coupling with ship motions in time domain. *Journal of Hydrodynamics, Ser. B*. **24**(3), pp. 450–457.

Lien, F.-S. and Kalitzin, G. 2001. Computations of transonic flow with the v2–f turbulence model. *International Journal of Heat and Fluid Flow*. **22**(1), pp. 53–61.

Liu, D. and Lin, P. 2008. A numerical study of three-dimensional liquid sloshing in tanks. *Journal of Computational physics*. **227**(8), pp. 3921–3939.

Liu, D., Tang, W., Wang, J., Xue, H., and Wang, K. 2016. Comparison of laminar model, rans, les and vles for simulation of liquid sloshing. *Applied Ocean Research*. **59**, pp. 638–649.

Liu, Z. and Li, C. 2018. Influence of slosh baffles on thermodynamic performance in liquid hydrogen tank. *Journal of hazardous materials*. **346**, pp. 253–262.

Liu, Z., Feng, Y., Lei, G., and Li, Y. 2019a. Fluid sloshing dynamic performance in a liquid hydrogen tank. *International Journal of Hydrogen Energy*. **44**(26), pp. 13885–13894.

Liu, Z., Feng, Y., Lei, G., and Li, Y. 2019b. Hydrodynamic performance in a sloshing liquid oxygen tank under different initial liquid filling levels. *Aerospace Science and Technology*. **85**, pp. 544–555.

Liu, Z., Cai, H., Feng, Y., Liu, Y., and Li, Y. 2020. Thermodynamic characteristic in a cryogenic storage tank under an intermittent sloshing excitation. *International Journal of Hydrogen Energy*. **45**(21), pp. 12082–12094.

Liu, Z., Chen, H., Chen, Q., and Chen, L. 2021. Numerical study on thermodynamic performance in a cryogenic fuel storage tank under external sloshing excitation. *International Journal of Aeronautical and Space Sciences*. **22**(5), pp. 1062–1074.

Lo, S., Tomasello, A., et al. Recent progress in cfd modelling of multiphase flow in horizontal and near-horizontal pipes. In *7th North American Conference on Multiphase Technology*. BHR Group, 2010.

Lombardi, P., De Angelis, V., and Banerjee, S. 1996. Direct numerical simulation of near-interface turbulence in coupled gas-liquid flow. *Physics of Fluids*. **8**(6), pp. 1643–1665.

Lucy, L. B. 1977. A numerical approach to the testing of the fission hypothesis. *The astronomical journal*. **82**, pp. 1013–1024.

Ma, C., Oka, M., Ando, T., and Matsubara, N. 2018. A study on sloshing behavior for moss-type lng tank based on sph numerical simulation and large-scale model experiment. *International Journal of Offshore and Polar Engineering*. **28**(04), pp. 350–360.

Ma, C., Ando, T., and Oka, M. 2020. Numerical simulation for sloshing behavior of moss-type lng tank based on an improved sph model. *International Journal of Offshore and Polar Engineering*. **30**(02), pp. 149–160.

Marrone, S., Colagrossi, A., Park, J., and Campana, E. 2017. Challenges on the numerical prediction of slamming loads on lng tank insulation panels. *Ocean Engineering*. **141**, pp. 512–530.

Mayer, S. and Madsen, P. A. Simulation of breaking waves in the surf zone using a navier-stokes solver. In *Coastal Engineering 2000*, pp. 928–941. 2001.

McKee, S., Tomé, M. F., Ferreira, V. G., Cuminato, J. A., Castelo, A., Sousa, F., and Mangiavacchi, N. 2008. The mac method. *Computers & Fluids*. **37**(8), pp. 907–930.

Meier, M., Yadigaroglu, G., and Smith, B. L. 2002. A novel technique for including surface tension in plic-vof methods. *European Journal of Mechanics-B/Fluids*. **21** (1), pp. 61–73.

Menter, F. R. 1994. Two-equation eddy-viscosity turbulence models for engineering applications. *AIAA journal*. **32**(8), pp. 1598–1605.

Merchant, V., Duggirala, R., and Kumar, A. 2016. Validation of openfoam's volume of fluid model.

Moir, I. and Seabridge, A. 2011. *Aircraft Systems: Mechanical, electrical, and avionics subsystems integration*, volume 52. John Wiley & Sons.

Nagaosa, R. and Saito, T. 1997. Turbulence structure and scalar transfer in stratified free–surface flows. *AIChE journal*. **43**(10), pp. 2393–2404.

Nezu, I. and Rodi, W. 1986. Open-channel flow measurements with a laser doppler anemometer. *Journal of hydraulic engineering*. **112**(5), pp. 335–355.

Nguyen, C. T., Nguyen, C. T., Bui, H. H., Nguyen, G. D., and Fukagawa, R. 2017. A new sph-based approach to simulation of granular flows using viscous damping and stress regularisation. *Landslides*. **14**(1), pp. 69–81.

Ozdemir, Z., Souli, M., and Fahjan, Y. M. 2010. Fsi methods for seismic analysis of sloshing tank problems. *Mechanics & Industry*. **11**(2), pp. 133–147.

Pan, Z., Weibel, J. A., and Garimella, S. V. 2015. Spurious current suppression in vof-csf simulation of slug flow through small channels. *Numerical Heat Transfer, Part A: Applications*. **67**(1), pp. 1–12.

Pang, L., Li, S., Liu, M., Li, A., Meng, F., et al. 2018. Influence of the design parameters of a fuel thermal management system on its thermal endurance. *Energies*. **11**(7), pp. 1677.

Peng, C., Wang, S., Wu, W., Yu, H.-s., Wang, C., and Chen, J.-y. 2019. Loquat: an open-source gpu-accelerated sph solver for geotechnical modeling. *Acta Geotechnica*. **14**(5), pp. 1269–1287.

Peric, M., Zorn, T., el Moctar, O., Schellin, T. E., and Kim, Y.-S. 2009. Simulation of sloshing in lng-tanks. *Journal of offshore mechanics and Arctic engineering*. **131**(3).

Pilloton, C., Bardazzi, A., Colagrossi, A., and Marrone, S. 2022. Sph method for long-time simulations of sloshing flows in lng tanks. *European Journal of Mechanics-B/Fluids*.

Pope, S. B. and Pope, S. B. 2000. *Turbulent flows*. Cambridge university press.

Popov, G., Sankar, S., Sankar, T., and Vatistas, G. 1992. Liquid sloshing in rectangular road containers. *Computers & fluids*. **21**(4), pp. 551–569.

Popov, G., Sankar, S., and Sankar, T. 1993a. Dynamics of liquid sloshing in baffled and compartmented road containers. *Journal of fluids and structures*. **7**(7), pp. 803–821.

Popov, G., Sankar, S., Sankar, T., and Vatistas, G. 1993b. Dynamics of liquid sloshing in horizontal cylindrical road containers. *Proceedings of the Institution of Mechanical Engineers, Part C: Journal of Mechanical Engineering Science.* **207** (6), pp. 399–406.

Qiu, G., Cai, W., and Jiang, Y. 2018. Development and validation of numerical model of condensation heat transfer and frictional pressure drop in a circular tube. *Applied Thermal Engineering.* **143**, pp. 225–235.

Qu, S., Liu, S., and Ong, M. C. 2021. An evaluation of different rans turbulence models for simulating breaking waves past a vertical cylinder. *Ocean Engineering.* **234**, pp. 109195.

Rafiee, A., Pistani, F., and Thiagarajan, K. 2011. Study of liquid sloshing: numerical and experimental approach. *Computational Mechanics.* **47**(1), pp. 65–75.

Rashidi, M. and Banerjee, S. 1988. Turbulence structure in free-surface channel flows. *The Physics of fluids.* **31**(9), pp. 2491–2503.

Rashidi, M. t. and Banerjee, S. 1990. The effect of boundary conditions and shear rate on streak formation and breakdown in turbulent channel flows. *Physics of Fluids A: Fluid Dynamics.* **2**(10), pp. 1827–1838.

Rhee, S. H. 2005. Unstructured grid based reynolds-averaged navier-stokes method for liquid tank sloshing.

Rudman, M. and Cleary, P. W. Modeling sloshing in lng tanks. In *7th International Conference on CFD in the Minerals and Process Industries, CSIRO, Melbourne, Australia*, pp. 9–11, 2009.

Sabri, F. and Lakis, A. A. 2010. Finite element method applied to supersonic flutter of circular cylindrical shells. *AIAA journal.* **48**(1), pp. 73–81.

Sabri, F. and Lakis, A. A. 2011. Effects of sloshing on flutter prediction of liquid-filled circular cylindrical shell. *Journal of Aircraft.* **48**(6), pp. 1829–1839.

Samkhaniani, N. and Ansari, M. 2016. Numerical simulation of bubble condensation using cf-vof. *Progress in Nuclear Energy*. **89**, pp. 120–131.

Sanapala, V., Velusamy, K., and Patnaik, B. 2016. Cfd simulations on the dynamics of liquid sloshing and its control in a storage tank for spent fuel applications. *Annals of Nuclear Energy*. **94**, pp. 494–509.

Satoru, K., Hiromasa, U., Fumimaru, O., and Tokuro, M. 1982. Turbulence structure and transport mechanism at the free surface in an open channel flow. *International Journal of Heat and Mass Transfer*. **25**(4), pp. 513–521.

Shao, J., Li, H., Liu, G., and Liu, M. 2012. An improved sph method for modeling liquid sloshing dynamics. *Computers & Structures*. **100**, pp. 18–26.

Shen, L., Triantafyllou, G. S., and Yue, D. K. 2000. Turbulent diffusion near a free surface. *Journal of Fluid Mechanics*. **407**, pp. 145–166.

Smagorinsky, J. 1963. General circulation experiments with the primitive equations: I. the basic experiment. *Monthly weather review*. **91**(3), pp. 99–164.

Souto-Iglesias, A., Botia-Vera, E., Martín, A., and Pérez-Arribas, F. 2011. A set of canonical problems in sloshing. part 0: Experimental setup and data processing. *Ocean Engineering*. **38**(16), pp. 1823–1830.

Souto-Iglesias, A., Botia-Vera, E., and Bulian, G. Repeatability and two-dimensionality of model scale sloshing impacts. In *The twenty-second international offshore and polar engineering conference*. OnePetro, 2012.

Spalart, P. and Allmaras, S. A one-equation turbulence model for aerodynamic flows. In *30th aerospace sciences meeting and exhibit*, pp. 439, 1992.

Sussman, M., Smereka, P., and Osher, S. 1994. A level set approach for computing solutions to incompressible two-phase flow. *Journal of Computational physics*. **114**(1), pp. 146–159.

Tahmasebi, M. K., Shamsoddini, R., and Abolpour, B. 2020. Performances of different turbulence models for simulating shallow water sloshing in rectangular tank. *Journal of Marine Science and Application*. **19**(3), pp. 381–387.

Terzuoli, F., Galassi, M., Mazzini, D., and D'Auria, F. 2008. Cfd code validation against stratified air-water flow experimental data. *Science and Technology of Nuclear Installations*. **2008**.

Ting, F. C. and Kirby, J. T. 1994. Observation of undertow and turbulence in a laboratory surf zone. *Coastal Engineering*. **24**(1-2), pp. 51–80.

Ubbink, O. 1997. Numerical prediction of two fluid systems with sharp interfaces. *Doctoral Thesis*.

Ubbink, O. and Issa, R. 1999. A method for capturing sharp fluid interfaces on arbitrary meshes. *Journal of computational physics*. **153**(1), pp. 26–50.

Van Driest, E. R. 1956. On turbulent flow near a wall. *Journal of the aeronautical sciences*. **23**(11), pp. 1007–1011.

Van Leer, B. 1974. Towards the ultimate conservative difference scheme. ii. monotonicity and conservation combined in a second-order scheme. *Journal of computational physics*. **14**(4), pp. 361–370.

Van Maele, K. and Merci, B. 2006. Application of two buoyancy-modified k–ε turbulence models to different types of buoyant plumes. *Fire Safety Journal*. **41** (2), pp. 122–138.

Vignjevic, R. and Campbell, J. Review of development of the smooth particle hydrodynamics (sph) method. In *Predictive modeling of dynamic processes*, pp. 367–396. Springer, 2009.

Wacławczyk, T. and Koronowicz, T. 2008. Comparison of cicsam and hric high-resolution schemes for interface capturing. *Journal of theoretical and applied mechanics*. **46**, pp. 325–345.

Weller, H. G., Tabor, G., Jasak, H., and Fureby, C. 1998. A tensorial approach to computational continuum mechanics using object-oriented techniques. *Computers in physics*. **12**(6), pp. 620–631.

Wilcox, D. C. et al. 1998. *Turbulence modeling for CFD*, volume 2. DCW industries La Canada, CA.

Wu, S. and Ju, Y. 2021. Numerical study of the boil-off gas (bog) generation characteristics in a type c independent liquefied natural gas (lng) tank under sloshing excitation. *Energy*. **223**, pp. 120001.

Xue, M.-A., Chen, Y., Zheng, J., Qian, L., and Yuan, X. 2019. Fluid dynamics analysis of sloshing pressure distribution in storage vessels of different shapes. *Ocean Engineering*. **192**, pp. 106582.

Yakhot, V. and Orszag, S. A. 1986. Renormalization group analysis of turbulence. i. basic theory. *Journal of scientific computing*. **1**(1), pp. 3–51.

Youngs, D. L. 1982. Time-dependent multi-material flow with large fluid distortion. *Numerical methods for fluid dynamics*.

Yu, Y.-M., Ma, N., Fan, S.-M., and Gu, X.-C. 2017. Experimental and numerical studies on sloshing in a membrane-type lng tank with two floating plates. *Ocean Engineering*. **129**, pp. 217–227.

Zhang, H. and Sun, B. 2014. Numerical simulation of sloshing in 2d rectangular tanks based on the prediction of free surface. *Mathematical problems in engineering*. **2014**.

Zheng, S., Gao, F., Zhang, Z., Liu, H., and Li, B. 2021. Topology optimization on fuel tank rib structures for fuel sloshing suppression based on hybrid fluid–solid sph simulation. *Thin-Walled Structures*. **165**, pp. 107938.

Zhiyin, Y. 2015. Large-eddy simulation: Past, present and the future. *Chinese journal of Aeronautics*. **28**(1), pp. 11–24.

Appendix A

Supplementary content for Chapter 7

A.1 Temperature contours

A.1.1 Deep tanks, $h_{\text{fs}}/L_x = 0.7$

Temperature difference, $\Delta T = 1$. Forcing frequency, $\omega = \omega_1$

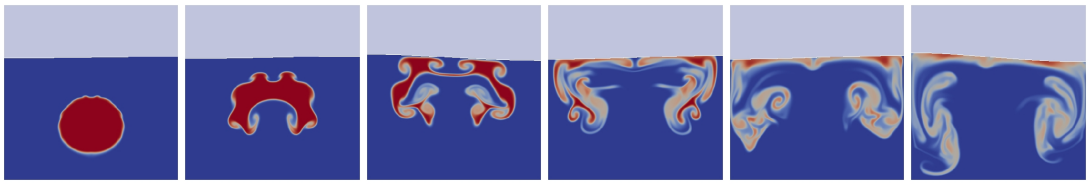

(a) $t = 10s$ (b) $t = 20s$ (c) $t = 30s$ (d) $t = 40s$ (e) $t = 50s$ (f) $t = 60s$

Figure A.1: $\boldsymbol{A^* = 2 \times 10^{-4}}$

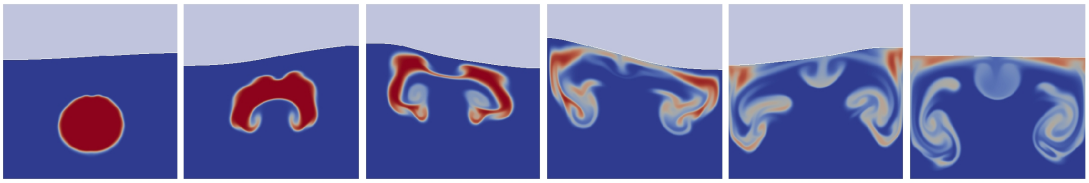

(a) $t = 10s$ (b) $t = 20s$ (c) $t = 30s$ (d) $t = 40s$ (e) $t = 50s$ (f) $t = 60s$

Figure A.2: $\boldsymbol{A^* = 1 \times 10^{-3}}$

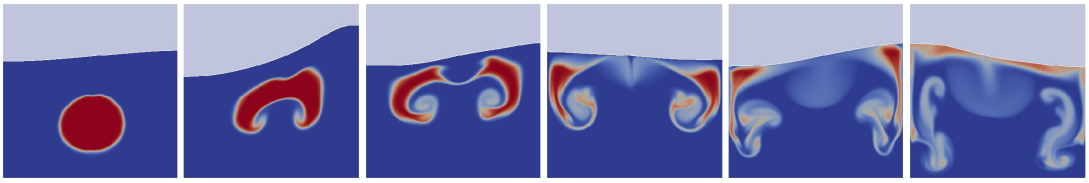

(a) $t = 10s$ (b) $t = 20s$ (c) $t = 30s$ (d) $t = 40s$ (e) $t = 50s$ (f) $t = 60s$

Figure A.3: $\boldsymbol{A^* = 2 \times 10^{-3}}$

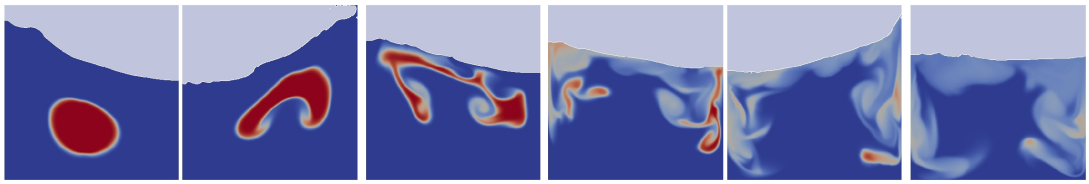

(a) $t = 10s$ (b) $t = 20s$ (c) $t = 30s$ (d) $t = 40s$ (e) $t = 50s$ (f) $t = 60s$

Figure A.4: $\boldsymbol{A^* = 1 \times 10^{-2}}$

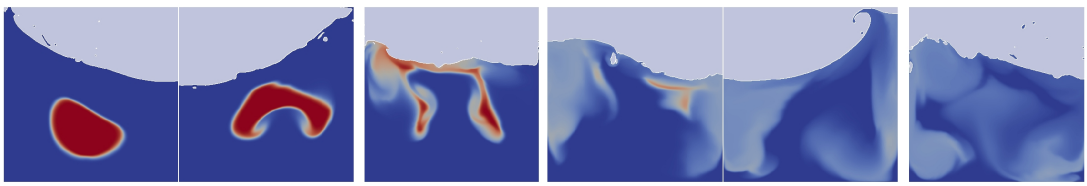

(a) $t = 10s$ (b) $t = 20s$ (c) $t = 30s$ (d) $t = 40s$ (e) $t = 50s$ (f) $t = 60s$

Figure A.5: $\boldsymbol{A^* = 2 \times 10^{-2}}$

Temperature difference, $\Delta T = 1$. Forcing frequency, $\omega = \omega_2$

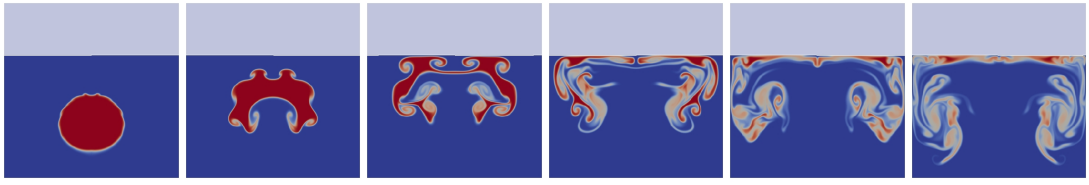

(a) $t = 10s$ (b) $t = 20s$ (c) $t = 30s$ (d) $t = 40s$ (e) $t = 50s$ (f) $t = 60s$

Figure A.6: $\boldsymbol{A^* = 2 \times 10^{-4}}$

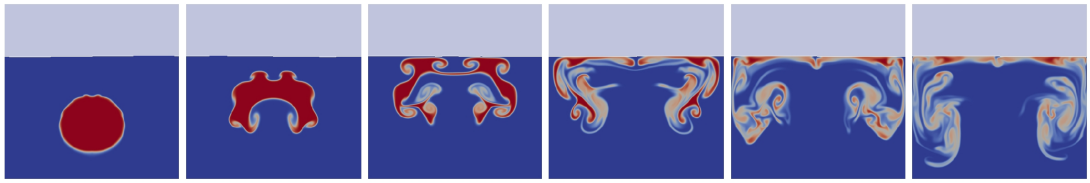

(a) $t = 10s$ (b) $t = 20s$ (c) $t = 30s$ (d) $t = 40s$ (e) $t = 50s$ (f) $t = 60s$

Figure A.7: $\boldsymbol{A^* = 1 \times 10^{-3}}$

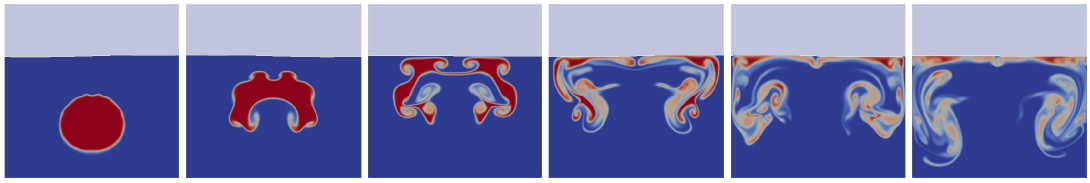

(a) $t = 10s$ (b) $t = 20s$ (c) $t = 30s$ (d) $t = 40s$ (e) $t = 50s$ (f) $t = 60s$

Figure A.8: $\boldsymbol{A^* = 2 \times 10^{-3}}$

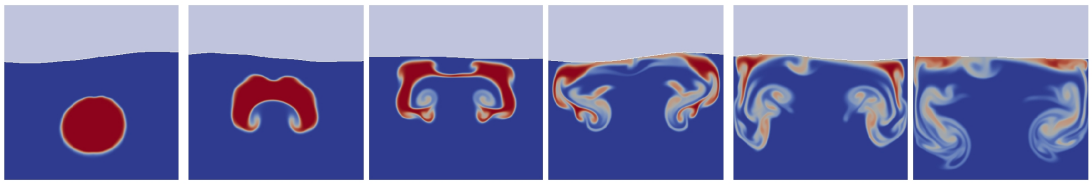

(a) $t = 10s$ (b) $t = 20s$ (c) $t = 30s$ (d) $t = 40s$ (e) $t = 50s$ (f) $t = 60s$

Figure A.9: $\boldsymbol{A^* = 1 \times 10^{-2}}$

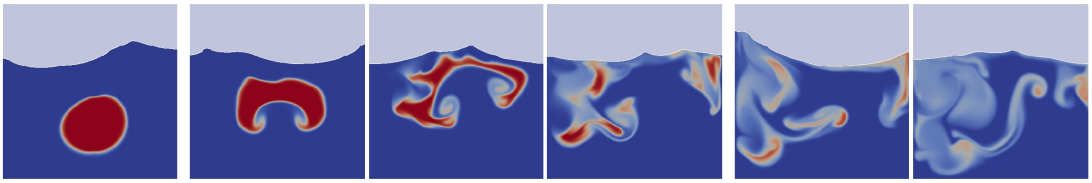

(a) $t = 10s$ (b) $t = 20s$ (c) $t = 30s$ (d) $t = 40s$ (e) $t = 50s$ (f) $t = 60s$

Figure A.10: $\boldsymbol{A^* = 2 \times 10^{-2}}$

Temperature difference, $\Delta T = 1$. Forcing frequency, $\omega = \omega_3$

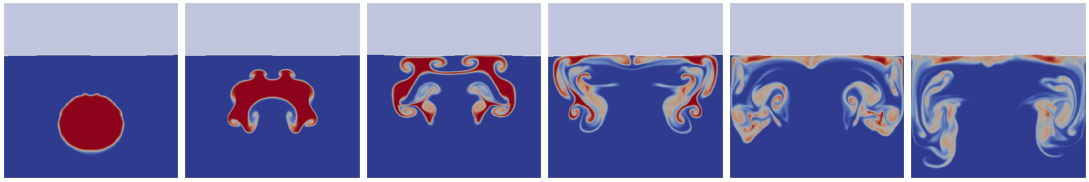

(a) $t = 10s$ (b) $t = 20s$ (c) $t = 30s$ (d) $t = 40s$ (e) $t = 50s$ (f) $t = 60s$

Figure A.11: $\boldsymbol{A^* = 2 \times 10^{-4}}$

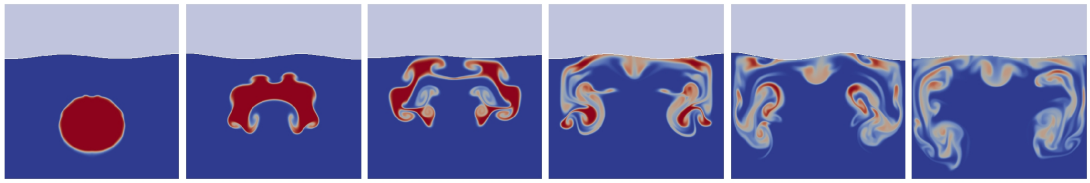

(a) $t = 10s$ (b) $t = 20s$ (c) $t = 30s$ (d) $t = 40s$ (e) $t = 50s$ (f) $t = 60s$

Figure A.12: $\boldsymbol{A^* = 1 \times 10^{-3}}$

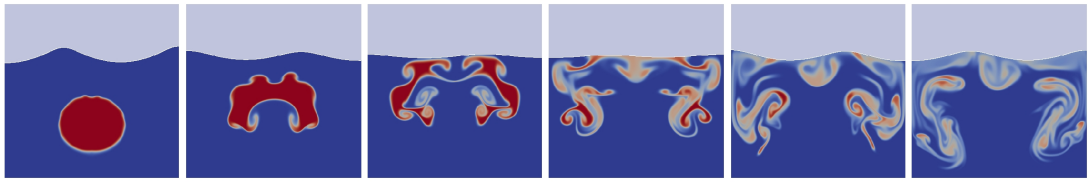

(a) $t = 10s$ (b) $t = 20s$ (c) $t = 30s$ (d) $t = 40s$ (e) $t = 50s$ (f) $t = 60s$

Figure A.13: $\boldsymbol{A^* = 2 \times 10^{-3}}$

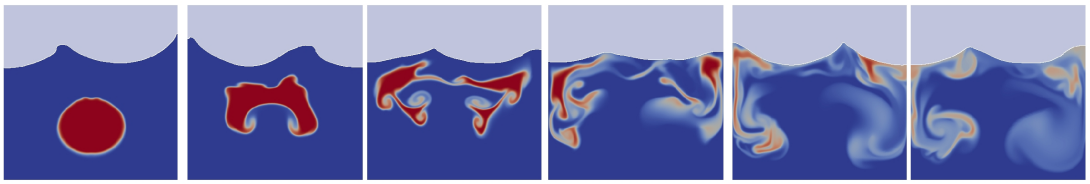

(a) $t = 10s$ (b) $t = 20s$ (c) $t = 30s$ (d) $t = 40s$ (e) $t = 50s$ (f) $t = 60s$

Figure A.14: $\boldsymbol{A^* = 1 \times 10^{-2}}$

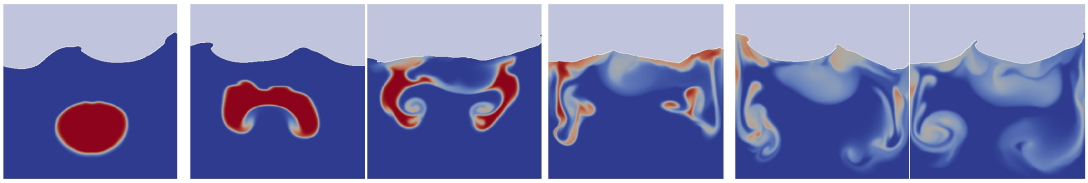

(a) $t = 10s$ (b) $t = 20s$ (c) $t = 30s$ (d) $t = 40s$ (e) $t = 50s$ (f) $t = 60s$

Figure A.15: $\boldsymbol{A^* = 2 \times 10^{-2}}$

Temperature difference, $\Delta T = 1$. Forcing frequency, $\omega = \omega_4$

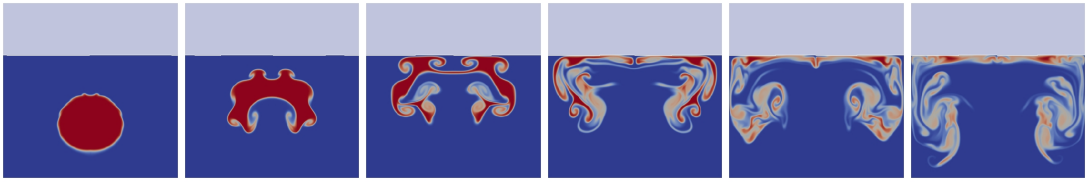

(a) $t = 10s$ (b) $t = 20s$ (c) $t = 30s$ (d) $t = 40s$ (e) $t = 50s$ (f) $t = 60s$

Figure A.16: $\boldsymbol{A^* = 2 \times 10^{-4}}$

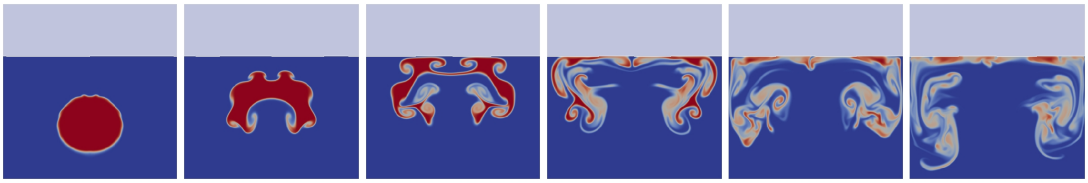

(a) $t = 10s$ (b) $t = 20s$ (c) $t = 30s$ (d) $t = 40s$ (e) $t = 50s$ (f) $t = 60s$

Figure A.17: $\boldsymbol{A^* = 1 \times 10^{-3}}$

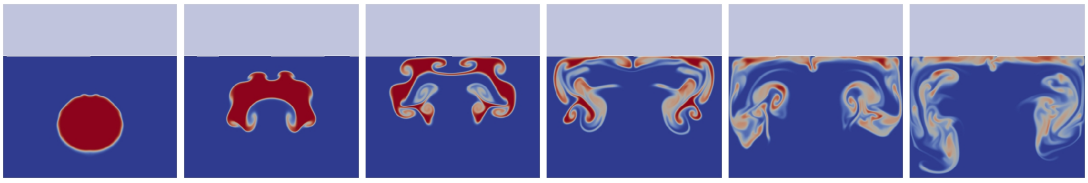

(a) $t = 10s$ (b) $t = 20s$ (c) $t = 30s$ (d) $t = 40s$ (e) $t = 50s$ (f) $t = 60s$

Figure A.18: $\boldsymbol{A^* = 2 \times 10^{-3}}$

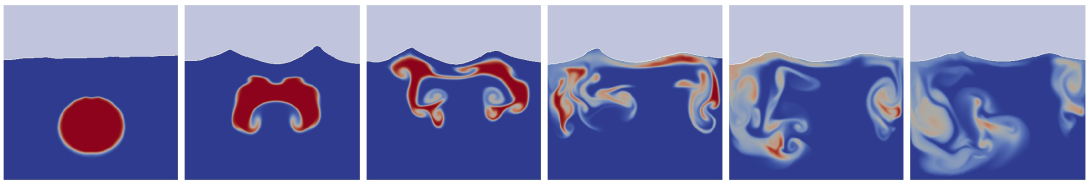

(a) $t = 10s$ (b) $t = 20s$ (c) $t = 30s$ (d) $t = 40s$ (e) $t = 50s$ (f) $t = 60s$

Figure A.19: $\boldsymbol{A^* = 1 \times 10^{-2}}$

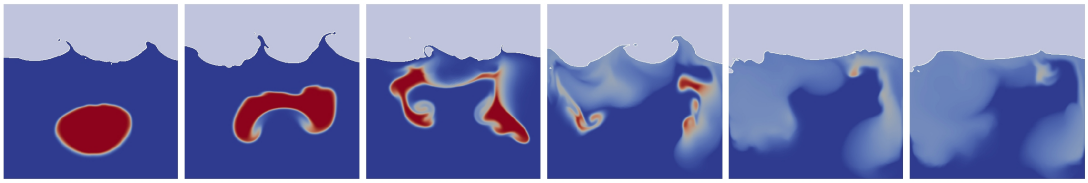

(a) $t = 10s$ (b) $t = 20s$ (c) $t = 30s$ (d) $t = 40s$ (e) $t = 50s$ (f) $t = 60s$

Figure A.20: $\boldsymbol{A^* = 2 \times 10^{-2}}$

Temperature difference, $\Delta T = 4$. Forcing frequency, $\omega = \omega_1$

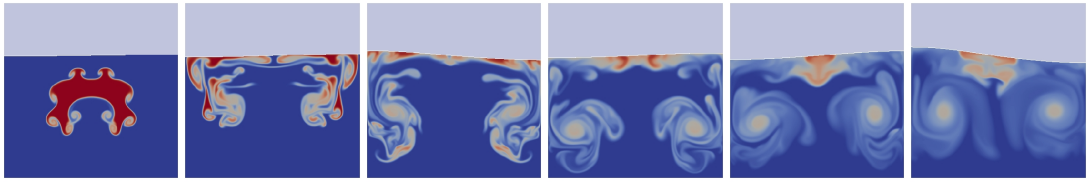

(a) $t = 10s$ (b) $t = 20s$ (c) $t = 30s$ (d) $t = 40s$ (e) $t = 50s$ (f) $t = 60s$

Figure A.21: $\boldsymbol{A^* = 2 \times 10^{-4}}$

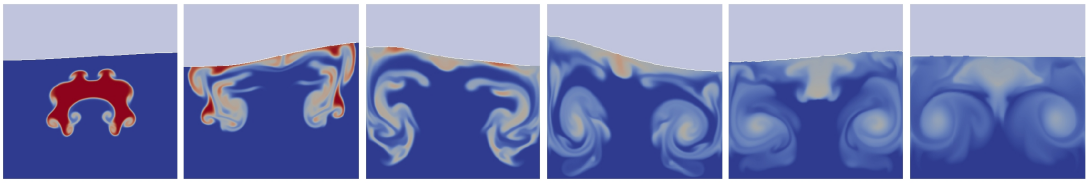

(a) $t = 10s$ (b) $t = 20s$ (c) $t = 30s$ (d) $t = 40s$ (e) $t = 50s$ (f) $t = 60s$

Figure A.22: $\boldsymbol{A^* = 1 \times 10^{-3}}$

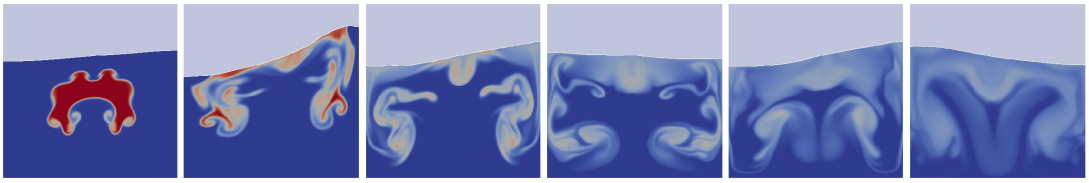

(a) $t = 10s$ (b) $t = 20s$ (c) $t = 30s$ (d) $t = 40s$ (e) $t = 50s$ (f) $t = 60s$

Figure A.23: $\boldsymbol{A^* = 2 \times 10^{-3}}$

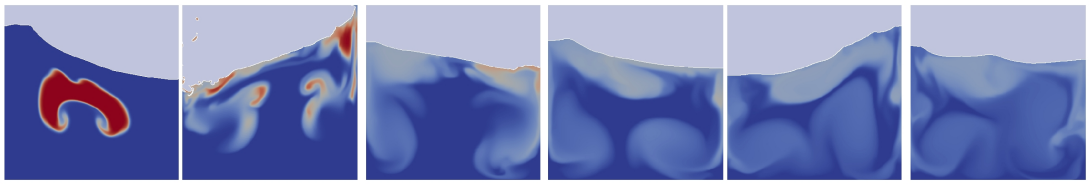

(a) $t = 10s$ (b) $t = 20s$ (c) $t = 30s$ (d) $t = 40s$ (e) $t = 50s$ (f) $t = 60s$

Figure A.24: $\boldsymbol{A^* = 1 \times 10^{-2}}$

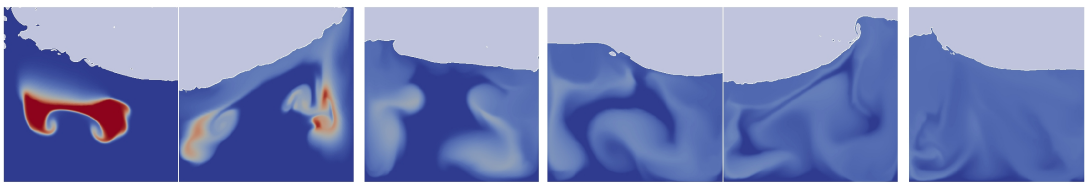

(a) $t = 10s$ (b) $t = 20s$ (c) $t = 30s$ (d) $t = 40s$ (e) $t = 50s$ (f) $t = 60s$

Figure A.25: $\boldsymbol{A^* = 2 \times 10^{-2}}$

Temperature difference, $\Delta T = 4$. Forcing frequency, $\omega = \omega_2$

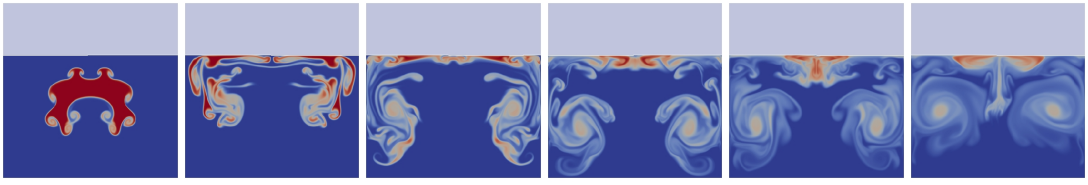

(a) $t = 10s$ (b) $t = 20s$ (c) $t = 30s$ (d) $t = 40s$ (e) $t = 50s$ (f) $t = 60s$

Figure A.26: $\boldsymbol{A^* = 2 \times 10^{-4}}$

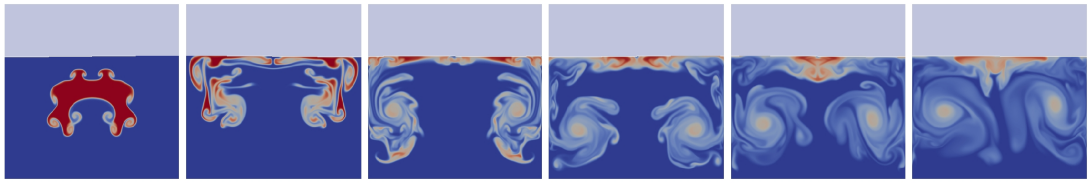

(a) $t = 10s$ (b) $t = 20s$ (c) $t = 30s$ (d) $t = 40s$ (e) $t = 50s$ (f) $t = 60s$

Figure A.27: $\boldsymbol{A^* = 1 \times 10^{-3}}$

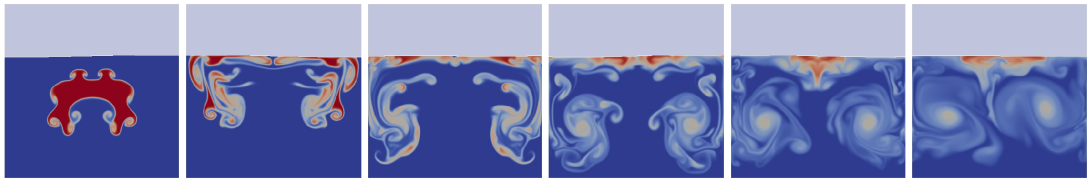

(a) $t = 10s$ (b) $t = 20s$ (c) $t = 30s$ (d) $t = 40s$ (e) $t = 50s$ (f) $t = 60s$

Figure A.28: $\boldsymbol{A^* = 2 \times 10^{-3}}$

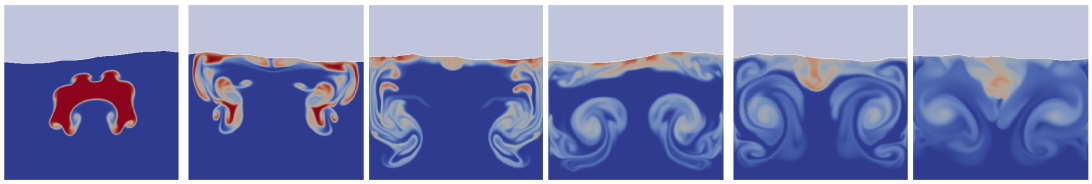

(a) $t = 10s$ (b) $t = 20s$ (c) $t = 30s$ (d) $t = 40s$ (e) $t = 50s$ (f) $t = 60s$

Figure A.29: $\boldsymbol{A^* = 1 \times 10^{-2}}$

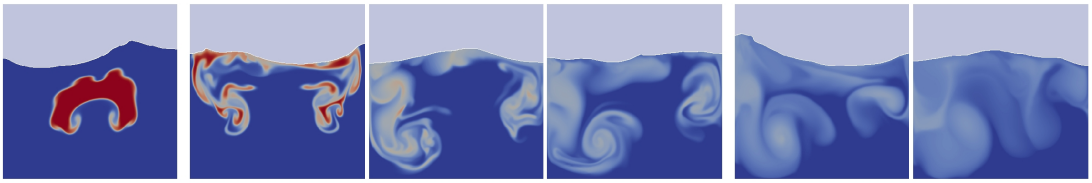

(a) $t = 10s$ (b) $t = 20s$ (c) $t = 30s$ (d) $t = 40s$ (e) $t = 50s$ (f) $t = 60s$

Figure A.30: $\boldsymbol{A^* = 2 \times 10^{-2}}$

Temperature difference, $\Delta T = 4$. Forcing frequency, $\omega = \omega_3$

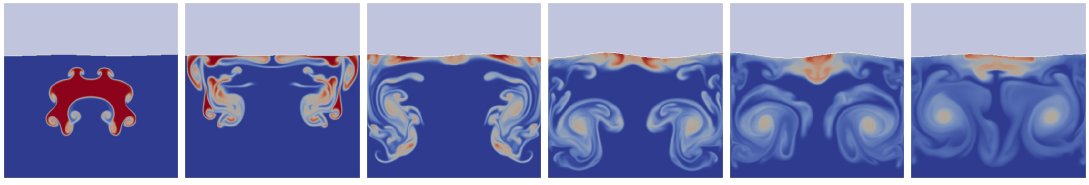

(a) $t = 10s$ (b) $t = 20s$ (c) $t = 30s$ (d) $t = 40s$ (e) $t = 50s$ (f) $t = 60s$

Figure A.31: $\boldsymbol{A^* = 2 \times 10^{-4}}$

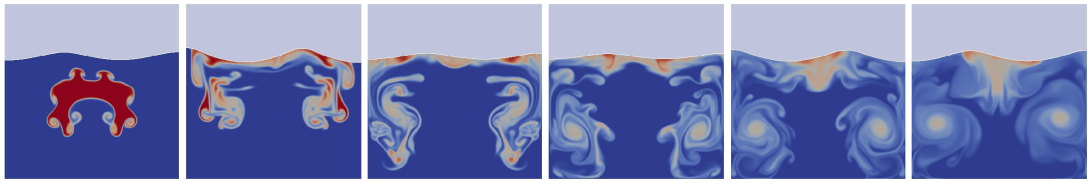

(a) $t = 10s$ (b) $t = 20s$ (c) $t = 30s$ (d) $t = 40s$ (e) $t = 50s$ (f) $t = 60s$

Figure A.32: $\boldsymbol{A^* = 1 \times 10^{-3}}$

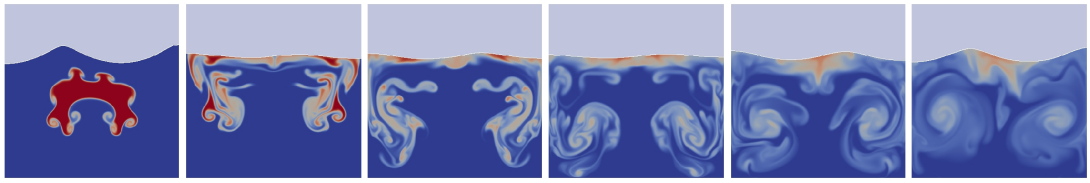

(a) $t = 10s$ (b) $t = 20s$ (c) $t = 30s$ (d) $t = 40s$ (e) $t = 50s$ (f) $t = 60s$

Figure A.33: $\boldsymbol{A^* = 2 \times 10^{-3}}$

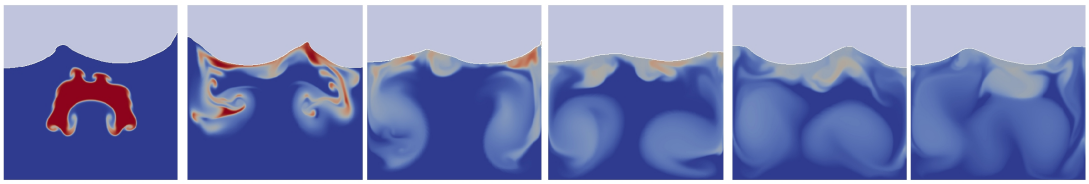

(a) $t = 10s$ (b) $t = 20s$ (c) $t = 30s$ (d) $t = 40s$ (e) $t = 50s$ (f) $t = 60s$

Figure A.34: $\boldsymbol{A^* = 1 \times 10^{-2}}$

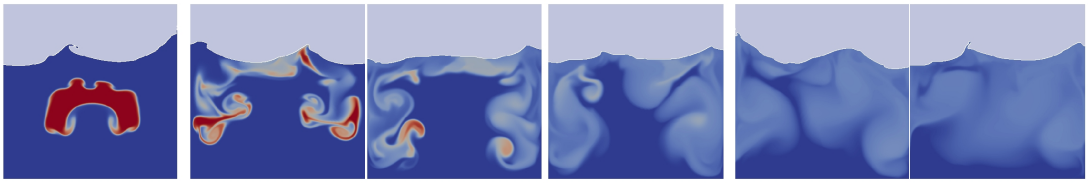

(a) $t = 10s$ (b) $t = 20s$ (c) $t = 30s$ (d) $t = 40s$ (e) $t = 50s$ (f) $t = 60s$

Figure A.35: $\boldsymbol{A^* = 2 \times 10^{-2}}$

Temperature difference, $\Delta T = 4$. Forcing frequency, $\omega = \omega_4$

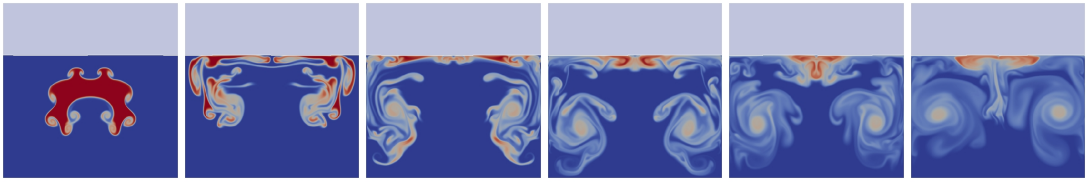

(a) $t = 10s$ (b) $t = 20s$ (c) $t = 30s$ (d) $t = 40s$ (e) $t = 50s$ (f) $t = 60s$

Figure A.36: $\boldsymbol{A^* = 2 \times 10^{-4}}$

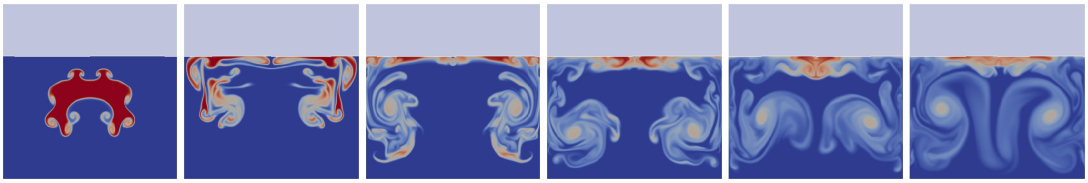

(a) $t = 10s$ (b) $t = 20s$ (c) $t = 30s$ (d) $t = 40s$ (e) $t = 50s$ (f) $t = 60s$

Figure A.37: $\boldsymbol{A^* = 1 \times 10^{-3}}$

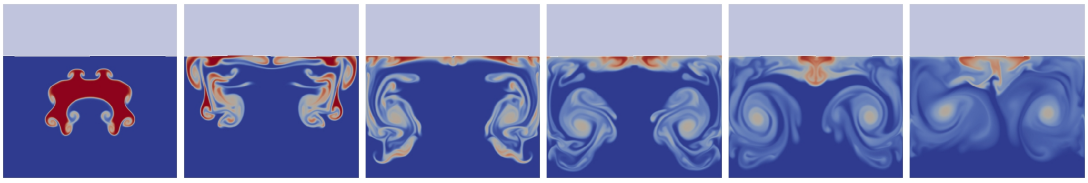

(a) $t = 10s$ (b) $t = 20s$ (c) $t = 30s$ (d) $t = 40s$ (e) $t = 50s$ (f) $t = 60s$

Figure A.38: $\boldsymbol{A^* = 2 \times 10^{-3}}$

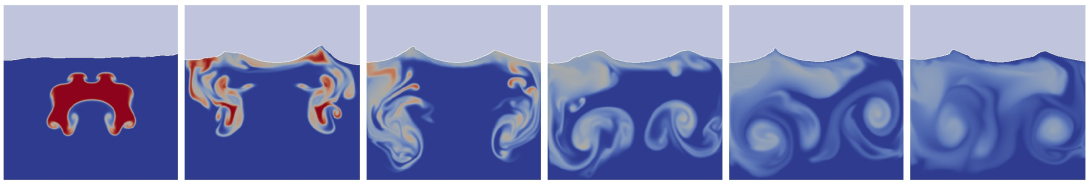

(a) $t = 10s$ (b) $t = 20s$ (c) $t = 30s$ (d) $t = 40s$ (e) $t = 50s$ (f) $t = 60s$

Figure A.39: $\boldsymbol{A^* = 1 \times 10^{-2}}$

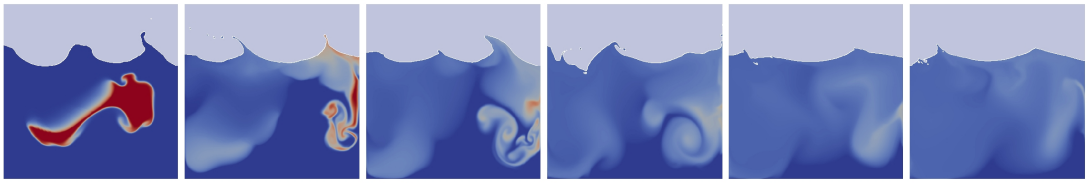

(a) $t = 10s$ (b) $t = 20s$ (c) $t = 30s$ (d) $t = 40s$ (e) $t = 50s$ (f) $t = 60s$

Figure A.40: $\boldsymbol{A^* = 2 \times 10^{-2}}$

Temperature difference, $\Delta T = 16$. Forcing frequency, $\omega = \omega_1$

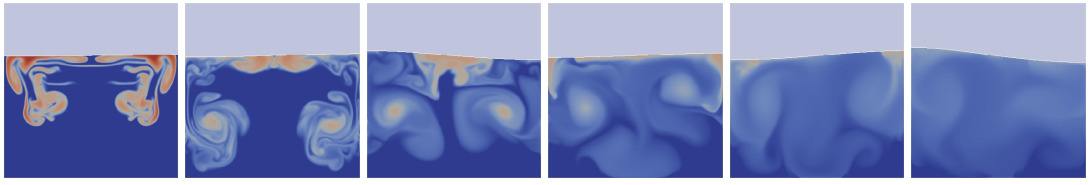

(a) $t = 10s$ (b) $t = 20s$ (c) $t = 30s$ (d) $t = 40s$ (e) $t = 50s$ (f) $t = 60s$

Figure A.41: $\boldsymbol{A^* = 2 \times 10^{-4}}$

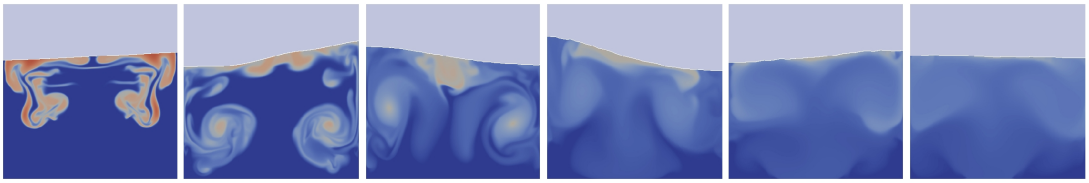

(a) $t = 10s$ (b) $t = 20s$ (c) $t = 30s$ (d) $t = 40s$ (e) $t = 50s$ (f) $t = 60s$

Figure A.42: $\boldsymbol{A^* = 1 \times 10^{-3}}$

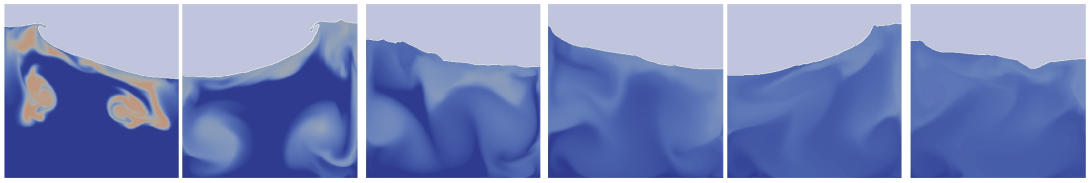

(a) $t = 10s$ (b) $t = 20s$ (c) $t = 30s$ (d) $t = 40s$ (e) $t = 50s$ (f) $t = 60s$

Figure A.43: $\boldsymbol{A^* = 1 \times 10^{-2}}$

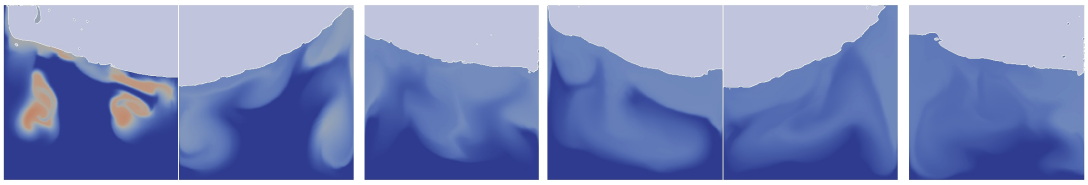

(a) $t = 10s$ (b) $t = 20s$ (c) $t = 30s$ (d) $t = 40s$ (e) $t = 50s$ (f) $t = 60s$

Figure A.44: $\boldsymbol{A^* = 2 \times 10^{-2}}$

Temperature difference, $\Delta T = 16$. Forcing frequency, $\omega = \omega_2$

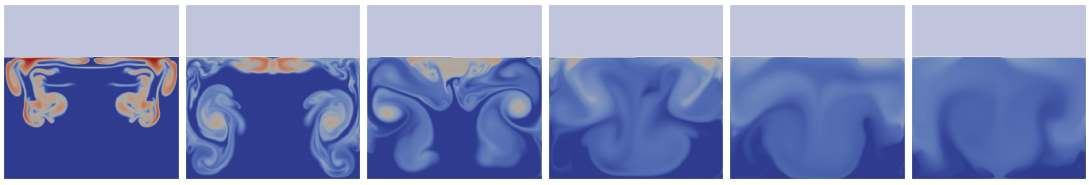

(a) $t = 10s$ (b) $t = 20s$ (c) $t = 30s$ (d) $t = 40s$ (e) $t = 50s$ (f) $t = 60s$

Figure A.45: $\boldsymbol{A^* = 2 \times 10^{-4}}$

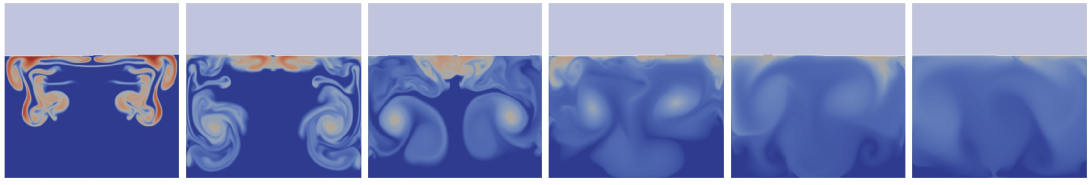

(a) $t = 10s$ (b) $t = 20s$ (c) $t = 30s$ (d) $t = 40s$ (e) $t = 50s$ (f) $t = 60s$

Figure A.46: $\boldsymbol{A^* = 1 \times 10^{-3}}$

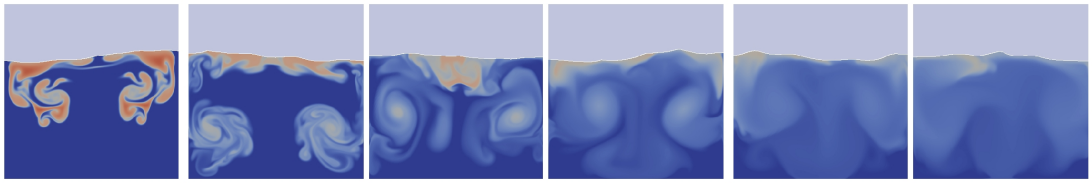

(a) $t = 10s$ (b) $t = 20s$ (c) $t = 30s$ (d) $t = 40s$ (e) $t = 50s$ (f) $t = 60s$

Figure A.47: $\boldsymbol{A^* = 1 \times 10^{-2}}$

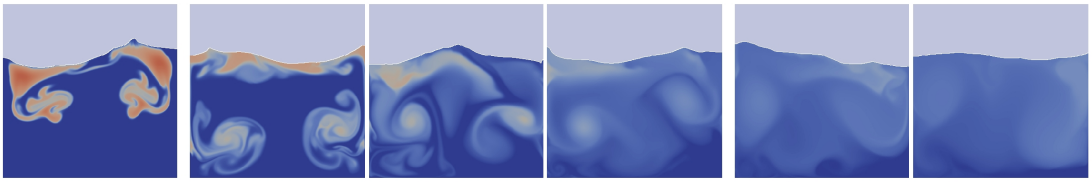

(a) $t = 10s$ (b) $t = 20s$ (c) $t = 30s$ (d) $t = 40s$ (e) $t = 50s$ (f) $t = 60s$

Figure A.48: $\boldsymbol{A^* = 2 \times 10^{-2}}$

Temperature difference, $\Delta T = 16$. Forcing frequency, $\omega = \omega_3$

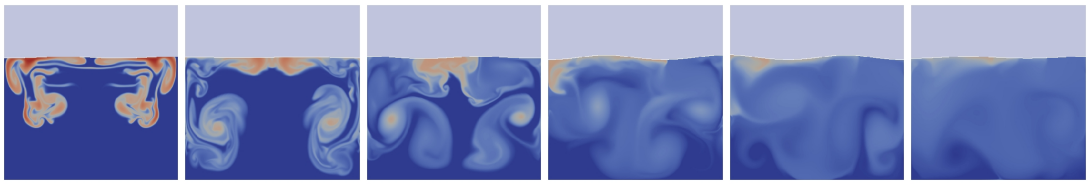

(a) $t = 10s$ (b) $t = 20s$ (c) $t = 30s$ (d) $t = 40s$ (e) $t = 50s$ (f) $t = 60s$

Figure A.49: $\boldsymbol{A^* = 2 \times 10^{-4}}$

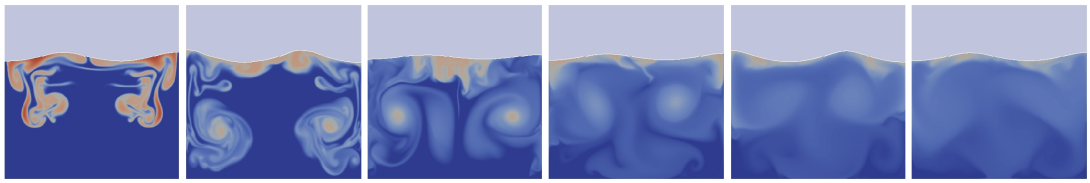

(a) $t = 10s$ (b) $t = 20s$ (c) $t = 30s$ (d) $t = 40s$ (e) $t = 50s$ (f) $t = 60s$

Figure A.50: $\boldsymbol{A^* = 1 \times 10^{-3}}$

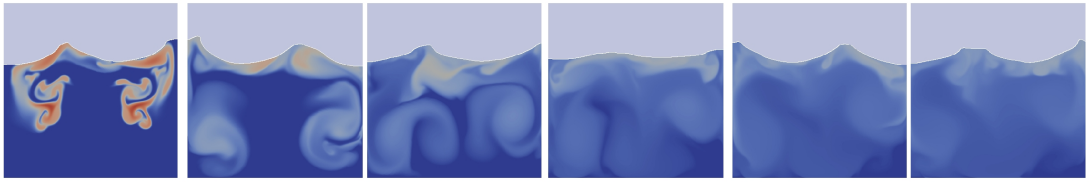

(a) $t = 10s$ (b) $t = 20s$ (c) $t = 30s$ (d) $t = 40s$ (e) $t = 50s$ (f) $t = 60s$

Figure A.51: $\boldsymbol{A^* = 1 \times 10^{-2}}$

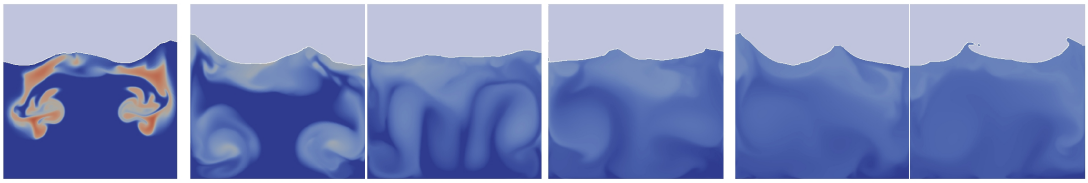

(a) $t = 10s$ (b) $t = 20s$ (c) $t = 30s$ (d) $t = 40s$ (e) $t = 50s$ (f) $t = 60s$

Figure A.52: $\boldsymbol{A^* = 2 \times 10^{-2}}$

Temperature difference, $\Delta T = 16$**. Forcing frequency,** $\omega = \omega_4$

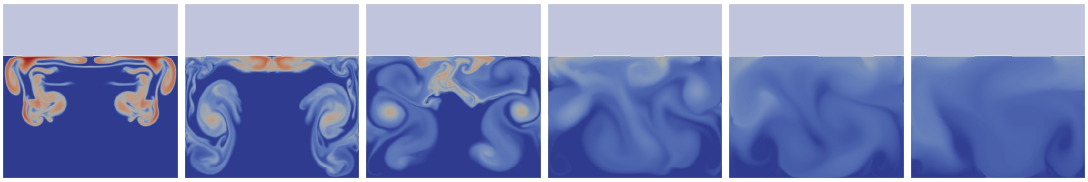

(a) $t = 10s$ (b) $t = 20s$ (c) $t = 30s$ (d) $t = 40s$ (e) $t = 50s$ (f) $t = 60s$

Figure A.53: $\boldsymbol{A^* = 2 \times 10^{-4}}$

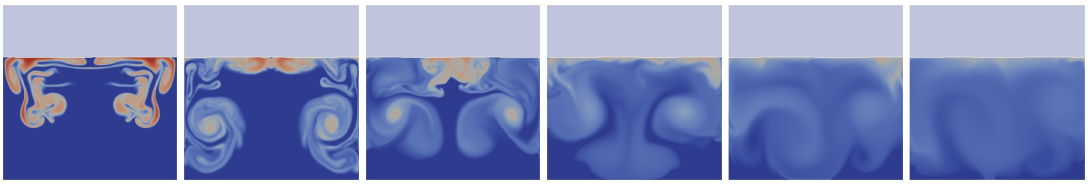

(a) $t = 10s$ (b) $t = 20s$ (c) $t = 30s$ (d) $t = 40s$ (e) $t = 50s$ (f) $t = 60s$

Figure A.54: $\boldsymbol{A^* = 1 \times 10^{-3}}$

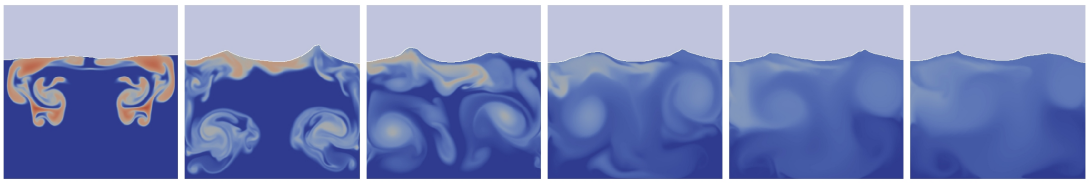

(a) $t = 10s$ (b) $t = 20s$ (c) $t = 30s$ (d) $t = 40s$ (e) $t = 50s$ (f) $t = 60s$

Figure A.55: $\boldsymbol{A^* = 1 \times 10^{-2}}$

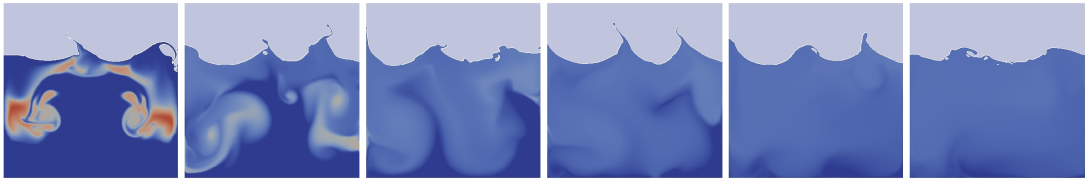

(a) $t = 10s$ (b) $t = 20s$ (c) $t = 30s$ (d) $t = 40s$ (e) $t = 50s$ (f) $t = 60s$

Figure A.56: $\boldsymbol{A^* = 2 \times 10^{-2}}$

A.1.2 Shallow tanks, $h_{\mathrm{fs}}/L_x = 0.15$

Temperature difference, $\Delta T = 1$. Forcing frequency, $\omega = \omega_1$

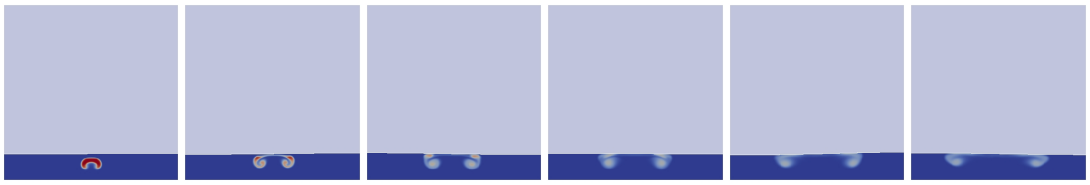

(a) $t = 10s$ (b) $t = 20s$ (c) $t = 30s$ (d) $t = 40s$ (e) $t = 50s$ (f) $t = 60s$

Figure A.57: $\boldsymbol{A^* = 2 \times 10^{-4}}$

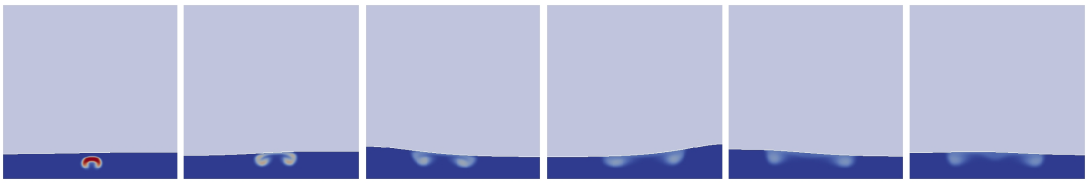

(a) $t = 10s$ (b) $t = 20s$ (c) $t = 30s$ (d) $t = 40s$ (e) $t = 50s$ (f) $t = 60s$

Figure A.58: $\boldsymbol{A^* = 1 \times 10^{-3}}$

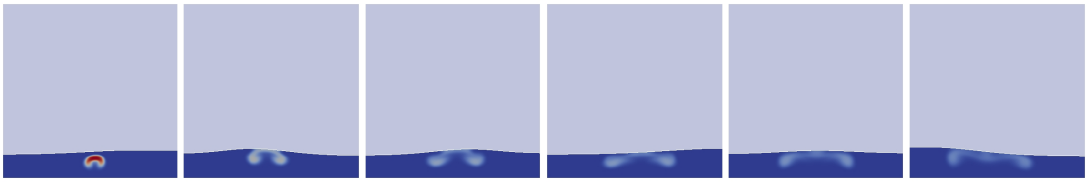

(a) $t = 10s$ (b) $t = 20s$ (c) $t = 30s$ (d) $t = 40s$ (e) $t = 50s$ (f) $t = 60s$

Figure A.59: $\boldsymbol{A^* = 2 \times 10^{-3}}$

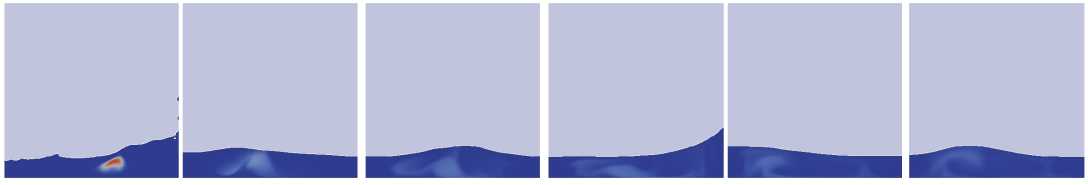

(a) $t = 10s$ (b) $t = 20s$ (c) $t = 30s$ (d) $t = 40s$ (e) $t = 50s$ (f) $t = 60s$

Figure A.60: $\boldsymbol{A^* = 1 \times 10^{-2}}$

(a) $t = 10s$ (b) $t = 20s$ (c) $t = 30s$ (d) $t = 40s$ (e) $t = 50s$ (f) $t = 60s$

Figure A.61: $\boldsymbol{A^* = 2 \times 10^{-2}}$

Temperature difference, $\Delta T = 1$. Forcing frequency, $\omega = \omega_2$

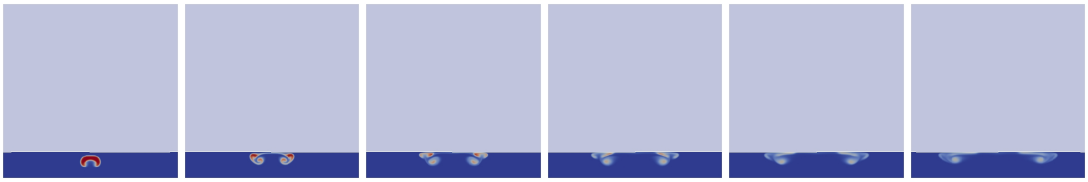

(a) $t = 10s$ (b) $t = 20s$ (c) $t = 30s$ (d) $t = 40s$ (e) $t = 50s$ (f) $t = 60s$

Figure A.62: $\boldsymbol{A^* = 2 \times 10^{-4}}$

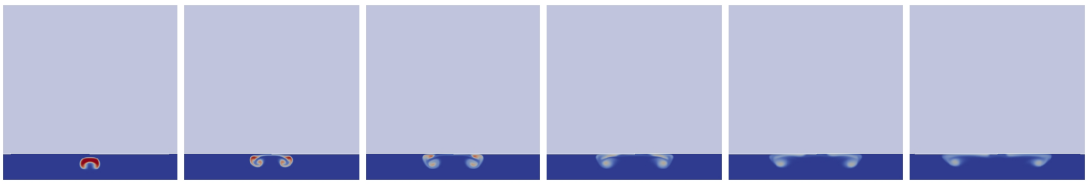

(a) $t = 10s$ (b) $t = 20s$ (c) $t = 30s$ (d) $t = 40s$ (e) $t = 50s$ (f) $t = 60s$

Figure A.63: $\boldsymbol{A^* = 1 \times 10^{-3}}$

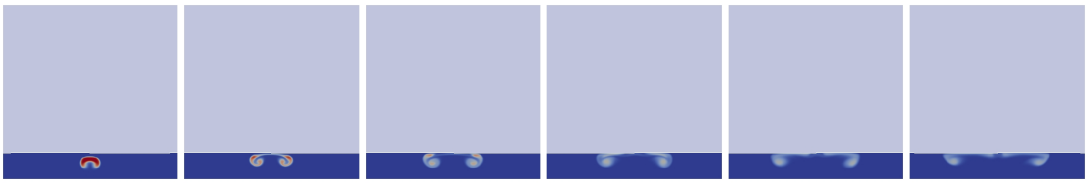

(a) $t = 10s$ (b) $t = 20s$ (c) $t = 30s$ (d) $t = 40s$ (e) $t = 50s$ (f) $t = 60s$

Figure A.64: $\boldsymbol{A^* = 2 \times 10^{-3}}$

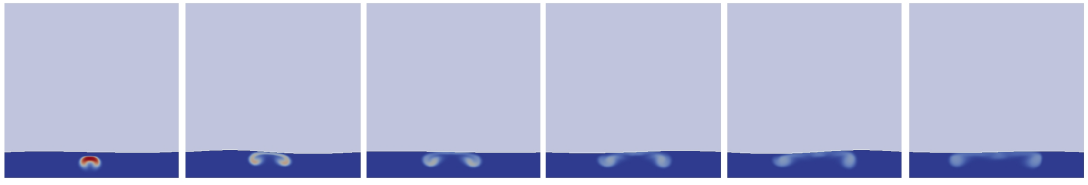

(a) $t = 10s$ (b) $t = 20s$ (c) $t = 30s$ (d) $t = 40s$ (e) $t = 50s$ (f) $t = 60s$

Figure A.65: $\boldsymbol{A^* = 1 \times 10^{-2}}$

(a) $t = 10s$ (b) $t = 20s$ (c) $t = 30s$ (d) $t = 40s$ (e) $t = 50s$ (f) $t = 60s$

Figure A.66: $\boldsymbol{A^* = 2 \times 10^{-2}}$

Temperature difference, $\Delta T = 1$**. Forcing frequency,** $\omega = \omega_3$

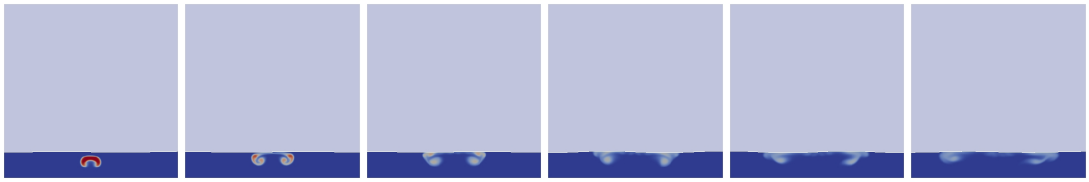

(a) $t = 10s$ (b) $t = 20s$ (c) $t = 30s$ (d) $t = 40s$ (e) $t = 50s$ (f) $t = 60s$

Figure A.67: $\boldsymbol{A^* = 2 \times 10^{-4}}$

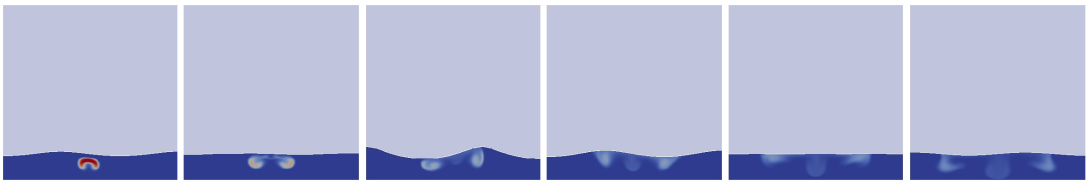

(a) $t = 10s$ (b) $t = 20s$ (c) $t = 30s$ (d) $t = 40s$ (e) $t = 50s$ (f) $t = 60s$

Figure A.68: $\boldsymbol{A^* = 1 \times 10^{-3}}$

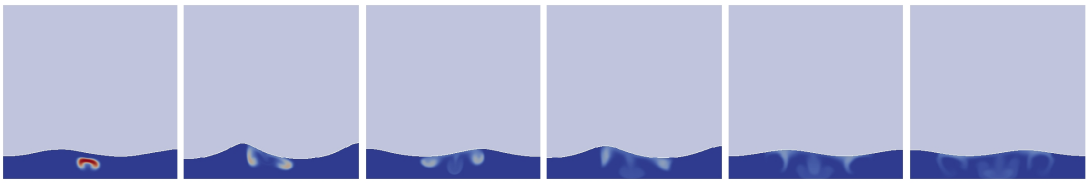

(a) $t = 10s$ (b) $t = 20s$ (c) $t = 30s$ (d) $t = 40s$ (e) $t = 50s$ (f) $t = 60s$

Figure A.69: $\boldsymbol{A^* = 2 \times 10^{-3}}$

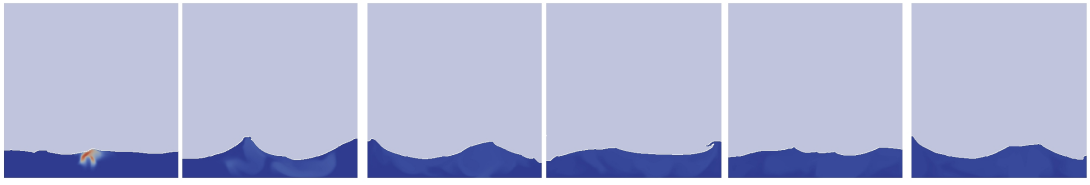

(a) $t = 10s$ (b) $t = 20s$ (c) $t = 30s$ (d) $t = 40s$ (e) $t = 50s$ (f) $t = 60s$

Figure A.70: $\boldsymbol{A^* = 1 \times 10^{-2}}$

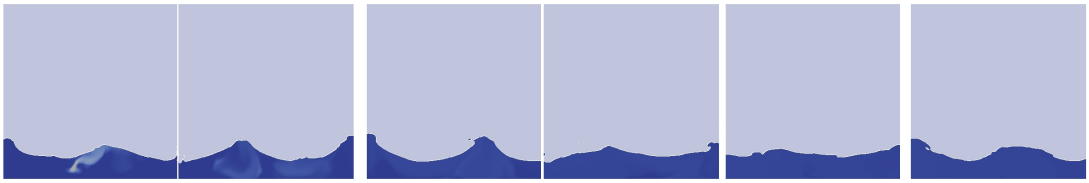

(a) $t = 10s$ (b) $t = 20s$ (c) $t = 30s$ (d) $t = 40s$ (e) $t = 50s$ (f) $t = 60s$

Figure A.71: $\boldsymbol{A^* = 2 \times 10^{-2}}$

Temperature difference, $\Delta T = 1$. Forcing frequency, $\omega = \omega_4$

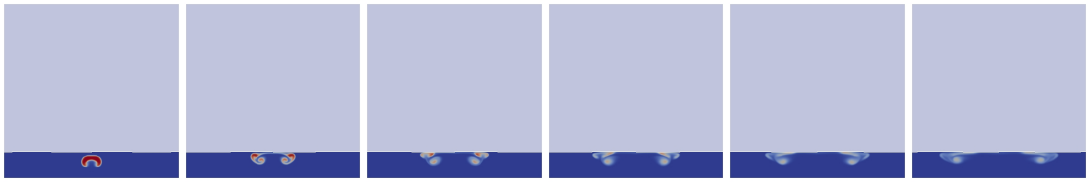

(a) $t = 10s$ (b) $t = 20s$ (c) $t = 30s$ (d) $t = 40s$ (e) $t = 50s$ (f) $t = 60s$

Figure A.72: $\boldsymbol{A^* = 2 \times 10^{-4}}$

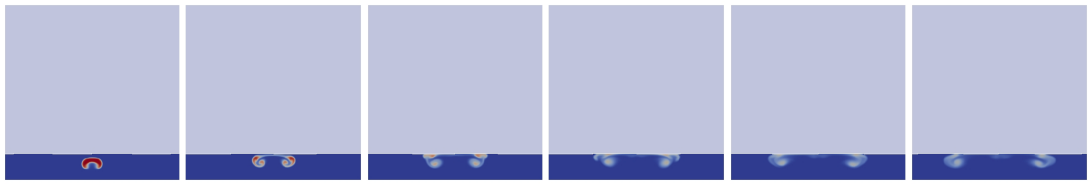

(a) $t = 10s$ (b) $t = 20s$ (c) $t = 30s$ (d) $t = 40s$ (e) $t = 50s$ (f) $t = 60s$

Figure A.73: $\boldsymbol{A^* = 1 \times 10^{-3}}$

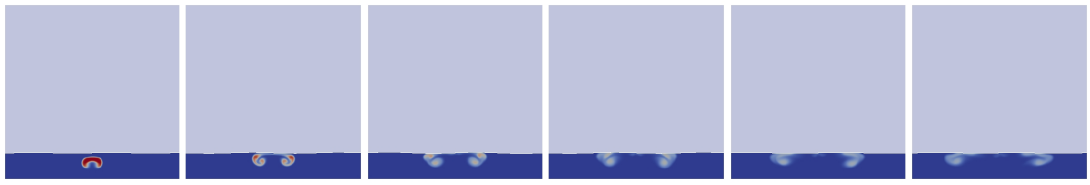

(a) $t = 10s$ (b) $t = 20s$ (c) $t = 30s$ (d) $t = 40s$ (e) $t = 50s$ (f) $t = 60s$

Figure A.74: $\boldsymbol{A^* = 2 \times 10^{-3}}$

(a) $t = 10s$ (b) $t = 20s$ (c) $t = 30s$ (d) $t = 40s$ (e) $t = 50s$ (f) $t = 60s$

Figure A.75: $\boldsymbol{A^* = 1 \times 10^{-2}}$

(a) $t = 10s$ (b) $t = 20s$ (c) $t = 30s$ (d) $t = 40s$ (e) $t = 50s$ (f) $t = 60s$

Figure A.76: $\boldsymbol{A^* = 2 \times 10^{-2}}$

Temperature difference, $\Delta T = 4$**. Forcing frequency,** $\omega = \omega_1$

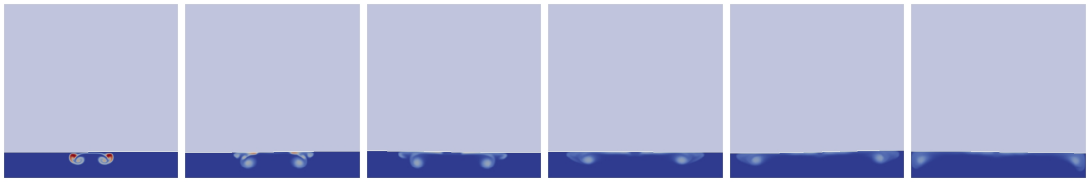

(a) $t = 10s$ (b) $t = 20s$ (c) $t = 30s$ (d) $t = 40s$ (e) $t = 50s$ (f) $t = 60s$

Figure A.77: $\boldsymbol{A^* = 2 \times 10^{-4}}$

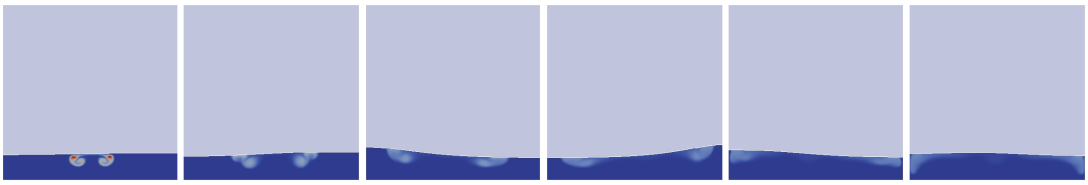

(a) $t = 10s$ (b) $t = 20s$ (c) $t = 30s$ (d) $t = 40s$ (e) $t = 50s$ (f) $t = 60s$

Figure A.78: $\boldsymbol{A^* = 1 \times 10^{-3}}$

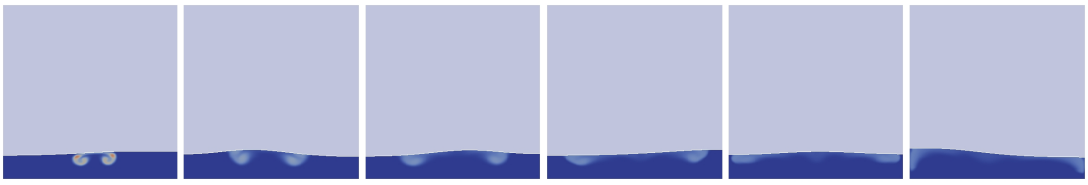

(a) $t = 10s$ (b) $t = 20s$ (c) $t = 30s$ (d) $t = 40s$ (e) $t = 50s$ (f) $t = 60s$

Figure A.79: $\boldsymbol{A^* = 2 \times 10^{-3}}$

(a) $t = 10s$ (b) $t = 20s$ (c) $t = 30s$ (d) $t = 40s$ (e) $t = 50s$ (f) $t = 60s$

Figure A.80: $\boldsymbol{A^* = 1 \times 10^{-2}}$

(a) $t = 10s$ (b) $t = 20s$ (c) $t = 30s$ (d) $t = 40s$ (e) $t = 50s$ (f) $t = 60s$

Figure A.81: $\boldsymbol{A^* = 2 \times 10^{-2}}$

Temperature difference, $\Delta T = 4$. Forcing frequency, $\omega = \omega_2$

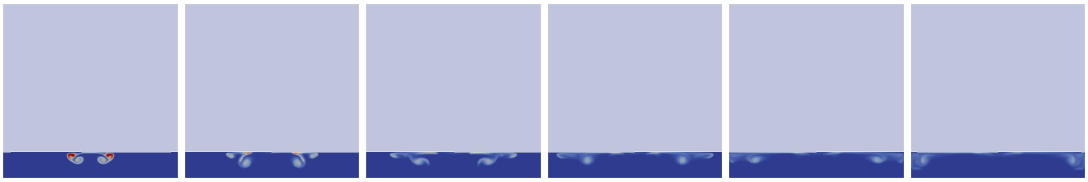

(a) $t = 10s$ (b) $t = 20s$ (c) $t = 30s$ (d) $t = 40s$ (e) $t = 50s$ (f) $t = 60s$

Figure A.82: $\boldsymbol{A^* = 2 \times 10^{-4}}$

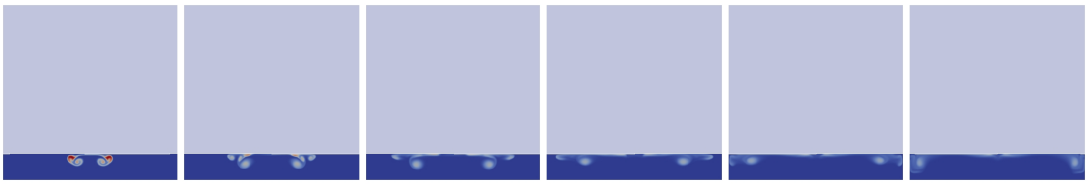

(a) $t = 10s$ (b) $t = 20s$ (c) $t = 30s$ (d) $t = 40s$ (e) $t = 50s$ (f) $t = 60s$

Figure A.83: $\boldsymbol{A^* = 1 \times 10^{-3}}$

(a) $t = 10s$ (b) $t = 20s$ (c) $t = 30s$ (d) $t = 40s$ (e) $t = 50s$ (f) $t = 60s$

Figure A.84: $\boldsymbol{A^* = 2 \times 10^{-3}}$

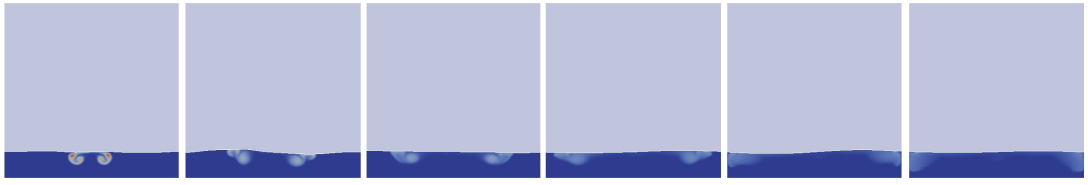

(a) $t = 10s$ (b) $t = 20s$ (c) $t = 30s$ (d) $t = 40s$ (e) $t = 50s$ (f) $t = 60s$

Figure A.85: $\boldsymbol{A^* = 1 \times 10^{-2}}$

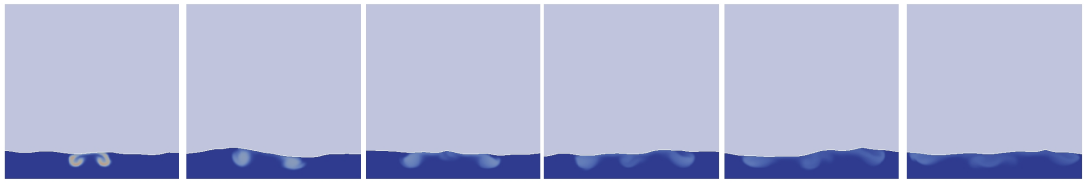

(a) $t = 10s$ (b) $t = 20s$ (c) $t = 30s$ (d) $t = 40s$ (e) $t = 50s$ (f) $t = 60s$

Figure A.86: $\boldsymbol{A^* = 2 \times 10^{-2}}$

Temperature difference, $\Delta T = 4$**. Forcing frequency,** $\omega = \omega_3$

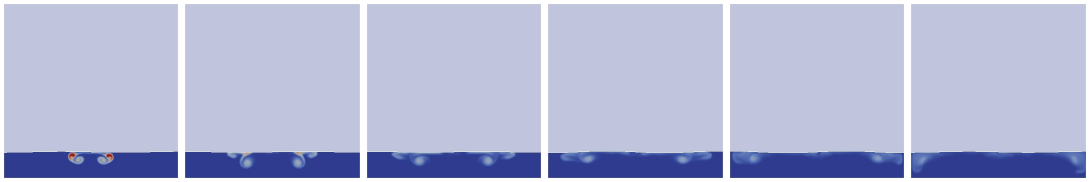

(a) $t = 10s$ (b) $t = 20s$ (c) $t = 30s$ (d) $t = 40s$ (e) $t = 50s$ (f) $t = 60s$

Figure A.87: $\boldsymbol{A^* = 2 \times 10^{-4}}$

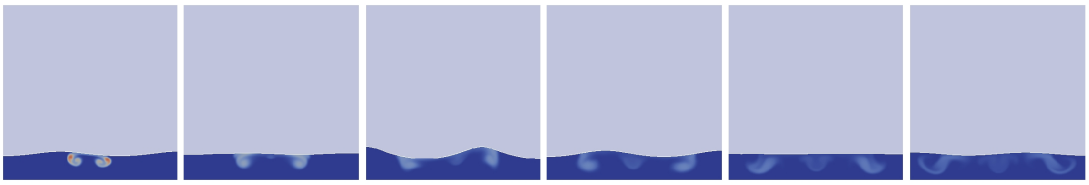

(a) $t = 10s$ (b) $t = 20s$ (c) $t = 30s$ (d) $t = 40s$ (e) $t = 50s$ (f) $t = 60s$

Figure A.88: $\boldsymbol{A^* = 1 \times 10^{-3}}$

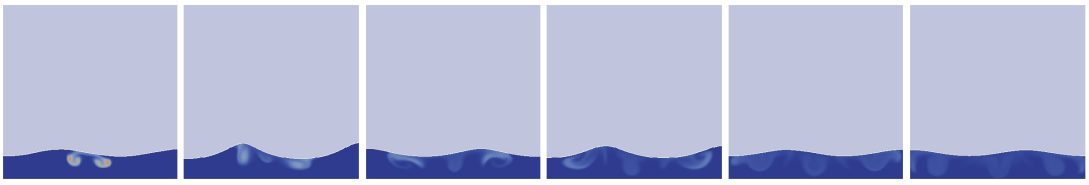

(a) $t = 10s$ (b) $t = 20s$ (c) $t = 30s$ (d) $t = 40s$ (e) $t = 50s$ (f) $t = 60s$

Figure A.89: $\boldsymbol{A^* = 2 \times 10^{-3}}$

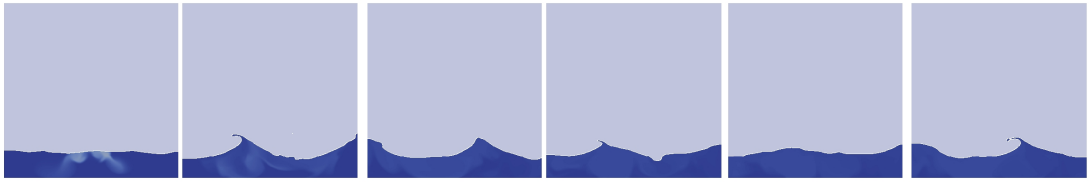

(a) $t = 10s$ (b) $t = 20s$ (c) $t = 30s$ (d) $t = 40s$ (e) $t = 50s$ (f) $t = 60s$

Figure A.90: $\boldsymbol{A^* = 1 \times 10^{-2}}$

(a) $t = 10s$ (b) $t = 20s$ (c) $t = 30s$ (d) $t = 40s$ (e) $t = 50s$ (f) $t = 60s$

Figure A.91: $\boldsymbol{A^* = 2 \times 10^{-2}}$

Temperature difference, $\Delta T = 4$. Forcing frequency, $\omega = \omega_4$

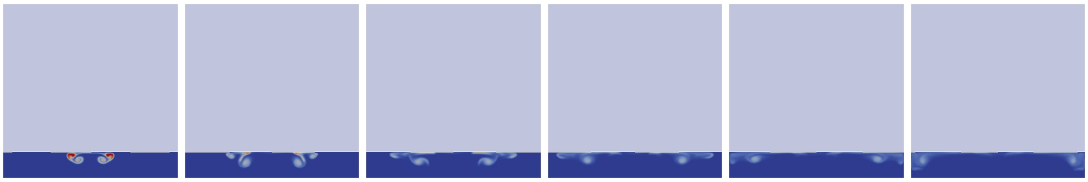

(a) $t = 10s$ (b) $t = 20s$ (c) $t = 30s$ (d) $t = 40s$ (e) $t = 50s$ (f) $t = 60s$

Figure A.92: $\boldsymbol{A^* = 2 \times 10^{-4}}$

(a) $t = 10s$ (b) $t = 20s$ (c) $t = 30s$ (d) $t = 40s$ (e) $t = 50s$ (f) $t = 60s$

Figure A.93: $\boldsymbol{A^* = 1 \times 10^{-3}}$

(a) $t = 10s$ (b) $t = 20s$ (c) $t = 30s$ (d) $t = 40s$ (e) $t = 50s$ (f) $t = 60s$

Figure A.94: $\boldsymbol{A^* = 2 \times 10^{-3}}$

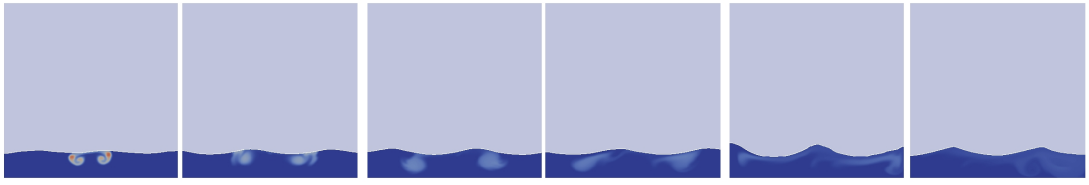

(a) $t = 10s$ (b) $t = 20s$ (c) $t = 30s$ (d) $t = 40s$ (e) $t = 50s$ (f) $t = 60s$

Figure A.95: $\boldsymbol{A^* = 1 \times 10^{-2}}$

(a) $t = 10s$ (b) $t = 20s$ (c) $t = 30s$ (d) $t = 40s$ (e) $t = 50s$ (f) $t = 60s$

Figure A.96: $\boldsymbol{A^* = 2 \times 10^{-2}}$

Temperature difference, $\Delta T = 16$**. Forcing frequency,** $\omega = \omega_1$

(a) $t = 10s$ (b) $t = 20s$ (c) $t = 30s$ (d) $t = 40s$ (e) $t = 50s$ (f) $t = 60s$

Figure A.97: $\boldsymbol{A^* = 2 \times 10^{-4}}$

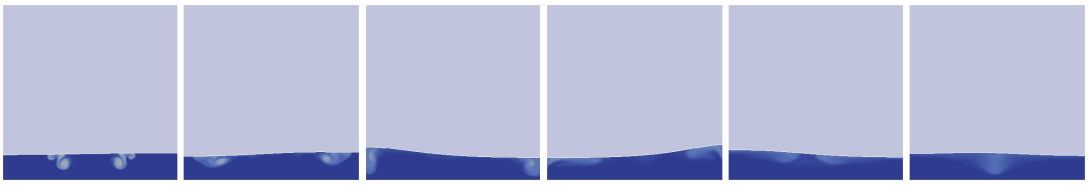

(a) $t = 10s$ (b) $t = 20s$ (c) $t = 30s$ (d) $t = 40s$ (e) $t = 50s$ (f) $t = 60s$

Figure A.98: $\boldsymbol{A^* = 1 \times 10^{-3}}$

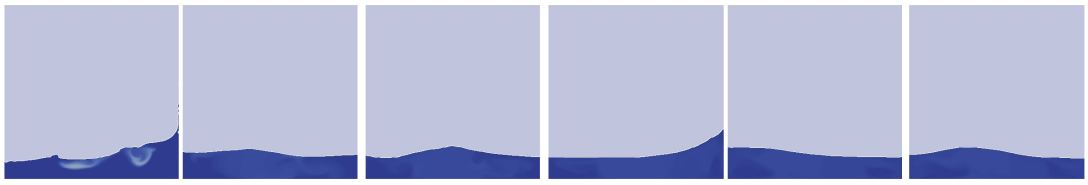

(a) $t = 10s$ (b) $t = 20s$ (c) $t = 30s$ (d) $t = 40s$ (e) $t = 50s$ (f) $t = 60s$

Figure A.99: $\boldsymbol{A^* = 1 \times 10^{-2}}$

(a) $t = 10s$ (b) $t = 20s$ (c) $t = 30s$ (d) $t = 40s$ (e) $t = 50s$ (f) $t = 60s$

Figure A.100: $\boldsymbol{A^* = 2 \times 10^{-2}}$

Temperature difference, $\Delta T = 16$. Forcing frequency, $\omega = \omega_2$

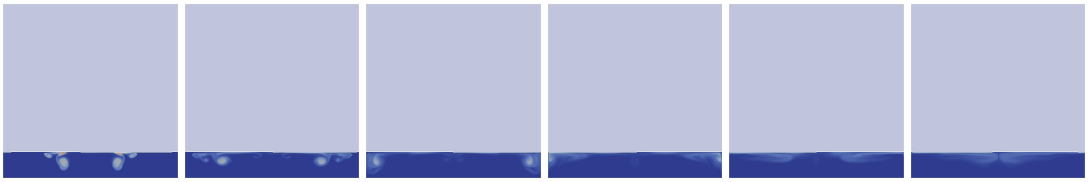

(a) $t = 10s$ (b) $t = 20s$ (c) $t = 30s$ (d) $t = 40s$ (e) $t = 50s$ (f) $t = 60s$

Figure A.101: $\boldsymbol{A^* = 2 \times 10^{-4}}$

(a) $t = 10s$ (b) $t = 20s$ (c) $t = 30s$ (d) $t = 40s$ (e) $t = 50s$ (f) $t = 60s$

Figure A.102: $\boldsymbol{A^* = 1 \times 10^{-3}}$

(a) $t = 10s$ (b) $t = 20s$ (c) $t = 30s$ (d) $t = 40s$ (e) $t = 50s$ (f) $t = 60s$

Figure A.103: $\boldsymbol{A^* = 1 \times 10^{-2}}$

(a) $t = 10s$ (b) $t = 20s$ (c) $t = 30s$ (d) $t = 40s$ (e) $t = 50s$ (f) $t = 60s$

Figure A.104: $\boldsymbol{A^* = 2 \times 10^{-2}}$

Temperature difference, $\Delta T = 16$. Forcing frequency, $\omega = \omega_3$

(a) $t = 10s$ (b) $t = 20s$ (c) $t = 30s$ (d) $t = 40s$ (e) $t = 50s$ (f) $t = 60s$

Figure A.105: $\boldsymbol{A^* = 2 \times 10^{-4}}$

(a) $t = 10s$ (b) $t = 20s$ (c) $t = 30s$ (d) $t = 40s$ (e) $t = 50s$ (f) $t = 60s$

Figure A.106: $\boldsymbol{A^* = 1 \times 10^{-3}}$

(a) $t = 10s$ (b) $t = 20s$ (c) $t = 30s$ (d) $t = 40s$ (e) $t = 50s$ (f) $t = 60s$

Figure A.107: $\boldsymbol{A^* = 1 \times 10^{-2}}$

(a) $t = 10s$ (b) $t = 20s$ (c) $t = 30s$ (d) $t = 40s$ (e) $t = 50s$ (f) $t = 60s$

Figure A.108: $\boldsymbol{A^* = 2 \times 10^{-2}}$

Temperature difference, $\Delta T = 16$. Forcing frequency, $\omega = \omega_4$

(a) $t = 10s$ (b) $t = 20s$ (c) $t = 30s$ (d) $t = 40s$ (e) $t = 50s$ (f) $t = 60s$

Figure A.109: $\boldsymbol{A^* = 2 \times 10^{-4}}$

(a) $t = 10s$ (b) $t = 20s$ (c) $t = 30s$ (d) $t = 40s$ (e) $t = 50s$ (f) $t = 60s$

Figure A.110: $\boldsymbol{A^* = 1 \times 10^{-3}}$

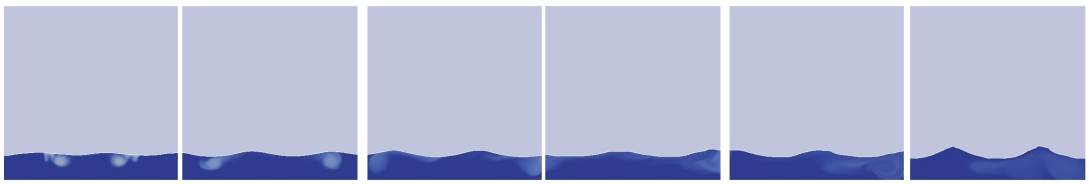

(a) $t = 10s$ (b) $t = 20s$ (c) $t = 30s$ (d) $t = 40s$ (e) $t = 50s$ (f) $t = 60s$

Figure A.111: $\boldsymbol{A^* = 1 \times 10^{-2}}$

(a) $t = 10s$ (b) $t = 20s$ (c) $t = 30s$ (d) $t = 40s$ (e) $t = 50s$ (f) $t = 60s$

Figure A.112: $\boldsymbol{A^* = 2 \times 10^{-2}}$